UNIVERSITY of the
WESTERN CAPE

2D Geomechanical Model for an Offshore Gas Field in the Bredasdorp Basin, South Africa.

Master of Science in Applied Geology

By

Kalidhasen Ramiah

Supervisor: Dr. Mimonitu Opuwari

A thesis submitted in fulfilment of the requirements for the degree of Magister Scientiae in the Department of Earth Sciences, University of the Western Cape, South Africa.

August 2016

2D Geomechanical Model for an Offshore Gas Field in the Bredasdorp Basin, South Africa.

Keywords

Bredasdorp Basin

KR-Field

Well log data

Drilling

Mud window/s

Geomechanical

Tectonic

Overburden

Pore Pressure

Fracture Gradient

Geopressure

Lower hemisphere plot

Maximum/minimum horizontal stress

Abstract

2D Geomechanical Model for an Offshore Gas Field in the Bredasdorp Basin, South Africa.

This thesis provides a 2D geomechanical model for the K-R field, Bredasdorp Basin and describes the workflow and process to do so. This study has a unique density correction software applied to density data, prior to the estimation of geopressure gradients. The aim of this research is to create a model that evaluates the geomechanical behaviour of the upper shallow marine reservoir (USM) and provide a safe drilling mud window for future in the area.

The K-R field has a strong NW-SE fault trend, resulting in a maximum horizontal stress orientation of 125^0, determined from structural depth maps. All geopressure gradients were modelled on the drillworks software at the top (TUSM) and bottom (BUSM) of the reservoir. The Eaton method was used to calculate both pore pressure and fracture gradient and then calibrated with "real" data from well completion and driller's reports. The pore pressure and fracture gradient is what sets the upper and lower mudweight limits. These values range between 8.46-9.60 ppg and 10.12-15.33 ppg respectively.

The rock mechanical properties (Friction angle, cohesive strength and uniaxial compressive strength) were empirically derived and show a similar trend for all wells. The drilling mud window gets more constricted at depths below 2600m, to the TD of the well.

Declaration

I declare that, ***2D Geomechanical Model for an Offshore Gas Field in the Bredasdorp Basin, South Africa*** is my own work and that it has not been submitted for any degree or examination at any other university. Furthermore, all of the sources I have used or quoted have been indicated and acknowledged by complete references.

_____ _____

Kalidhasen Ramiah **Date**

Acknowledgements

I'm immensely grateful to my supervisor Dr. Mimonitu Opuwari, for awarding me the privilege of being one of his Master's students, actively taking an interest in my research and patiently availing himself to discuss my thesis whenever I had any queries.

A huge thank you to my parents for their unwavering and ongoing support, albeit, being in another province, some 1695 kilometres away. I'm highly grateful for your consistent love, words of wisdom and encouragement on a daily basis.

I am incredibly indebted to Mr. Leonardo Santana; genius and geomechanical specialist supreme, for imparting a wealth of knowledge on to me and always being able to assist or demystify any concepts that I might be unclear about.

A warm thank you to K.B. Trivedi and Portia Manuel for being astute mentors and providing both technical and emotional guidance during my time at PetroSA.

To my special group of Homo Sapiens - also known as "PetroSA Graduates In Training" we've formed a close, family bond that has tacitly kept me driven and motivated at all times. We've had a lifetime of memorable moments and I hope that we will work together again in the future.

Contents Page

List of figures

Page

List of Tables Page

List of Appendices Page

Glossary of Terms

Bscf	Billion standard cubic feet
Mscf	Thousand standard cubic feet
MMscf	Million standard cubic feet
MMbbl	Million barrels
Ma	Million years ago
CS	Cohesive strength (Mpa) or (psi)
UCS	Unconfined Compressive strength (Mpa) or (psi)
E	Young's modulus (Gpa)
FA	Friction Angle (^{0})
FG	Fracture Gradient (ppg)
g	Gravitational constant
MMm^3	Million cubic metres
z	Depth (m/ ft)
μs/ft	Microseconds per foot
σ_v	Vertical Stress
σ_H	Maxmimum Horizontal Stress
σ_h	Minimum Horizontal Stress
psi/ft	Pounds per square inch per foot
ppg	Pounds per gallon
P_p	Pore pressure gradient
g/cc /gcm^3	Grams per centimetre cubed
μ	Coefficient of internal friction
API	American Petroleum Institute
RFT	Repeat Formation Test
GR	Gamma Ray
V_{clay}	Volume of Clay
USM	Upper Shallow Marine
BUSM	Bottom Upper Shallow Marine
TUSM	Top Upper Shallow Marine
AFFZ	Agulhas-Falkland Fracture Zone

Chapter 1: Overview

1.1 Introduction

The increase in offshore petroleum exploration world-wide has placed an unprecedented need for understanding wellbore stability conditions. According to Geomechanics International (GMI), the problems associated with wellbore stability cost the industry several trillion dollars per year on the global level.

Geomechanics is a tool that has proven to be highly effective throughout the whole life cycle of a well. The ability to understand the stress field of a basin, calculate geomechnical parameters and recommend a mud window for drilling can lead to greater production and less cost implications.

My research involves creating a 2D geomechanical model for a tight gas field in the Bredasdorp Basin, offshore South Africa. The field is owned by PetroSA, who supplied the data to me and due to a confidentiality clause; the field will be called the "K-R Field" from here on. Seven vertical wells which have already been drilled in the K-R Field were selected to create the model. Each well had accompanying geological well completion reports, well logs, core samples, driller's reports and drill tests.

1.2 Background

Sediments of the Bredasdorp Basin are mainly derived from fluvial and marine channels and are predominantly clastic, organic and clays. In addition, there are biogenic, detrital sediments; hydrocarbon reservoirs in the basin are Cretaceous sandstones. The basin topography follows the direction of the Northwest and Southeast axis of the basin and overpressure exists below 3000m within the basin. However, overpressure in the shale and sandstone units above this depth may exist due to or a combination of geological factors or buoyancy and centroid effects.

Geomechanical work offshore in South Africa is in its infancy. This research study is poised towards calculating the magnitude and providing the direction of principal stresses, calculating rock strength parameters and calculating pore pressure and fracture gradient to evaluate the

safe drilling mud window. The model will assess the principal stresses at reservoir depth, wellbore stability and the mud window for safe drilling.

1.3 Study Area

The K-R Field is located within Block 9, Bredasdorp Basin, offshore South Africa. The extent of the basin is approximately 18,000km^2 with a water depth of less than 200m (Wood, 1995). Geographical coordinates of longitude - 21^0 26'E and 21^0, bound the east west of the study area whilst the north and south are bounded by coordinates (latitude) 35^0 07'S and 35^0 24'S respectively with reference to the equator.

The PetroSA concession Block 9 is demarcated in red, in Figure 1.1. Seven wells of the K-R Field are selected for the geomechanical model and they can be seen on a Petrel base map in Figure 1.2.

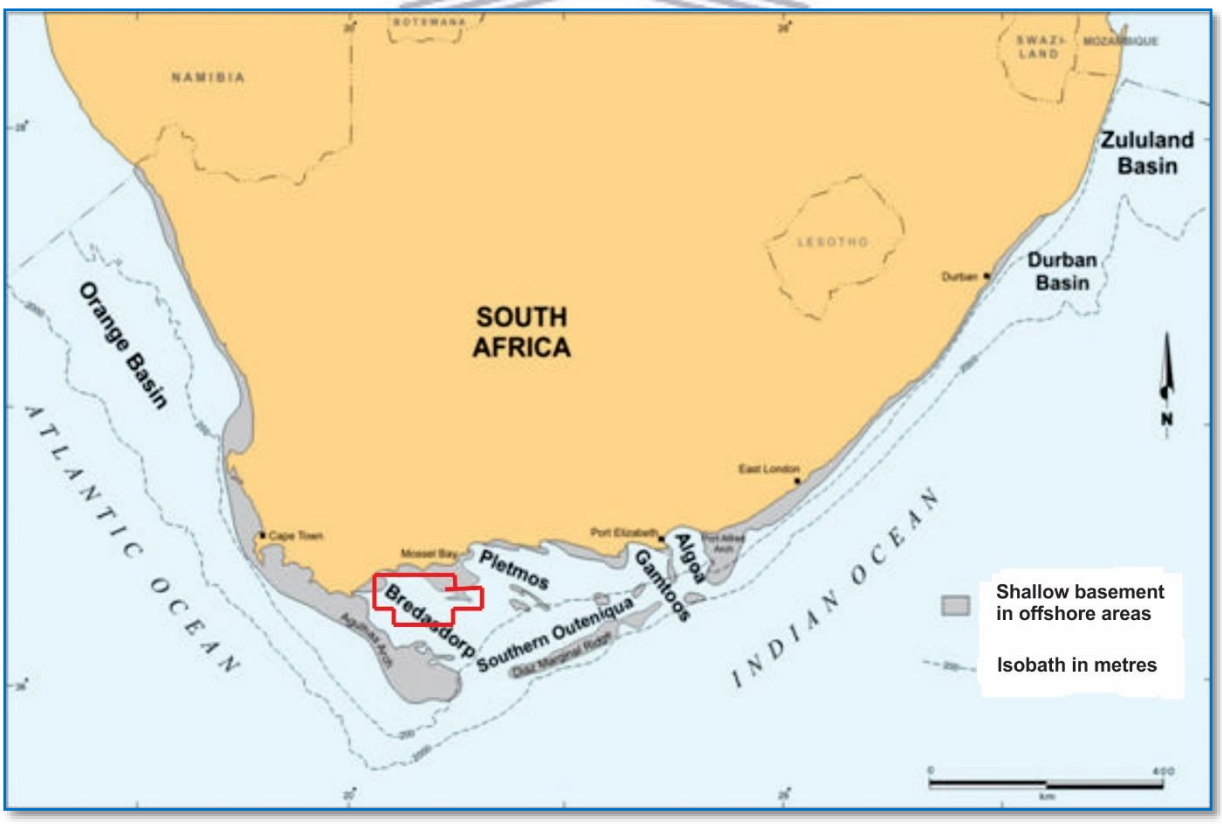

Figure 1.1: Map showing the location and outline of Block 9, Bredasdorp Basin (modified after Petroleum South Africa brochure).

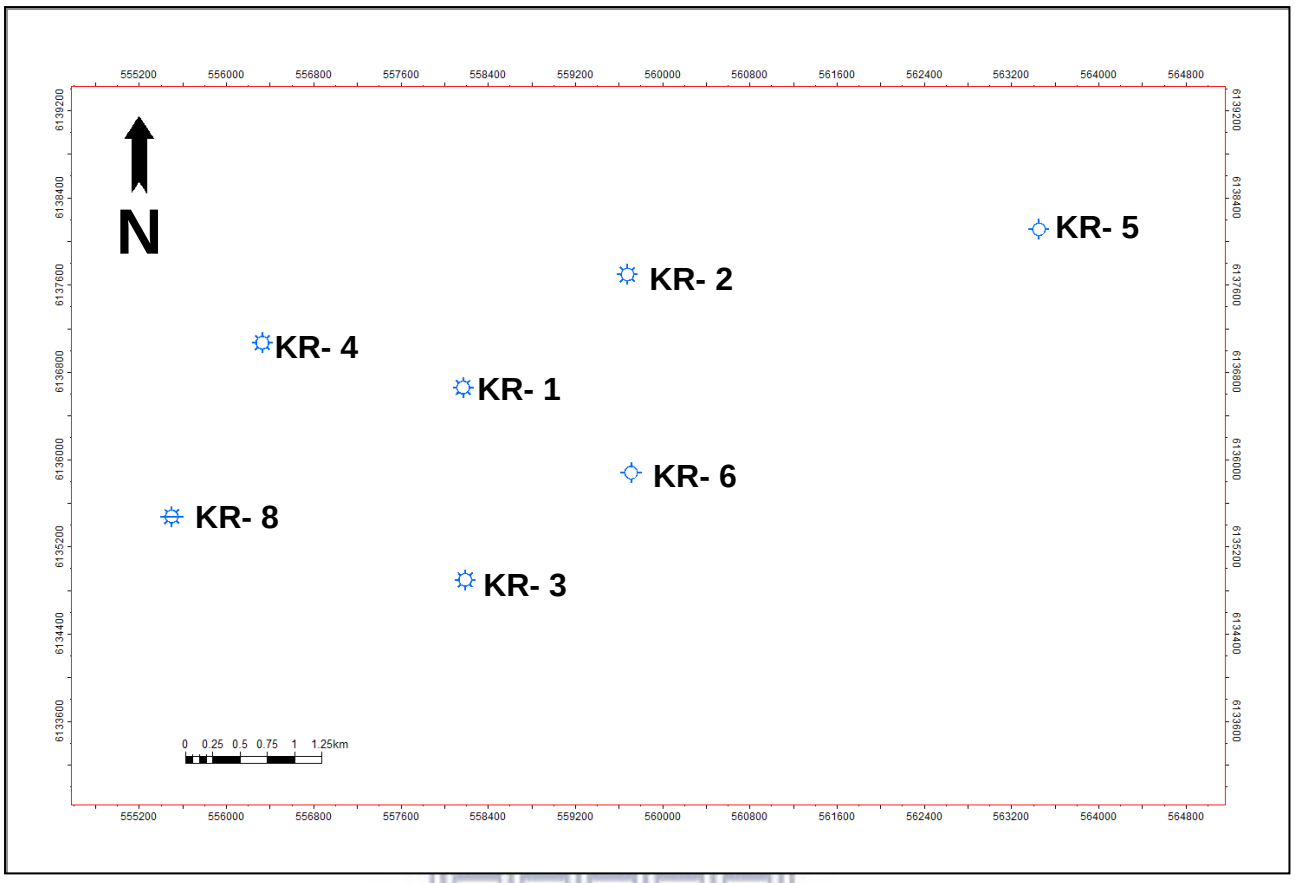

Figure 1.2: Base map showing well location (UTM coordinates) generated in PETREL.

1.4 Aim and Significance of Research

The aim of this research is to provide a post-mortem geomechanical study of the K-R Field wells drilled by PetroSA, and thus, provides a safe operational mud window for any future wells in the field.

Geomechanics is an integrated field that requires knowledge of geology, geochemistry, geophysics, fault tectonics, fluid mechanics, stress and strain behaviour as well as an understanding of engineering principles. This leads to a more holistic understanding of the field and better equips us to derive solutions for problems faced throughout the operational lifecycle.

The K-R Field has had 3 producing wells, KR-1, KR-2, KR-3 which flowed and all the wells have faced poor wellbore conditions with regard to washouts (borehole instabilities), which led to a loss of time that had a direct impact on costs. The study, utilizing density correction

software, unique to PetroSA, addresses some of the reasons as to why this happened and how to avoid such problems in the future.

1.5 Methodology for Geomechanical Modelling

(1) **Data Collating:** This step involved data gathering and well selection. The data I used to construct the geomechanical model included well logging data, core data, drilling surveys and drill tests, drilling and completion reports as well as geological well completion reports.

(2) **Lithology determination:** Lithology classifications were determined from the gamma ray log and Vclay.

(3) **Empirical correlations for elastic moduli and rock strength:** I used well log data to develop empirical correlations for secondary velocity (V_p), unconfined compressive strength, friction angle, Poisson's ratio and Young's modulus.

(4) **Vertical stress:** This was calculated by integrating the corrected bulk density logs.

(5) **Pore Pressure:** Calculated based on the sonic logs using the Eaton pore pressure equation and calibrated using the RFT data.

(6) **Minimum horizontal stress:** Calculated using the Eaton fracture gradient equation and calibrated with leak - off test data.

(7) **Stress direction:** The stress direction ascertained from structural fault maps of the K-R Field.

(8) **Maximum horizontal stress:** This parameter was derived from the wellbore stability simulation since it cannot be measured in-situ.

(9) **Wellbore simulation:** All parameters were modelled two-dimensionally on the Drillworks software to create a predictive geomechanical model for future wells.

1.6 Objectives for Geomechanical Modelling

The objectives for constructing and interpreting the model were to:

(1) Determine rock strength and elastic parameters from logs through empirical correlations.
(2) Understand how the stress regime is a result of faulting at KR.
(3) Indicate the safe operational drilling mud window.
(4) Analyse areas where wellbore failures have occurred.
(5) Provide wellbore stability analysis.
(6) Make recommendations for the safe drilling mud weights that should be used if future wells are to be drilled in the K-R Field.

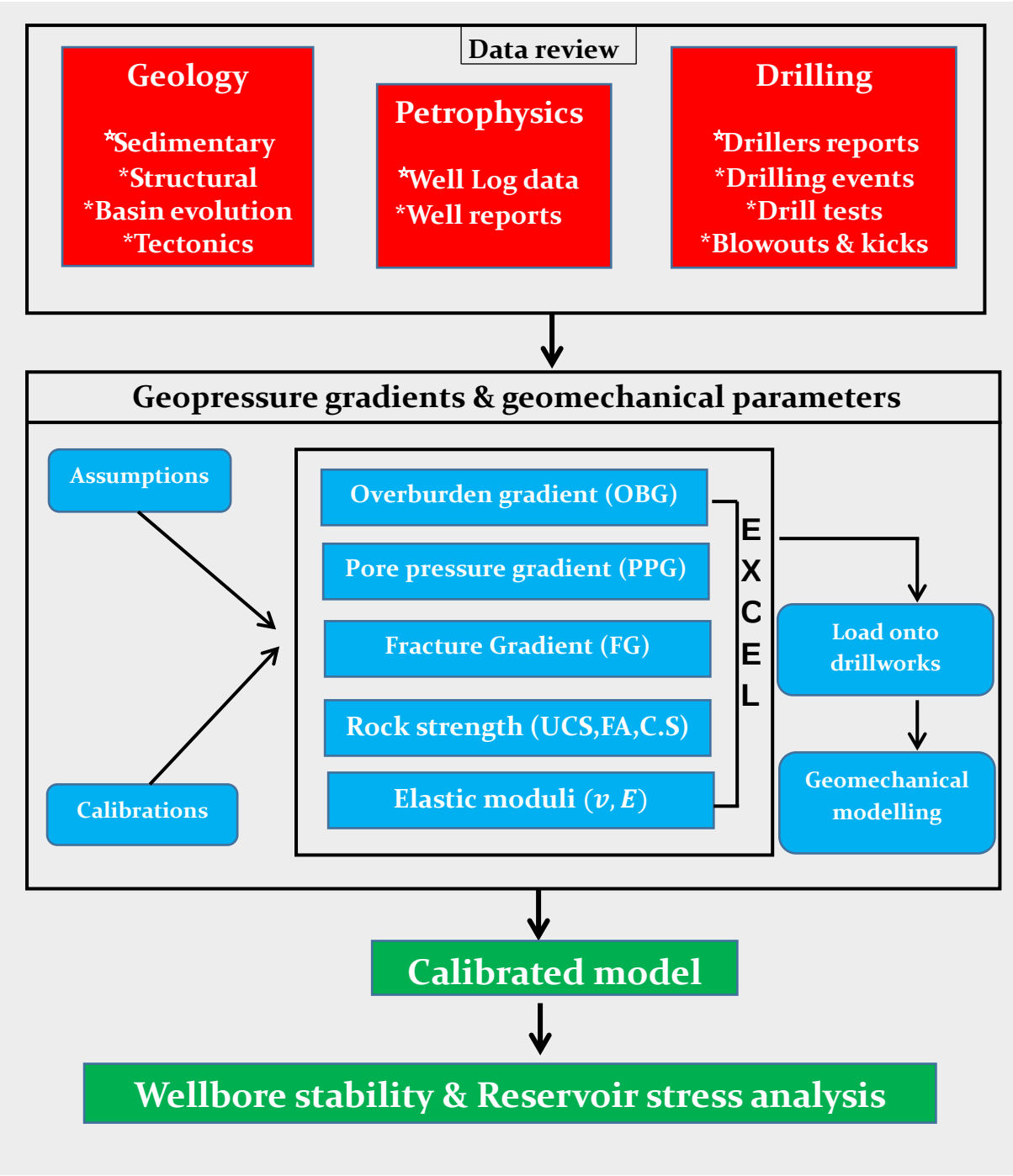

Figure 1.3: Flow chart showing the framework for geomechanical modelling (Halliburton, 2012).

1.7 Geomechanics for Wellbore Stability and Reservoir Characterization

Oil and gas companies generally hire consultants to do geomechanical work, which is then kept privately and not shared with the rest of the industry. In South Africa, geomechanics is a relatively new branch with minimal work being done both onshore and offshore.
Reservoir geomechanics is an integrated study which combines: geology, petrophysics, geophysics, geochemistry, engineering, fracture and fault mechanics, and rock mechanics. A geomechanical model is a mathematical representation of the state of stress and rock mechanical properties for a field. These models are largely constructed from in-situ stress magnitudes and stress directions, pore pressure, static elastic parameters and rock strength properties (Plumb, *et al*., 2000).

Geomechanics can be used throughout the technical life cycle of a field. Areas in which this tool is utilized in the petroleum industry include wellbore stability issues, sand production, pore pressure prediction, bit selection and casing design, mud weight window prediction, subsidence, compaction and fully coupled simulation (Chardac, *et al*., 2005).

The K-R Field is compartmentalized by faults and geomechanics is used primarily to understand how stress magnitudes, stress orientations and rock properties contribute to wellbore stability, thus outlining a safe mud window.

1.8 Outline of Thesis

This thesis is made up of seven chapters which cover the study area as stated in the objectives. Chapters one and two serve as a foundation which gives a fundamental understanding of the basin. Chapter one introduces the research topic and then proceeds by giving some background information, highlighting the study area, a brief summary of geomechanics in this research, together with the challenges and objectives of this research.

Chapter two expounds on the geology of the Bredasdorp Basin, its stratigraphy, depositional environment, petroleum systems, structural tectonics and deformation of the basin as well as the tectonics of the K-R Field in particular.

Chapter three, “petrophysics and empirical correlations” introduces the concept of petrophysics, its importance for geomechanics and describes some of the selected petrophysical tools. The methodologies for all the empirical correlations and their derivations are explained. Chapter four provides insight into geomechanical modelling and the way in which the model was created using the drillworks software. The derivation of principal stresses, pore pressure and information used as calibration are explained here.

Chapter five, “simulation and results” covers the geomechanical results of reservoir stress states and wellbore stability analysis which were simulated from the software.

Chapter six is the discussion of the results and chapter seven provides conclusions and recommendations.

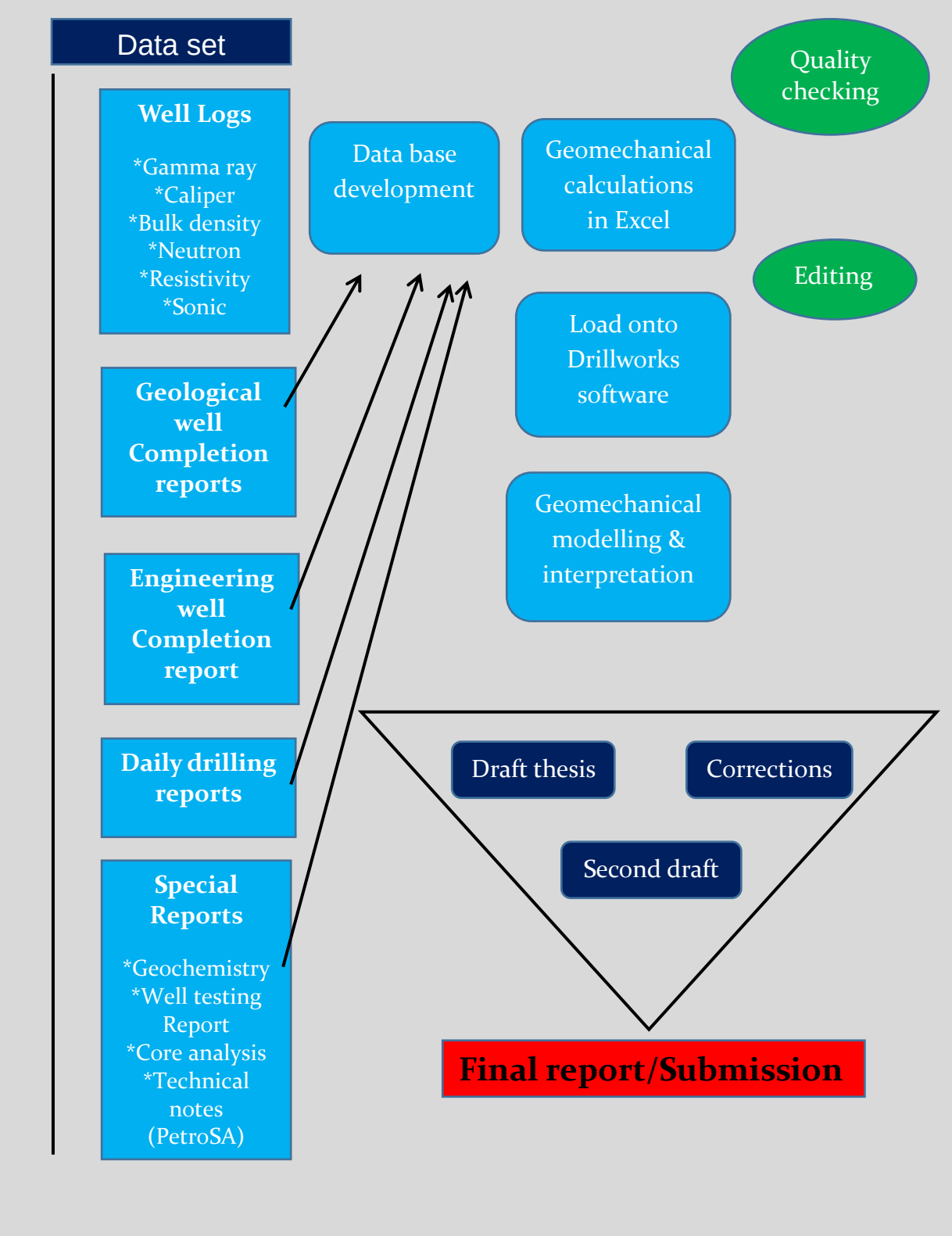

Figure 1.4: Diagram showing elements that make up this thesis.

Chapter 2: Geological Background of the Bredasdorp Basin

2.1 Introduction

The Bredasdorp Basin is a south-easterly trending basin which formed along with other sub-basins of the larger Outeniqua Basin, during the break-up of Gondwana along the Agulhas-Falkland Fracture Zone. Van der Merwe, *et al*., (1992), points toward the evidence for high tectonic inversion within the basin. The basin contains two syndrift phases of sedimentation. The first phase (syndrift 1) of sedimentation is an unconformity which formed due to tilting and can be dated to the early Jurassic period. The blocks are faulted with deep marine sediments underlying shallow marine sediments. The second phase (syndrift 2) contains deep water marine sediments found over tilted fault blocks; and indicator of rapid subsidence and wide spread flooding.

The K-R Field within the Bredasdorp Basin has a peculiar anticlinal structure with immense faulting creating compartments of shale and sandstone sequences. This section covers the geological history, tectonism, pressure gradients and sequence stratigraphy of the basin, zoning in the K-R Field, to understand the area of study.

2.2 Regional Tectonic Setting

The structural setting of the South African offshore basins is best understood with reference to the plate tectonic development of the southern African plate before, during and after the break-up of Gondwana (Broad *et al.*, 1996). Subduction during the Late Carboniferous to Early Permian period along the southwest margin of Gondwana led to the passive margin being changed into a foreland basin, which is now known as the Karoo Basin (Petroleum Agency Handbook SA, 2005). Sediments were sourced into the basin from the south. The Cape Fold Belt (CBM) formed during the Permo-Triassic period by the formation of an arc which thrusted up the Cape Supergroup (Figure 2.1) that spans over four continents (Petroleum Agency Handbook SA, 2005).

Volcanic activity during the Early to Middle Jurassic period marked the end of erosion. Evidence of this is observed in South Africa, Antarctica and the Falklands (Petroleum Agency

Handbook SA, 2005). The eastern region of Africa started to break away with Madagascar and Antarctica pulling away; leading to the formation of the Durban and Zululand Basins (Petroleum Agency SA Handbook, 2005).

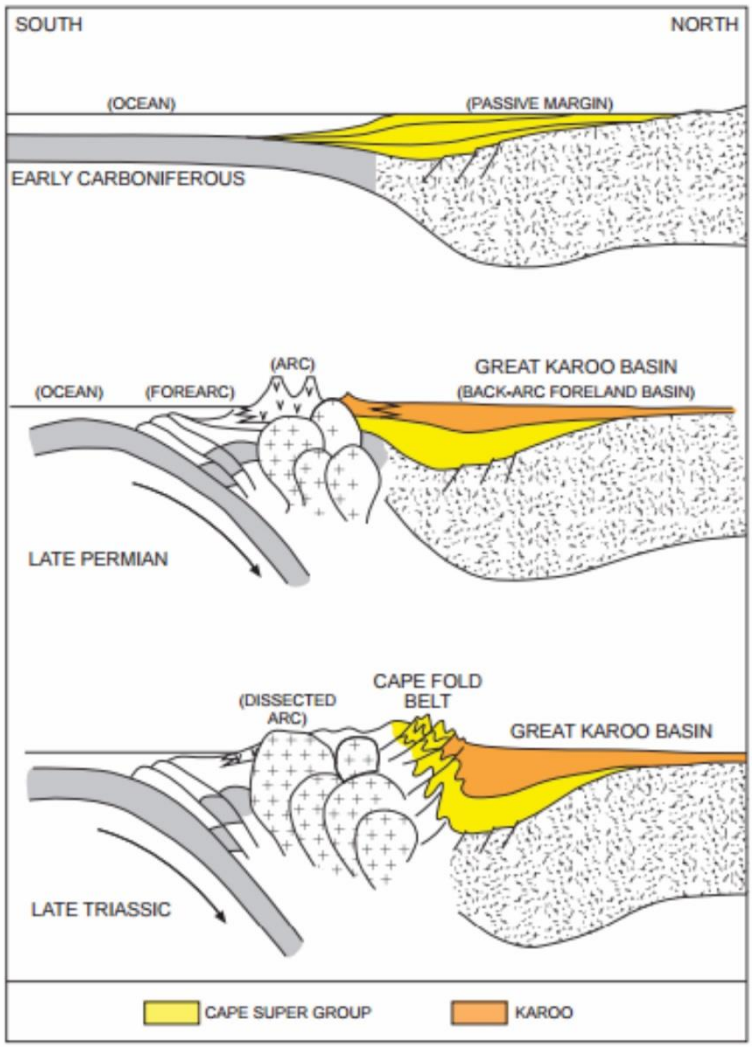

Figure 2.1: Evolution of Cape Fold Belt and Great Karoo Basin (Petroleum SA Handbook, 2005).

The Falkland Plateau moved along the south coast of Africa during the Early to Middle-Cretaceous period, resulting in dexteral shearing which gave rise to the sub-basins of the Outeniqua Basin (Petroleum Agency SA handbook, 2005). These basins are a product of failed rifting which created half grabens starting in the east (Algoa Basin) and progressing towards the west (Bredasdorp Basin). The rift phase of the south coast ended in the lower Valanginian, which is associated with the onset of the drift unconformity (1At1) (Petroleum Agency SA Handbook, 2005). The Mid-Albian period saw the end of the drift phase, as the Falkland

Plateau separated from Africa, giving rise to a passive margin (Petroleum Agency SA Handbook, 2005).

2.2.1 The Outeniqua Basin

The Northern Outeniqua Basin is composed of a number of en-echelon sub-basins; the Bredasdorp, Pletmos, Gamtoos and Algoa Basins which, together with the smaller Infanta Embayment, converge to the south to form the deeper Southern Outeniqua Basin (Figure 2.2; Broad *et al*., 1996). The sub-basins are grabens separated by basement arches of Ordovician to Devonian meta-sediments of the Cape Supergroup with its arcuate trend inherited from the structural grain of the orogenic Cape Fold Belt (Broad *et al*., 1996). Numerous structural characteristics of the Outeniqua sub-basins can be elucidated in terms of strike-slip faulting, and more so in the basins closest to the Agulhas-Falkland Fracture Zone (AFFZ; Broad *et al*., 1996). In addition it has also been suggested that inversion tectonics due to periodic movement on the AFFZ contributed significantly to the structure of the basins (Broad *et al*., 1996).

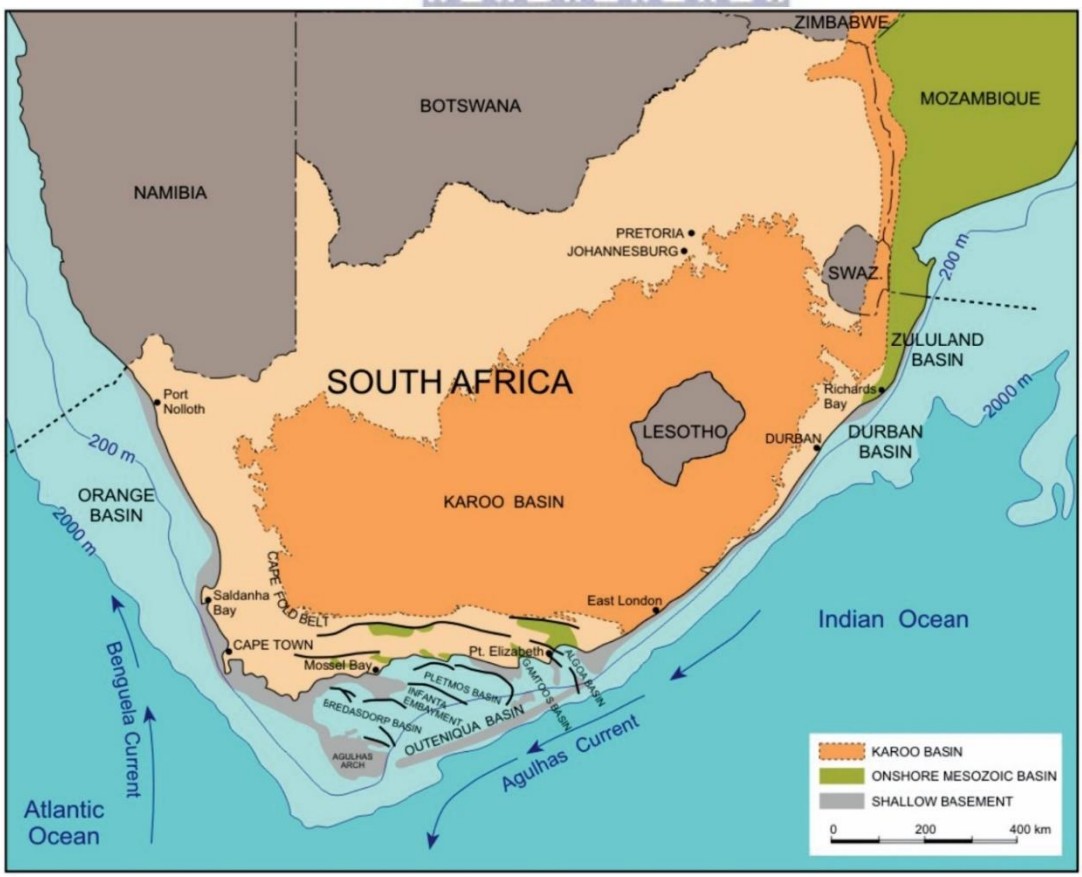

Figure 2.2: Sedimentary basins of South Africa (www.petrosa.co.za).

2.3 The Bredasdorp Basin

The Bredasdorp Basin is a sub-basin of the Outeniqua Basin that covers an area of 18000km^2 beneath the Indian Ocean on the southern South African Coast. It is located off the south coast of South Africa, southeast of Cape Town and west-southwest of Port Elizabeth (Turner J.R. *et al*., 2000). The geology comprises Upper Jurassic, Lower Cretaceous (Synrift continental and marine strata) and Cretaceous and Cenozoic (post-rift divergent margin strata). The Bredasdorp Basin is bounded by the Agulhas Arch (west and southwest) and the Infanta Arch (northeast) as can also be seen in Figure 2.2 (Brown, *et al*., 1995, Turner *et al*., 2000). A structural cross section of the Bredasdorp Basin is shown in Figure 2.3.

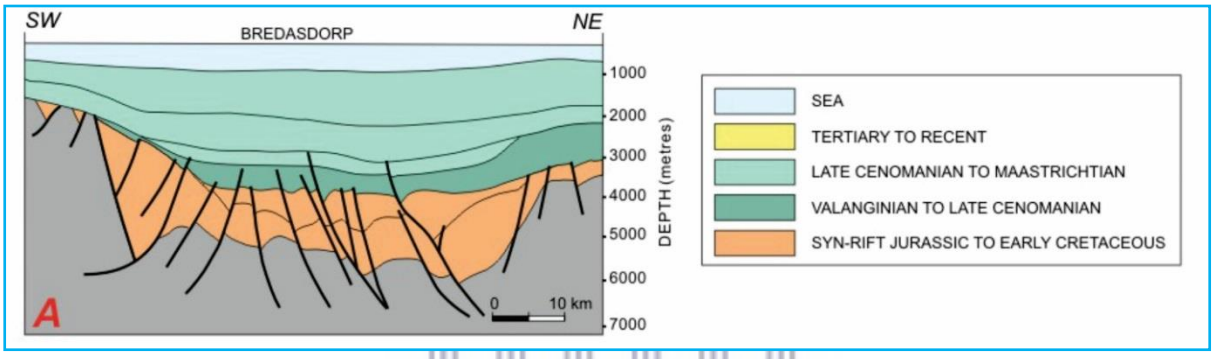

Figure 2.3: Geological cross-section of the Bredasdorp Basin (Petroleum Agency Handbook SA, 2005).

2.3.1 Tectonic Setting of the Bredasdorp Basin

McMillian *et al*., 1997 stated that break up in the east caused dexteral transtensional stresses which gave rise to normal faulting in the northern Agulhas-Falkland Fracture Zone. Faults between the Agulhas Arch and the Infanta Arch trend northwest to southeast. This normal faulting resulted in graben and half-graben basins (Brown *et al*., 1995, McMillan *et al*., 1997). Sedimentation from Horizon D to 1At1 (Figure 2.4) ceased at ~126Ma from; tectonics, erosions and deposition then commenced (Brown *et al*., 1995). During the rift phase, the Bredasdorp Basin was sourced from provenances in the north and northeast comprising slates and orthoquartzites eroded from the Cape Supergroup as well as sandstones and shales from the Karoo Supergroup (McMillan *et al*., 1997).

Brown *et al*., 1995 stated that the 1At1 unconformity is a result of upliftment of the arches and horst block which terminated rift sedimentation. Unconformities 1At1 up to 13At1 were formed by thermal subsidence, reactivated faulting and continued deposition of post-rift onlap-fill sequences which took place in the central Bredasdorp Basin between 126 - 117.5Ma (McMillan *et al*., 1997). This period is associated with a subsiding basin due to rift faulting. Subsidence was rapid during the formation of the 1At1 sequence but diminished towards the end of 5At1 marking the first supercycle (Brown *et al*., 1995). Erosion occurred carving submarine valleys and canyons into the strata above the 1At1 sequence; providing sediment supply deeper into the basin area from the northwest, west and southwest (Brown *et al*., 1995, McMillan *et al*., 1997). Unconformity 6At1 was triggered by Uplift (Brown *et al*., 1995). Sediment supply from sequences 5At1 to 13At1 were due to turbidity currents (McMillan *et al*., 1997). A second supercycle (6-12) occurred between 115.5 – 112Ma with high rates of regional subsidence producing sequence 6A (Brown *et al*., 1995). Subsidence rates and faulting slowed down between 115.5 -112Ma which led to the deposition of sequences 8-12 with sequence 7 being removed by 8At1 erosion during 116 - 115Ma (Brown *et al*., 1995).

Turner *et al*., 2000 noted that a sea level drop (112 - 103Ma) caused erosion from the highstand shelf sandstones which were transported into the central Bredasdorp Basin by turbidity currents from west to south west. These sediments were then deposited as "stacked and amalgamated channels and lobes" with fan lobes exhibiting coarsening upwards sequences and reservoirs characterized by fining-upwards (Turner *et al.*, 2000). Channels dominate the western to south-western area; lobes dominate the eastern portion of the basin (Turner *et al.*, 2000).

A drop in sea level between the period of 103Ma-112Ma, resulted in material being eroded from highstand shelf sandstones, which were transported into the centre of the basin by turbidity currents from west to southwest (Turner *et al*., 2000). These sediments formed "stacked and amalgamated channels and lobes" (Turner *et al*., 2000), which include fan lobes of a coarsening-upward nature with reservoirs consisting of channel deposits characterised by fining-upwards (Turner *et al*., 2000). The Channels dominate the western to south-western area whereas the fan lobes are dominant in the eastern parts of the basin (Turner *et al*., 2000). Source rocks of Aptian age can be found in the south of the basin (this being due to the formation of a 5km wide and 50km long submarine channel with tributaries updip serving as conduits of deeper sedimentation) (McMillan *et al*., 1997) and the organic material is mainly type 2 (Van

Der Spuy, 2000). Oil accumulation occurs in the 13A channel and the basin floor-fan sandstones of the 14A sequence contains some oil bearing reservoirs (McMillan *et al*., 1997). Erosion is marked by sequence 15At1 during the late Cenomanian period and was at its maximum in the eastern most part of the basin. Progradation occurred between Turonian and mid Coniacian; the late Cretaceous period saw the formation of a domal structure in the south eastern region of the Bredasdorp Basin (McMillan *et al*., 1997).

Deposition of highstand shelf deposits (biogenic clays, glauconitic clay and sands) occurred during the Tertiary period. These sediments were derived from erosion of the Agulhas Arch flanks due to uplift in the Late Cretaceous period, which concluded in the Early Miocene period (McMillan *et al*., 1997). Unconformities in the Holocene and Late Pleistocene overlay the Miocene strata which mark several Type-1 sequence boundaries that can be seen in the chronostratigraphic log in Figure 2.4 (McMillan *et al*., 1997). Two synrift phases are displayed, the first from the Early Jurassic period (157.1 Ma) to the Lower Cretaceous period (121Ma) the second being a much shorter synrift phase within the Hauterivian, which was separated by the first Type-1 Unconformity (1At1).

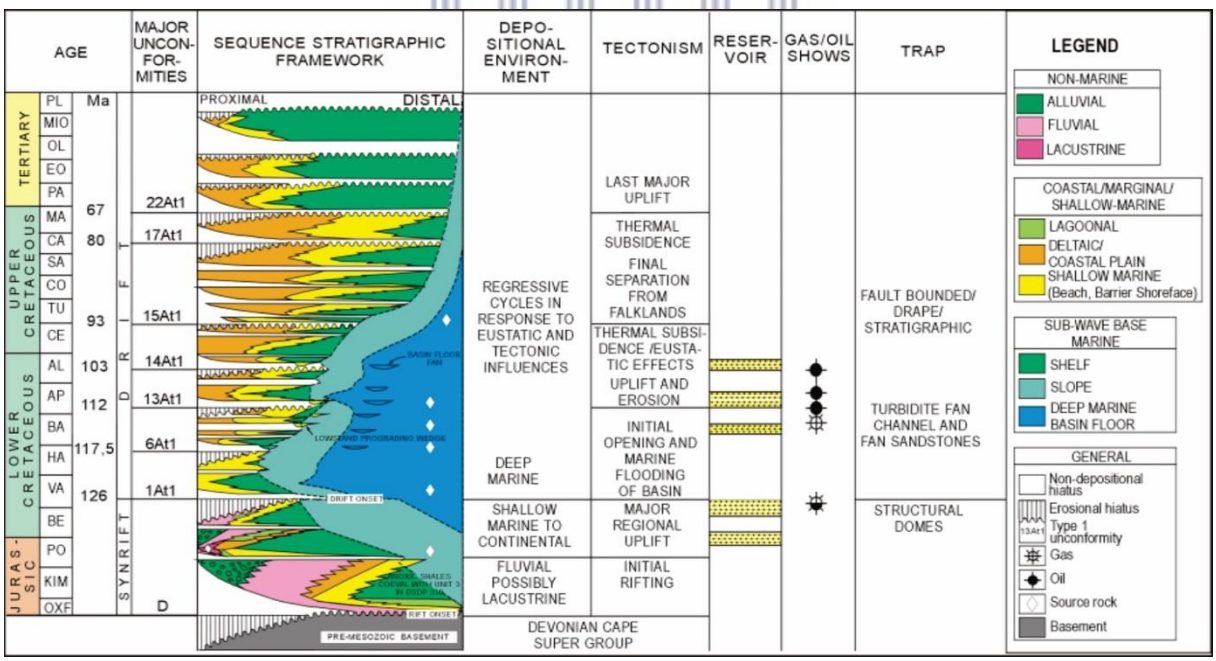

Figure 2.4: Chronostratigraphy of the Bredasdorp Basin (Petroleum Agency Handbook SA, 2005).

The transitional phase marks the development of a lowstand prograding wedge due to shelf deposition and basin floor and slope fans towards the distal part is evident (Figure 2.4). It is

apparent that the main organic-rich shale, which is a good possible source rock for petroleum generation, occurs predominantly in the distal part within the transitional phase. The onset of the drift phase is marked by unconformity 14At1 as well as the onset of thermally induced sag.

2.3.2 Thermal Gradient History of the Bredasdorp Basin

The present thermal gradient of the Bredasdorp Basin lies between 35-49^{0}C.km^{-1} (Davies, 1997). Temperature reduction during the Late Cretaceous period was due to reduced heat flow and subsidence after rifting. Africa migrated over a mantle plume during the late Cretaceous to early Tertiary periods, causing regional uplift which increased heat flow into the Bredasdorp Basin. Prior to ~80Ma, temperatures within the basin increased at a rate of >3^{0}C/Ma. Sedimentation rates decreased at about ~80Ma to ~55Ma, resulting in an average temperature rate drop of <0.3^{0}C/Ma (Early Tertiary) which increased again during the Miocene to Pliocene periods (Davies, 1997). Oil bearing source rocks of the Turonian saw a temperature increase of ~10^{0}C between ~80Ma to ~55Ma (Davies, 1997). Migration of formation waters from the southern Outeniqua Basin into the Bredasdorp Basin increased the temperatures by ~20^{0}C. Early burial, hotspot transit and a hydrothermal event affected the maturation of Aptian and older formations. (Davies, 1997).

2.3.3 Formation Pressures in the Bredasdorp Basin

Regional pressure studies on the basin were based mainly on data from Cretaceous reservoirs which indicate three pressure regimes (Winter, 1981; Brink and Winters, 1989; McAloon *et al*., 1990; Larsen, 1995). The three pressure regimes are:

1) A normally pressured zone down to ~3000m (Davies, 1988b).
2) A second zone associated with thick source rocks (mainly 13A Aptian), in which equivalent mud weights (MW_{equiv}) are as high as 1.15 psi/ft.
3) A third zone where high overpressures are developed (>3000psi above hydrostatic). These pressures as recorded from RFT and DST readings are also estimated from petrophysical calculations (Verfaille, 1993).

High formation pressures are found in Valanginian sandstones and the highest pressured reservoirs, Hauterivian (5A) sandstones, show pressure readings of ~0.73 psi/ft (Davies, 1997). The regional pressure distribution in a few reservoirs differs. Overpressure is recorded in the Lower Albian (13B) sandstones just above ~2600 metres bKb. Oil-bearing fractures in diagenetically calcitised sandstones may suggest 'possible intermittent pressure build up/release episodes' (Brown, 1991; Davies, 1995c).

2.3.4 Periods of Tectonic Adjustment

Compression in the Mid-Jurassic period, which is probably synonymous with early separation of the Falkland Plate, affected all offshore basins (Van der Merwe and Fouché, 1992). As a result, uplift and erosion of Palaeozoic metasediments and Karoo sedimentary rocks occurred (Rowsell and De Swardt, 1976). The second phase of compression happened during the Hauterivian period and could be related to the impact of the Falklands plate on the south coast of Africa. This resulted in an anglar unconformity at horizon 5At1, which is the product of major uplift and erosion (Davies, 1997). Shortly after the deposition of Albian 14A, a third phase of compression occurred. This formed the central basin structural highs. Davies, 1997 stated that 'this phase of compression is probably related to the passage of the eastern end of the Falkland Plate past the Agulhas Arch'. The Bredasdorp Basin subsided again; according to Honiball, 1995, this probably happened when the Falkland Islands finally cleared the southern tip of the Agulhas Arch and no further compressional events occurred.

The Late Maastrichtian period saw the start of the final major uplift of the Agulhas Arch which reached a maximum of ~300m during the period 66-64Ma (McMillan, 1986). This uplift, together with associated erosion could be due to heat flux during passage of the Bouvet/Shona hotspot (McMillan *et al*., 1997). A major uplift of the western part of the basin is thought to have been the result of mid-Oligocene tilting which could have resulted in erosion of >1000m (McMillan, 1986).

2.3.5 Faulting

Early rifting during the formation of the Bredasdorp Basin resulted in a WNW-ESE trending grabens with several half-grabens which are most prominent in the north and south flanks

(Davies, 1997). The regional trend of the Bredasdorp Basin (WNW-ESE) is 'modified by trending NW-SE at the western and eastern ends' (Davies, 1997). Fouché *et al*., 1992 stated that these fault trends may be due to drag along the Agulhas-Falkland Fracture Zone; or inherited Cape Fold Belt faults (Cartwright, 1989). Some faults may have been reinitiated during 5At1 times and some of them at a much later period during 9At1 formation (Hodges, 1996). Davies, 1996c suggests that these faults are conduits for gas migration.

2.3.6 Sequence Stratigraphy of the Bredasdorp Basin

Sequence stratigraphy is an important field that has been applied to the post rift (Lower Cretaceous) sequences of the Bredasdorp Basin for correlation of deposition tracts and facies mapping. It is the study of genetically related facies within a framework of chronostratigraphically significant surfaces (Van Wagoner *et al*., 1990). It integrates time and relative sea level, used in seismic stratigraphic and sequence analyses and is a prediction tool for facies, chronostratigraphically bounded by unconformities.

Approximately 10 cyclic sequences and mega sequences occurred during the mid-Valanginian and lower Santonian periods, as a result of: decreased rifting, thermal cooling and eustatic variations in global sea levels. Various units of the low stand system tracts (LST) appear to be prospective for hydrocarbons. LST are developed on type 1 unconformities, which resulted from sea levels fall below the shelf edge. Erosional type 1 unconformities, which often exhibit canyons and incised valleys, provide surfaces on which the following are deposited:

1. Sheet like submarine/basin-floor fans.
2. Submarine channel fill, mounds and fans.
3. Prograding deltaic wedges.

These features formed together with the erosion of incised valleys and submarine canyons, are followed by channelized slope fans and deltaic lowstand wedges that prograded during sea level rise (Figure 2.5 (a), (b) and (c)).

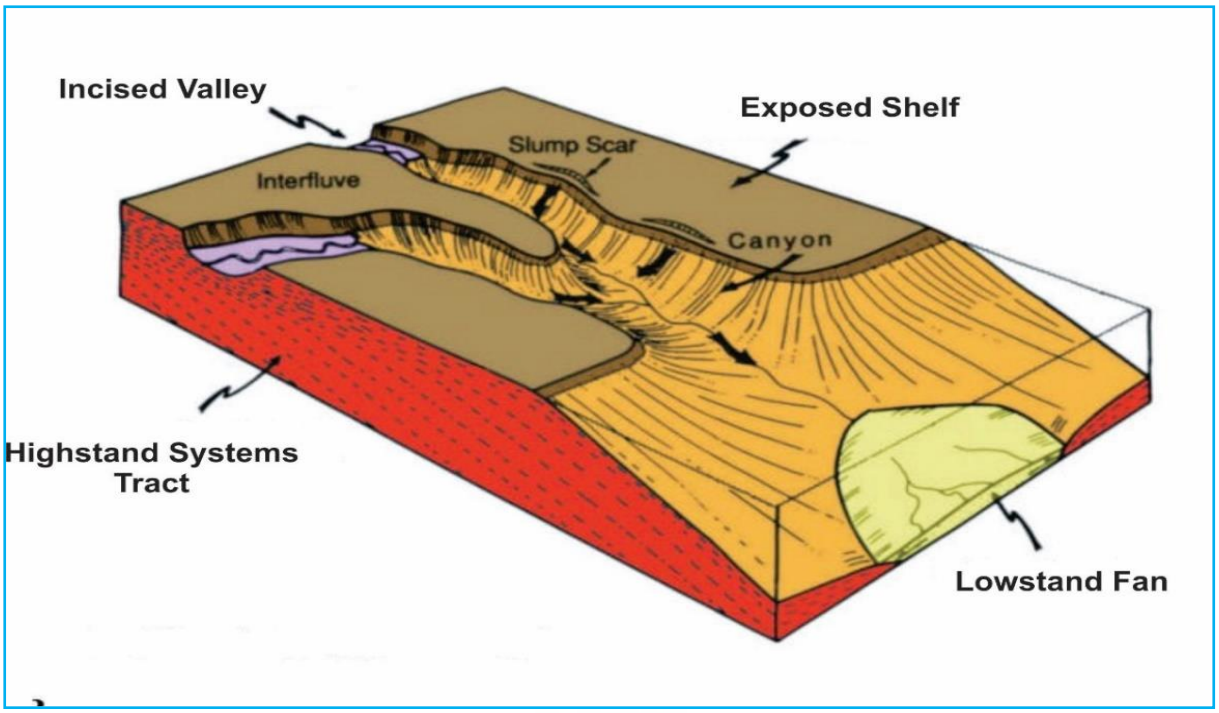

Figure 2.5a: Basin floor fan (Lowstand fan) on canyon floor (modified from Broad, 2004).

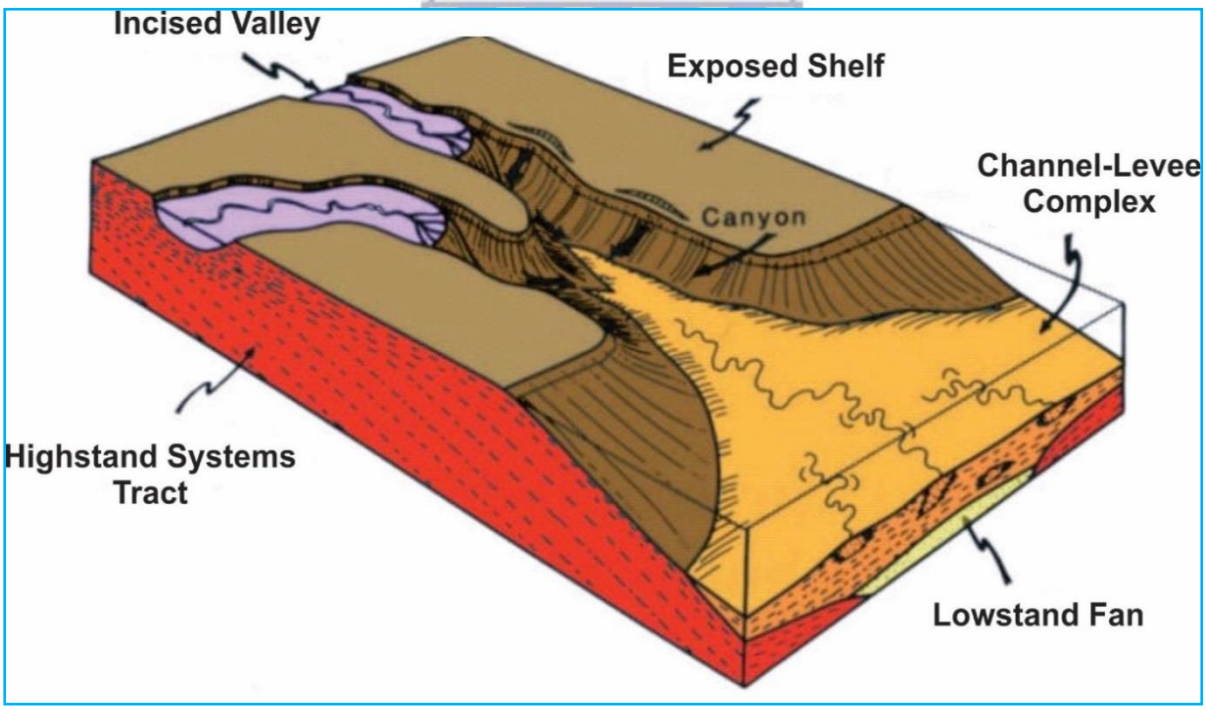

Figure 2.5b: Basin floor fan (Lowstand fan) on canyon floor (modified from Broad, 2004).

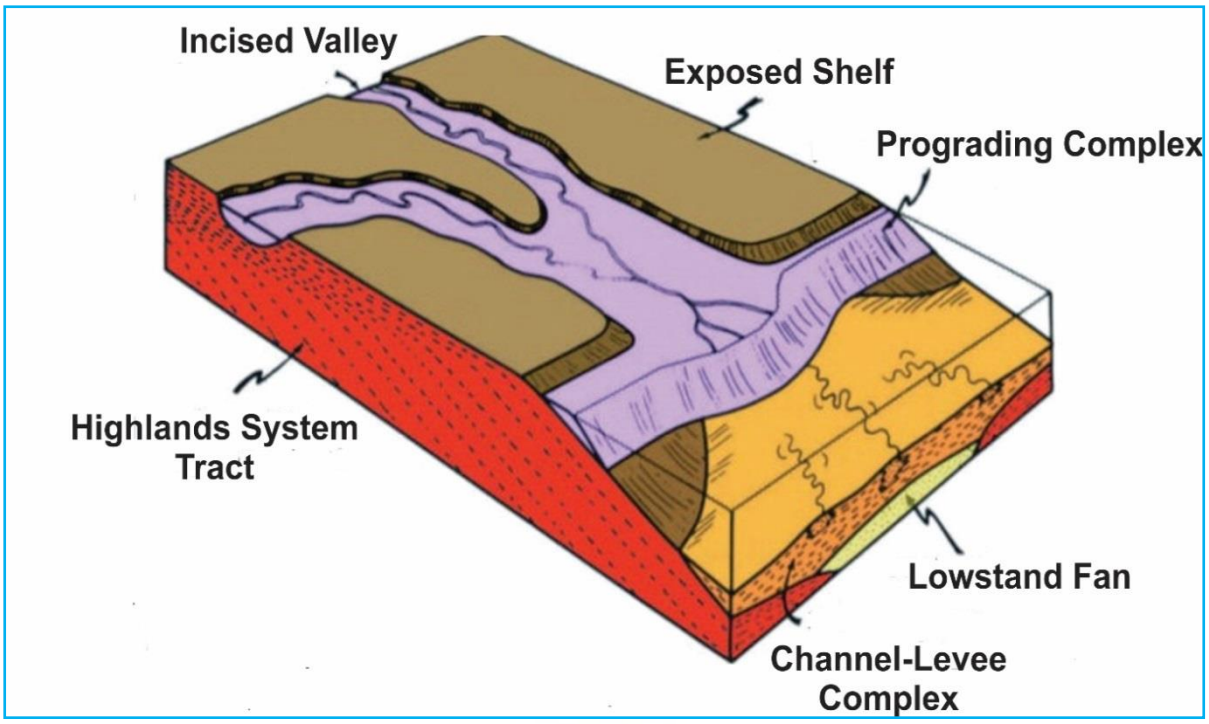

Figure 2.5c: Termination of prograding complex and canyon filling episode (modified from Broad, 2004).

The fans, channel fills, and wedges are sourced by shales and marine condensed sections developed during the transgressive phase, deposited at a time of regional transgression of the shoreline. Flooding of the shelf due to sea level rise resulted in poorly defined transgressive system tracts. Extensively developed deltaic systems prograded basinward, thus exhibiting well-defined clinoforms; the relative sea level at a highstand.

2.4 The K-R Field

The K-R gas field was discovered in 1983 about 50km west, off the F-A gas field (Figure 2.6). Its discovery can be attributed to rigorous offshore exploration in South Africa. The completion of the K-R gas field took place in 2001 by Petroleum South Africa (PetroSA) who owns the license to the field.

During exploration; gas discoveries were made in well KR-1 and KR-8, potentially commercial gas and encouraging oil flow rates in well KR-2, KR-4 and KR-6, a dry well for KR-5 and a dry well with encouraging oil shows in KR-3. Broad, 2004 asserts that the Bredasdorp Basin

is the most explored basin with proven reserves in South Africa. The basin has a complex tectonic setting and peculiar geological structures.

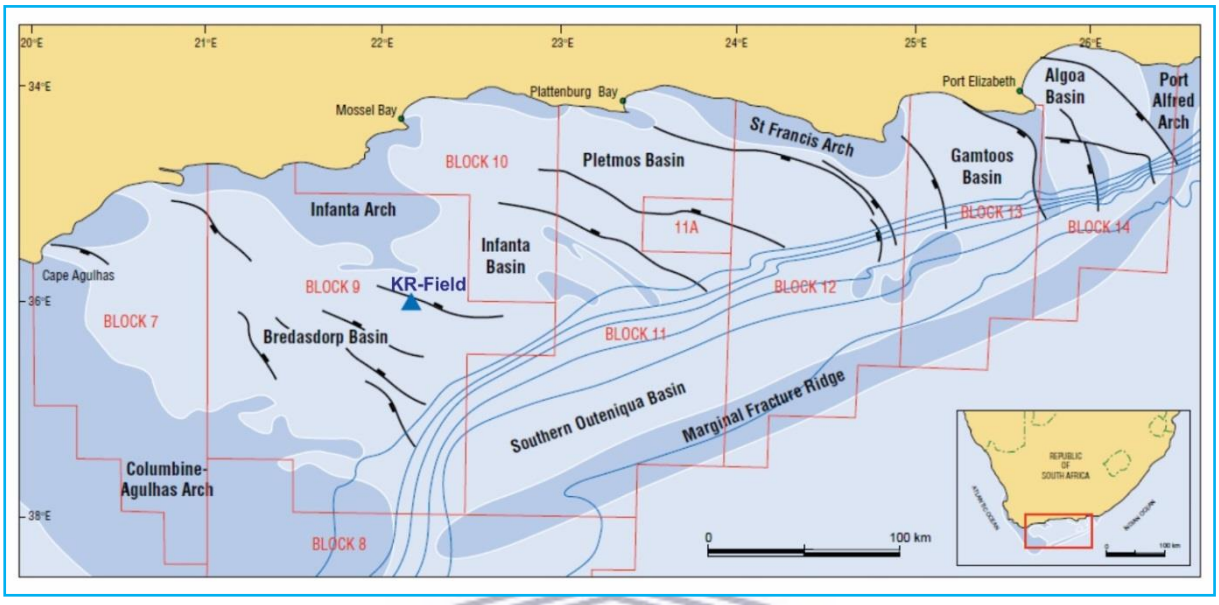

Figure 2.6: Location of the KR-Field within the Bredasdorp Basin in relation to different blocks in the Outeniqua Basin (Modified from Petroleum Agency Handbook SA, 2005)

2.4.1 Reservoir Geology

The K-R reservoir comprises the syn-rift, Berriasian-Valanginian (Lower Cretaceous) Upper Shallow Marine (USM) Sandstone, which is defined seismically by the Top Upper Shallow Marine (TUSM). The Base Upper Shallow Marine (BUSM) horizon is poorly defined and no intrareservoir horizons are seismically mappable. Several other seismic horizons have been mapped in the reservoir overburden: 1At1, 6At1, 8At1, 13At1, which can be seen in Figure 2.7. The 1At1 and 6At1 are known to be unconformable indicating local erosion downwards into the USM, especially along the southern flank of the field and possibly on the western and eastern flanks in the saddle separating KR-5 from the K-R structure.

The USM provides the prospective reservoir sections along the north-eastern margin of the basin in Block 9 and is subdivided into Zones 2, 3 and 4 (Table 1).

Table 1: Reservoir zones for USM

Zone	Depositional Environment
Zone 2B	Shallow Marine
Zone 2A	Shallow Marine
Zone 3	Fluvial
Zone 4	Shallow Marine

Zones 2 and 4 represent shallow marine sandstones whereas Zone 3 essentially comprises fluvio-deltaic sandstones, but with some marine influence to the south. The lowermost interval, Zone 4, is Berriasian in age, based upon palynofacies studies (Timetrax, 1999). The USM varies in thickness between 158m and 338m in wells on the field but generally thickens northwards into the hanging wall of a major east-west trending fault system located beyond the field limit.

Table 2: Reservoir depths at TUSM and BUSM for all K-R wells.

Wells	KR- 1	KR- 2	KR- 3	KR-4	KR-5	KR-6	KR-7
TUSM	2499.7	2593.2	2564.0	2558.0	2505.5	2557.0	2565.8
Zone 2B	2499.7	2593.2	-	2558.0	2505.5	2557.0	2565.8
Zone 2A	2524.0	2622.0	-	2584.0	2533.5	2578.0	2594.8
Zone 3	2561.0	2656.5	2564.0	2617.0	2559.0	2608.0	2623.5
Zone 4	2642.0	2750.0	2621.0	2707.0	2655.0	2683.0	2715.5
BUSM	2737.0	2859.5	2722.0	2830.8	2759.0	2723.0	2828.7

Table 3: Porosity and Permeability values for all K-R wells.

Wells	KR- 1	KR- 2	KR- 3	KR-4	KR-5	KR-6	KR-7
Poro (%)	15.5	13.5	11.7	14	15.7	10	14.5
Perm (mD)	210	66	2.5	53	71.4	3.2	94

Table 3 shows a distinct drop in permeability within the K-R structure but the porosity is somewhat maintained. The reservoir is porous to slightly porous and the shallow marine sandstones are underlain by non-glauconitic channel sandstones and green and red claystone beds.

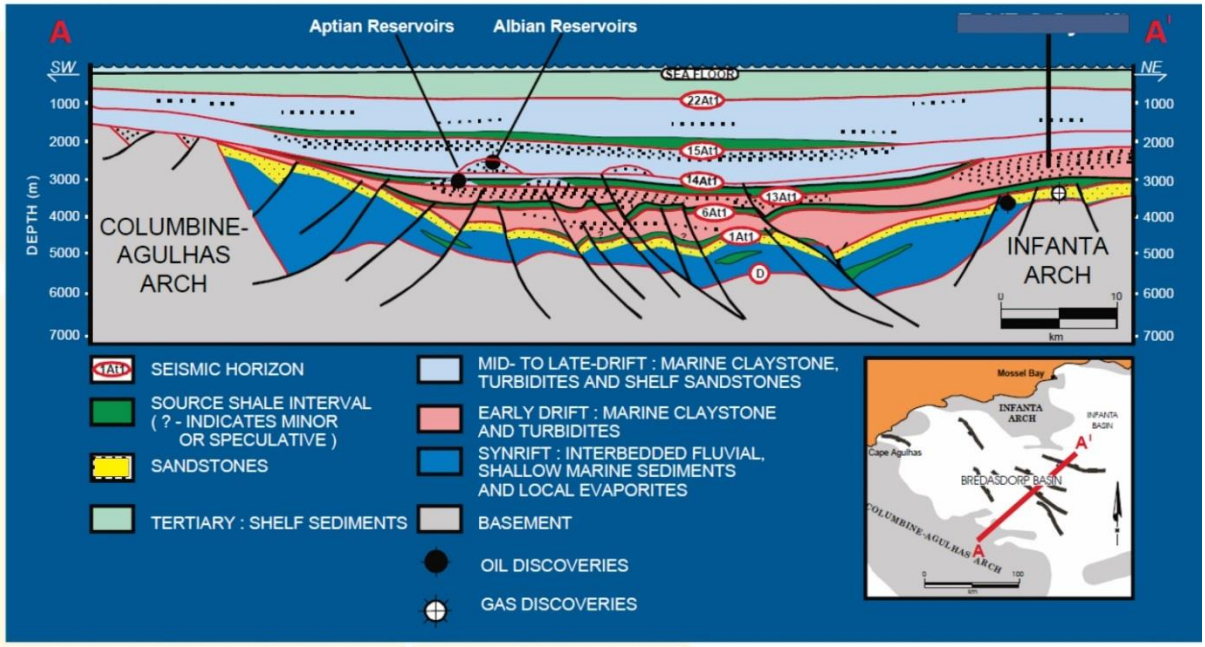

Figure 2.7: Schematic Section across the Bredasdorp Basin, K-R Field located in the sandstones below 1At1 regional unconformity (Petroleum Agency Handbook SA, 2005).

2.4.2 Structural Setting at K-R

Right lateral wrench faulting along the Agulhas/Falkland Fracture Zone on the Southern boundary of the basin resulted in strong NW to SE fault alignments, defining the Bredasdorp and other rifted sub-basins that developed along the southern margin of the African continent. The earliest syn-rift sedimentation within the Bredasdorp sub-basin was identified by TimeTrax (1999) in the E-S area as Late Jurassic (Early Tithonian to Kimmeridgian).

The NE and SW margins of the Bredasdorp Basin are faulted structural uplifts; the Infanta and Columbine-Agulhas Arches respectively. Although these uplifts may well have provided sediment input, the continental area to the north-northwest, offering an extensive drainage area eroding basement rocks and Palaeozoic sedimentary sequences, could potentially also have provided the sediment influx with coarse sediment reworked along shore by wave, storm and long-shore drift. The basin was open to the south and would have been in communication with an elongate and rather restricted seaway, the proto-Indian Ocean, along the East African margin. To the south lay the Antarctic/Falklands landmass, this would have been largely vegetated at that time (Cretaceous 'greenhouse' earth conditions).

The K-R structure is known to be only partly dip-closed and is highly compartmentalised by faulting. Normal faults and some reverse faults occur but some strike slip movements may also have occurred, although they are difficult to identify. Most of the faults in the field trend either north-north west to south-south east (NNW – SSE) or North West to south east (NW – SE) as shown in Figure 2.8. The USM reservoir thickens markedly into a major east west trending regional boundary fault to the north of the K-R Field.

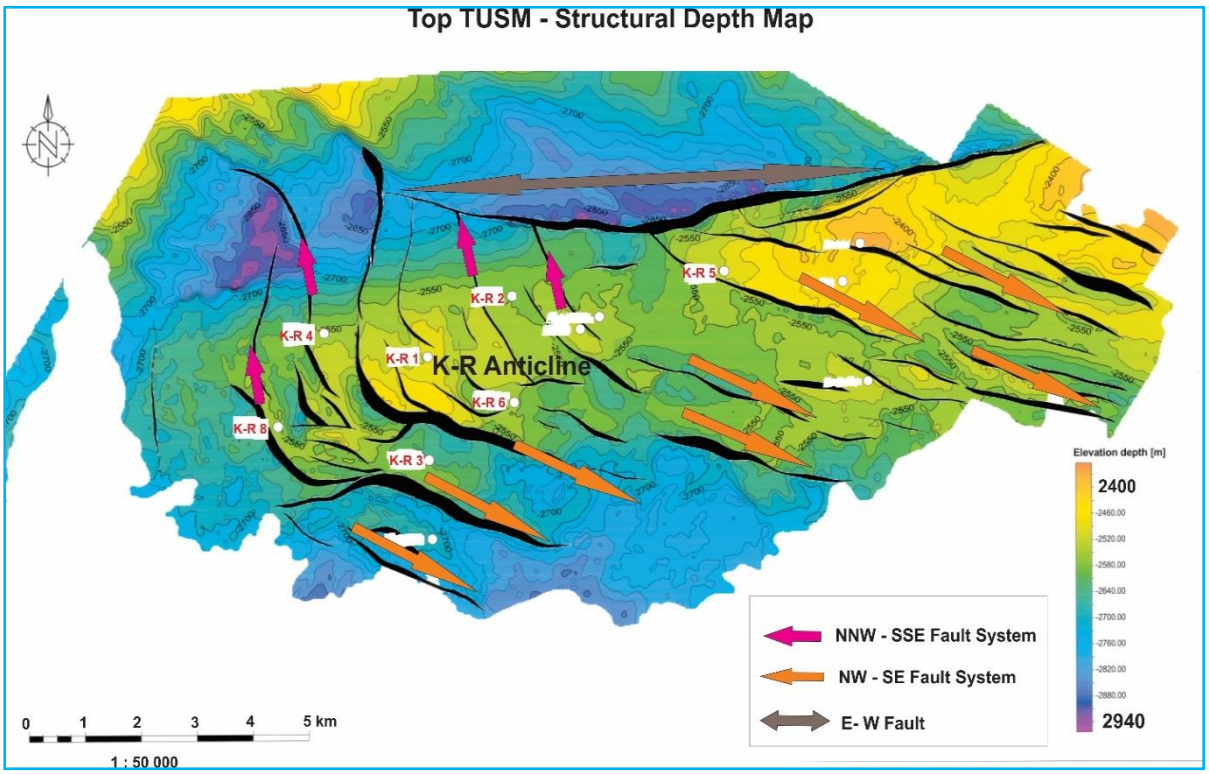

Figure 2.8: A structural depth map showing the fault system of the KR-Anticline at TUSM.

Chapter 3: Petrophysics and Empirical Correlations

3.1 Introduction

Petrophysics is a very important branch in the petroleum industry which deals with characterising the physical and chemical properties of rock-pore-fluid systems by merging geology, well logs, rock and fluid sample analyses and their production histories (Opuwari, 2010). Often data is difficult to obtain at depths; and wireline well logs need to be used to provide us with information. Petrophysical tools need to be understood properly and are vital to the field of geomechanics.

The density wireline well log is an essential petrophysical log that gives information about bulk rock density of formations as per depth. Unique density correction software has been developed within PetroSA by geomechanics specialist Leonardo Santana. This software was used to correct all the K-R wells and will be expounded upon.

To construct a geomechanical model of seven wells in the K-R Field, it is essential to use accurate values of elastic parameters and in-situ rock strength. These include the Uniaxial (or unconfined) Compressive Strength (UCS), Friction angle (ϕ), Young's modulus (E) and Poisson's ratio (PR).

Tests performed on cores provide more accurate static properties for modelling than dynamic properties calculated from log data. However, no laboratory strength tests were performed on the cores for the K-R Field and thus, empirical calculation had to be done using well log data.

3.2 Core Samples

These are cylindrical samples of rock taken from the formation of interest in situ, for either analysis purposes or laboratory strength tests. Coring is done by using a drilling bit instead of the drill pipe core barrel. This allows us to obtain samples various depths as it penetrated the formation.

Cores are usually cut using a special core bit and retrieved via a core barrel. Two types of cores are recovered; whole cores and side-wall core as shown in Figure 3.1.

Core samples are used for both qualitative (visual) and quantitative analysis: the latter focusing mainly on measuring porosity, directional permeability, fluid saturation, grain size density and other properties of the rock and fluid within it. In geomechanics, cores are used to perform important laboratory strength tests (triaxial, Brazilian disc, uniaxial compressive strength), to give an idea of how competent the rocks are, as well as to calibrate wireline logs.

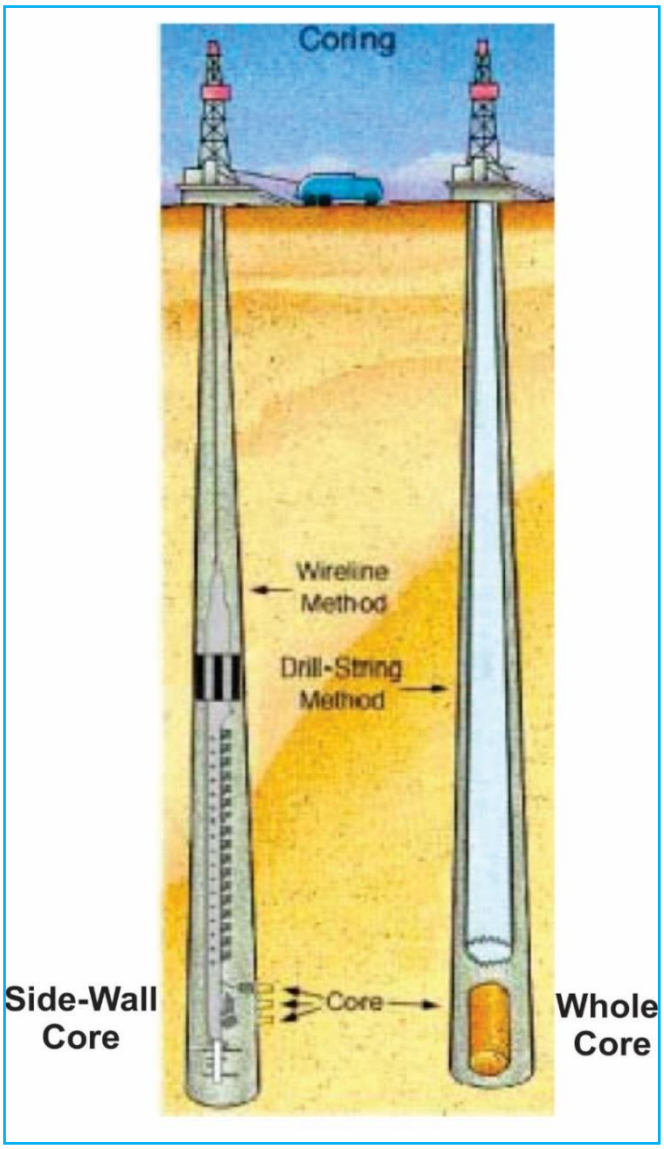

Figure 3.1: Diagram showing coring methodology for side-wall and whole cores. (modified from PetroSA GIT presentation, 2013)

3.3 Productivity Test Data

Productivity Test Data includes: The Formation Tester and Drill Stem Test (DST). The Repeat Formation Tester (RFT), designed by Schlumberger was used in the K-R Field. Formation testing is regarded as "true" data as it represents a collection of data on a formation to determine its potential productivity, before installing the well casing. Thus, the data indicated by the RFT or DST tests cannot be repudiated by the well logs – instead, it is used to calibrate the wireline logs and cores.

3.3.1 Drill Stem Test (DST) and Wireline Formation Testing

A drill stem test is done as a procedure for testing a formation through a drill pipe. The DST tool is made up of packers, valves (that can be opened or shut from surface) and a pressure-recording device. The formation fluid is recovered in the drill pipe and hydrostatic, flowing and shut in pressure are recorded against time.

A DST is essential as it not only confirms hydrocarbons in the reservoir but also gives important information about its size and ability to produce.

Wireline Formation Testing complements the drill stem test by its ability to sample several different zones encountered by the well. It provides fluid samples and detailed formation pressure data that is almost impossible to obtain from DST testing alone.

The repeat formation tester (RFT) tool, designed by Schlumberger, is used to measure formation pressure and to obtain fluid samples for testing. The tool enables us to record formation pressure at a multitude of point and enables the logging engineer to test the formation permeability before opting to produce from it. The RFT tool was used for KR-1, KR-2, KR-3, KR-4, KR-5 and KR-6; recording three different types of pressure:

1. Hydrostatic pressure of fluids in a well.
2. Pore pressure of the formation.
3. The pressure transient induced by withdrawing two samples.

The pressureXpress (XPT) tool was used in well KR-7. This is a more advanced tool that provides a number of benefits such as:

1. Reduced time involved and reduced risk of sticking.
2. Measurements of reservoir fluid density including pressure gradients.
3. A wider range for identifying depleted zones.
4. Increased survey efficiency.

3.4 Well Logs

These are arguably the most important tools available to petroleum geoscientists to: determine mineralogy, to identify and correlate rocks at depth, and to give information about the nature of fluids in the formation. Although well logs require interpretation from competent geoscientists, their strength lies in the precision and ability to bridge the gap between well cuttings and core samples.

During well logging, the tool is lowered into the borehole and the sensors are stimulated to send signals into the formation; recorders are attached to the tool to detect any reflected signals (Hugh, 2005). The tools are suspended by means of steel cables (wireline) or embedded in drilling strings (logging while drilling – LWD). As the cable is lowered or raised, it activates a depth measuring device, which provides depth information to the surface electronic and recording devices (Hugh, 2005). When the log is acquired, the information recorded is filtered, quality checked and environmental corrections are made before essential information can be obtained from it.

3.5 Characteristics of Selected Wireline Tools

Many wireline logging tools exist and improvements as well as new tools are poured forth regularly. Wireline logs are an essential component for creating geomechanical models as they are the most efficient way of gathering data at depths. Geomechanical parameters can be calculated by using empirical methods and then validating it against true readings from drilling information. For the purpose of this study, only the logging tools available for wells in the K-R Field will be concisely described, along with their individual characteristics.

3.5.1 Gamma Ray Logs (GR)

The functions of the gamma ray logs are to measure the natural radioactivity of the formations by the three main radioactive families: Uranium, Thorium, and Potassium (Figure 3.2). These radioisotopes are mostly concentrated in clays, thus, the gamma ray log gives a reading that reflects clay contents. However, there are some caveats as potassium feldspar, volcanic ash, and salts rich deposits containing potassium, could also display high gamma ray readings. The opposite is observed in shale-free sandstones and carbonates, which have low radioactive elements, thus, giving a low gamma ray reading. The standard unit of measurement is API (American Petroleum Institute) and all well in the K-R Field as calibrated from 0-150 API.

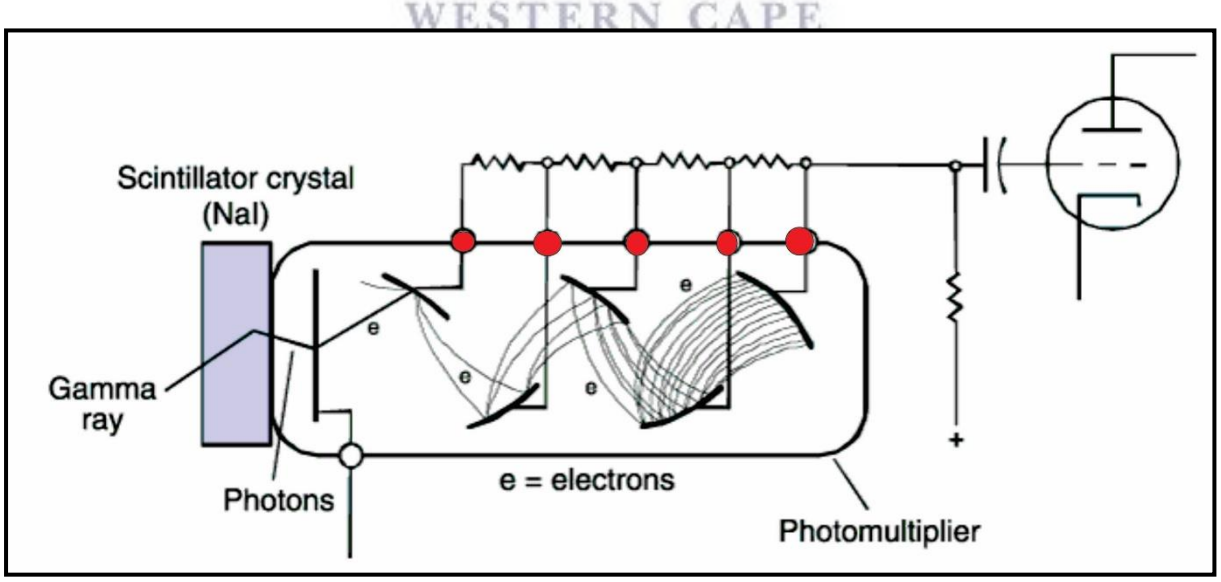

Figure 3.2: Scintillation counter Gamma ray too (after Rider, 2002).

High gamma ray readings may often signify shales, but potassium rich feldspathic, glauconitic or micaceous sandstones can produce a similar result. Gamma ray logs are of great importance as they are used for lithology analysis, correlating formations, estimation of clay content, mineral identification and facies analysis.

The volume of clay in a formation (denoted as V_{clay}) can be derived from the Gamma ray log by means of calculation (equation 3.1) and is expressed as a fraction ranging from 0-1. Notable methods include the Clavier, Steiber and the Bateman method as shown in Figure 3.3. The most commonly used is the linear method which is given by the formula:

$$V_{clay} = \left[\frac{(GR - GR_{clean})}{(GR_{clay} - GR_{clean})}\right] \qquad \text{Equation 3.1}$$

Where GR_{clean} is the value selected that represents zero to no clay and GR_{clay} is the value selected that represents clay.

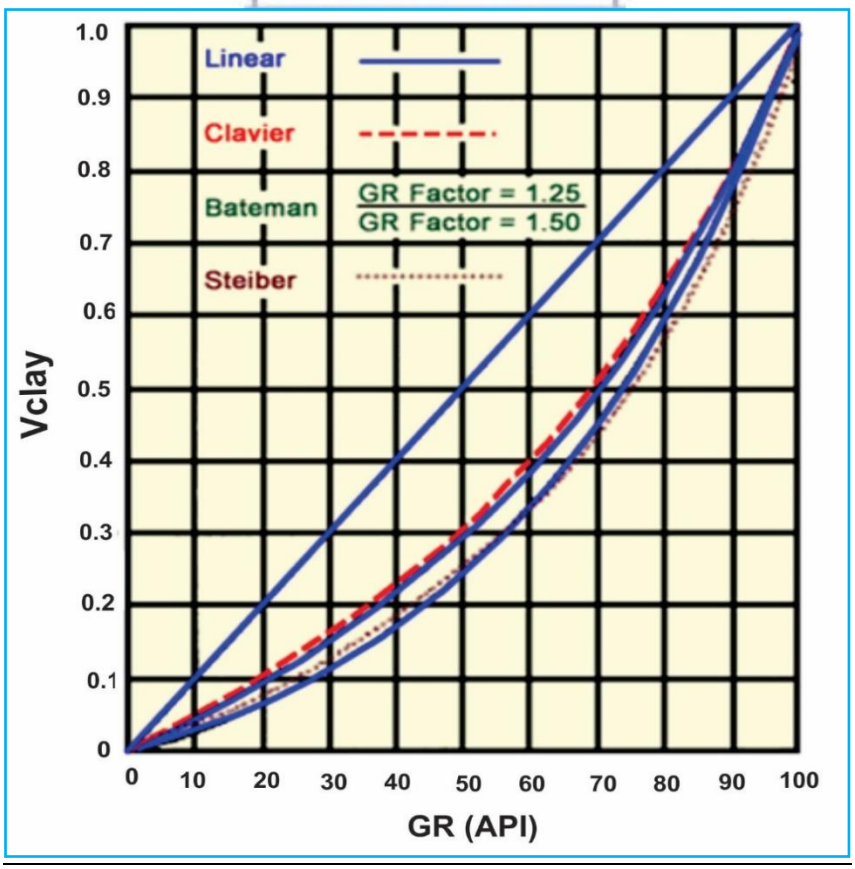

Figure 3.3: Different methods available for deriving V_{clay} values. Modified from PetroSA GIT presentation (2013).

3.5.2 Sonic Logs

The sonic log measures compressional wave transit time (μs/ft) and is reciprocal of compressional wave velocity. The tool consists of one or more transmitters and two or more receivers (Figure 3.4). The sonic log tool transmits an acoustic signal and measures the time of first arrival at the receivers, whereby transit time is then computed. Borehole compensated sonic logs are made up of two transmitters, fixed above and below the receiver. Alternating use of two transmitter-receiver pairs compensates for effects of hold size changes and tool tilts.

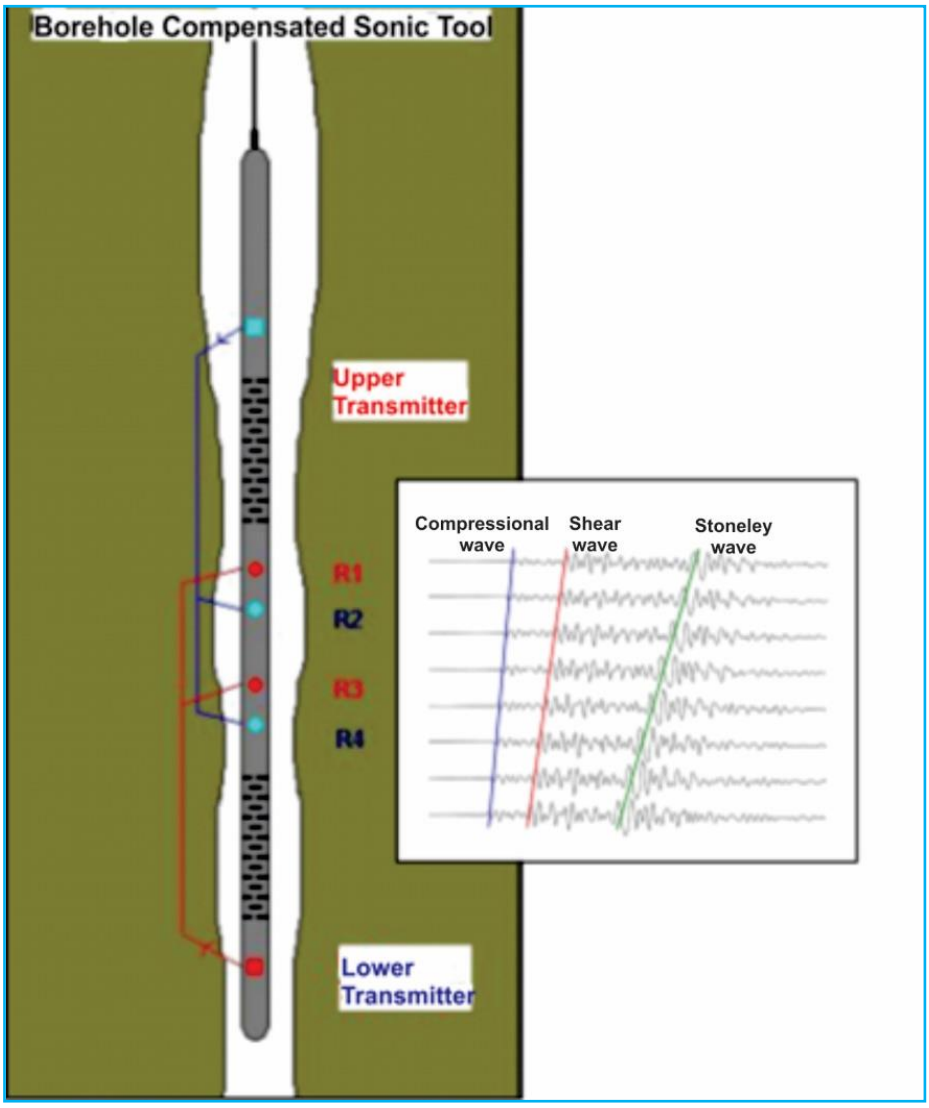

Figure 3.4: Sonic tool showing the upper and lower transmitters together with the types of waves recorded. Modified from PetroSA GIT notes (2013).

3.5.3 Resistivity Logs

These logs measure the difficulty of electric currents passing through formations. The tool has electrodes which are connected to a generator as a power source. Current flows from these electrodes through the borehole fluid into the formation and then to the remote reference electrode (Figure 3.5). Resistivity logs can be grouped into laterlog, induction logs and micro-resistivity measurements (Hugh, 2005). Resistivity is the function of the volume measured and the configuration of the measuring instrument; resistivity indicates the presence of fluids. Water has a low resistivity due to it being highly conductive whilst hydrocarbons are typically non-conductive and show high values of resistivity. All measurements are in Ohm-m and resistivity logs are available for the KR-wells: Deep resistivity, shallow resistivity and micro resistivity.

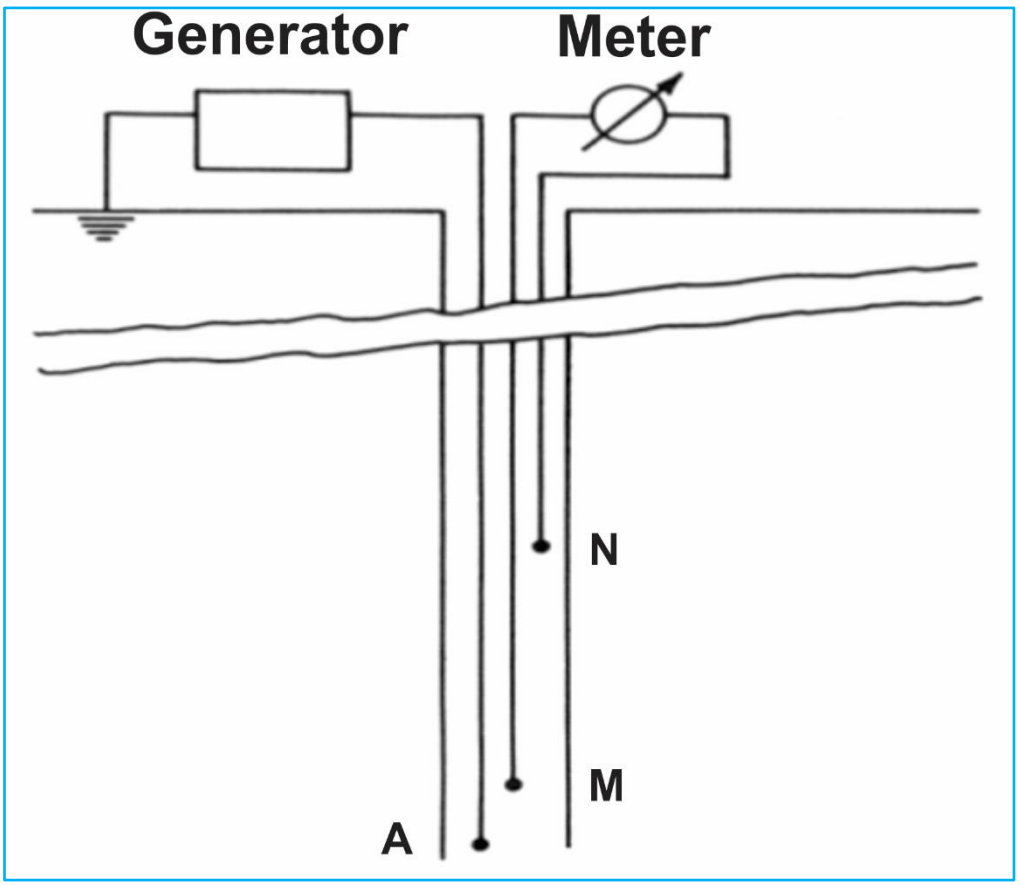

Figure 3.5: A typical normal device electrode resistivity tool with electrodes N, M and A (Schlumberger, 1989).

3.5.4 Density Log (RHOB)

This wireline log measures formation bulk densities. The bulk density is the sum of the rock matrix and pore fluid. The logging tool consists of a gamma ray source (such as Cs^{137}) and a detector shielded from the source, so that it records backscattered gamma rays from the formation, depending on the electron density of the formation (Figure 3.6). The formation electron density is proportional to the bulk density as shown in Equation 3.2.

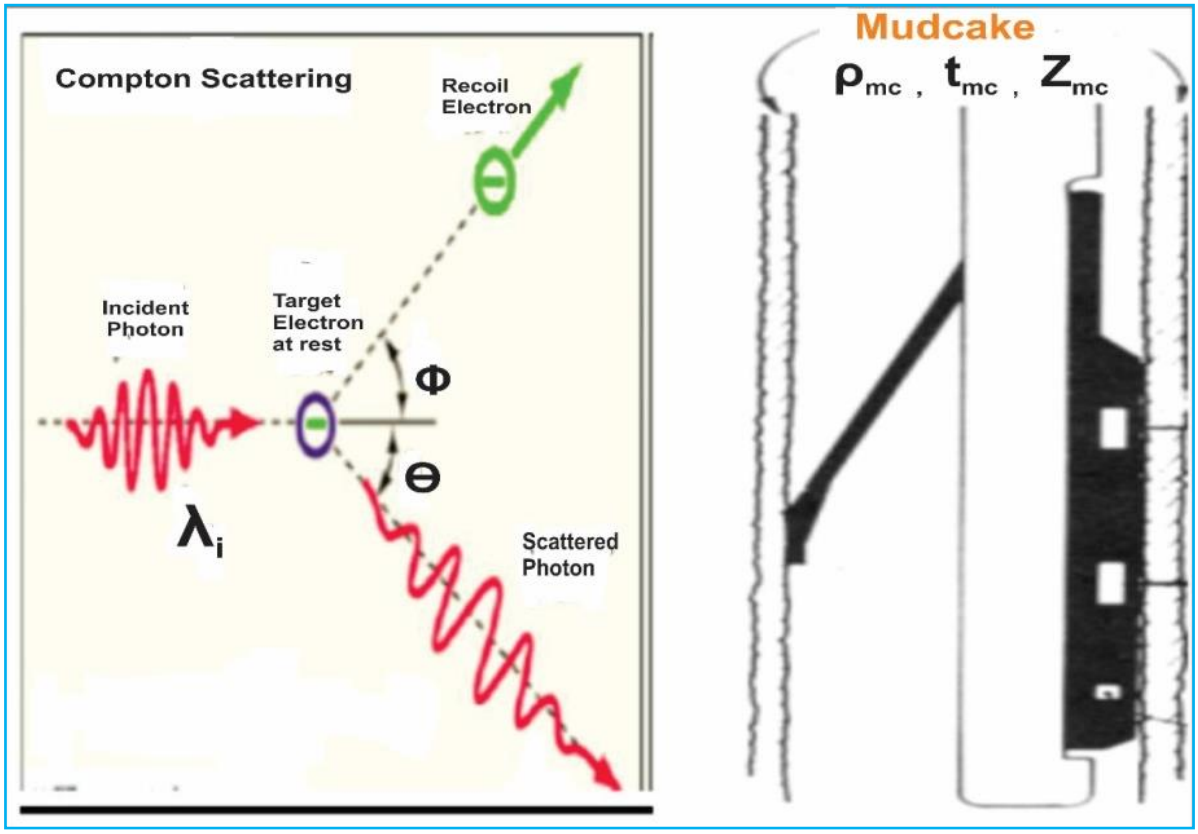

Figure 3.6: Compensated density logging tool showing Compton scattering and the principles behind measuring the bulk density of rocks (modified from Hugh, 2005).

$$\rho_b = \varphi * \rho_f + (1 - \varphi)\rho_{ma} \qquad \text{Equation 3.2}$$

Where: ρ_b is the formation bulk density, ρ_f the average density of pore fluid ρ_{ma} the matrix density and Φ being the porosity

The compensated density logging tool includes a secondary detector that picks up mud cakes and other borehole irregularities. The response of the secondary detector is used to correct the

measurements of the primary detector. Density log units are displayed in $g.cm^3$ for all K-R wells.

3.5.5 Caliper Logs (Cali)

The caliper log is a measurement of wellbore diameter. The tool is made up of four spring-actuated arms which when opened; make direct contact with the borehole walls (Figure 3.7). Four arm caliper tools are commonly run to obtain information about the formation (attitudes of bedding). However, unprocessed oriented four arm calipers can be used to interpret borehole breakouts.

The arms of the tool are hinged to a chamber that is connected to a rheostat. As the tool moves along the borehole, the variation in diameter affects the pressure of the arm which is recorded by the rheostat as potential change. This potential change is plotted as the caliper log which is generally in inches. The basic uses of the caliper log:

- To calculate the volume of cement needed to fill up the annular space between the well and casing.
- The selection of parker seats.
- To give an accurate representation of borehole diameter.

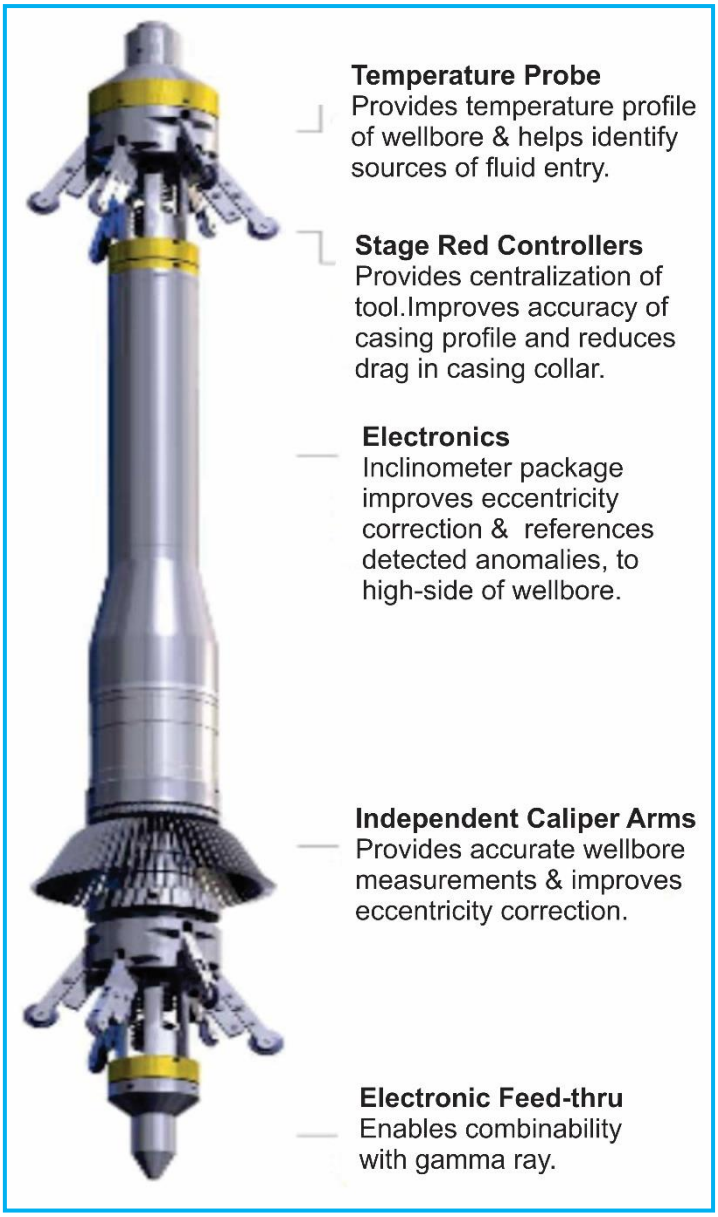

Figure 3.7: Illustration of a four arm caliper tool used to measure the borehole diameter (Schlumberger, 1989).

3.5.6 Spontaneous Potential Log (SP)

Also known as self-potential logs, the SP logs measure the potential difference between two electrodes: one in the borehole and the other on surface (reference electrode). The SP-log records the difference in electrical charges of the drilling mud and the contacting formation that causes charged particles to flow from high to low potential. The main sources of electric current are electrochemical and electrokinetic in nature.

The SP log can be used in identifying formation water resistivity, permeable beds and could occasionally be used in calculating the volume of shale. Rider, 1996 states that this log is most useful when:

- Drilling mud is fresher than formation water.
- Good contrast between mud filtrate and formation water resistivity.
- Formation resistivity is sufficiently low.

The SP log is generally recorded in millivolts (Mv) with the range being from positive to negative depending on the deflection of the curve; deflection to the right is positive whilst deflection to the left is negative (Figure 3.8).

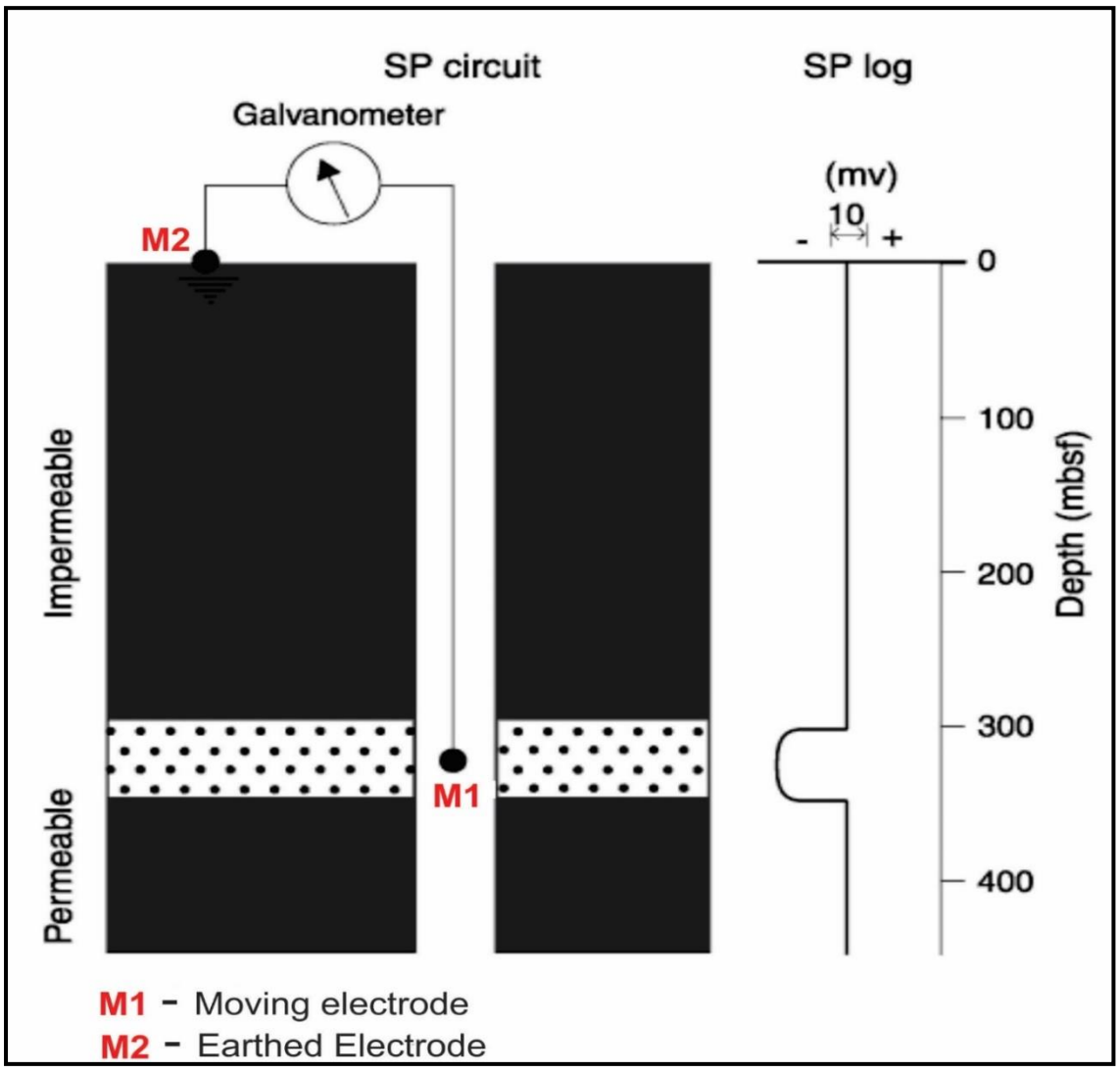

Figure 3.8: Spontaneous potential logging tool. Modified from (Rider, 1996).

3.5.7 Neutron Logs

These logs are indirect porosity logs which measure the density of hydrogen content of fluid occupying the pore spaces of rocks (Tiab, D and Donaldson, E.C., 2012). In formations where the pores are occupied, the neutron log measure liquid-filled porosity. When gas is present in the formation, the neutron log yields low values and can thus, be used to detect gas bearing zones or gas-liquid contact. There are three types of neutron logging tools:

- Compensated neutron.
- Sidewall epithermal neutron.
- Convectional neutron-gamma.

The tool contains a continuously emitting neutron source in which high energy neutron are slowed down by collisions with atomic nuclei (Figure 3.9). Hydrogen atoms have a mass that is nearly equal to the neutron and is therefore most effective in slowing down the process.

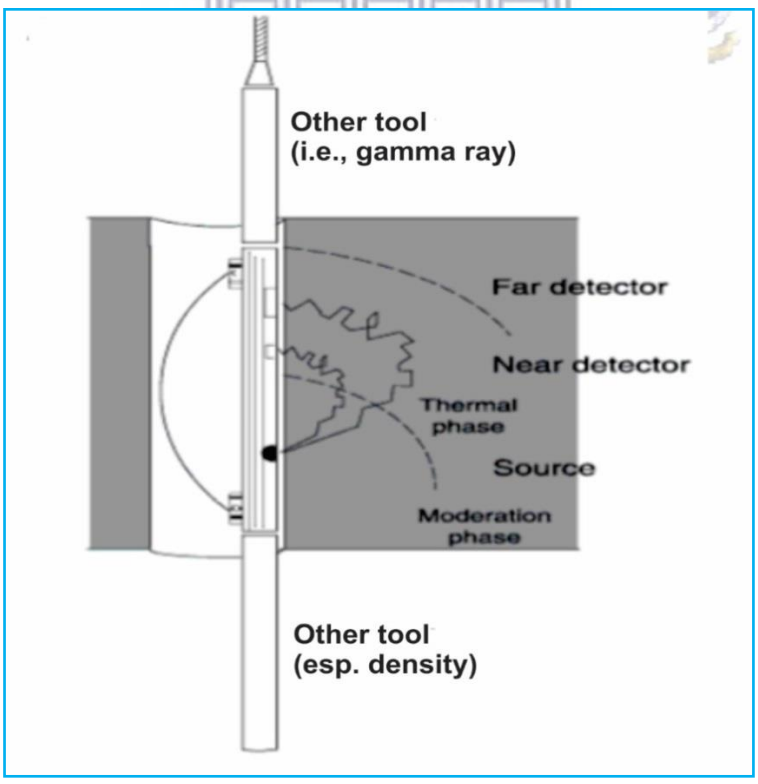

Figure 3.9: Drawing of a compensated neutron logging tool. Modified from (Rider, 1996).

Neutron logs are affected by mineralogy and borehole effects. Better precision can be achieved by combining neutron logs with density and acoustic logs to determine porosity and identify mixed lithology.

3.6 K-R Field Well Logs

The well logs are essential to this thesis, especially in the case of the K-R Field, where geomechanical parameters have to be derived from them. The reservoir of the K-R Field is of main importance for this study and the well logs displayed in Figures 3.10, highlight the top and bottom of upper shallow marine reservoir sections which are indicated as TUSM and BUSM respectively.

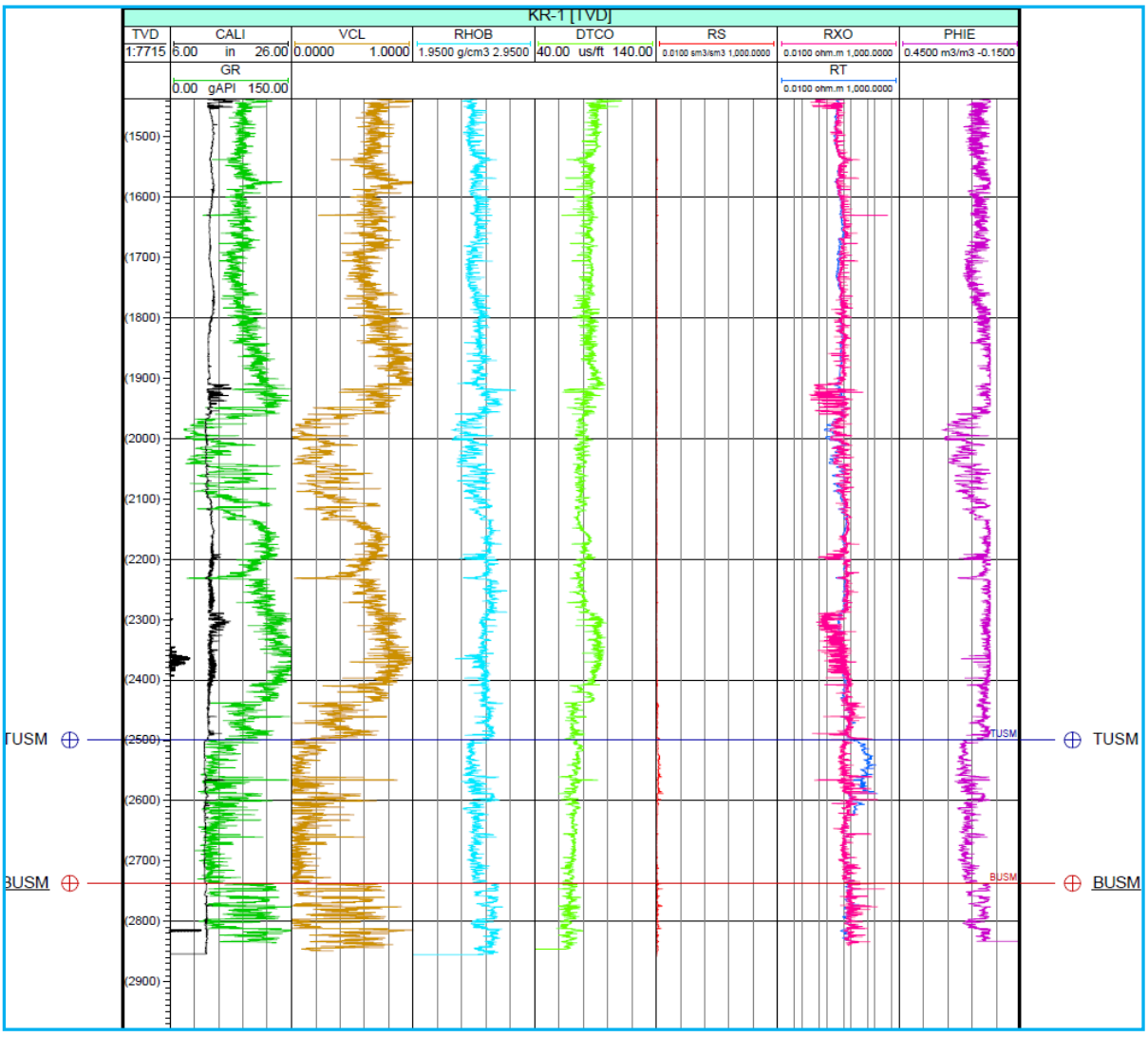

Figure 3.10 (a): Display of well log suites for well KR-1.

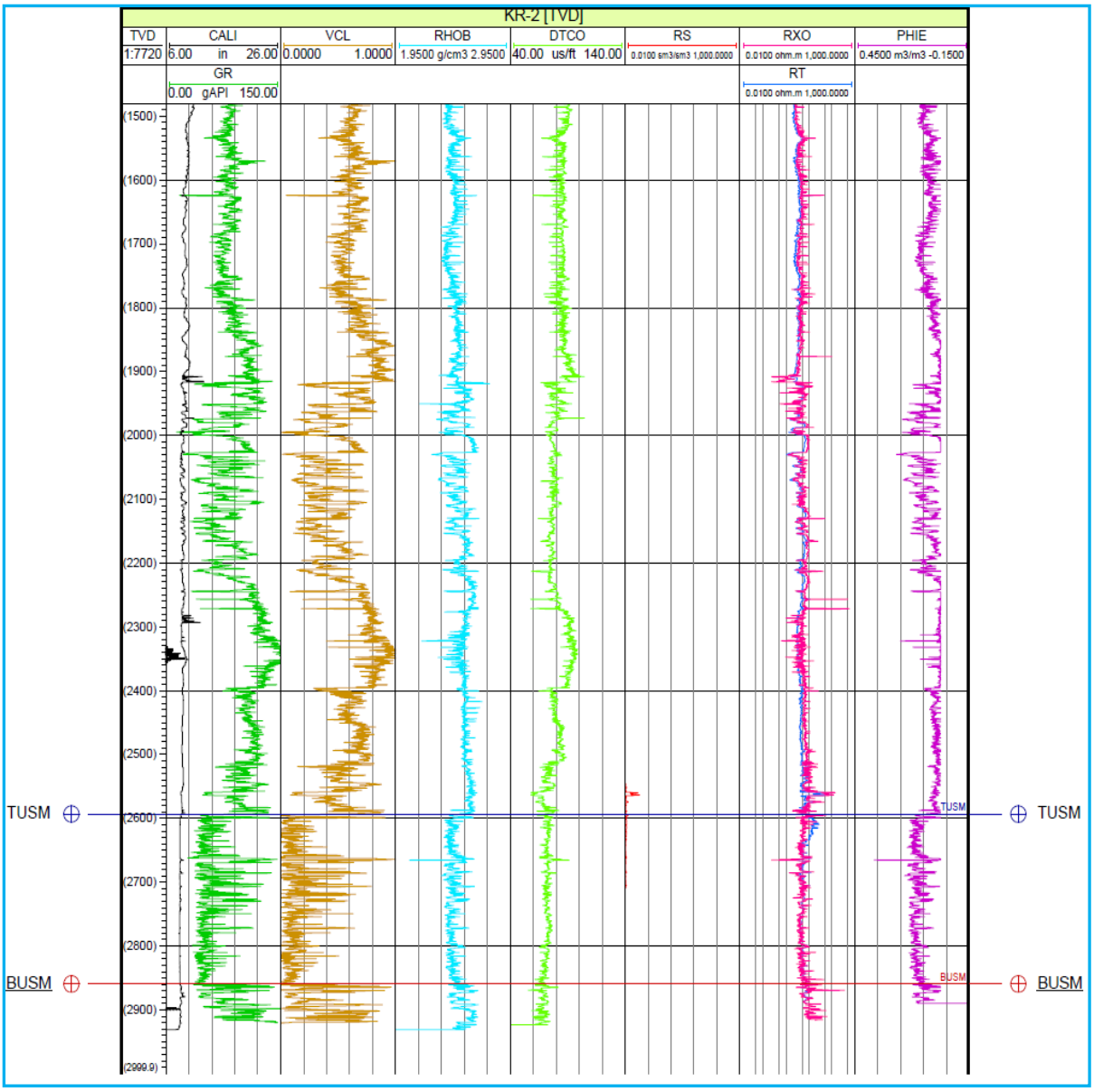

Figure 3.10 (b): Display of well log suites for well KR-2.

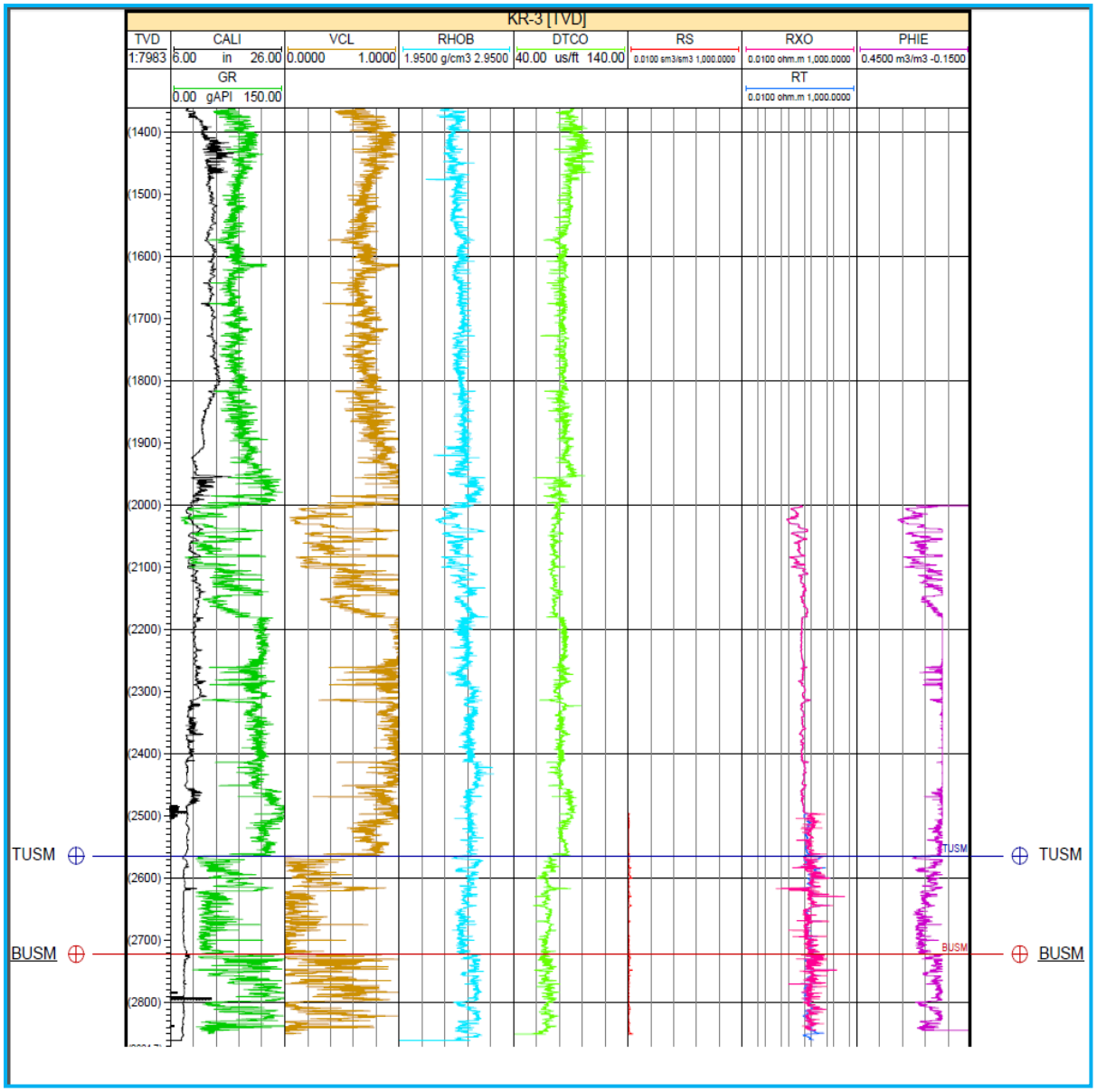

Figure 3.10 (c): Display of well log suites for well KR-3.

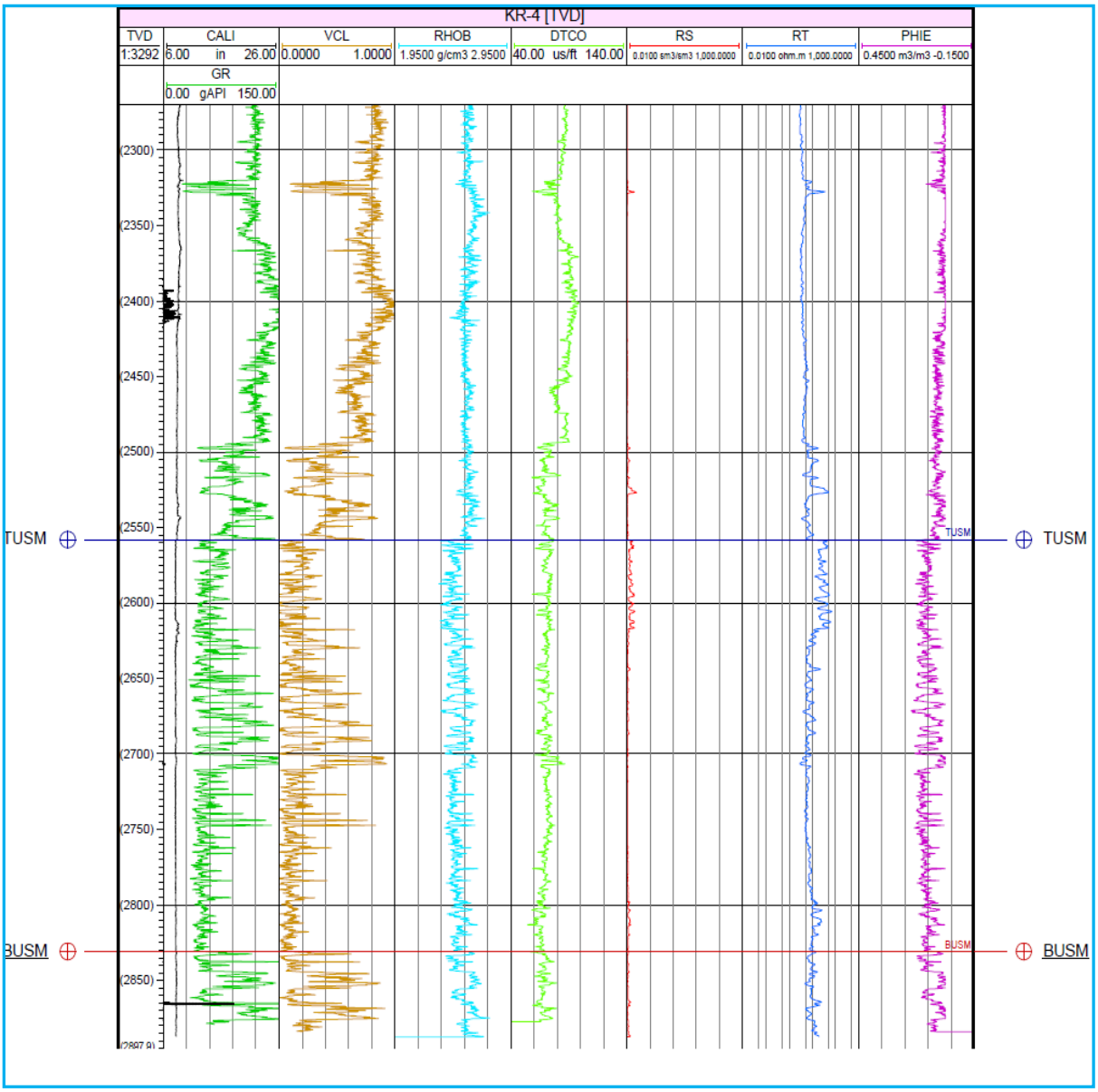

Figure 3.10 (d): Display of well log suites for well KR-4.

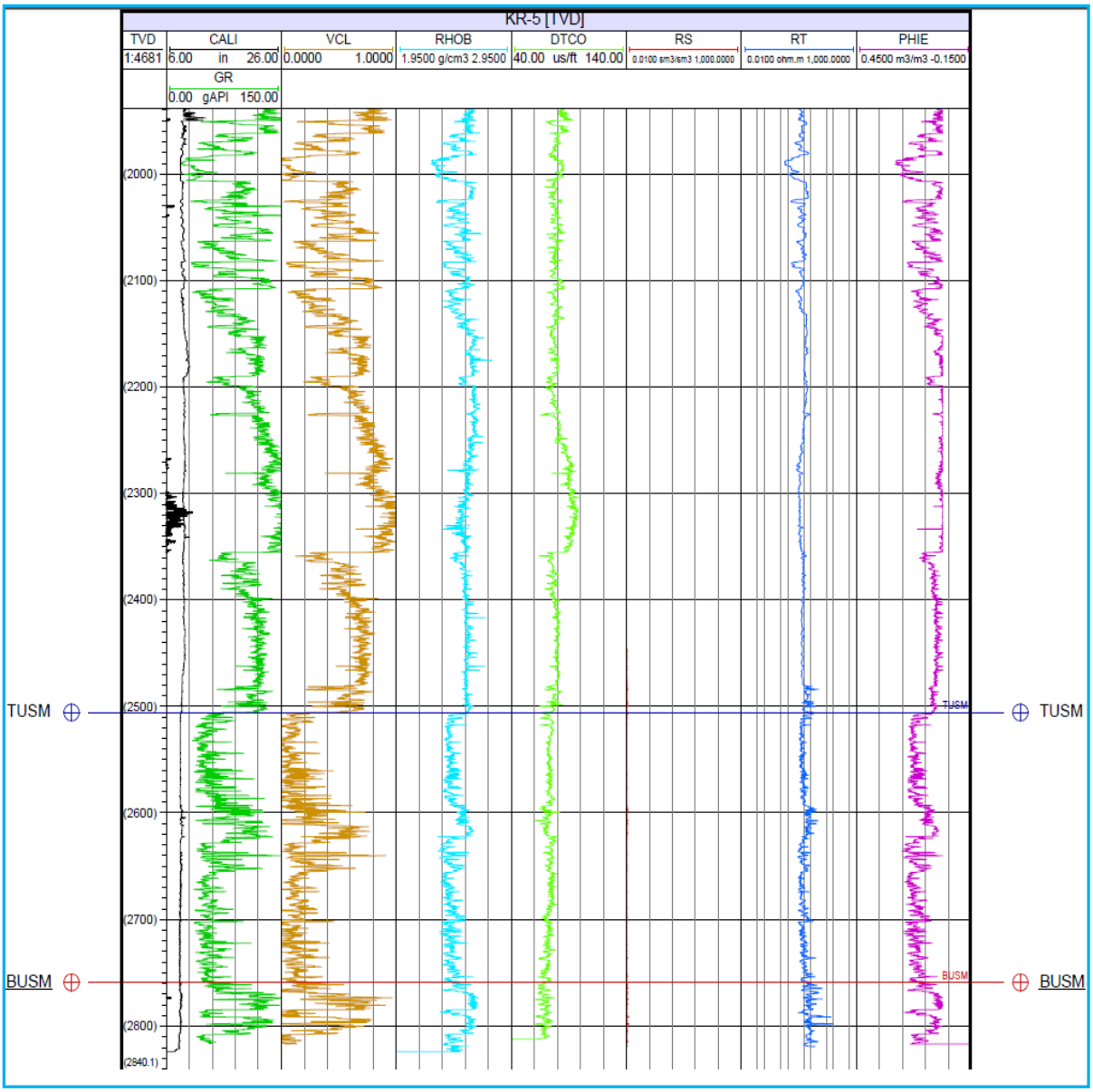

Figure 3.10 (e): Display of well log suites for well KR-5.

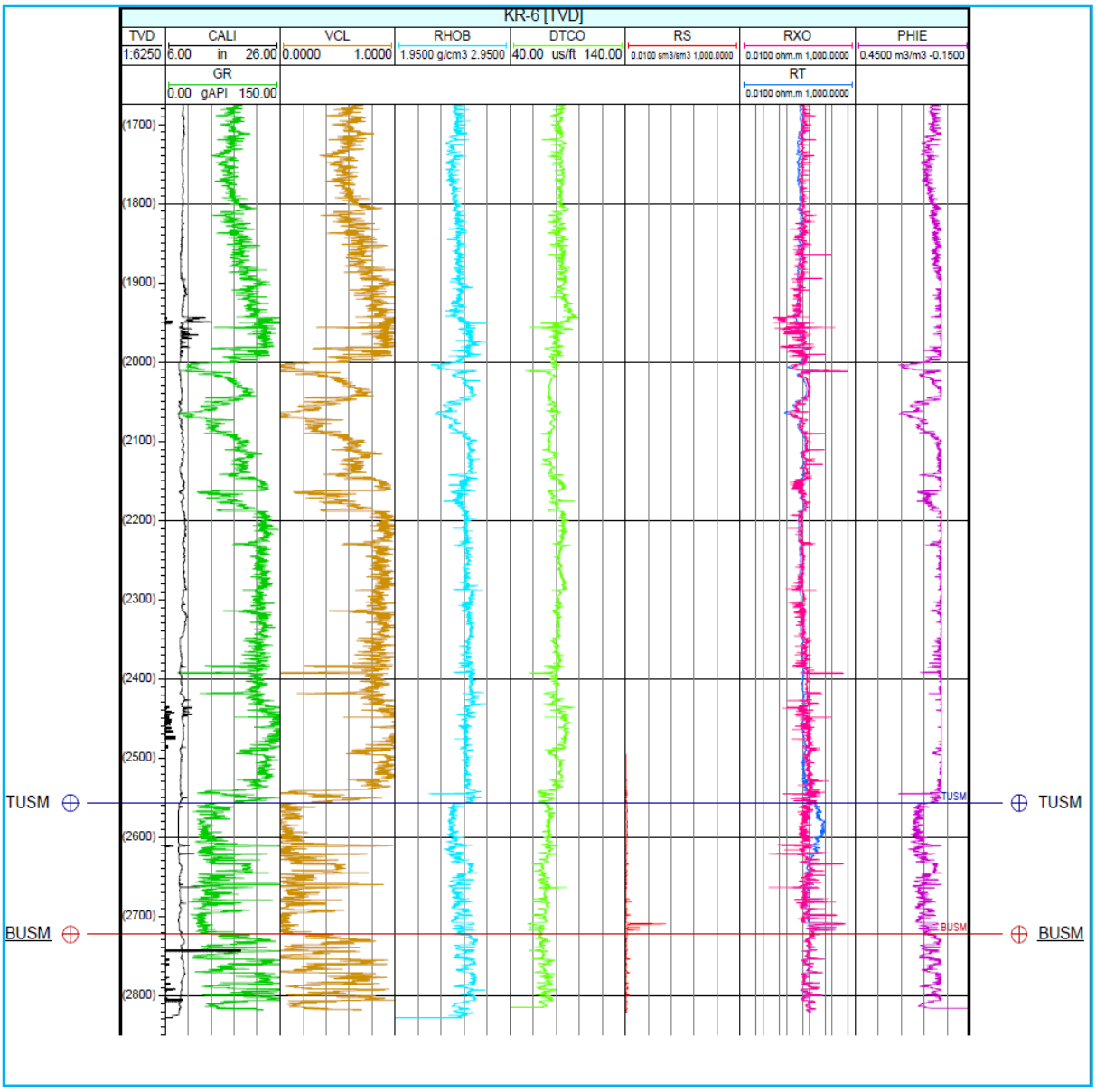

Figure 3.10 (f): Display of well log suites for well KR-6.

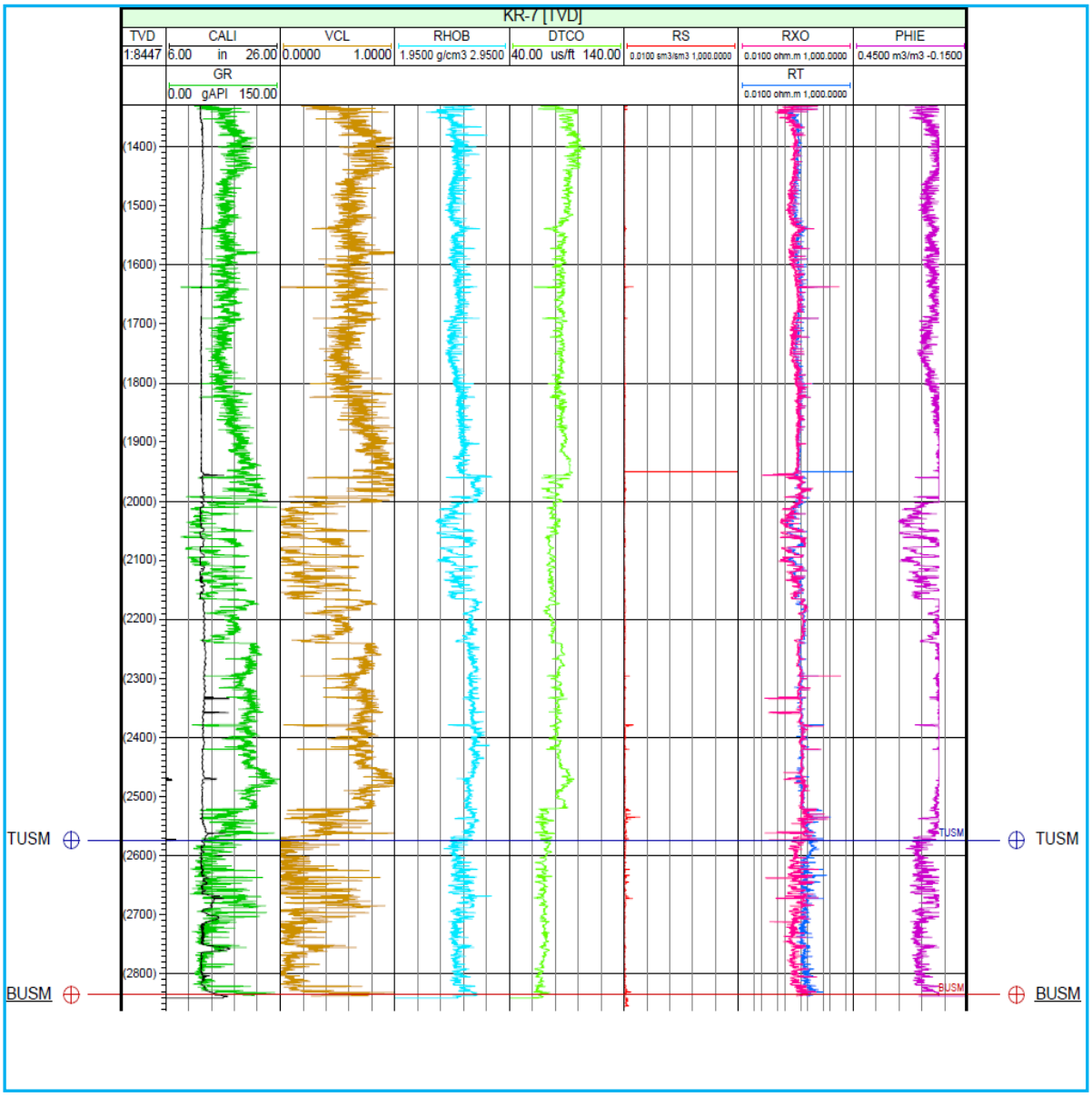

Figure 3.10 (g): Display of well log suites for well KR-7.

3.7 Density Correction

3.7.1 Introduction

Vertical stress can be obtained in several ways; the most accurate is by using recorded rock density values. However, the density log is often seriously affected by environmental factors of the hole, mainly of the geometry. Traditionally, in areas where the hole is seriously affected, these readings are discarded. It is thus imperative to correct the density log to avoid erroneous readings.

A density correction software, was created by Leonardo Santana (Geomechanics specialist - PetroSA), to be used internally at PetroSA. This correction was applied to the density logs of the KR-wells and the methodology behind it will be explained in subsequent sections. The results of the corrected density log and its impact on the vertical stress will be shown in Chapter 4.

3.7.2 Correcting the Density Log

To correct the density log that is affected by geometry of the wellbore, we first need to use an equation that relates the density and velocity obtained from the sonic log, since the latter is not affected by this geometry effect (Santana, 2010). This equation can be determined using rock physics concepts relating porosity and clay content with both logs.

The correction process starts with determining the density of the matrix as a function of clay content (Equation 3.3). Assuming no porosity, it is possible to determine the matrix density for any possible values of clay content.

$$RHOM = \rho_1\big(1 - V_{sh}(i)\big) + \rho_2\big(V_{sh}(i)\big) \qquad \text{Equation 3.3}$$

Where: RHOM is the matrix density (g/cm^3), ρ_1 is the density of quartzitic sandstone (g/cm^3, ρ_2 is the density of shale (g/cm^3), V_{sh} is the volume of clay and i represents values between 0 and 1.

Equation 3.3 is iterative and must be solved for all possible values of V_{sh} content, ranging from 0 to 100% (Santana, 2010). Densities are dependent on rock mineralogy. Table 4 presents the values of densities and average velocities for the most common minerals.

Table 4: Densities and velocities of common minerals (Rider, 1996).

Mineral	Density (g/cm^3)	Velocity (Km/s)
Quartz (Sandstone)	2.65	6.05
Calcite (Limestone)	2.71	6.64
Dolomite (Dolomite)	2.85	7.34
Shales	2.55	3.81

After obtaining the matrix density values for all V_{sh} values, rock density is determined as a function of porosity, using the relation between porosity - density as shown in Equation 3.4.

$$RHOB(i) = (\varphi * RHOFL) + \big((1-\varphi) * RHOM\big) \qquad \text{Equation 3.4}$$

Where: $RHOB(i)$ is the density of rock (g/cm^3), φ is porosity (fraction), $RHOFL$ is the density of formation fluid (usually between 1 and 1.1 g/cm^3) and $RHOM$ being the matrix density (g/cm^3).

This equation must be applied to values of porosity in a predefined range, for example for more strictly to zero values (because these values were calculated previously using equation 3.3 and less than or equal to 50%. This will generate a matrix whose number of columns depends on the values of clay content and the number of rows, on the values of porosity. Once associations have been obtained with porosity and bulk density of clay, a relationship between between velocity, porosity, and clay content needs to be ascertained (Santana, 2010).

Equation 3.5 provides this relationship in which it is possible to obtain velocity values of the matrix, in a manner similar to how the density values of the volume-dependent matrix were obtained from the clay. Again, Equation 3.5 is iterative and must be solved for all possible

values of clay content between zero and one hundred percent. Velocity values for quarts (sandstone) and shale can be obtained from the table 4.

$$VMA(i) = \left(V_1 * \left(1 - V_{sh}(i)\right)\right) + \left(V_2 * V_{sh}(i)\right) \quad \text{Equation 3.5}$$

Where: $VMA(i)$ is the matrix velocity (m.sec / ft), V_1 is the velocity of clean rock (m.sec / ft) and V_2 is the velocity of shales (m.sec / ft).

A quick look analysis of Equations 3.3 and 3.5 indicates that when the clay content value is zero (no clay present in the matrix) both the density and velocity are dependent onlyV_1 . As the clay content increases, it veers more towards shale, which inevitably has lower output values of density and velocity.

After obtaining the matrix velocities for all possible values of clay volume, any model that links velocity to porosity may be used. In this case the equation of Raymer-Hunt-Gardner (Equation 3.6) which is an improvement of the previous work done by Wyllie was used.

$$V = (1 - \varphi)^2 * VMA + (\varphi * VFL) \quad \text{Equation 3.6}$$

Where: V is the velocity of rock (msec / ft), VMA is the velocity in the matrix (msec / ft), VFL is the fluid velocity expressed in msec / ft, usually close to 1.460 msec / ft.

This equation must be applied to values of porosity in a predefined range. This will generate a matrix whose number of columns depends on the values of clay content and the number of rows depends on the values of porosity (Santana, 2010). This array must have the same number of rows and columns that is obtained for densities, but now with velocity values. Table 5 shows an example of these matrices.

Table 5: Example of matrix density and velocity related to porosity and clay content.

		Vcl										
		0	**0.1**	**0.2**	**0.3**	**0.4**	**0.5**	**0.6**	**0.7**	**0.8**	**0.9**	**1**
		Calculated Density (g/cc)										
Porosity	**0**	**2.65**	2.648	2.646	2.644	2.642	2.64	2.638	2.636	2.634	2.632	**2.63**
	0.1	2.485	2.4832	2.4814	2.4796	2.4778	2.476	2.4742	2.4724	2.4706	2.4688	2.467
	0.2	2.32	2.3184	2.3168	2.3152	2.3136	2.312	2.3104	2.3088	2.3072	2.3056	2.304
	0.3	2.155	2.1536	2.1522	2.1508	2.1494	2.148	2.1466	2.1452	2.1438	2.1424	2.141
	0.4	1.99	1.9888	1.9876	1.9864	1.9852	1.984	1.9828	1.9816	1.9804	1.9792	1.978
	0.5	1.825	1.824	1.823	1.822	1.821	1.82	1.819	1.818	1.817	1.816	1.815
		Calculated Velocity (us/ft)										
Porosity	**0**	**5760**	5529	5298	5067	4836	4605	4374	4143	3912	3681	**3450**
	0.1	4811.9	4624.79	4437.68	4250.57	4063.46	3876.35	3689.24	3502.13	3315.02	3127.91	2940.8
	0.2	3979	3831.16	3683.32	3535.48	3387.64	3239.8	3091.96	2944.12	2796.28	2648.44	2500.6
	0.3	3261.3	3148.11	3034.92	2921.73	2808.54	2695.35	2582.16	2468.97	2355.78	2242.59	2129.4
	0.4	2658.8	2575.64	2492.48	2409.32	2326.16	2243	2159.84	2076.68	1993.52	1910.36	1827.2
	0.5	2171.5	2113.75	2056	1998.25	1940.5	1882.75	1825	1767.25	1709.5	1651.75	1594

Table 5 is an example of matrices of density and velocity values created from clay volume and porosity with increments of 0.1 (10%) in both cases. Note that the density to porosity and clay content of zero, corresponding to 2.65 g/cc, which is the density of. The velocity corresponding to these values of density and porosity is 5.760 µs/ft. For shales, the density value used is 2.63 g/cc and a velocity of 3,450 µs/ft.

Once these matrix densities and velocities have been generated, you have a set of values for each increase in clay content and porosity. It is then possible to adjust the data polynomial, so that at each denisty point, you get a corresponding porosity and velocity value (Santana, 2010). Figure 3.11 shows regression polynomial obtained from the data shown in Table 2. Each of these polynomial regressions is represented by an equation of degree 4 of the form shown in Equation 3.7.

$$RHOB = a * Vp^4 + b * Vp^3 + c * Vp^2 + d * Vp + e \qquad \text{Equation 3.7}$$

Where: $RHOB$ is the corrected density (g/cm^3), Vp is velocity (µs/ft) and the coefficients a, b, c, d, and e are values for the correction polynomial (g/cm^3)/ (µs/ft).

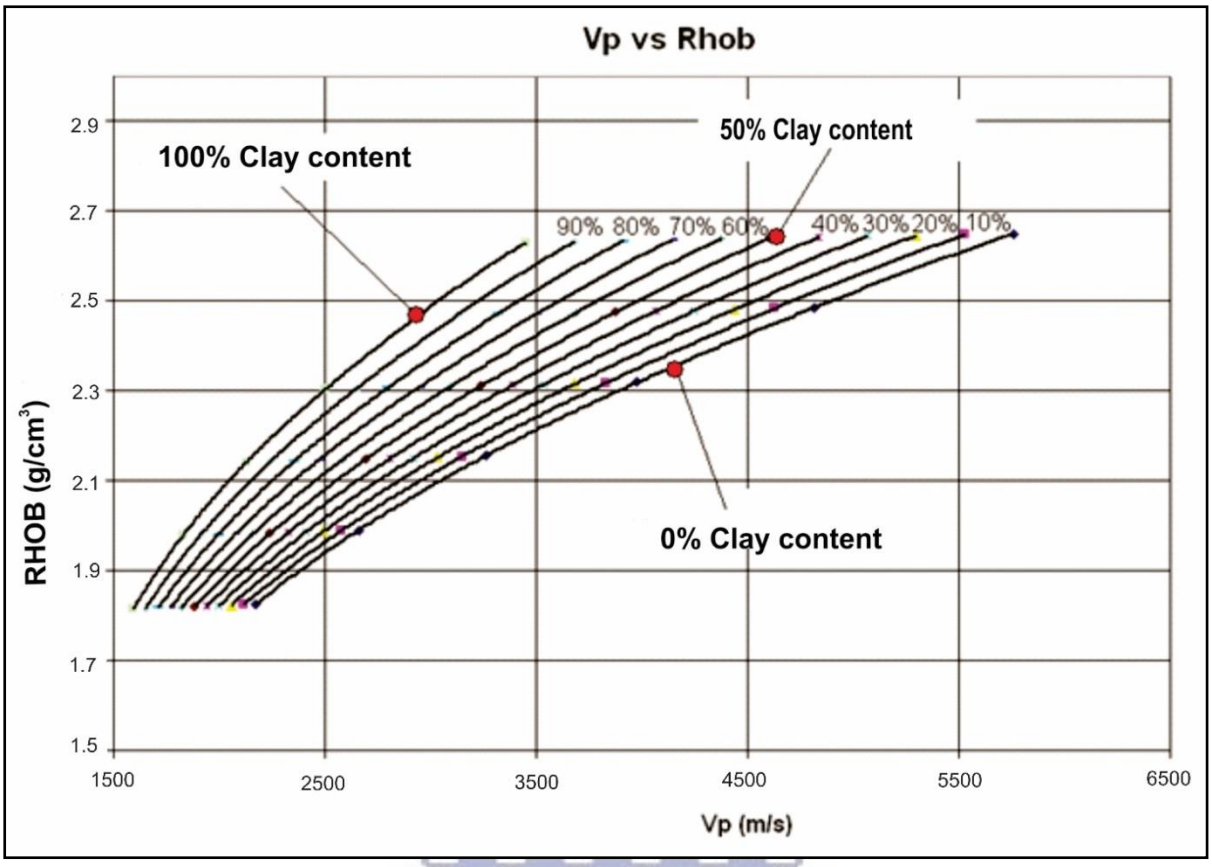

Figure 3.11: Graph showing polynomial regressions matrices for densities and velocities listed in Table 2.

3.8 Rock Strength

The strength of a rock is related to its mechanical properties. Determining rock strength is hugely important as it helps the well planner in casing design, well trajectory and the selection of the optimum mud weight. The rock strength inputs for the geomechanical model are Friction angle (FA), cohesive strength (CS) and the uniaxial compressive strength (UCS). The first two input parameters are derived from the Mohr-Coulomb failure criteria**.**

3.8.1 Mohr-Coulomb Failure Criteria

Numerous studies indicate that rock strength against shear failure increases monotonically with increasing confining pressure (Zoback, 2007). This fact was captured in 1990 when Mohr proposed that shear failure across a plane is related to normal and shear stress by a linear function as expressed in Equation 3.8 (Cook and Jaeger, 1976).

$$\tau = \mu\sigma + S \qquad \text{Equation 3.8}$$

Where: τ is the shear stress, μ is the coefficient of internal friction; σ is normal stress and S is the cohesion.

Cohesion can be defined as the strength that holds the grains together; coefficient of internal friction is the resistance to movement along a shear plane due to frictional forces (Rahim, *et al*., 2003). The Mohr-Coulomb failure criterion allows for us to develop a failure line if a rock sample has three unequal principal stresses: if the values of σ and τ fall below the line, failure does not occur (Cook and Jaeger, 1976). This is shown in Figure 3.12. The two main parameters derived from the Mohr-Coulomb failure criteria are the Friction Angle (FA) and Cohesion (S_0). The friction angle varies for different rock types and three correlations for sandstone, shales and shaley sedimentary rocks were used to obtain more representative results (Table 3). The cohesion is a parameter that cannot be measured physically and was therefore derived from Equation 3.9

$$C_0 = 2S_0\left[(\mu_i{}^2 + 1)^{0.5} + \mu_i\right] \qquad \text{Equation 3.9}$$

$$\Phi = tan^{-1}(\mu_i)$$

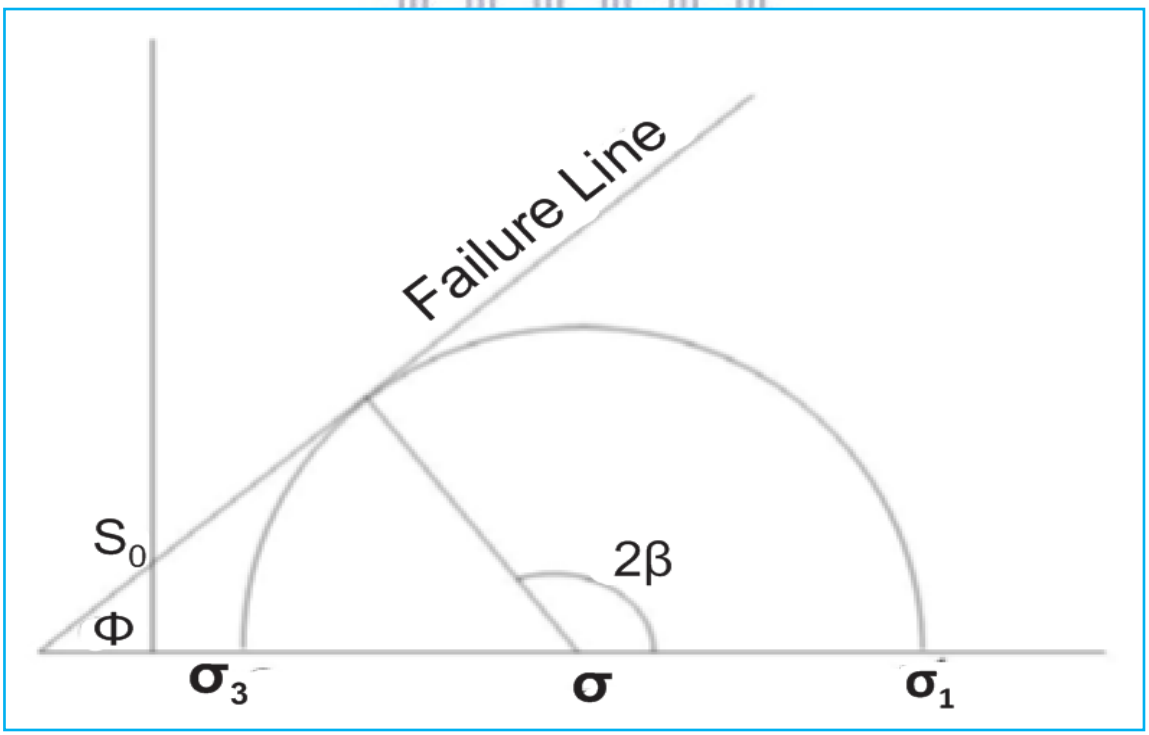

Figure 3.12: Illustration of Mohr-Coulomb Failure Criteria and Mohr's circle. Modified from Fjaer *et al*., (1992).

Generally, a triaxial test on core samples is done to provide us with the Mohr diagrams, however, in the case of the K-R Field, no lab tests were performed on the cores and thus empirical equations were used to estimate the Uniaxial compressive strength (UCS), Friction angle (FA), the coefficient of friction angle (μ_i) and cohesion (S_0) which are imperative for geomechanical modelling.

3.8.2 Uniaxial Compressive Strength

The uniaxial compressive strength (UCS) is the load per unit area where the rock will fail in compression and is generally determined in the lab from core samples. It is important to have UCS values for the entire depth of investigation as rock strength properties vary. The UCS for all K-R wells was calculated by using Equation 3.10, which was proposed by McNally (1978) and is utilized for fine – medium grained sandstones; and Equation 3.11 which is generally used for strong, compacted shales as is evident in the K-R Field.

$$1200^{(-0.036*\Delta t)} \quad \text{Equation 3.10}$$

$$7.22E^{(0.712)} \quad \text{Equation 3.11}$$

Where: Δt is transit time (μs/ft) and E is Young's modulus.

3.9 Static and Elastic Parameters

3.9.1 Seismic Interval Velocity: V_p and V_s

Velocity is a very important parameter in geophysics which has either direct or indirect influences on porosity, compaction history, density, elastic moduli, rock strength etc. interval velocity – the velocity of specific or multiple rock layers. It is generally measured from acoustic logs such as the sonic log (DTCO) in the case of K-R.

V_p is the primary (or compressional) velocity, which is easy to derive as shown in Equation 3.12, whilst V_s is the secondary (or shear) velocity which may not be as straightforward. Castagna *et al.*, (1985) introduced the concept of "mudrock line" through several laboratory tests which show a simple linear relationship between V_p and V_s. The V_s was calculated by

making it the subject of the formula and this relationship, together with the Castagna equation is best illustrated in Figure 3.13.

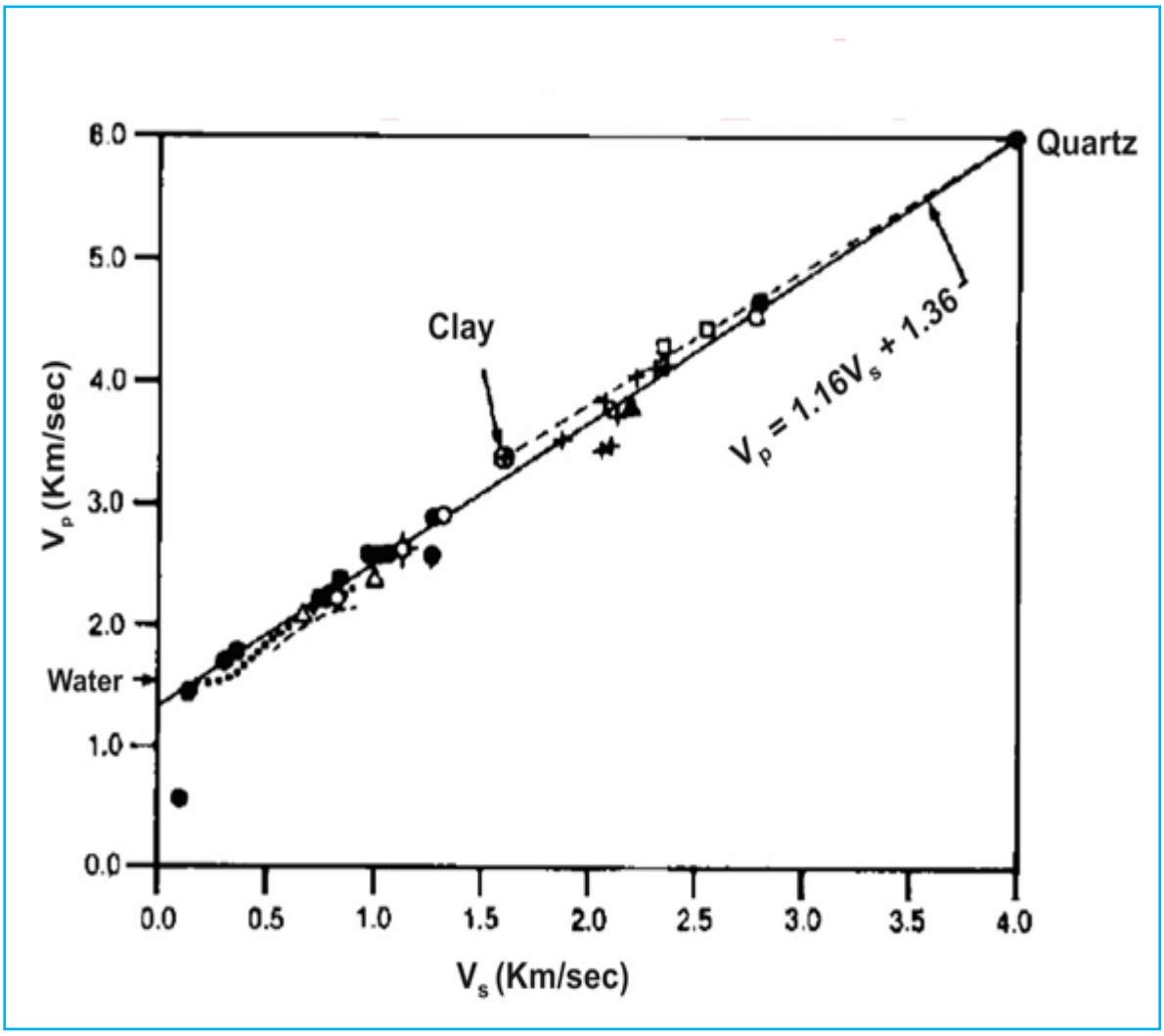

Figure 3.13: The Castagna Plot showing compressional and shear wave velocities derived from in-situ sonic and field seismic measurements. Modified from Castagna *et al*., (1985).

3.9.2 Poisson's Ratio and Young's Modulus

Poisson's ratio, which is basically the ratio of axial shortening to lateral expansion, provides us with information about the elasticity of the rock (Zoback, 2007). Many relationships between the Poisson's ratio and other parameters have been published; however, in this case, it is calculated solely from interval velocity as shown in Equation 3.13 highlighted by Zoback, 2007.

$$v = \frac{V_{p^2} - 2V_{s^2}}{2(V_{p^2} - V_{s^2})}$$ Equation 3.13

Where: v is Poisson's ratio, V_p is the primary velocity (m/sec) and V_s is the secondary velocity (m/sec).

Table 6: Approximate values of Poisson's ratio for several rock types. From Daines (1980).

Rock Type	Poisson's Ratio
Clay, very wet	0.50
Clay	0.17
Conglomerate	0.20
Dolomite	0.21
Greywacke:	
Coarse	0.07
Fine	0.23
Medium	0.24
Sandstone:	
Coarse	0.05
Coarse, cemented	0.10
Fine	0.03
Very fine	0.04
Medium	0.06
Poorly sorted. clayey	0.24
Fossiliferous	0.01
Limestone:	
Fine, micritic	0.28
Medium, calcarenitic	0.31
Porous	0.20
Stylolitic	0.27
Fossiliferous	0.09
Bedded fossils	0.17
Shaley	0.17
Shale:	
Calcareous (<50% $CaCO_3$)	0.14
Dolomitic	0.28
Siliceous	0.12
Silty (<70% silt)	0.17
Sandy (<70% sand)	0.12
Kerogenaceous	0.25
Siltstone	0.08
Slate	0.13
Tuff, glass	0.34

Young's modulus is another important parameter in geomechanics, especially when dealing with shales. It is simply defined as a measure of stiffness in an elastic material; like the Poisson's ratio, it is also related to other elastic moduli such as: Shear modulus (G), Bulk

modulus (K) and Lame's constant. The formula used to calculate the Young's modulus for the K-R wells is shown in Equation 3.14.

$$E = \rho . V_{s^2} \left(\frac{3V_{p^2} - 4V_{s^2}}{V_{p^2} - V_{s^2}} \right) \quad \text{Equation 3.14}$$

Where: E is Young's modulus (Pascals), ρ is density (Kg.m^3), V_p is primary velocity (m/sec) and V_s being the secondary velocity (m/sec).

Chapter 4: Geomechanical Modelling

4.1 Introduction

Rock mechanics is the theoretical and applied science of the mechanical behaviour of rocks. It entails studying the rocks response to acting forces (Judd, 1964). Mechanical properties define and describe the rocks' behaviour at changing stress conditions that are commonly investigated on rock masses accessible for exploitation. Rock mechanics deals with stresses and its inevitably resulting strain and these can be seen as broad fundamentals, on which applied geomechanics is based.

The objective of my geomechanical modelling is to determine the magnitude and direction of stress in the K-R Field. Stresses in the earth can be defined as vertical stress (σ_v), maximum horizontal stress (σ_H) and a minimum horizontal stress (σ_h) component. The vertical stress was determined by integrating the corrected bulk density log. Minimum horizontal stress was calculated as fracture gradient and calibrated through leak-off tests. Maximum horizontal stress was back-calculated from the drillworks software and the maximum horizontal stress direction was established from structural depth maps of the reservoir. The components allowed me to establish continuous stress profiles for the K-R Field.

4.2 Stresses for Geomechanical Modelling

Stress is defined as the force acting per unit area and is expressed in SI units as Pascals (Pa) (Equation 4.1). In the Petroleum industry, pound per square inch (psi) is often used. Geomechanics regards all compressive stresses in the earth to be positive (Fjaer *et al*, 2008; Zoback, 2007).

$$\sigma = \frac{F}{A} \qquad \text{Equation 4.1}$$

Where: σ is Stress (Pa), F is Force (Newtons) and A is the area given in m^2

Normal stress is the stress acting perpendicular to a point on a plane; shear stresses are those acting parallel. Figure 4.1 is a visual representation of the stress tensor for an infinitesimally small cube.

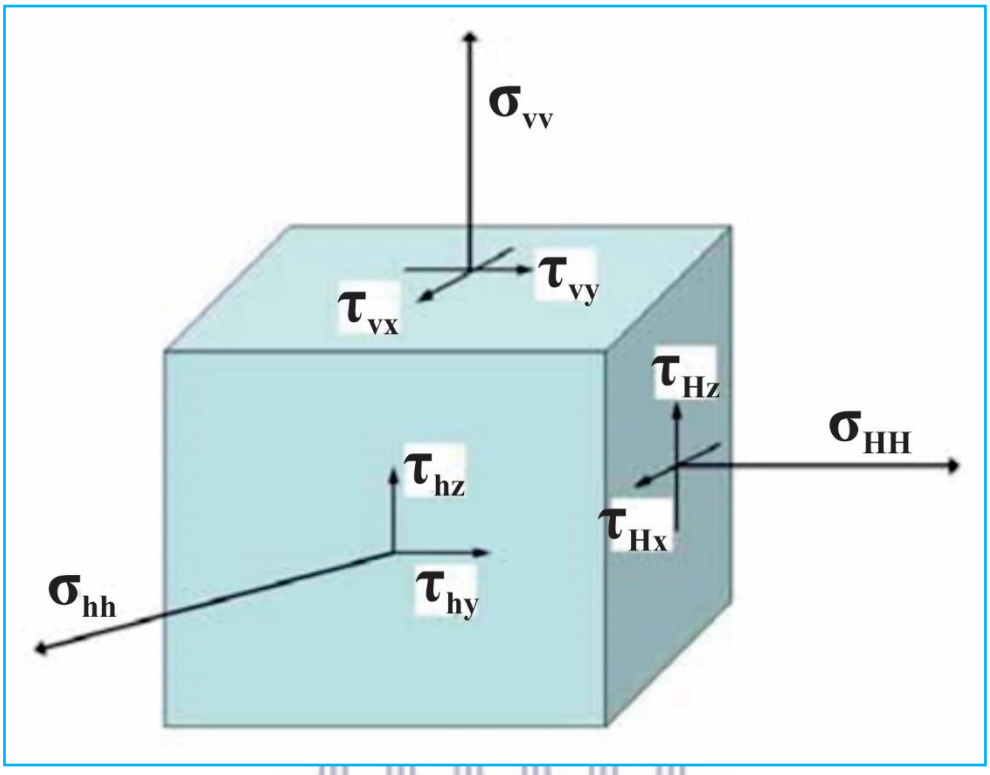

Figure 4.1: Cube illustrating the components of a typical stress matrix.

$$\begin{bmatrix} \sigma_{hh} & \tau_{hy} & \tau_{hz} \\ \tau_{Hx} & \sigma_{HH} & \tau_{Hz} \\ \tau_{vx} & \tau_{vy} & \sigma_{vv} \end{bmatrix}$$

Figure 4.2: Complete stress tensor.

The complete stress state of the cube is defined by three normal stresses and six shear stresses – as shown in Figure 4.2. A rotation can be applied where all six shear stress values are zero (Figure 4.3). Keaney, 2005 stated that three normal stresses results – principal stresses – and the directions they act in are called principal directions.

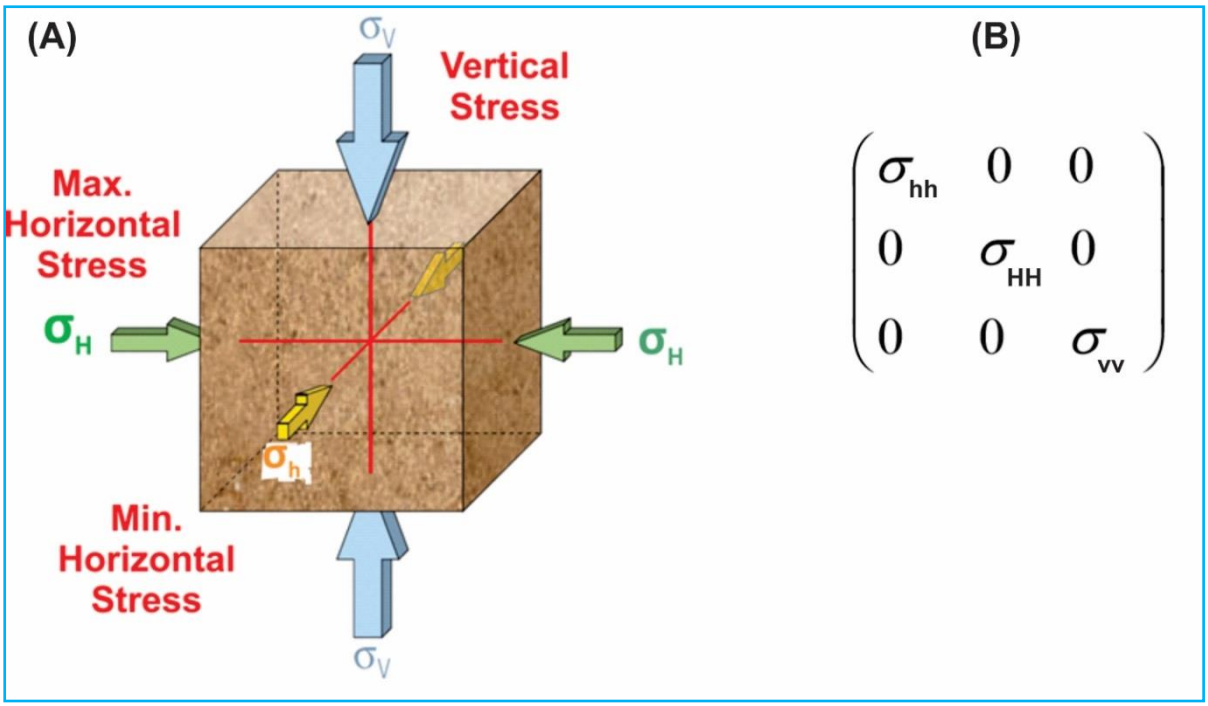

Figure 4.3: (A) Cube depicting the three principal stresses post rotation. (B) Principal stress tensor.

The Earth's surface essentially represents a principal stress plane due to its contact with either air or water (Zoback, 2007). This contact nullifies the support of any shear stress thus resulting in one principal stress being vertical to the Earth's surface and two orthogonal surfaces in the horizontal plane (Zoback, 2007). The state of stress in the Earth's crust is represented as the magnitude of vertical stress (σ_v) and the magnitude and direction of the maximum (σ_H) and minimum horizontal stress (σ_h).

Two sets of stresses are important for understanding the geomechanics of wellbore stability (Bratton, *et al*., 1999). The first are the in-situ far field stresses which exist away from the wellbore; the second set are nearer – wellbore stresses, which occur between the fluid–filled wellbore and the formation after a borehole has been drilled. Wellbore failure occurs when the strength of the surrounding rock has been exceeded. Geomechanical modelling begins by establishing the far field stress parameters which includes the direction of maximum horizontal stress and the three earth stresses; minimum horizontal stress (σ_h), maximum horizontal stress and the vertical stress (σ_v) which I have assumed to be principal stresses. All compressive stresses are taken as positive in geomechanics, thus, negative numbers will be regarded as tension in this thesis.

4.3 Tectonic Faulting Regimes

Fractures and faults are a product of brittle deformations: the former representing cracks or joints in rocks, with no or very little displacement (Jaeger *et al*., 2007). Faults are a result of shear deformation and are essentially fractures with significant displacement. Faults can either act as a conduit, a trap or a drilling hazard. Understanding the type of faults and their orientation in any field is fundamental to knowing how to proceed with the drilling operation. The type of faults present at K-R can be classified by order of magnitude of in – situ stresses. The Andersonian fault model proposed in 1951 still holds valid for today; it shows that the order of the three far – field stress magnitudes, σ_v, σ_h and σ_H will indicate which faulting will occur in the reservoir (Anderson, 1951). A representation of Anderson's model is shown diagrammatically in Figure 4.4.

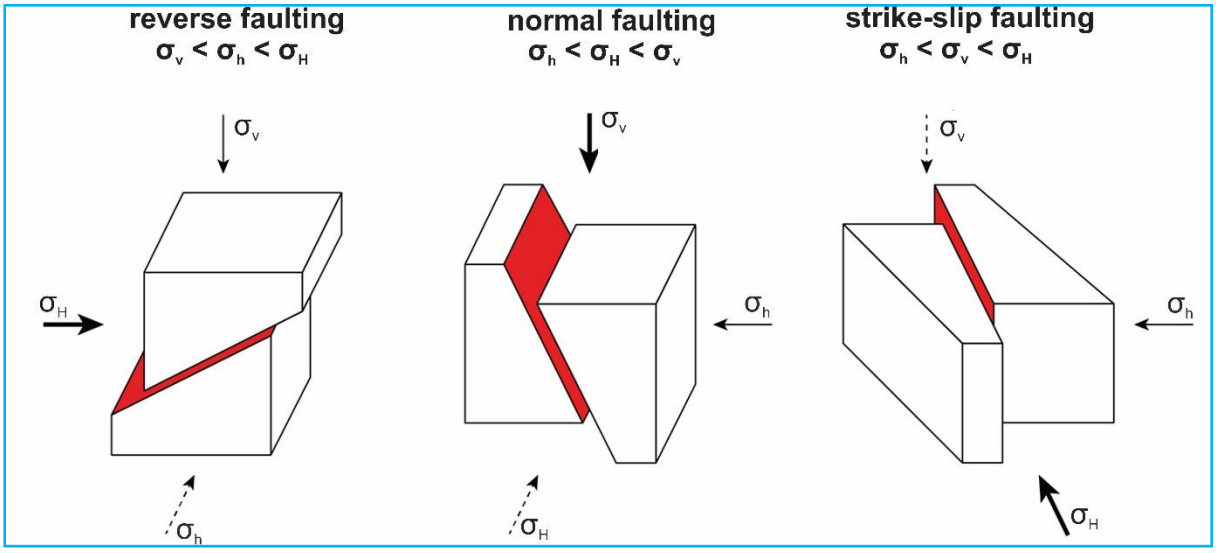

Figure 4.4: Diagram showing the Anderson fault model. Modified after Bratton (2005).

4.4 Estimation of Geopressure Gradients

The Schlumberger Oilfield Glossary (2012) defines geopressure as "*the pressure within earth or formation pressure*". This definition would then be applicable for overburden gradient, pore pressure and fracture gradient (Dutta, 1999).

Accuracy when determining geopressure is pivotal as it could have disastrous effects on wellbore stability and the cost of the project. In a high pressure, high temperature well, the

margin between the pore pressure gradient and fracture gradient is quite narrow, leaving very little room for error (Ward *et al*., 1999). Authors like Rocha *et al.* (2004) have stated that a small drilling window is probably the biggest challenge when it comes to deepwater drilling.

4.4.1 Overburden Gradient Estimation

The vertical stress (in-situ) is the result of the weight of rock per unit area above each point in the earth. Therefore, the magnitude of vertical stress can be derived by integrating the bulk density log (RHOB) for each well. The integration is expressed in Equation 4.2.

$$\sigma_v = \int_0^z \rho g \mathrm{dz} \qquad \text{Equation 4.2}$$

Where: σ_v is vertical stress, ρ is density, g is gravitational acceleration and z is the depth.

The density logs were first corrected by applying the correction software mentioned in Chapter 3, and then integrated into Equation 4.2. This is a highly important step as the accuracy of σ_v is dependent on the density log. An example of the "original" and "corrected" density logs for KR-1 is shown in Figure 4.5a and 4.5b. All graphs for original and corrected density can be found in Appendix A.

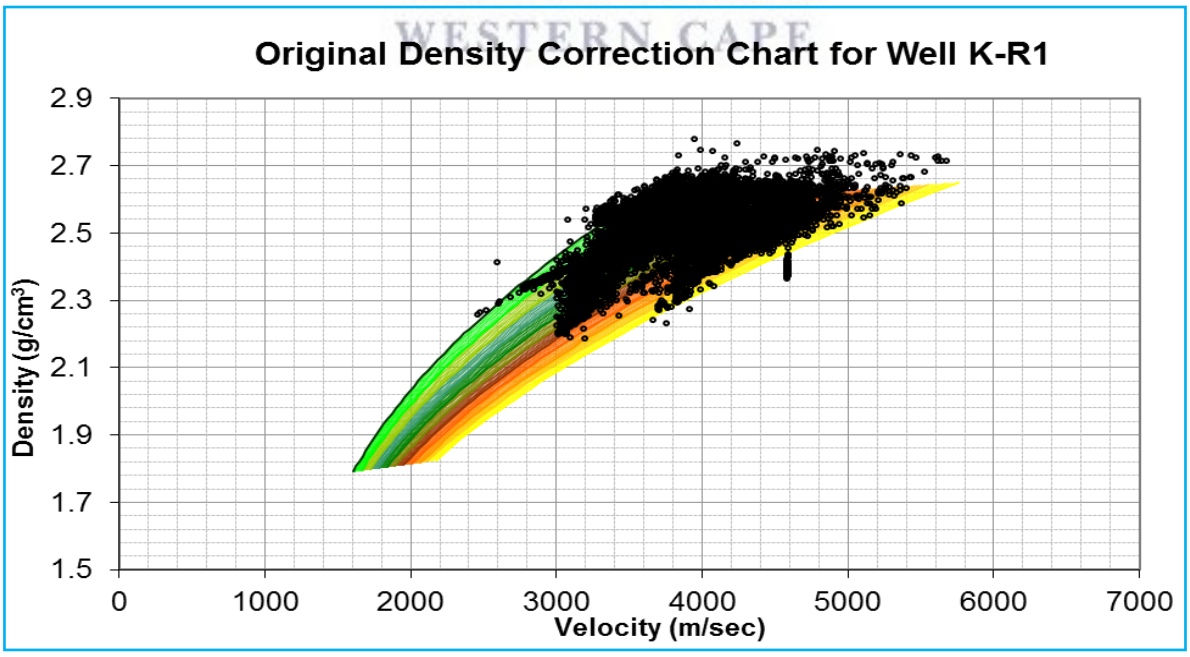

Figure 4.5 (a): Chart showing the spread of original density values for well K-R1.

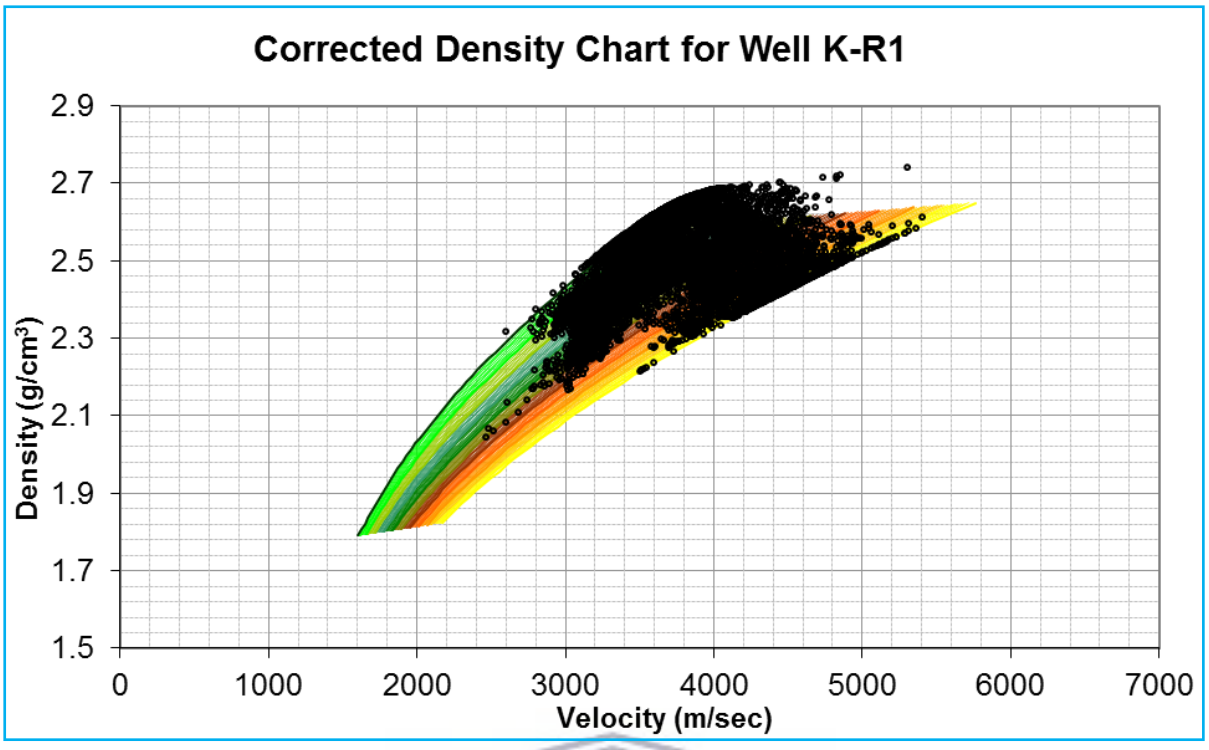

Figure 4.5 (b): Chart showing the spread of corrected density values for well K-R1.

The display of density data points in Figure 4.5 (b) shows a less erratic and more even distribution of density. The software provides the corrected values as per depth and as a means of comparison, the vertical stress was calculated using both the original density and corrected density and plotted against depth to show variation (Figure 4.6). The general plot of the original density log against the corrected ones for each well can be found in appendix B.

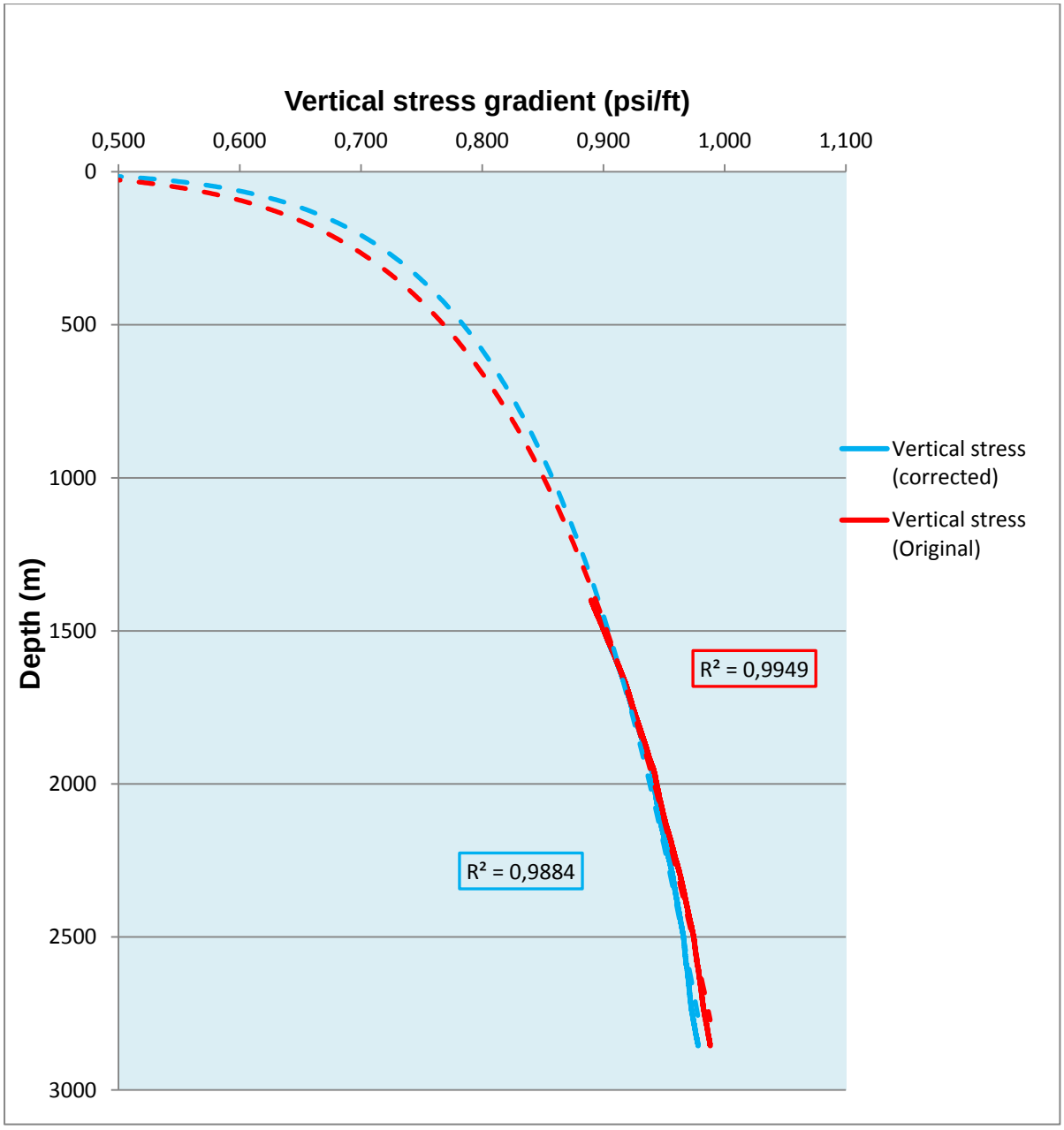

Figure 4.6: Graph showing vertical stress gradient before and after density correction with depth for well KR-1.

In well K-R1, the upper limit of the main reservoir (USM) is located at approximately 8201.12 feet. Figure 4.6 shows a vertical stress gradient using the original density, of 0.9949 psi / ft, which represents 8159.29 psi, against a vertical stress gradient obtained from the corrected density log of 0.9887 psi / ft or 8108.44 psi; yielding a difference of 50 psi.

Although this value may seem trivial, it may have a great impact on the limits of the mud window prediction since the vertical stress is incorporated in the empirical calculations of pore pressure gradient and fracture gradient as will be shown in Chapter 5. This could in turn have a domino effect on wellbore stability and the cost associated with it.

4.4.2 Determining the Pore Pressure Gradient

The estimation of this parameter is imperative as uncertainties and inaccurate results may lead to formation damage, wellbore stability issues, kicks and the worst case scenario of a blowout. Knowledge of pore pressure throughout the well is paramount to drilling safely and efficiently as well as assessing potential risk factors, migration of formation fluids and seal integrity (Tang *et al*., 2011).

Where the pore pressure of the formation is assumed to be almost equal to the theoretical hydrostatic head for the vertical well depth, the formation is considered to be normally pressurized or hydrostatic (Bourgoyne Jr. *et al*., 1986). Thus, the normal pore pressure can be estimated using the hydrostatic gradient of that area. This technique can't be executed for all areas as many areas are not normally pressured. This is referred to as *abnormal pore pressure*, i.e. where the pore pressure is either higher or lower than the normal pore pressure. The former can be referred to as an overpressure zone and drilling through this zone could lead to wellbore stability issues (Fjaer *et al*., 2008).

Several pore pressure estimation methods have been proposed over the last five decades and all are centred on compaction dependant properties of shale, i.e. density, porosity, sonic velocity, and resistivity. Estimation methods can be grouped into direct methods or effective stress methods (Tang *et al*., 2011).

The direct method involves the use of either crossplots or overlays to measure the amount a pore pressure indicator veers away from its normal trend line to the pore pressure gradient at that particular depth. The effective stress method is based on Terzaghi's effective stress principal. The principal states that the compaction a geological material experiences is controlled by the difference between the total confining pressure and pore fluid pressure, which is referred to as the "effective stress" (Tang *et al*., 2011).

Effective stress methods can be further sub-divided into vertical methods and horizontal methods. Vertical methods stay along the same vertical line by using the normal trend data available at a specific depth, while the horizontal methods use the normal trend data available at the same depth, thus, following the path of the same horizontal line (Bower, 1999a).

The pore pressure for each well was calculated using the Eaton method. Eaton (1975) defined pore pressure as a function of overburden pressure, hydrostatic pressure and an observed parameter / normal parameter ratio. The observed parameter could be the sonic travel time, resistivity or d' exponent (a drilling parameter). Originally established in the Gulf coast, the Eaton equations have been used worldwide as the exponents may be adjusted based on the environment:

$$P = S - (S - hyd)\left[\frac{R_{sh}observed}{R_{sh}\,normal}\right] \qquad \text{Equation 4.3}$$

$$P = S - (S - hyd)\left[\frac{\Delta_t observed}{\Delta_t normal}\right] \qquad \text{Equation 4.4}$$

$$P = S - (S - hyd)\left[\frac{dc\ - observed}{dc\ - normal}\right] \qquad \text{Equation 4.5}$$

Where: P is pore pressure, S is the overburden, hyd is the hydrostatic pressure (0.44 psi/ft), R_{sh} is the resistivity, Δ_t the sonic slowness and dc, the d' exponent. Equation 4.4 was used to calculate pore pressure; $\Delta_t observed$ is derived from normal compaction trend lines for shales only.

RFT data and mud weights used to drill these wells are used to calibrate the pore pressure values from the Eaton equation. No reservoir overpressure exists in the K-R Field, wherever overpressure is mentioned in the driller's report. It is due to buoyancy effects which occur when hydrocarbons migrate into a tilted reservoir. As the hydrocarbon column height grows, the top of the reservoir begins to experience elevated pressure.

4.4.3 Determining the Fracture Gradient

Fracture gradient is "the pressure gradient that will cause fracture of the formation" (Rocha *et al*., 2004). Hence, if the fracture gradient is exceeded, the formation will fracture resulting in a mud loss. Along with pore pressure gradient, the fracture gradient is one of the most important aspects to be considered during the planning and drilling phase.

Methods of fracture gradient estimation are generally derived from rock mechanics theories or simplified methods which may lack accuracy in representing underground rock conditions (Rocha, *et al*., 2004).

Numerous published methods for fractured gradient are available and can be categorised as either "direct" or "indirect" methods (Rocha *et al*., 2004). Direct methods give a measurement of pressure required to fracture the rock as well as propagating the resulting fracture. These methods are generally based on leak off tests (LOT) or extended leak-off tests (XLOT), which are a common calibration test in the Petroleum industry. A typical extended leak off test is illustrated in Figure 4.7.

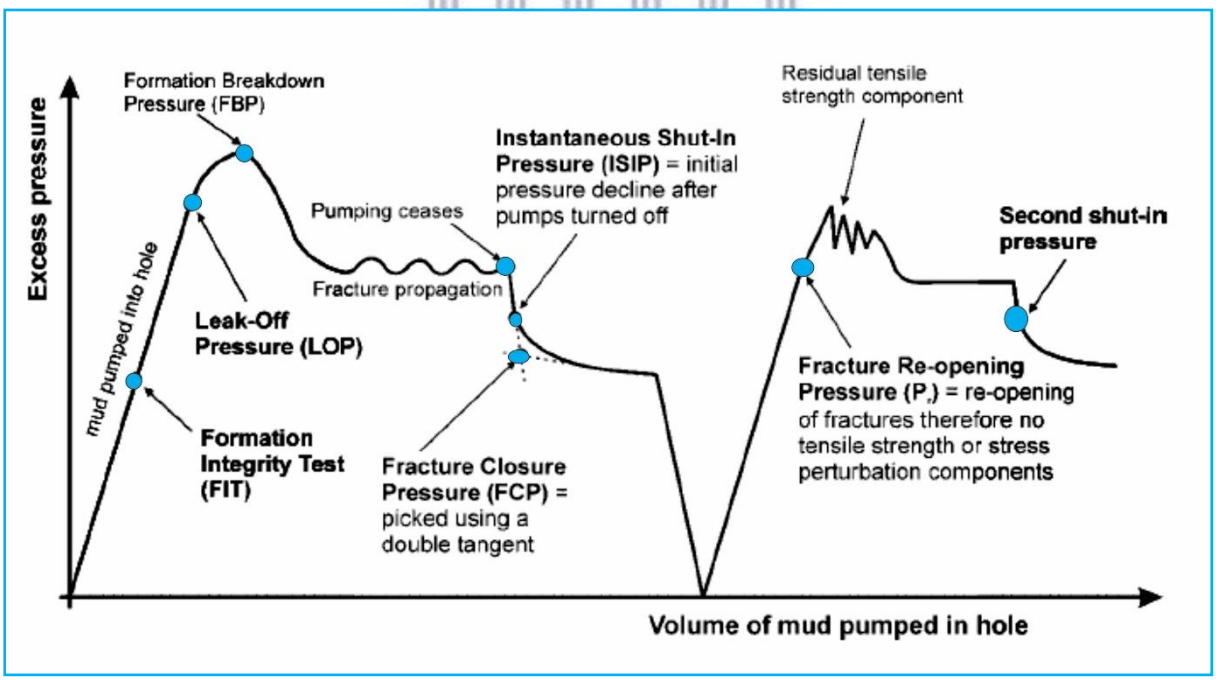

Figure 4.7: Graph showing the different phases of a typical leak off test. Modified after Rocha *et al*., (2004).

Indirect methods are based on analytical or numerical models which may be used to provide the fracture pressure gradient along the entire length of the well. These methods are generally built for a specific field or area and the data input requirements are often difficult to obtain.

There are numerous methods and models that are used to predict the minimum horizontal stress (σ_h). In this thesis, σ_h is taken as the fracture gradient. Eaton (1969), proposed a method for fracture gradient determination based on Poisson's ratio. From all available methods, the Eaton equation for fracture gradient was chosen due to the fact that it considers more parameters than other methods, thus improving the result. This expression is given in Equation 4.6.

$$FG = \left(\frac{\nu}{1-\nu}\right)(S_v - P_p) + P_p \qquad \text{Equation 4.6}$$

Where: FG is the fracture gradient (psi/ft), ν is Poisson's ratio, S_v is the vertical stress gradient (psi/ft) and P_p is the pore pressure gradient (psi/ft).

Data from leak-off tests and mud weights used while drilling the wells were used to calibrate the fracture gradient. When the fracture gradient is exceeded by the mud, the rock breaks and a fracture forms, causing mud losses. This phenomenon did not occur in any of the K-R wells according to the daily drilling reports.

4.5 Determining the Magnitude of Maximum Horizontal Stress

As stated in Chapter 1, this parameter cannot be determined in-situ and thus, had to be back - calculated from the drillworks software. Once all the geomechanical input parameters were loaded onto the drillworks software, the maximum horizontal stress (σ_H) was simulated by utilizing Equation 4.6.

$$SFG = ShG * \text{tf} \qquad \text{Equation 4.6}$$

Using Equation 4.6, the maximum horizontal stress (ShG) is calculated by the drillworks prediction software by utilizing the shear failure gradient (SFG) and the tectonic factor(tf). In

general, a tectonic factor between 0 and 1 is typical for normal faulting stress regimes, with other regimes having tf greater than 1 (Halliburton, 2009).

4.6 Horizontal Stress Direction

The direction of horizontal stress is vital for geomechanical modelling. Often, where the data is available, it is determined from image logs, micro seismic data and dipole sonic logs. In the case of the K-R Field, no such data is available; therefore, the horizontal stress direction had to be determined from the direction of fault trends using structural maps. Faults are essentially fractures with displacement, and it is widely accepted that fractures propagate perpendicular to the direction of σ_h, thus, the direction of σ_h can be determined since all principal stresses are orthogonal. As explained in Chapter 2, the dominant fault trends in the K-R Field are north-north west to south-south east (NNW – SSE). For modelling purposes, the direction of σ_H (Figure 4.3) was chosen as 125^0 although this assumption may not accurately depict the present day stress direction at K-R.

4.7 Post Drill Analysis and Calibration

Since the wells have been drilled, the geomechanical analysis is a post drill analysis and thus, calibrating the estimated curves to fit actual observed drilling events (kicks, losses, LOT's etc.) is most important. Observation made during the drilling process may be related to pressure gradients and could therefore help in pinpointing whether or not the curve is in the right location. By scouring through the daily drilling reports and other reports describing observations made during the drilling process, information regarding drilling incidents can be obtained and used to calibrate the pore pressure gradient and fracture gradient. This is done by shifting the curves to fit with observed fracture and pore pressures, ensuring the geomechanical model is as close to reality as possible.

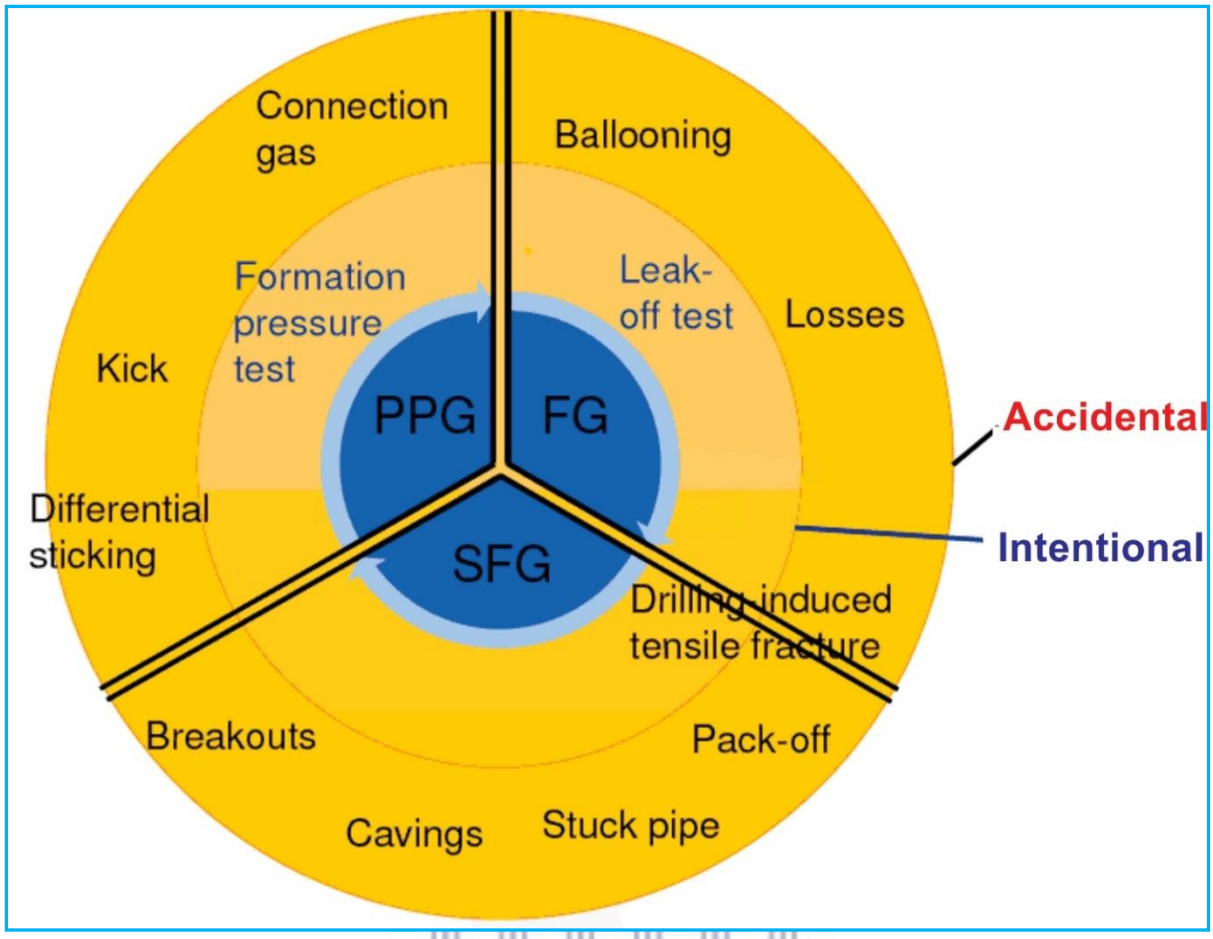

Figure 4.8: Schematic showing various calibration sources used in geomechanics. Modified from Baker Hughes Inc. (2011).

The different calibration sources used for calibrating the drilling mud window are shown in Figure 4.8. These sources are grouped into either accidental or intentional, i.e. if the pressure indicator was planned and executed or an observed incident while drilling the well.

SFG in Figure 4.8 is the shear failure gradient which is the minimum mudweight required to avoid plastic failure of the wellbore. Calibration should start with pore pressure as both the fracture gradient and shear failure gradient are dependent on estimated pore pressure values. As can be seen in Figure 4.8, the formation pressure test (LOT) is the only intentional source for pore pressure gradients. The accidentals sources are made up of connection gas, kick and differential sticking. Connection gas involves a short surge of gas into the mud when making a connection as a result of pumps being stopped, i.e. leading to a lower bottom hole pressure (Schlumberger, 2012). A kick occurs when there is an influx of formation fluid in the well

while drilling; a highly undesirable consequence of a kick could lead to a well blowout. Its relevance in geomechanical calibration is that it provides a direct indication of what the pore pressure is, due to it proving that modeled pressure was underestimated. Differential sticking generally occurs in highly permeable sand layers, because of a high pressure differential between the wellbore and the formation, the drillstring sticks to the borehole wall becoming an immovable pipe (Schlumberger, 2012).

The two accidental sources for fracture gradient are ballooning losses. Ballooning involves initial fluid loss into the formation, followed by an increase in mud when the pressure returns to "normal". In the case of losses, this is an indication that the fracture gradient has been exceeded and the wellbore is now losing drilling fluid into the fractured formation. A leak- off test which is done properly can give the real fracture pressure values. At times the breakdown pressure is read instead of leak-off pressure, leading to an overestimated fracture gradient.

Borehole image logs can help us detect drilling induced tensile fractures which can be used as pressure indicators for both fracture gradient and shear failure gradient. Although it does not quantify the exact pressure responsible for triggering the fracture, it can provide us with information so as to see whether we are over or under the fracture gradient and shear failure gradient. Only accidental sources exist for calibrating shear failure gradient which comes in the form of breakouts, cavings, stuck pipe and pack offs. These are all indicators that shear failure gradient has been estimated to be too low.

Sourcing the necessary data to perform a calibration for the seven wells proved to be very challenging. Most of the calibration sources simply weren't available for the K-R Field and leak-off tests were not performed on all wells. In addition, due to the age of the well, documentation regarding drilling events was scarce or non-existent. However, all drilling data that was available was used to calibrate and was incorporated into the drillworks model.

4.7.1 Well KR-1

Being the first well drilled in the K-R Field, the documentation for this well is of poor quality which makes it harder to interpret. Some of the initial reports were lost, however the relevant information could be extracted from the geological well completion report and daily drilling

report. The mud weights that were used at different depths during drilling are available and this was used to calibrate the safe mud window.

4.7.2 Well KR-2

The situation for this well is largely similar to well KR-1. No leak- off tests were performed at this well nor were there any drilling incidences, making calibration more difficult. However, the mud weights that were used to drill the well were recorded and can be used to validate the gradients.

4.7.3 Well KR-3

This well was the most poorly drilled of all the K-R Field wells. Major washouts exist throughout the well as can be seen in appendix C. The daily drilling report mentions ‘’wash and reaming” quite frequently, which is an indicator of a problematic well.

4.7.4 Well KR-4

The data for this well is similar to that of well KR-1, except, for the fact that this well experienced more equipment failures, which halted the drilling process. Since none of this information can be used as a calibration source, the data available, together with the drilling mud weights were used in the calibration of the model.

4.7.5 Well KR-5

This well is slightly better for calibration as more data exists. Mud losses of $5m^3$ are reported in the daily drilling report; however the reason provided is due to a “wiper trip”, which is the movement of the coil tubing in and out of the wellbore and thus, cannot be used for calibration. Apart from some damage to drill bits and down time, the daily drilling report only serves to provide the drilling mud weights and no further information for geomechanical calibration exists.

4.7.6 Well KR-6

In spite of core data not contributing as a calibration source for the K-R Field, this well has had the most number of cores extracted from it (8 in total). The recorded mud weights from the daily drilling reports helped validate the geopressure gradients.

4.7.7 Well KR-7

Being the most recent well to have been drilled, all documentation is clear and available. Equipment failures and drilling bits having to be ordered and replaced resulted in some loss of time. The mud weights provided on the daily drilling reports provided a calibration source.

4.8 Wellbore Stability

Before drilling can commence, the in-situ stresses present in the formation must be carefully considered. These are compressive stresses in the form of mostly unequal minimum and maximum horizontal stress, σ_h and σ_H, and the vertical / overburden stress, σ_v. In addition to the principal stresses, pore pressure, P_f, is also present. After the well has been drilled, these stresses get re-distributed along the borehole wall into hoop stresses (σ_θ), axial stress (σ_z), and radial stress (σ_r). In deviated wells, an additional shear stress ($\tau_{\theta z}$) component is created (McLean and Addis, 1990).

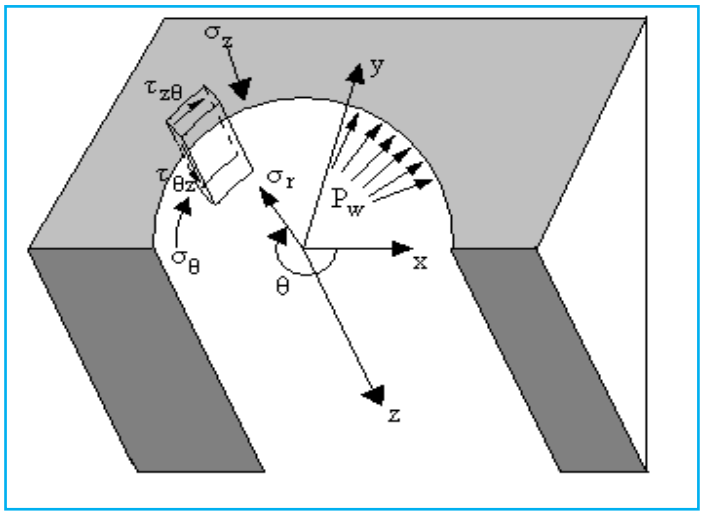

Figure 4.9: Stress components at the wall of a deviated wellbore. Modified after Mclean & Addis (1990).

During the drilling process, the drilling fluid must be of a certain weight to replace the weight of the rock being removed and thus, maintaining stability. Using the correct mud weight is critical as incorrect mud weights can lead to the two most common types of wellbore failure; shear failure and tensile failure (Figure 4.10). The first is caused by grains being forced together by two perpendicular stresses and the latter occurs when a single tensile stress pulls the grains apart.

Shear failure, also known as wellbore breakout occurs when the mud weight is too low and stresses around the wellbore are much higher. A mud weight that is too high can cause mud losses (Li, *et al*., 2012). Thus, rock failure will be avoided if the appropriate mud weight is used and the rock stresses are kept below a certain limit. During drilling, the allowance or window for failure may be higher than what stability models predict, as the initial borehole failures are not necessarily critical to the operations (Fjaer *et al*., 2008).

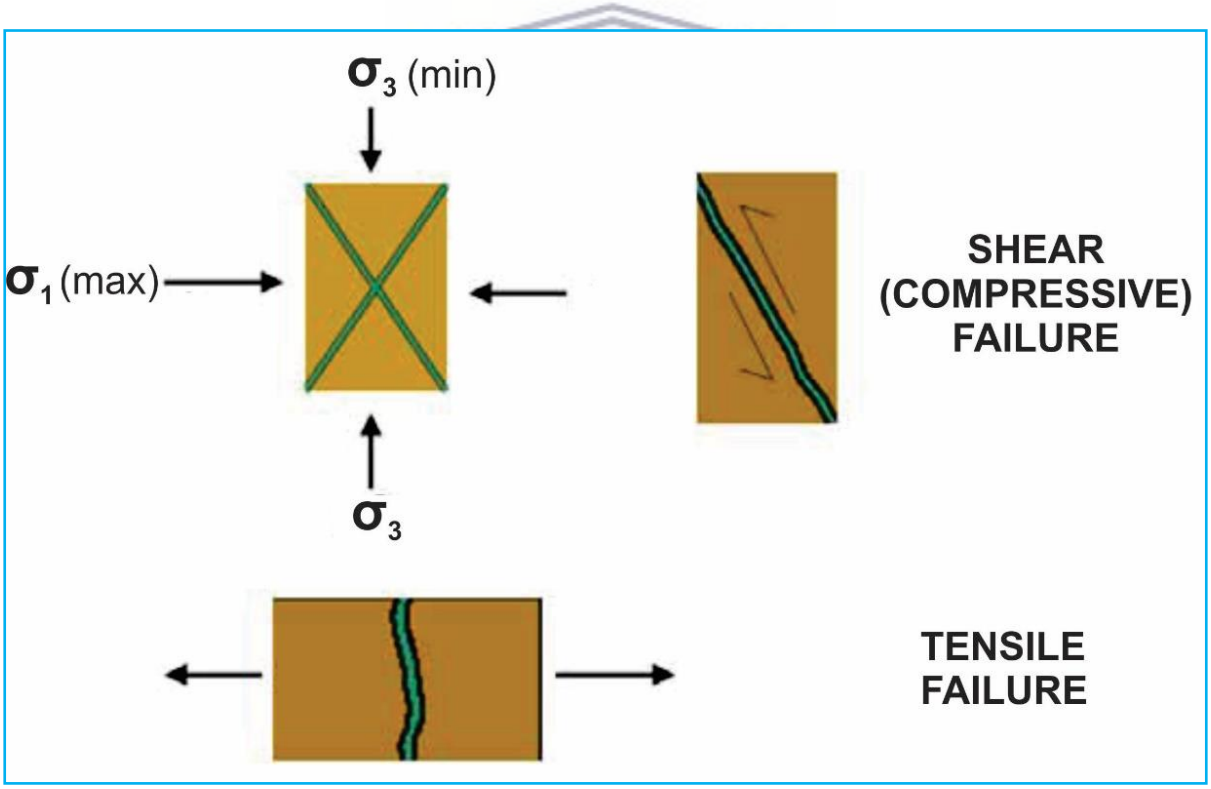

Figure 4.10: Shear and tensile. Modified after Bratton *et a*l. (1999).

Several wellbore stability models are used to estimate the required mud weight to avoid failure. The aim is to create a safe mud window which provides us with a mud weight that is high

enough to maintain wellbore stability but low enough to prevent mud losses into the formation (Zhang *et al*., 2008).

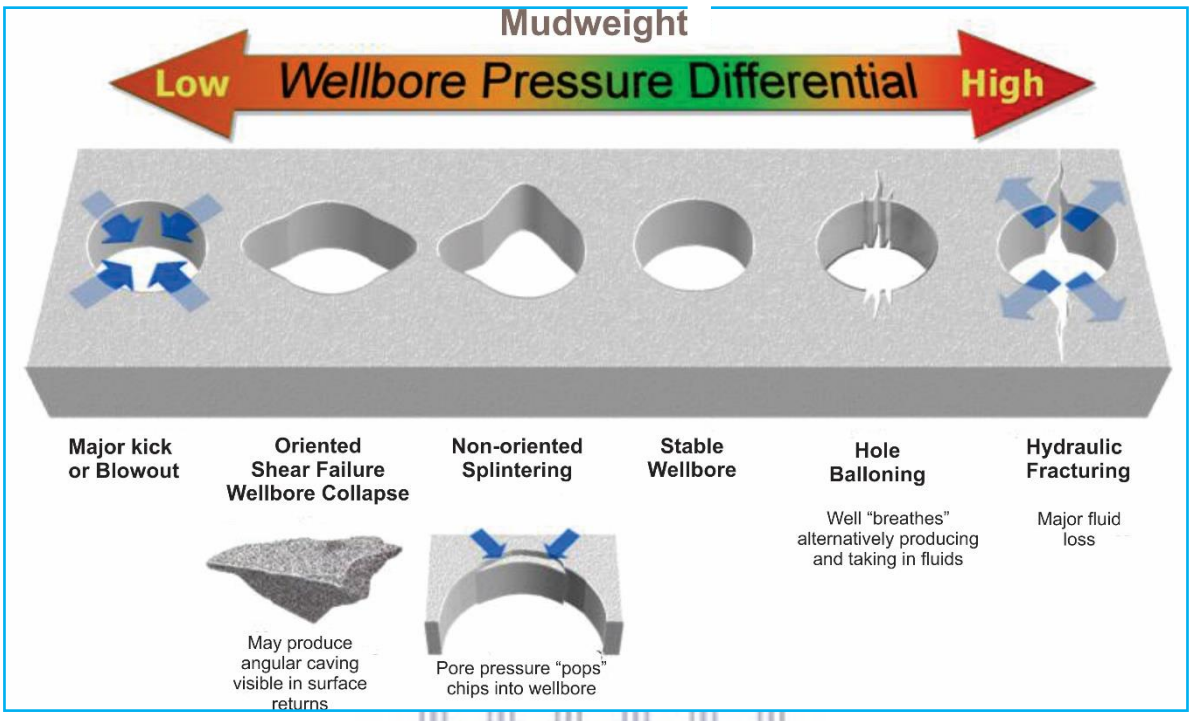

Figure 4.11: Different types of wellbore failures that occur with mudweight variations (Modified from Halliburton, 2012).

Figure 4.11 provides a schematic overview of the relationship between wellbore failures and mud weight. If the mud weight used is at the extreme low or high ends of the spectrum, the result is a major kick/blowout or fluid loss through fracturing of the formation. The ideal mudweight for a "stable wellbore" falls around central region and is represented by a strong green colour on the mud weight scale. Having a wide mud window is considered desirable as it gives the driller more allowance to drill the well safely.

4.9 Modelling Software

Once all geomechanical calculations were done on Microsoft excel, they were then imported onto the drillworks software for modelling. The following is a succinct description of the software used to complete the modeling in this thesis.

4.9.1 Drillworks – Predict

Pore pressure related issues lead to many drilling problems, which are both time consuming and costly. Inaccurate values of pore pressure, fracture pressure and overburden pressure may result in fluid losses and kicks and in some cases; the integrity of the well may be greatly compromised due to poor casing design (Knowledge Systems, 2006a).

Drillworks – Predict provides reliable forecasts of pore pressure gradient and fracture gradient - with several models and correlations available - which are the basis for analyzing the mud window. A major perk of the Predict simulation is its capability to offer pre-drill, real-time as well as post-drill analysis in order to enhance drilling performances and to avoid difficulties throughout the entire drilling process. The pre-drill analysis assists in choosing the optimal mud weight setting and casing design depths for a successful well. If the pre-drill analysis turns out to be erroneous, the real time analysis allows the user to implement modifications to the pre-planned model in order to maintain an optimal drilling process. The post-drill analysis tools allow for an improved knowledge for the planning and drilling of future wells (Knowledge systems, 2006a).

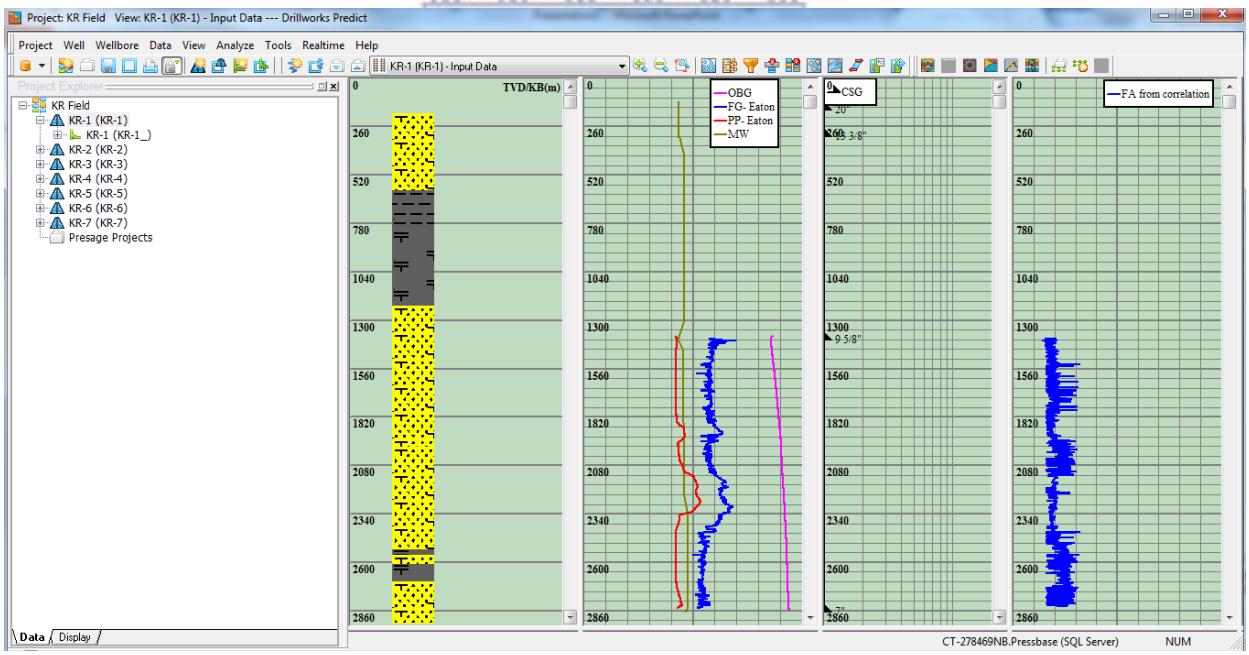

Figure 4.12: User output window on Drillworks – Predict.

The Predict software is easy to use and its interactive programming allows the user to make changes to various trend lines while viewing the output window. This function provides a user with the possibility to vary parameters that may be uncertain and investigate any outcomes this will have on the safe drilling window, i.e. the margin between shear failure gradient (SFG) and the fracture gradient.

4.9.2 Drillworks – Geostress

This software is a geomechanical analysis tool which allows the user to assess wellbore stability issues before and during drilling. Geostress may be used to plan the most suitable well path as well as to fine- tune and create the best mud weight design possible (Knowledge Systems, 2006b). The advantage of this being; fewer wellbore stability problems during drilling and thus, a safer and more cost effective drilling process. In this thesis, the Geostress tool has been used to investigate the safe wellbore trajectory and the safe mud window. Figure 4.13 shows what a typical hemisphere plot simulated on Geostress looks like.

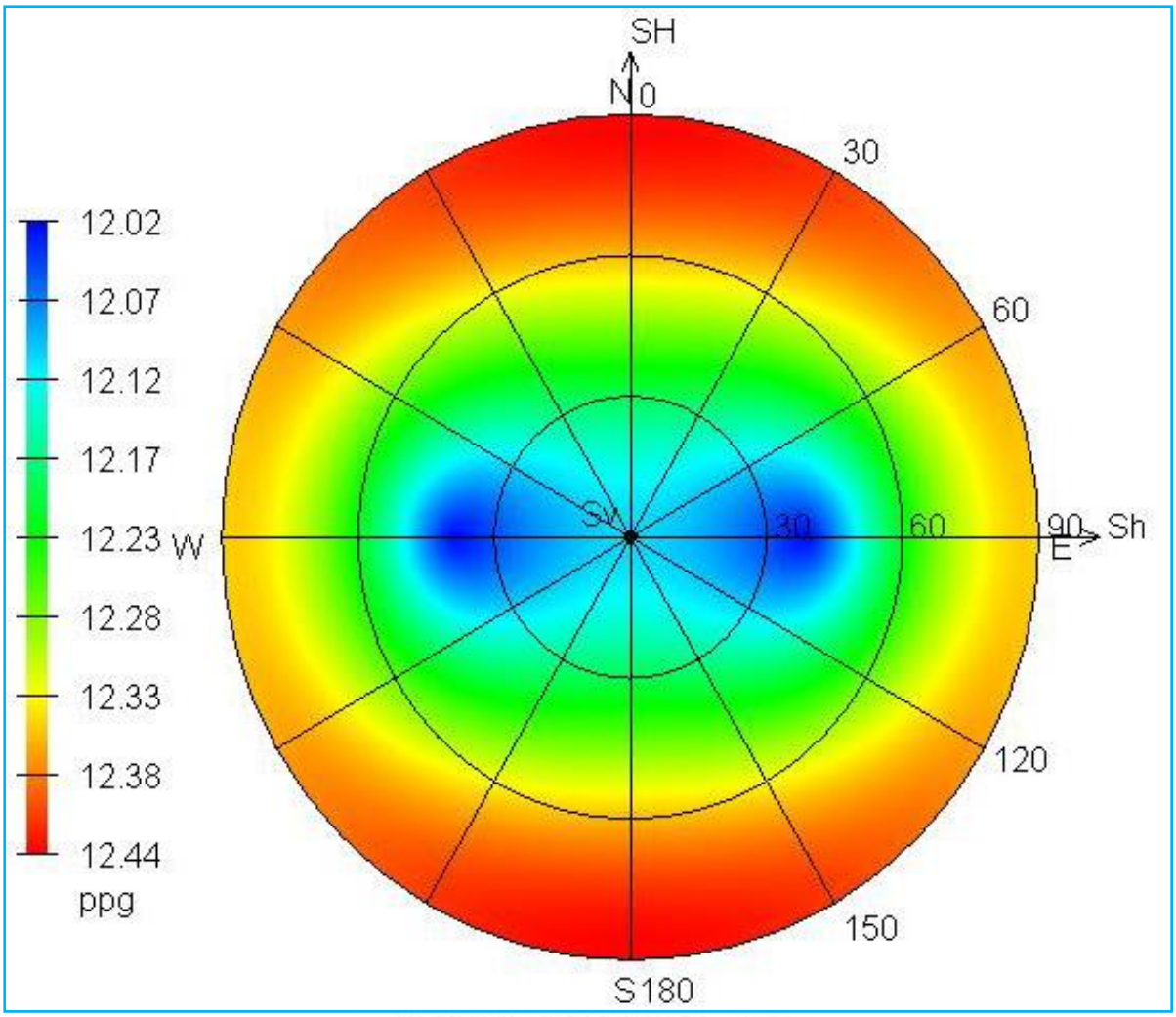

Figure 4.13: Lower hemisphere plot illustrates the impact of borehole geometry on mud weight (PPG) requirements. Wellbore direction is shown as the circumference of the diagram, wellbore inclination stems from the centre and mud weight shown by the colours.

Chapter 5: Results and Simulation

5.1 Introduction

The last two chapters describe how the geomechanical parameters were derived and the method in which the model was built. This section provides the results obtained from the geomechanical model and observations pertaining to the results. The track views showing geopressure gradient analysis, rock properties and wellbore trajectory are displayed for each well.

5.2 Well KR-1

As mentioned in Chapter 4, the data available for calibration is minimal and the mud weight used to drill the well was the main source. All calibrations were adjusted on Microsoft excel and then imported onto the drillworks software. The normal compaction trend lines for all wells can be found in Appendix D. The resulting geopressure gradients post calibrations are shown in Figure 5.1.

In addition, the rock mechanical properties obtained by using the correlations highlighted in Section 3.7 of Chapter 3 are displayed in Figure 5.2. Although somewhat erratic, the friction angle (FA), cohesive strength (CS), and uncompressive strength (UCS) show a general increase with depth, mainly towards the well's total depth (TD).

Graphs showing the safe drilling mud window at TUSM and BUSM are shown in Figure 5.3 and 5.4 respectively. A wider mud window is observed at BUSM, i.e. at the bottom of the reservoir.

Wellbore trajectory is central to wellbore stability issues and thus, hemisphere plots showing mud weight variations are presented in Figure 5.5 and 5.6. The plots show wellbore trajectory position relative to maximum and minimum horizontal stresses and the parameters used in the analysis are listed in Table 7 and 8.

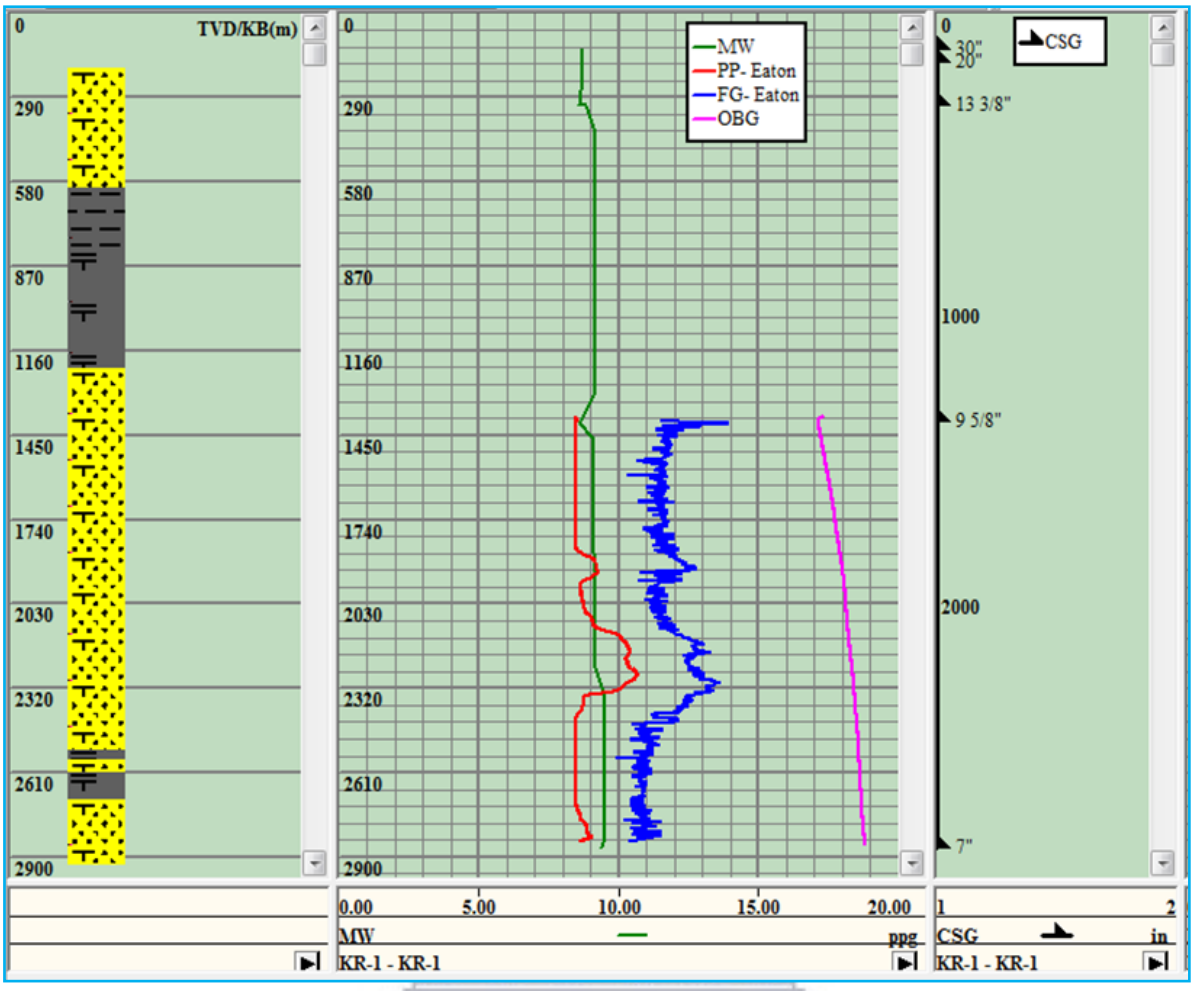

Figure 5.1: Modelled geopressure gradients for well KR-1 post calibration.

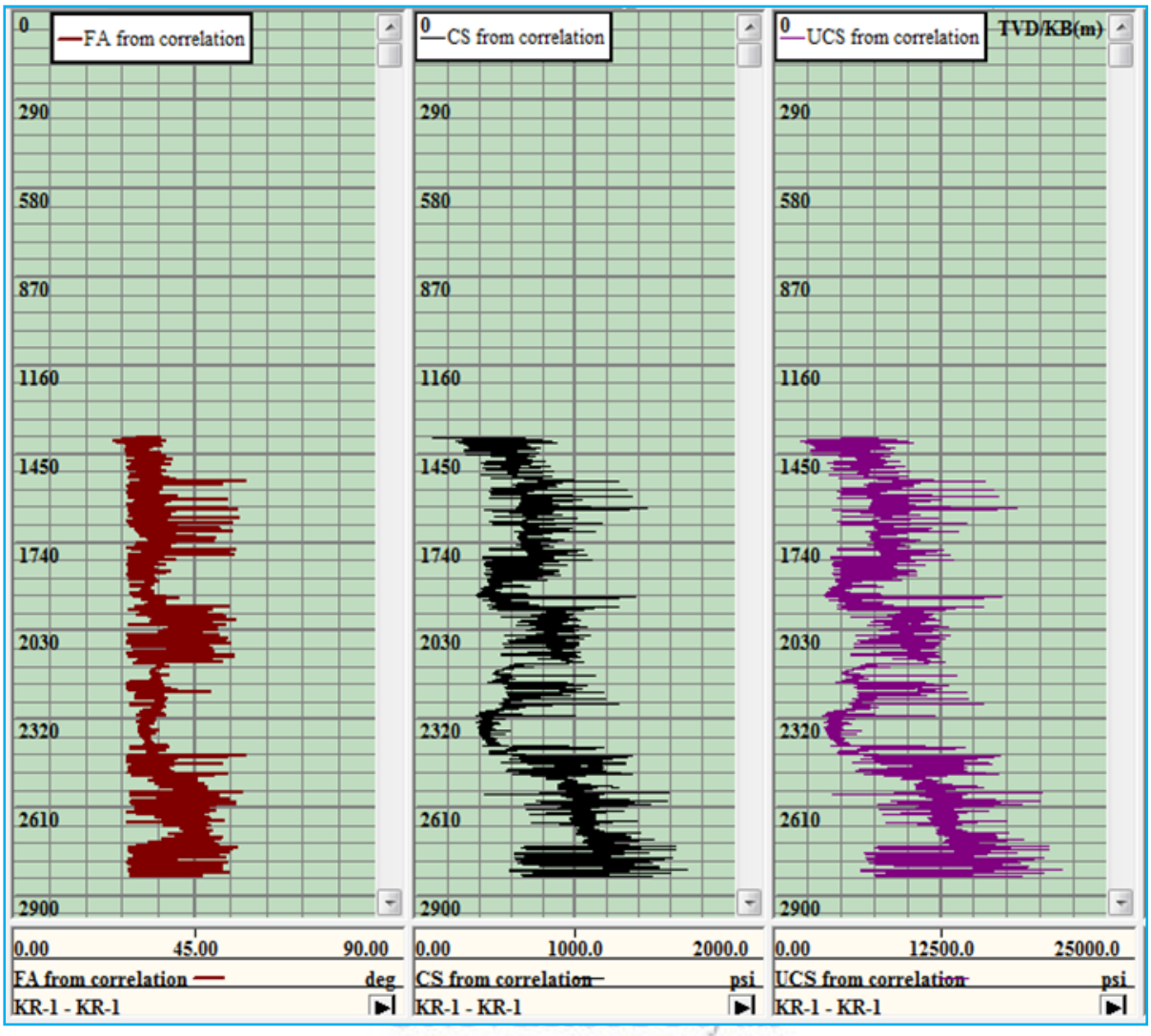

Figure 5.2: Rock mechanical properties for well KR-1.

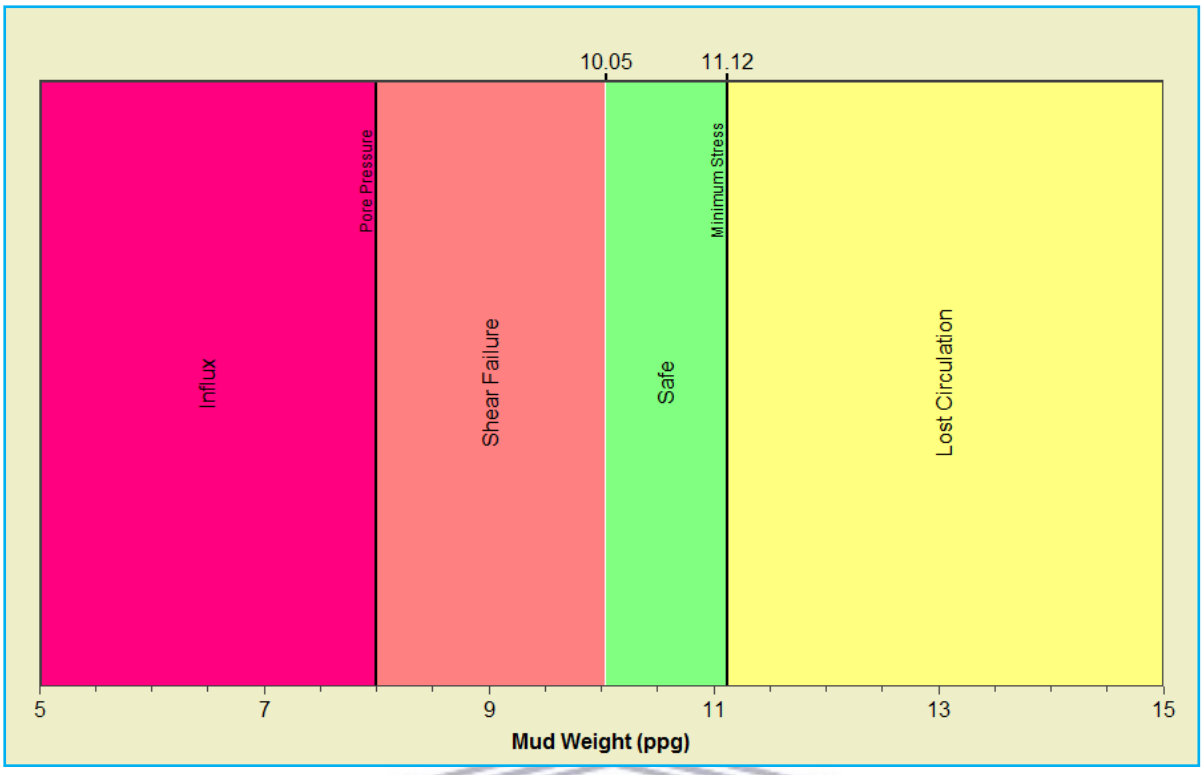

Figure 5.3: Safe drilling mud window for well KR-1 at TUSM.

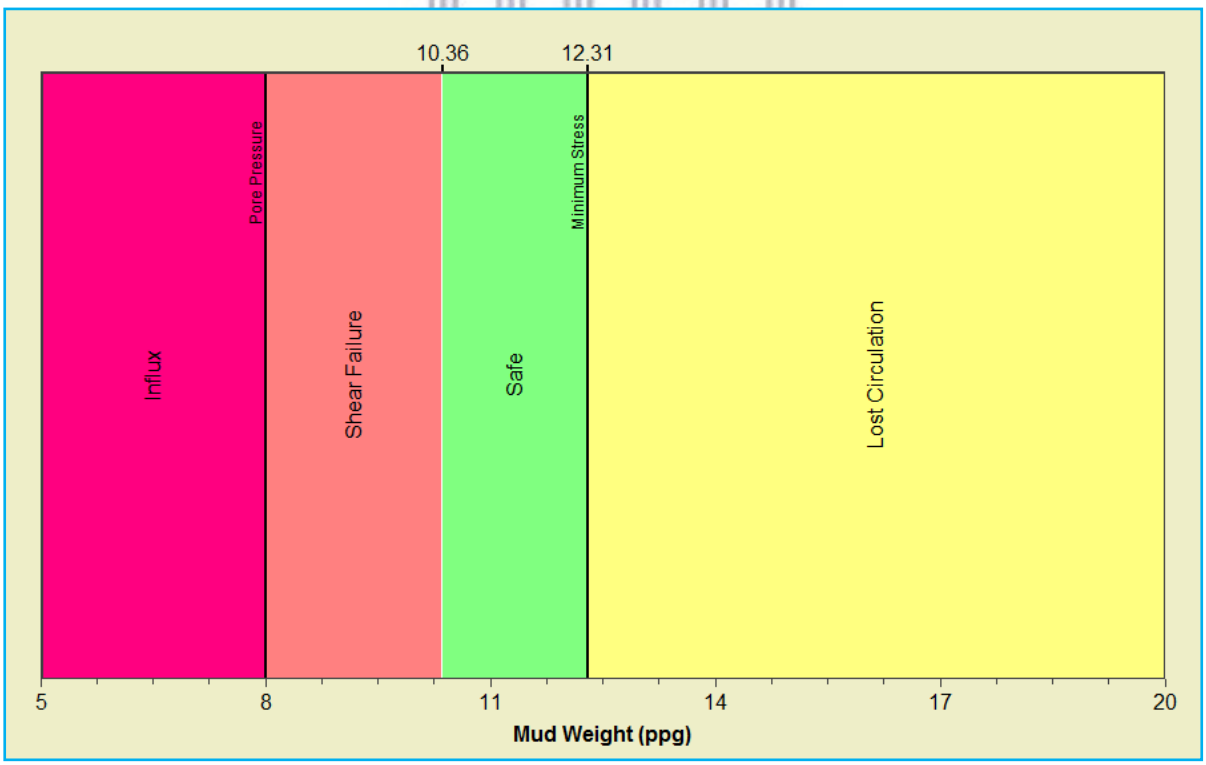

Figure 5.4: Safe drilling mud window for well KR-1 at BUSM.

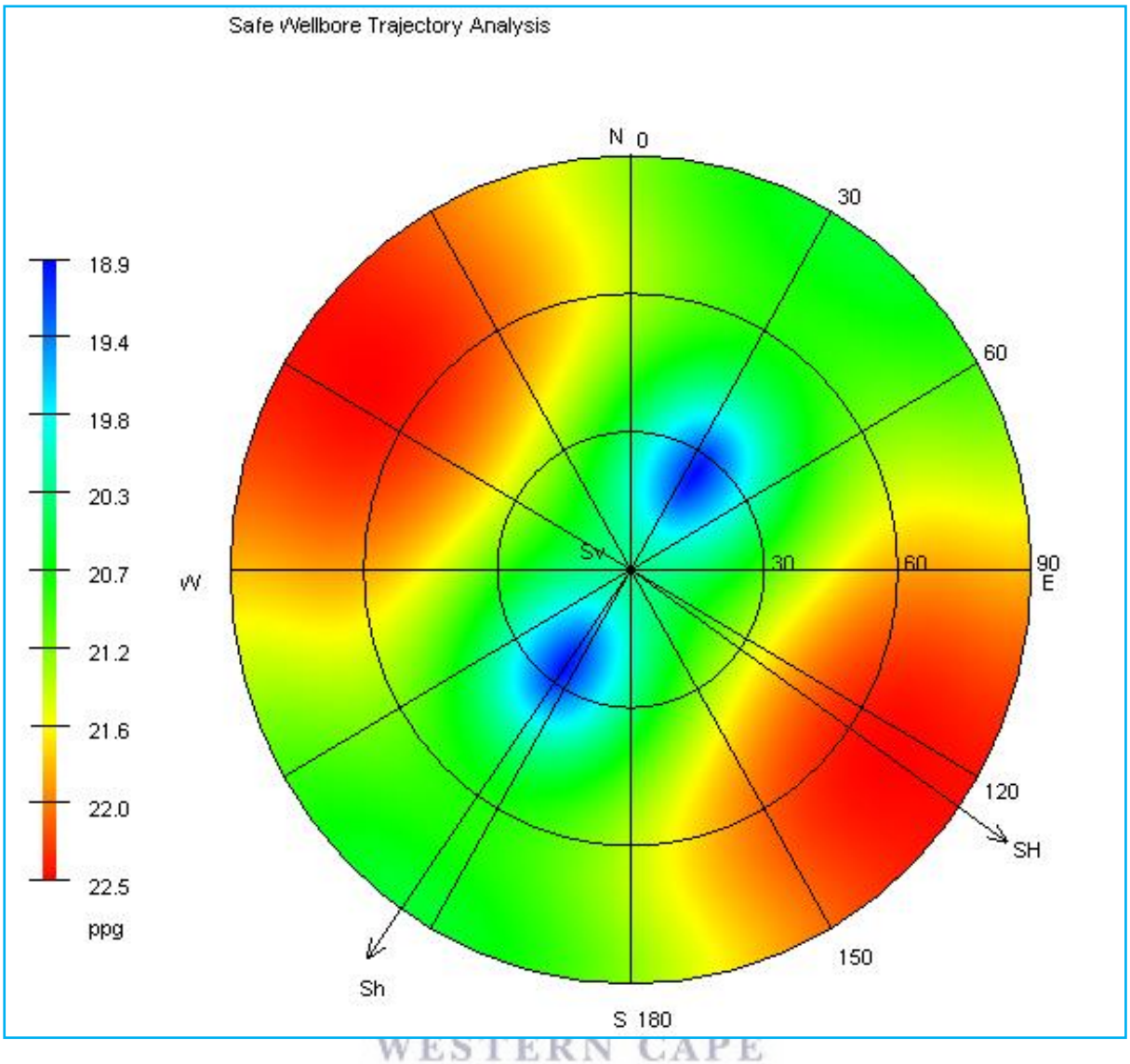

Figure 5.5: Lower Hemisphere plot for well KR-1 at TUSM.

Table 7: Parameters used for safe wellbore trajectory analysis of well KR-1 at TUSM.

Depth (m)	2499.7
Failure criterion	Mohr-Coulomb
Overburden Gradient (ppg)	18.66
Pore Pressure Gradient (ppg)	8.462
Minimum Horizontal Stress Gradient (ppg)	11.12
Maximum Horizontal Stress Gradient (ppg)	14.9
Maximum Horizontal Stress Azimuth	125
Poisson's Ratio	0.20770885
Friction Angle (deg)	34.852
Cohesive strength (psi)	979.274

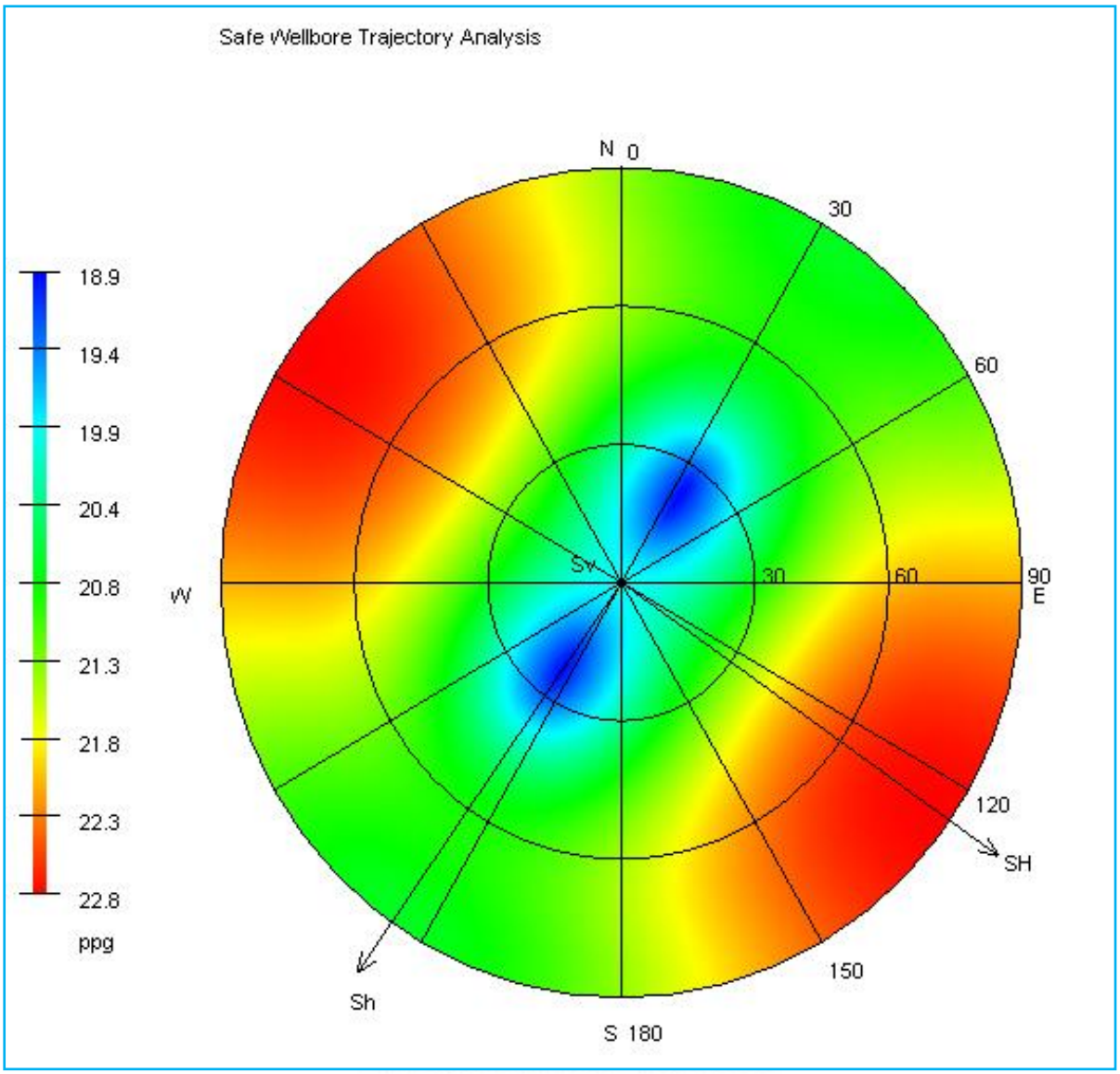

Figure 5.6: Lower Hemisphere plot for well KR-1 at BUSM.

Table 8: Parameters used for safe wellbore trajectory analysis of well KR-1 at BUSM.

Depth (m)	2737
Failure criterion	Mohr-Coulomb
Overburden Gradient (ppg)	18.66
Pore Pressure Gradient (ppg)	8.462
Minimum Horizontal Stress Gradient (ppg)	10.51
Maximum Horizontal Stress Gradient (ppg)	14.59
Maximum Horizontal Stress Azimuth	125
Poisson's Ratio	0.147580821
Friction Angle (deg)	34.852
Cohesive strength (psi)	979.274

5.3 Well KR-2

Well KR-2 has the most calibration sources; two leak-off tests were performed at depth intervals of 301-314m and 1425-1428m respectively. Well KR-2 was drilled predominantly with a mud weight of 9 ppg. The geopressure curves after calibration are shown in Figure 5.7.

The estimated rock mechanical properties obtained through correlations are shown in Figure 5.8. A similar trend to well KR-1 is observed for FA, CS and UCS, i.e. an increase with depth, especially close to the TD.

Graphs showing the safe drilling mud window at depths of 2593m and 2859.5m respectively is shown in Figure 5.9 and 5.10. For this well, a more constricted mud window is observed at the top of the reservoir.

Wellbore trajectory is central to wellbore stability issues and thus, a hemisphere plot showing mud weight variations is shown in Figure 5.5. The plot shows wellbore trajectory position relative to maximum and minimum horizontal stress and the parameters used in the analysis are listed in Table 9 and 10 respectively.

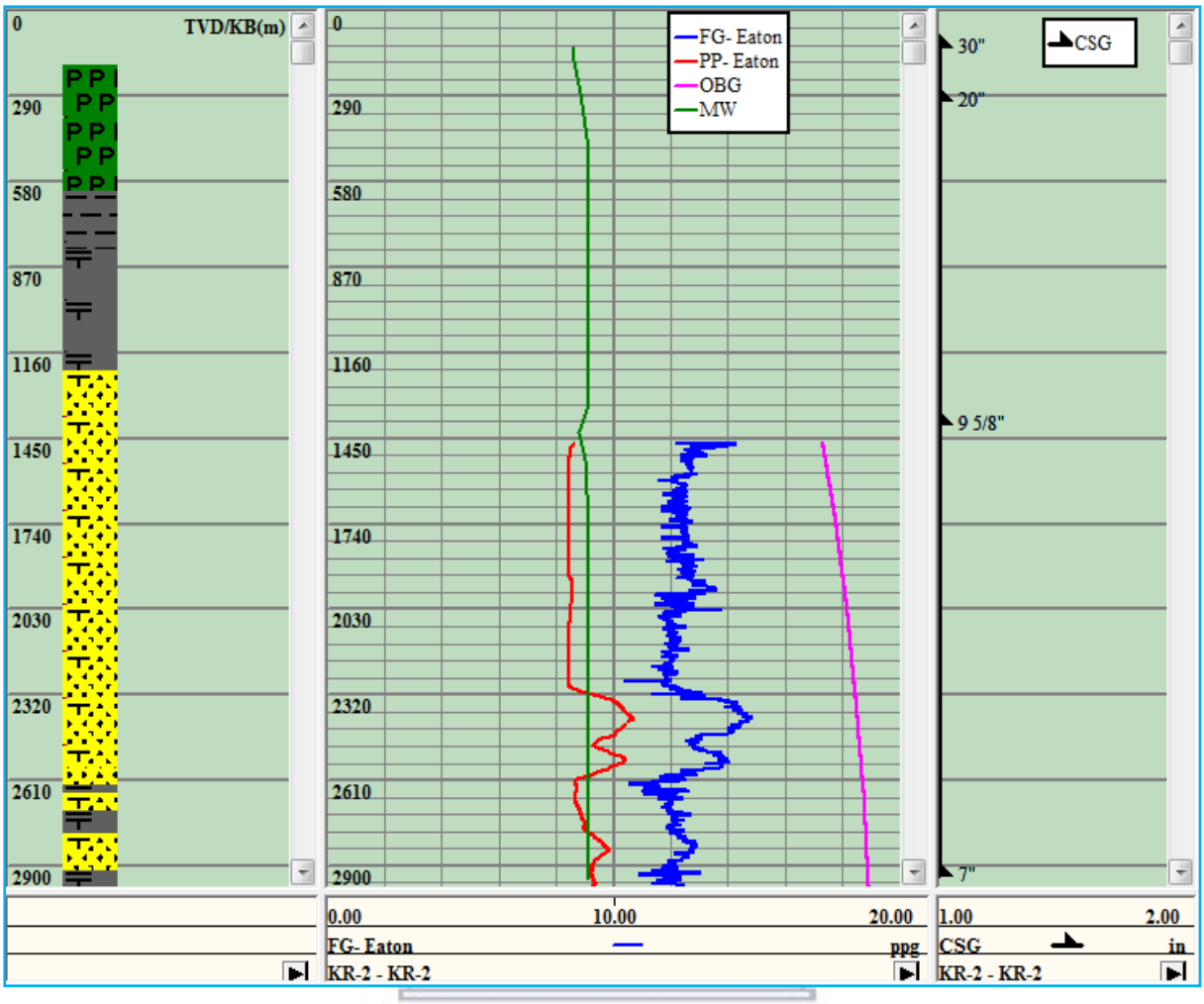

Figure 5.7: Modelled geopressure gradients for well KR-2 post calibration.

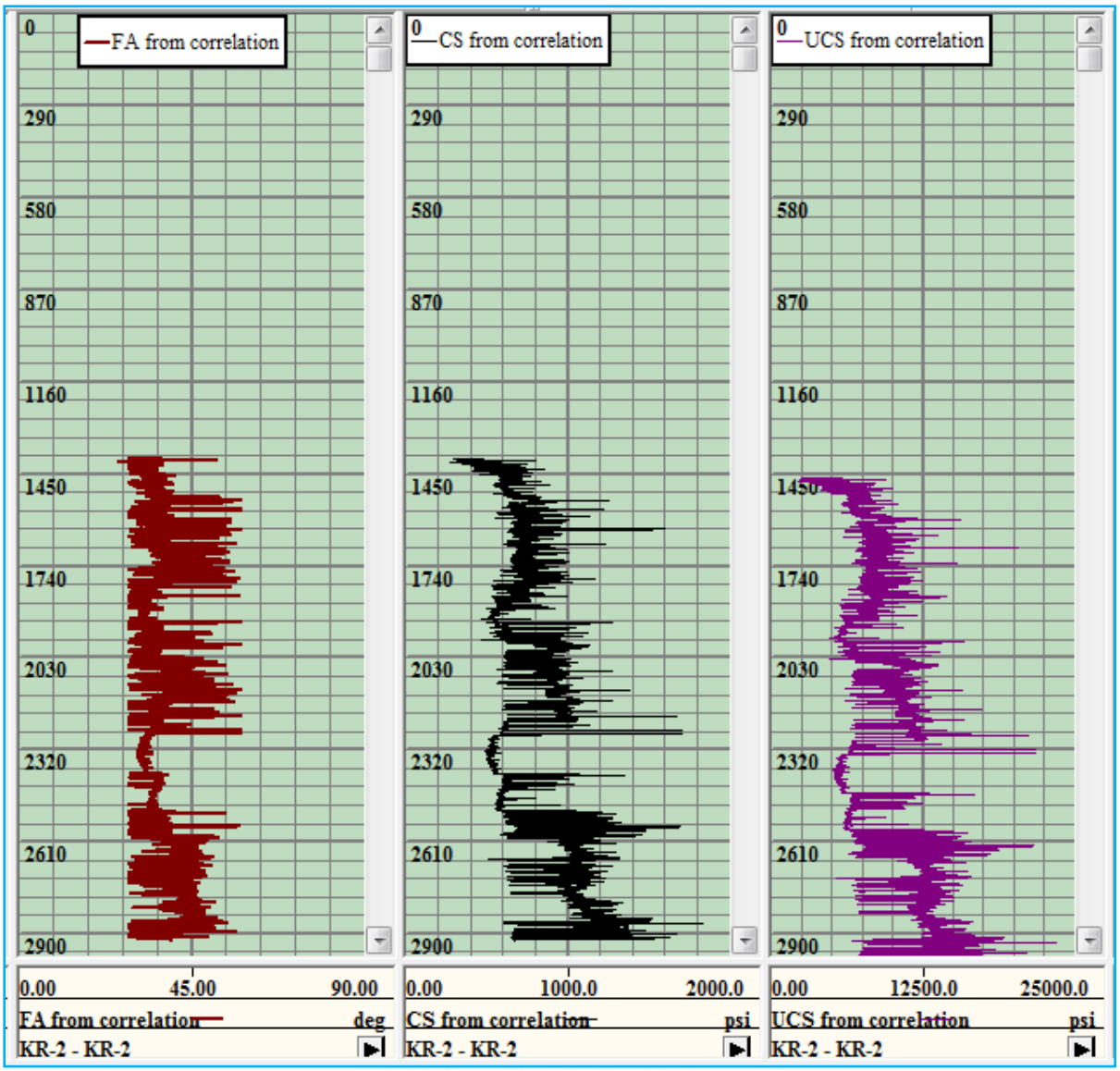

Figure 5.8: Rock mechanical properties for well KR-2.

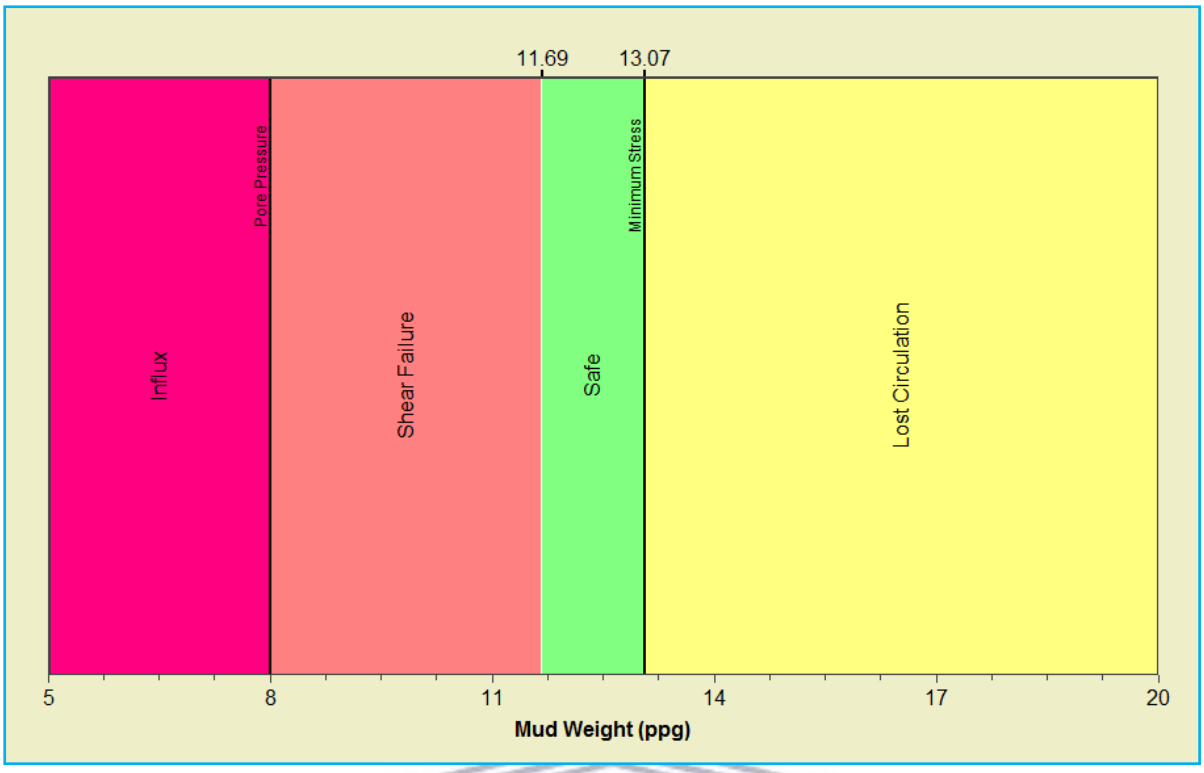

Figure 5.9: Safe drilling mud window for well KR-2 at TUSM.

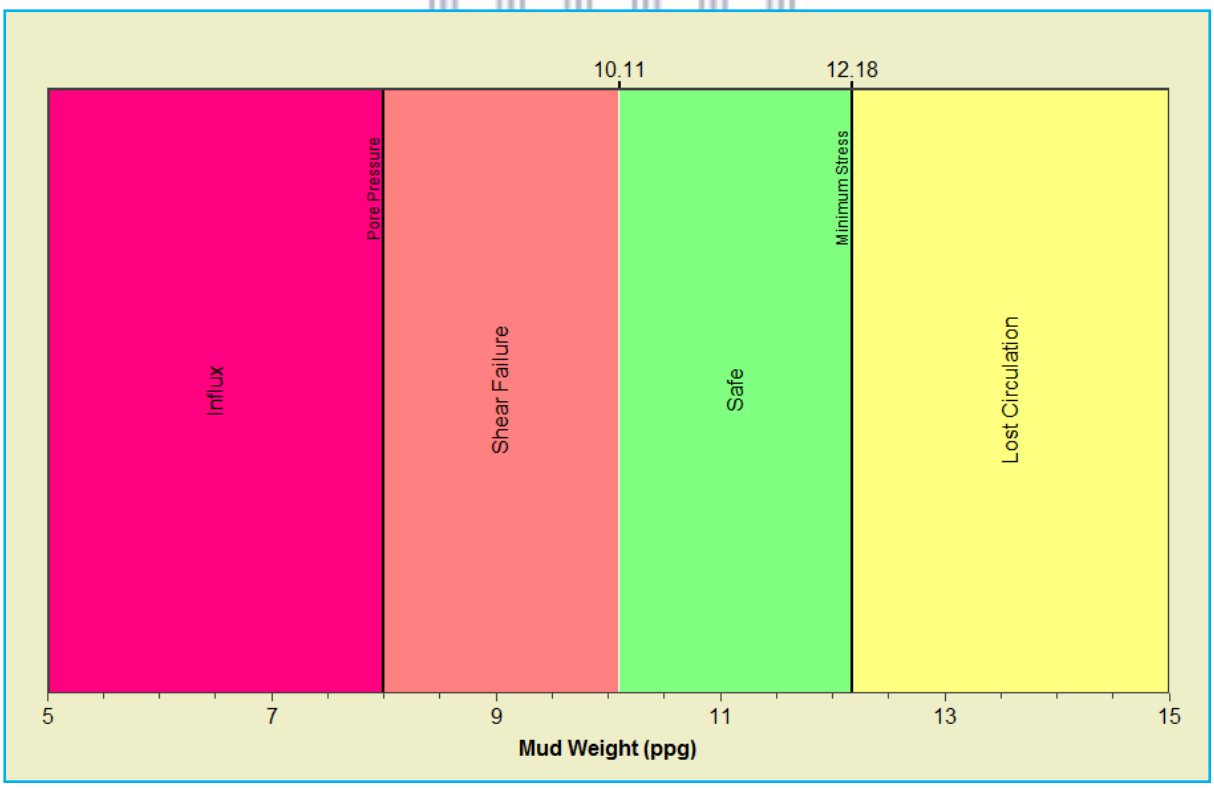

Figure 5.10: Safe drilling mud window for well KR-2 at BUSM.

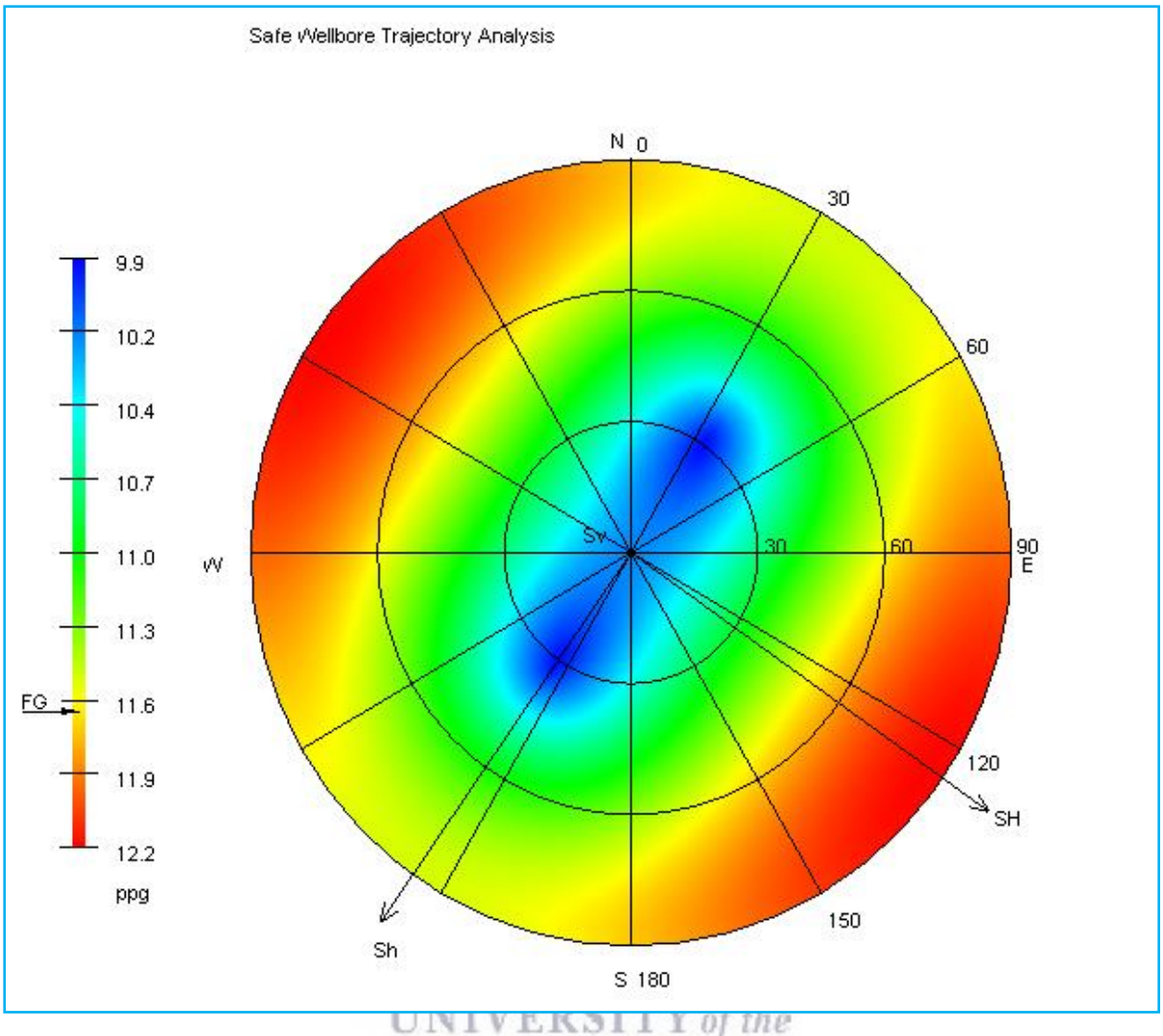

Figure 5.11: Lower Hemisphere plot for well KR-2 at TUSM.

Table 9: Parameters used for safe wellbore trajectory analysis of well KR-2 at TUSM.

Depth (m)	2593
Failure criterion	Mohr-Coulomb
Overburden Gradient (ppg)	18.66
Pore Pressure Gradient (ppg)	8.665
Minimum Horizontal Stress Gradient (ppg)	11.34
Maximum Horizontal Stress Gradient (ppg)	15.01
Maximum Horizontal Stress Azimuth	125
Poisson's Ratio	0.234686206
Friction Angle (deg)	30.899
Cohesive strength (psi)	1077.23

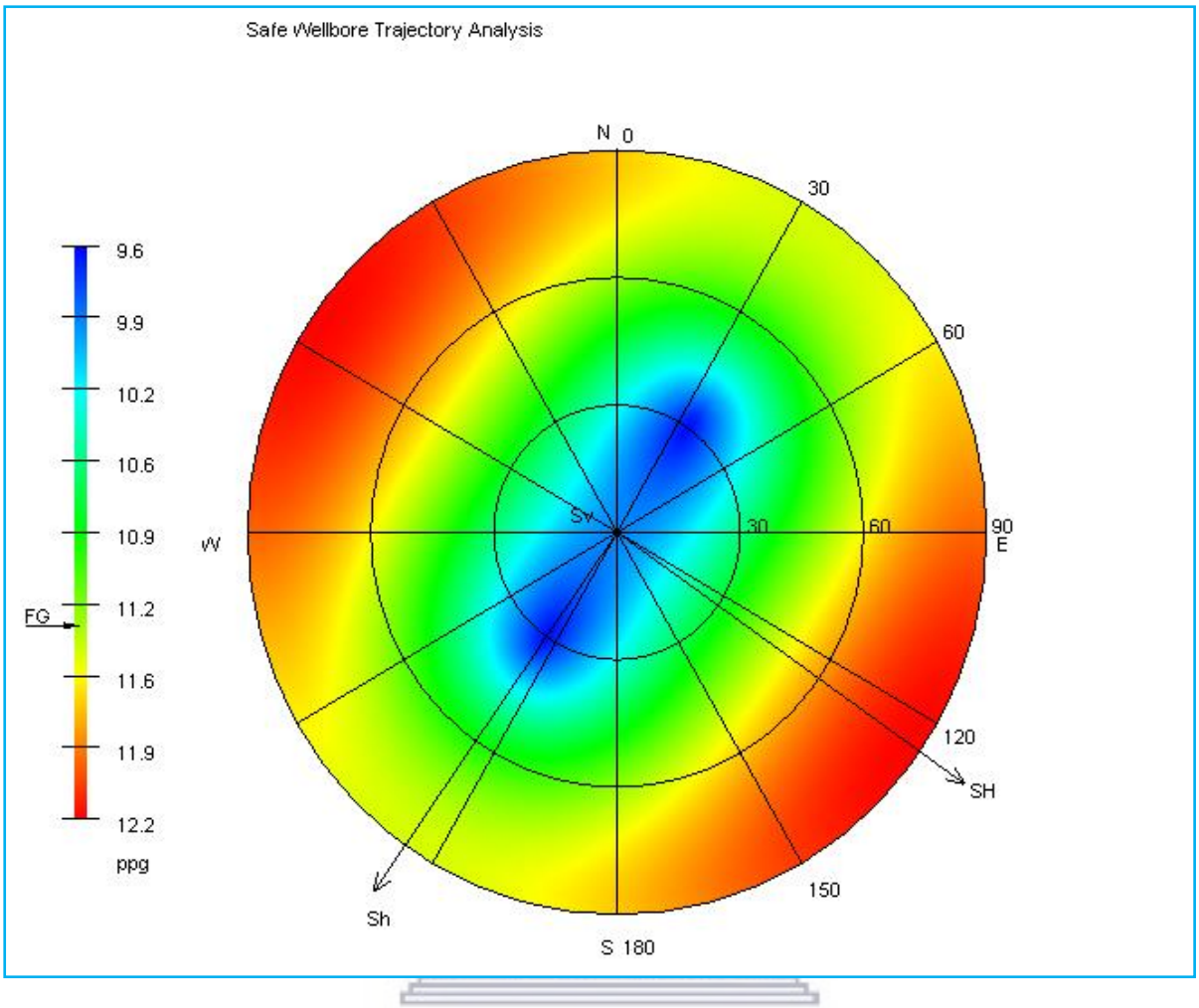

Figure 5.12: Lower Hemisphere plot for well KR-2 at BUSM.

Table 10: Parameters used for safe wellbore trajectory analysis of well KR-2 at BUSM.

Depth (m)	2859.5
Failure criterion	Mohr-Coulomb
Overburden Gradient (ppg)	18.85
Pore Pressure Gradient (ppg)	9.112
Minimum Horizontal Stress Gradient (ppg)	11.34
Maximum Horizontal Stress Gradient (ppg)	15.1
Maximum Horizontal Stress Azimuth	125
Poisson's Ratio	0.183508121
Friction Angle (deg)	36.039
Cohesive strength (psi)	1070.15

5.4 Well KR-3

Well KR-3 has the most calibration sources and was drilled predominantly with a mud weight of 9 ppg. At depths of approximately 2451 - 2563m, an elevation of pore pressure exists and the mudweight used to drill this section is lower than the pore pressure gradient. A resulting increase in fracture gradient is observed, which is shown in Figure 5.13. This pore pressure increase is observed in the overpressured shale just above the sandstone unit.

The rock mechanical properties for well KR-3 are presented in Figure 5.14. The friction angle has an erratic trend and the trends for CS and UCS show a more pronounced increase towards the TD when compared to wells KR-1 and KR-2.

The safe drilling mud window for well KR-3 at TUSM and BUSM, together with the equivalent circulating density (ECD) is shown in Figure 5.15 and 5.16 respectively. A larger mud window is shown towards the top of the reservoir.

The hemisphere plots shown in Figure 5.17 and 5.18 vary slightly to that of the previous wells. This is mainly due to well KR-3 having the highest overburden gradient at TUSM (19.23 ppg) for the K-R Field as well as higher friction angles than well KR-1 and KR-2, resulting in greater mud weight variation.

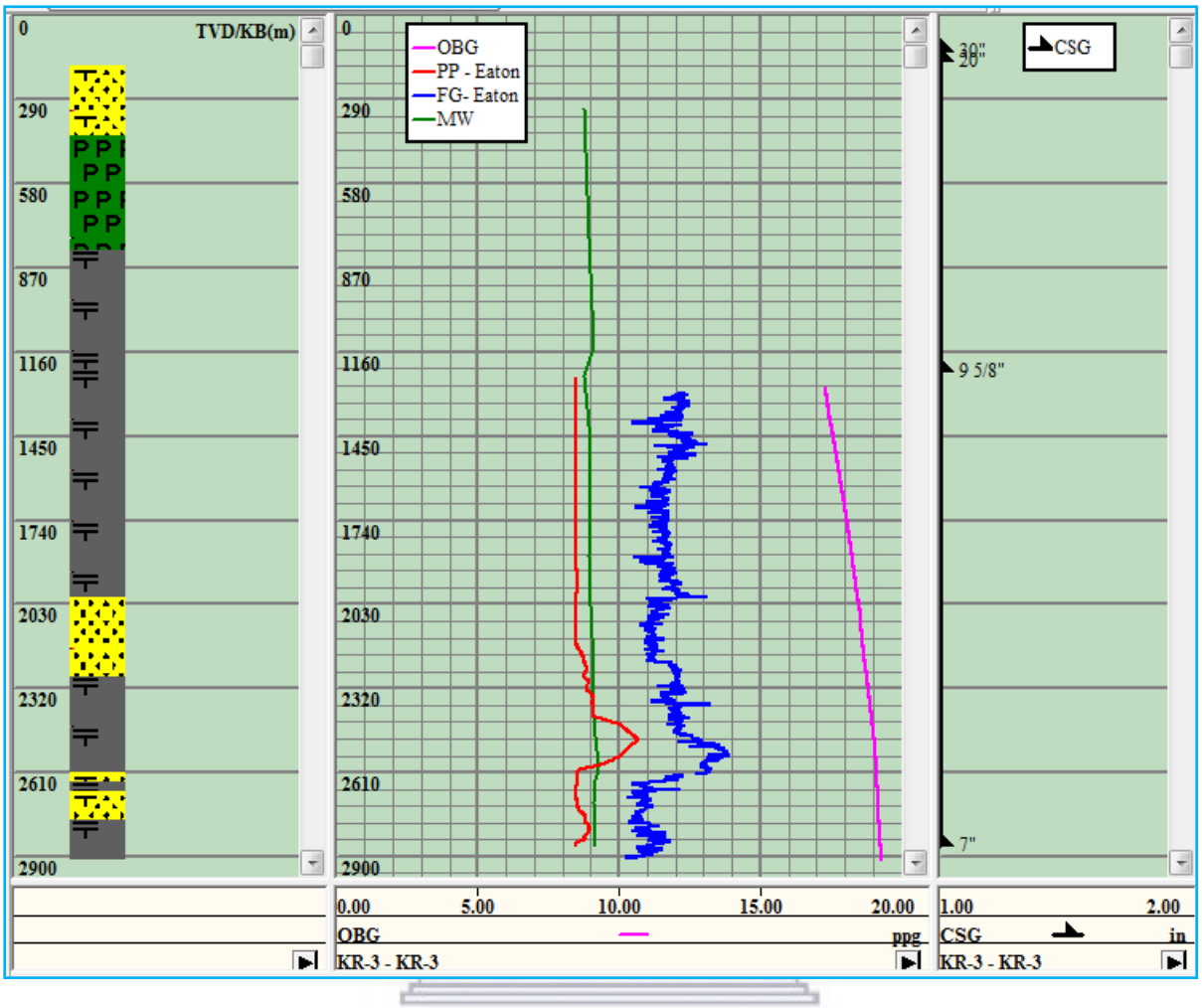

Figure 5.13: Modelled geopressure gradients for well KR-3 post calibration.

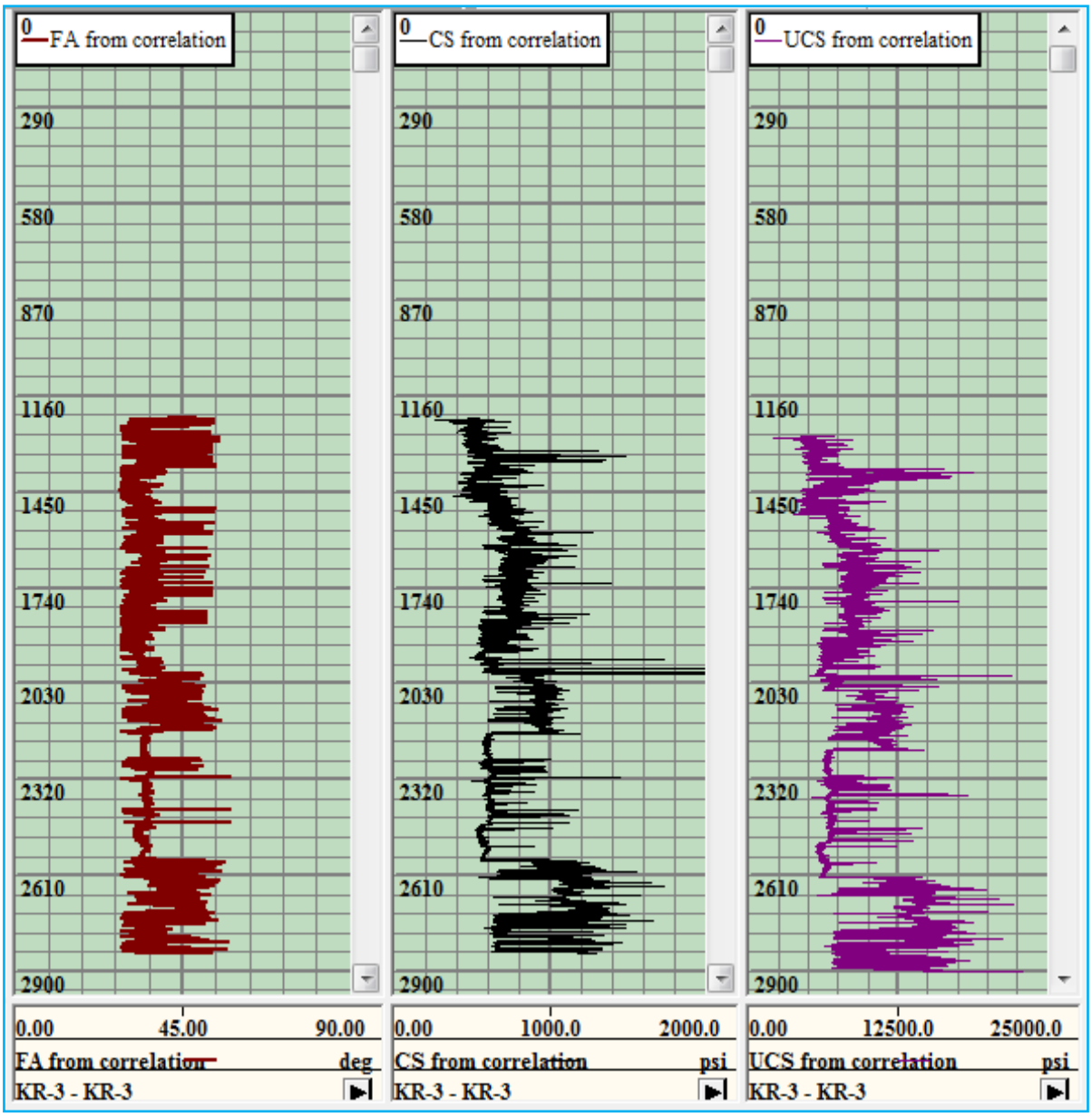

Figure 5.14: Rock mechanical properties for well KR-3.

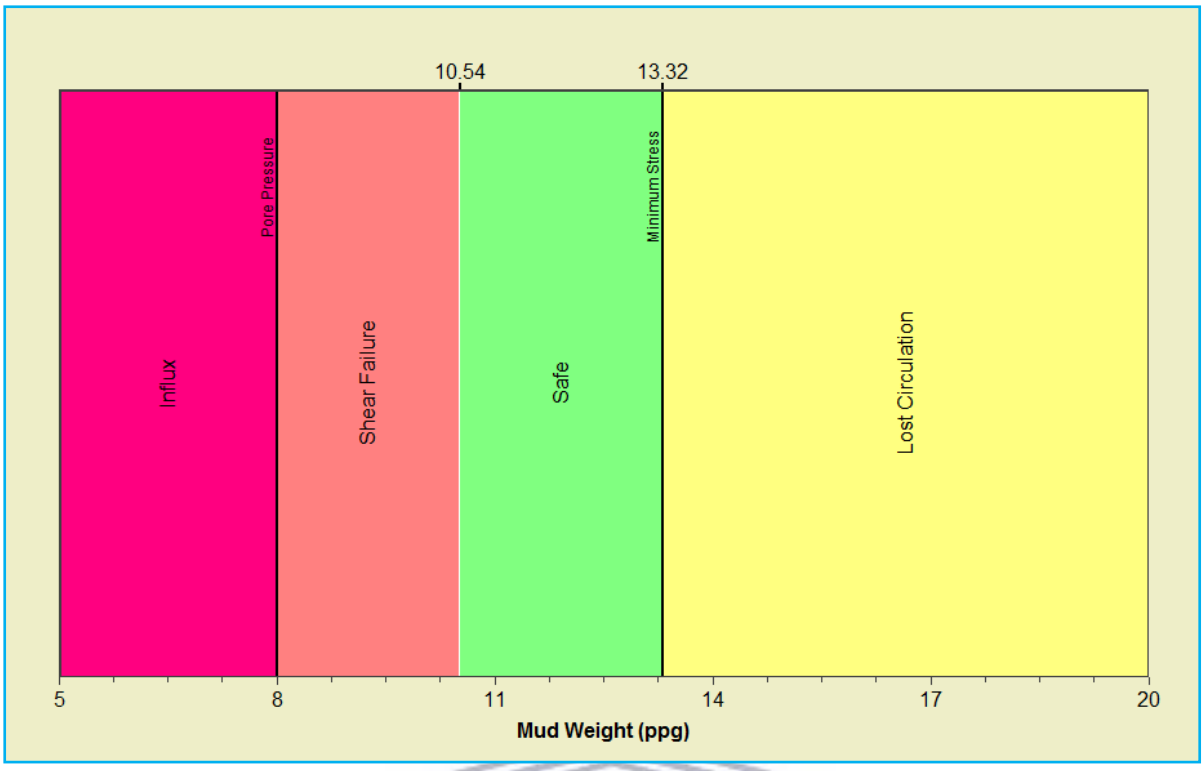

Figure 5.15: Safe mud window for well KR-3 at TUSM.

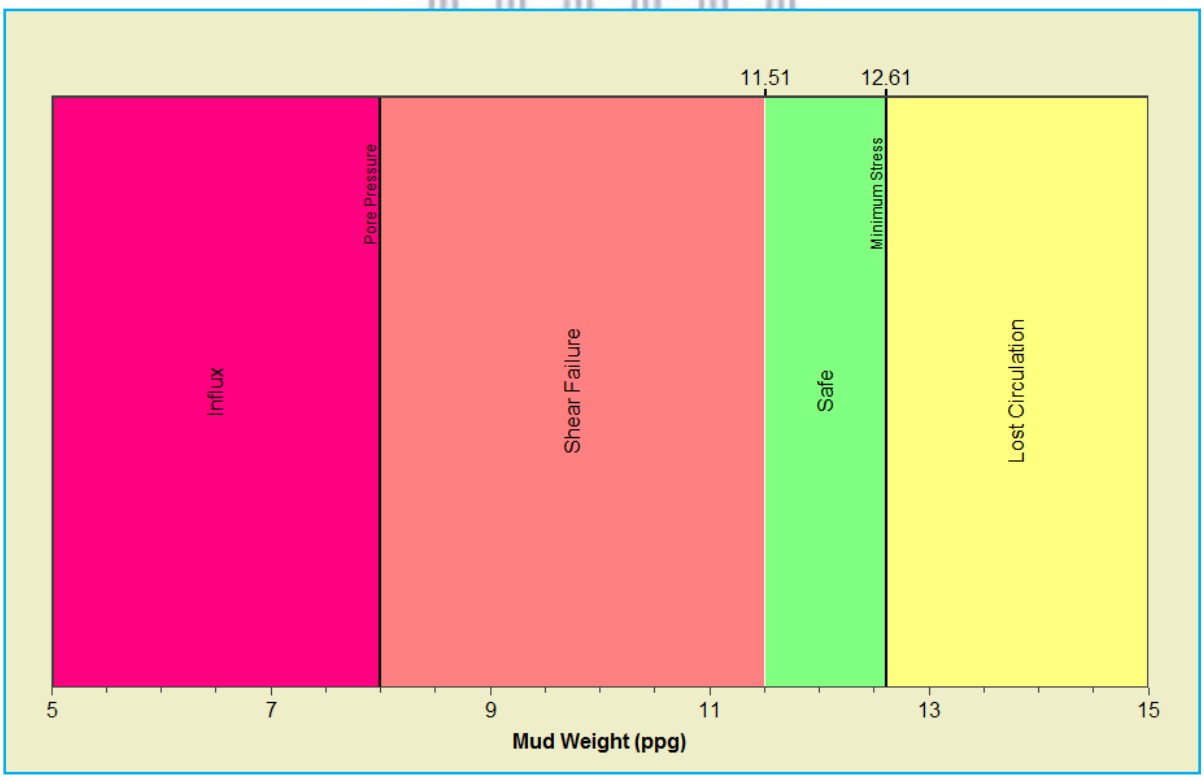

Figure 5.16: Safe mud window for well KR-3 at BUSM.

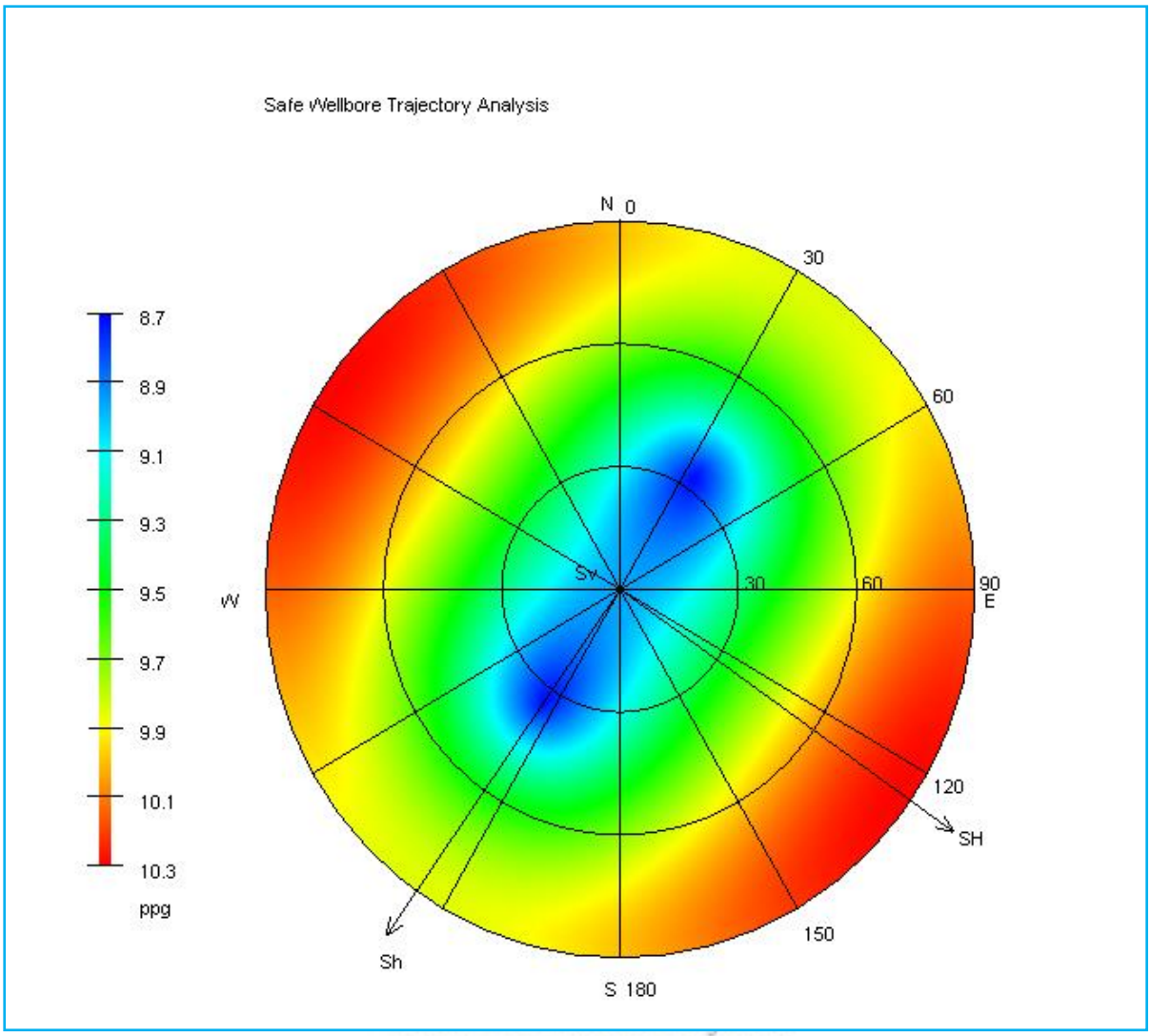

Figure 5.17: Lower Hemisphere plot for well KR-3 at TUSM.

Table 11: Parameters used for safe wellbore trajectory analysis of well KR-3 at TUSM.

Depth (m)	2564
Failure criterion	Mohr-Coulomb
Overburden Gradient (ppg)	19.23
Pore Pressure Gradient (ppg)	9.598
Minimum Horizontal Stress Gradient (ppg)	12.44
Maximum Horizontal Stress Gradient (ppg)	15.84
Maximum Horizontal Stress Azimuth	125
Poisson's Ratio	0.188962137
Friction Angle (deg)	37.425
Cohesive strength (psi)	1012.91

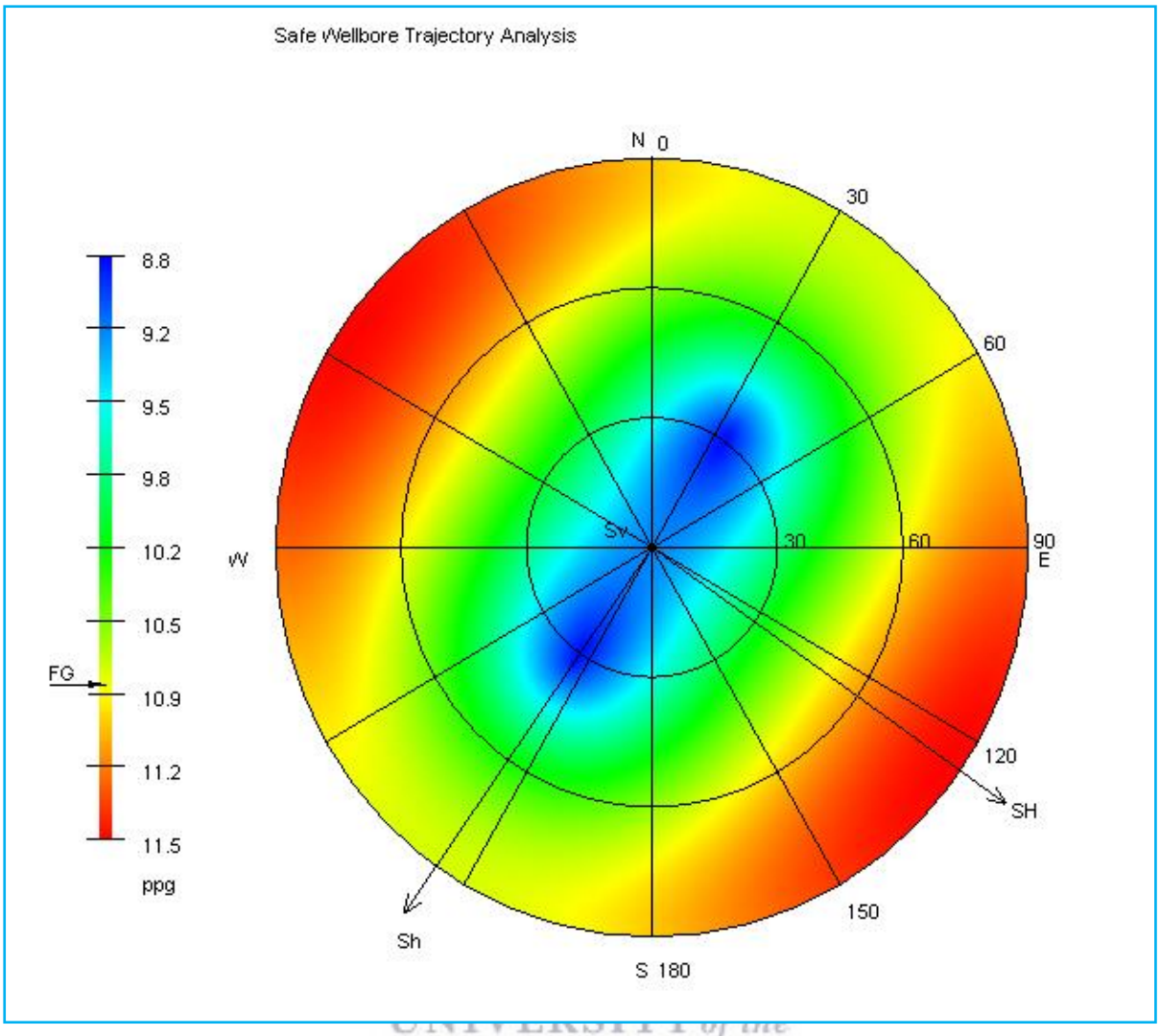

Figure 5.18: Lower Hemisphere plot for well KR-3 at BUSM.

Table 12: Parameters used for safe wellbore trajectory analysis of well KR-3 at BUSM.

Depth (m)	2722
Failure criterion	Mohr-Coulomb
Overburden Gradient (ppg)	19.23
Pore Pressure Gradient (ppg)	8.528
Minimum Horizontal Stress Gradient (ppg)	10.81
Maximum Horizontal Stress Gradient (ppg)	15.03
Maximum Horizontal Stress Azimuth	125
Poisson's Ratio	0.159284407
Friction Angle (deg)	39.103
Cohesive strength (psi)	1305.47

5.5 Well KR-4

The geopressure gradient curve after calibration is shown in Figure 5.19. The main calibration source for this well is the actual mudweights recorded whilst drilling. Elevated compartments of pore pressure are observed at various depth intervals, resulting in high fracture gradients.

The rock mechanical properties that are shown in Figure 5.20 show similar trends to previous wells. The cohesive strength and unconfined compressive strength show a pronounced increase at depths of approximately 2495m up to the TD of the well.

The safe mud window plots for the top and bottom of the reservoir are shown in Figure 5.21 and Figure 5.22 respectively. The top of the reservoir for well KR-4 shows a slightly more constricted mud window than observed at BUSM.

The lower hemisphere plots shown in Figure 5.23 and 5.24 are almost identical to that of well KR-1. This is due the values of overburden gradients and horizontal stresses being similar.

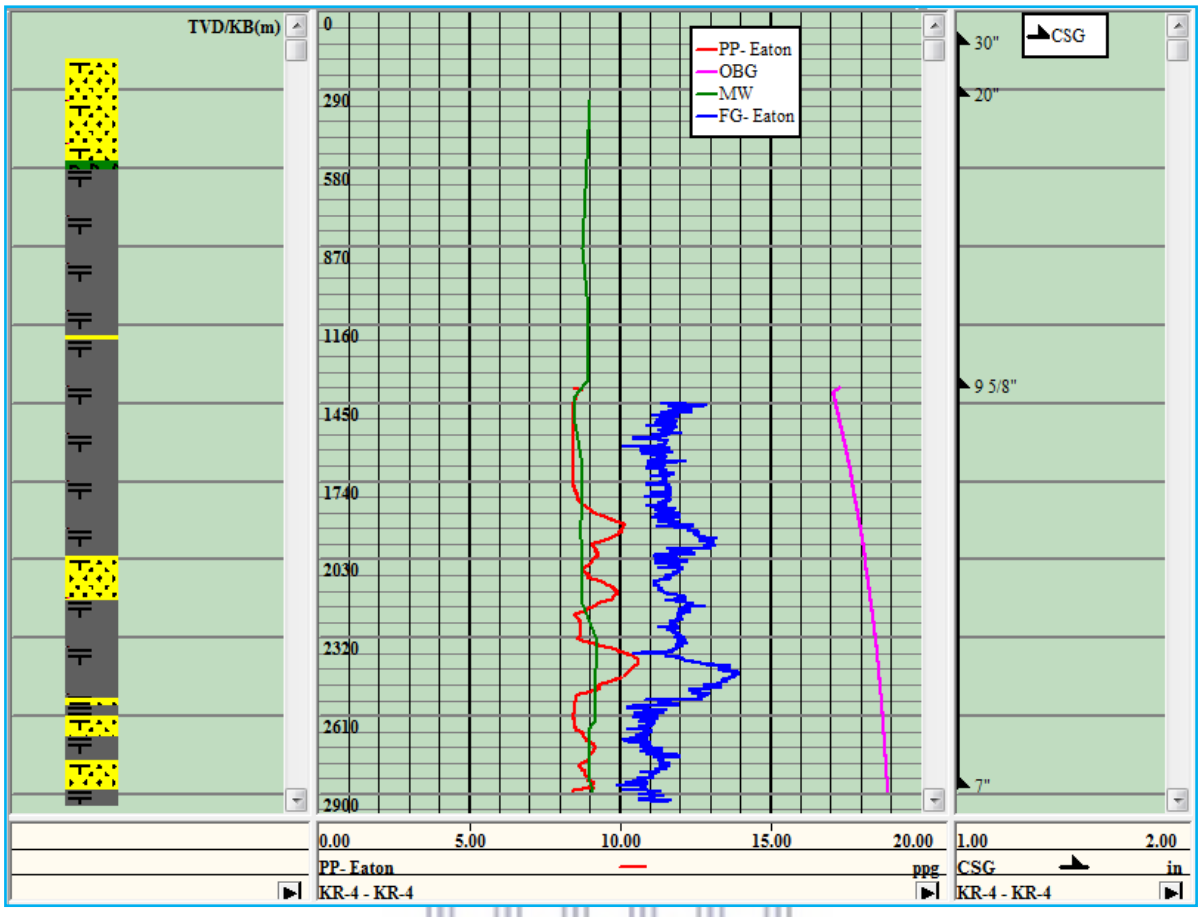

Figure 5.19: Modelled geopressure gradients for well KR-4 post calibration.

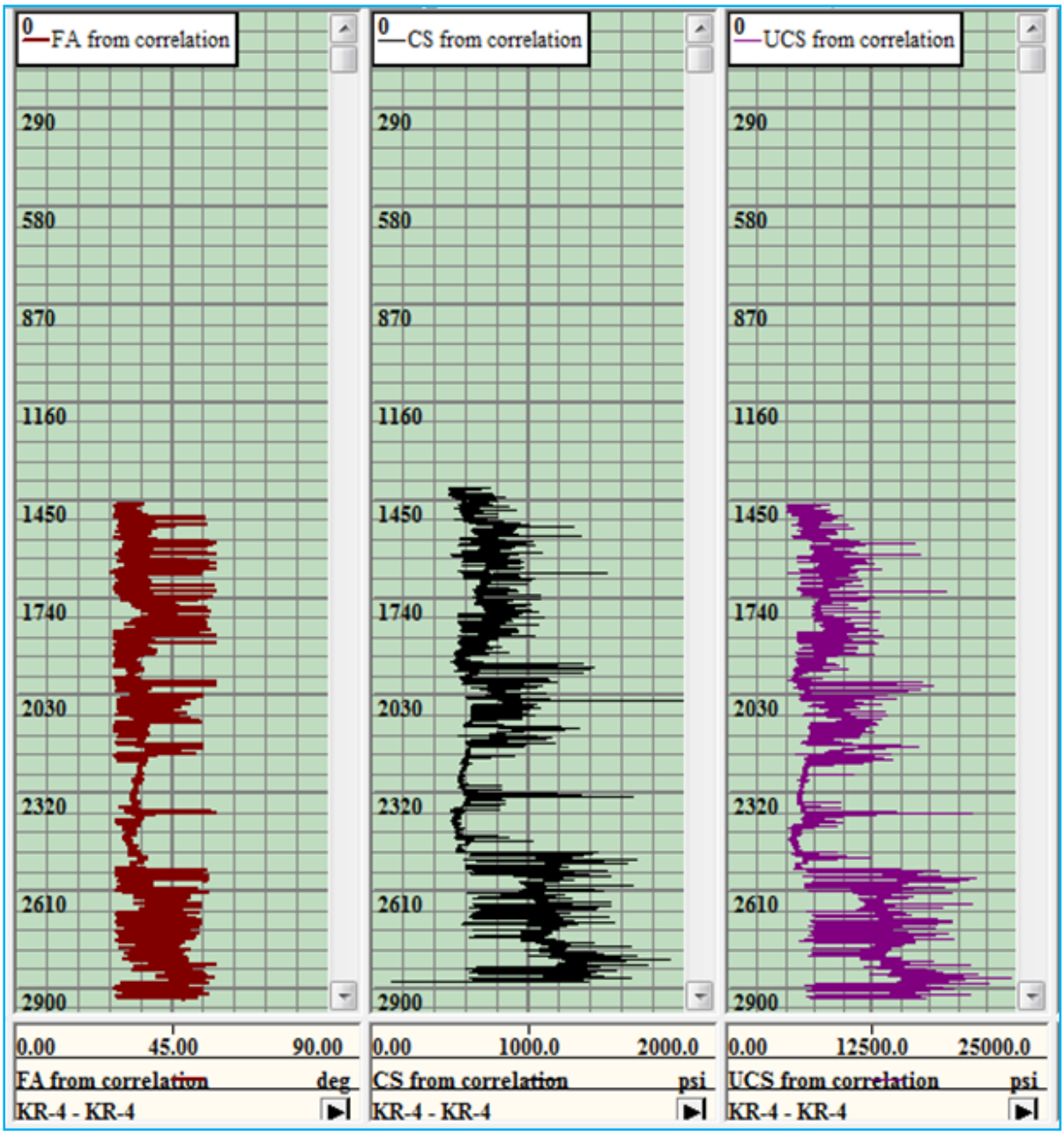

Figure 5.20: Rock mechanical properties for well KR-4.

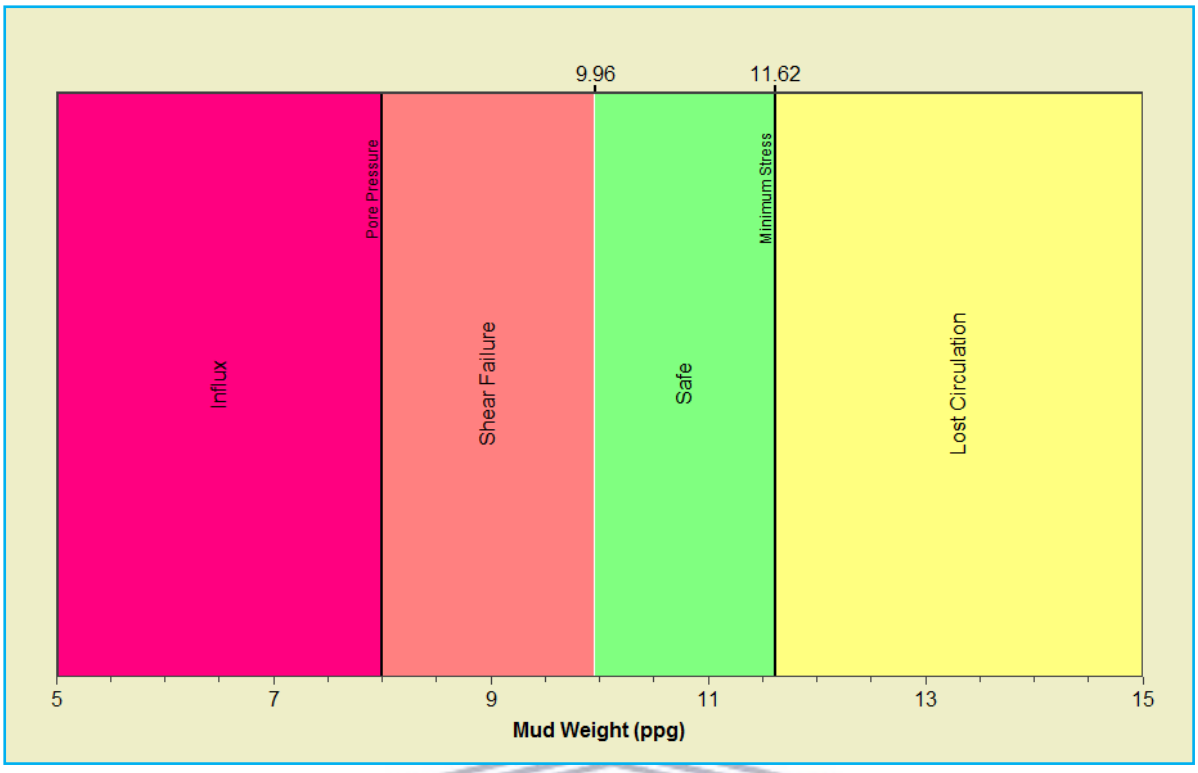

Figure 5.21: Safe mud window for well KR-4 at TUSM.

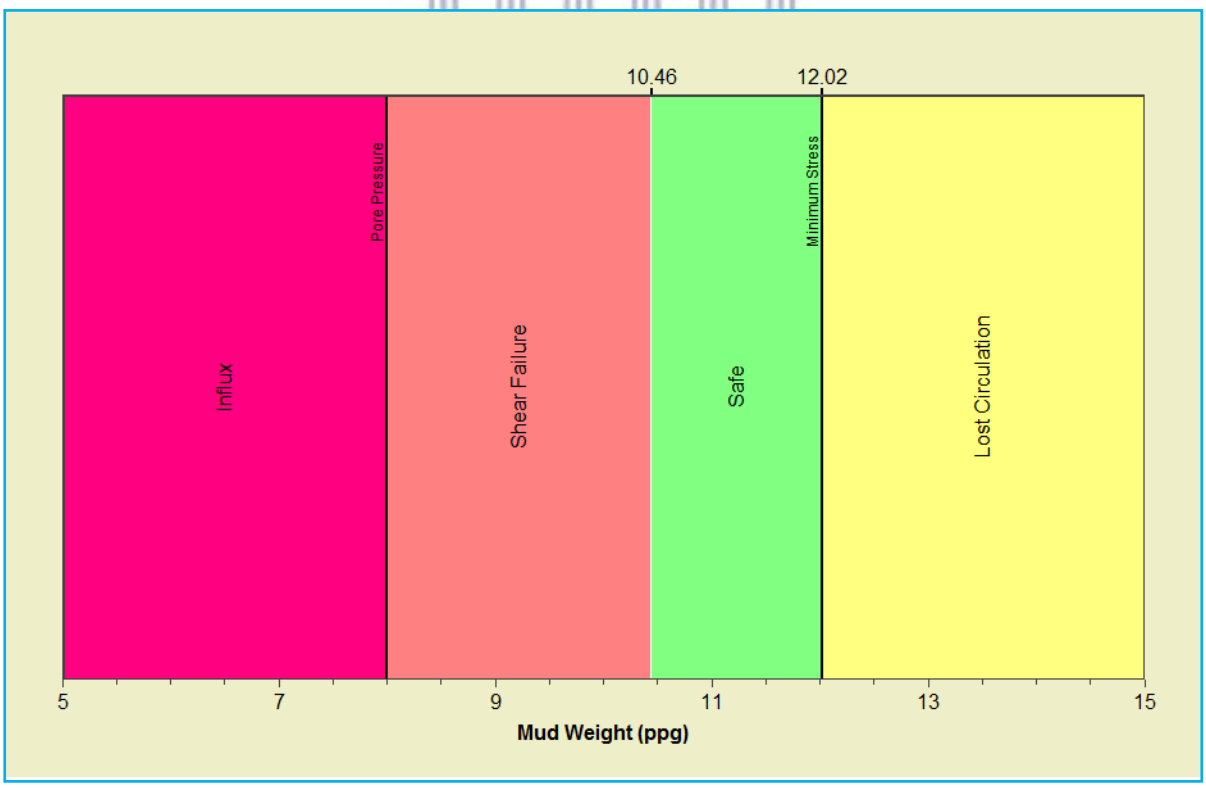

Figure 5.22: Safe mud window for well KR-4 at BUSM.

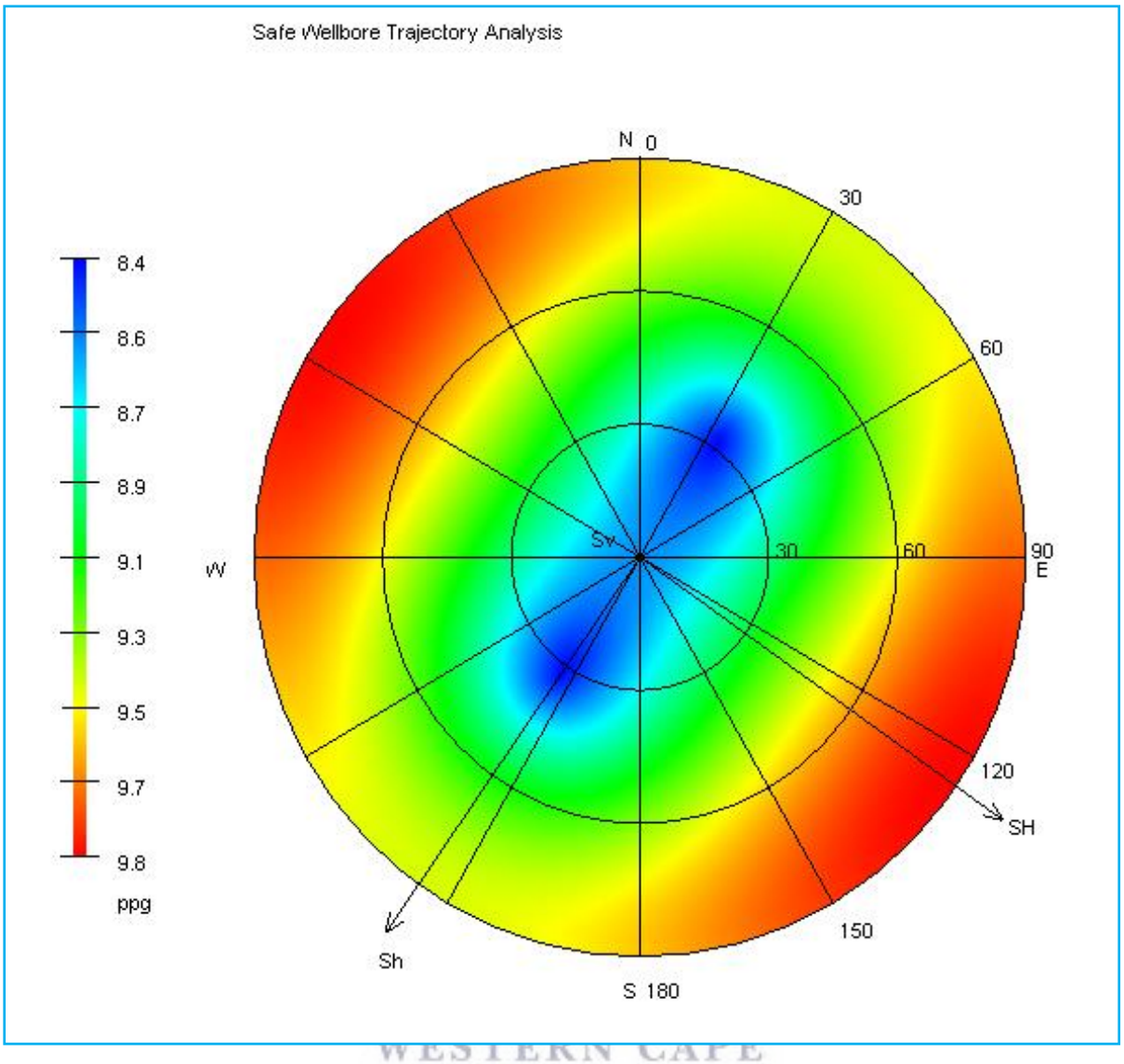

Figure 5.23: Lower Hemisphere plot for well KR-4 at TUSM.

Table 13: Parameters used for safe wellbore trajectory analysis of well KR-4 at TUSM.

Depth (m)	2558
Failure criterion	Mohr-Coulomb
Overburden Gradient (ppg)	18.65385
Pore Pressure Gradient (ppg)	8.525
Minimum Horizontal Stress Gradient (ppg)	11.02
Maximum Horizontal Stress Gradient (ppg)	14.85
Maximum Horizontal Stress Azimuth	125
Poisson's Ratio	0.196591467
Friction Angle (deg)	36.887
Cohesive strength (psi)	943.31

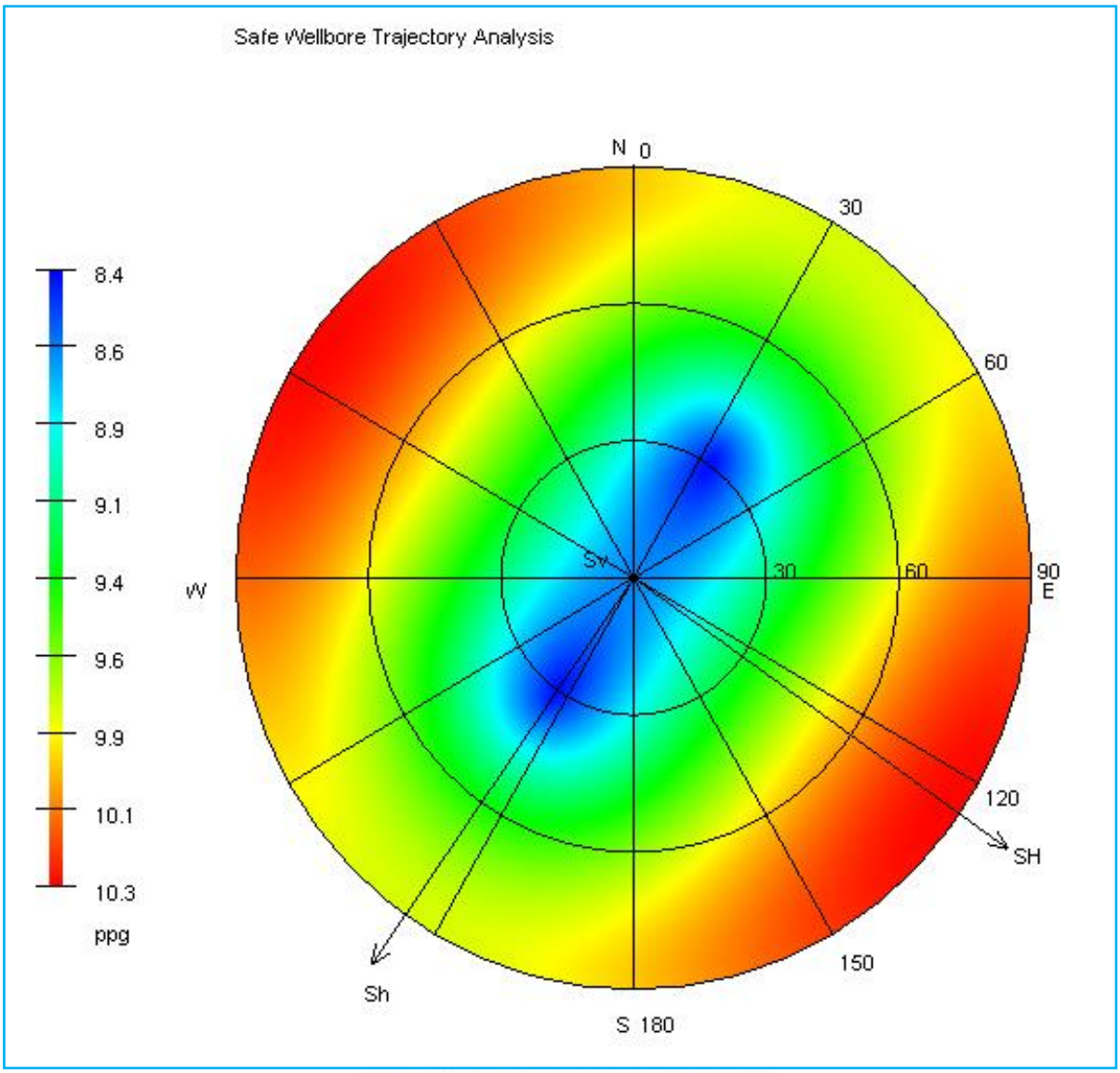

Figure 5.24: Lower Hemisphere plot for well KR-4 at BUSM.

Table 14: Parameters used for safe wellbore trajectory analysis of well KR-4 at BUSM.

Depth (m)	2830.80
Failure criterion	Mohr-Coulomb
Overburden Gradient (ppg)	18.84615
Pore Pressure Gradient (ppg)	8.868
Minimum Horizontal Stress Gradient (ppg)	10.12
Maximum Horizontal Stress Gradient (ppg)	14.49
Maximum Horizontal Stress Azimuth	125
Poisson's Ratio	0.160275027
Friction Angle (deg)	40.414
Cohesive strength (psi)	1652.42

5.6 Well KR-5

The geopressure gradient curve after calibration is shown in Figure 5.25. The main calibration sources for this well are the actual mudweights recorded whilst drilling. Elevated compartments of pore pressure are observed at various depth intervals, resulting in high fracture gradients.

The rock mechanical properties shown in Figure 5.26 show similar trends to previous wells. The cohesive strength and unconfined compressive strength shows a marked increase at depths of approximately 2504m up to the TD of the well.

The safe mud window plots for the top and bottom of the reservoir are shown in Figure 5.27 and Figure 5.28 respectively. The top of the reservoir for well KR-5 shows the narrowest safe drilling mud window for the K-R Field.

The lower hemisphere plots are shown in Figure 5.29 and 5.30. This well shows a contrast to well KR-3 as it has the lowest overburden gradient value for the entire field.

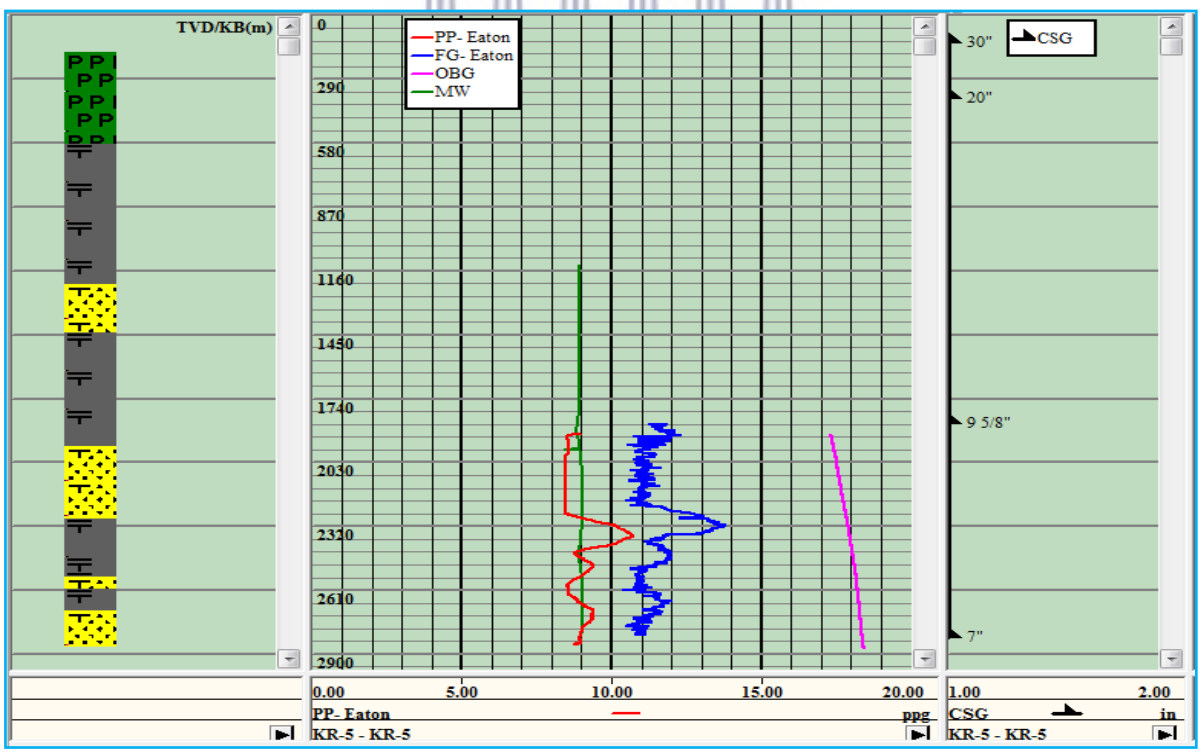

Figure 5.25: Modelled geopressure gradients for well KR-5 post calibration.

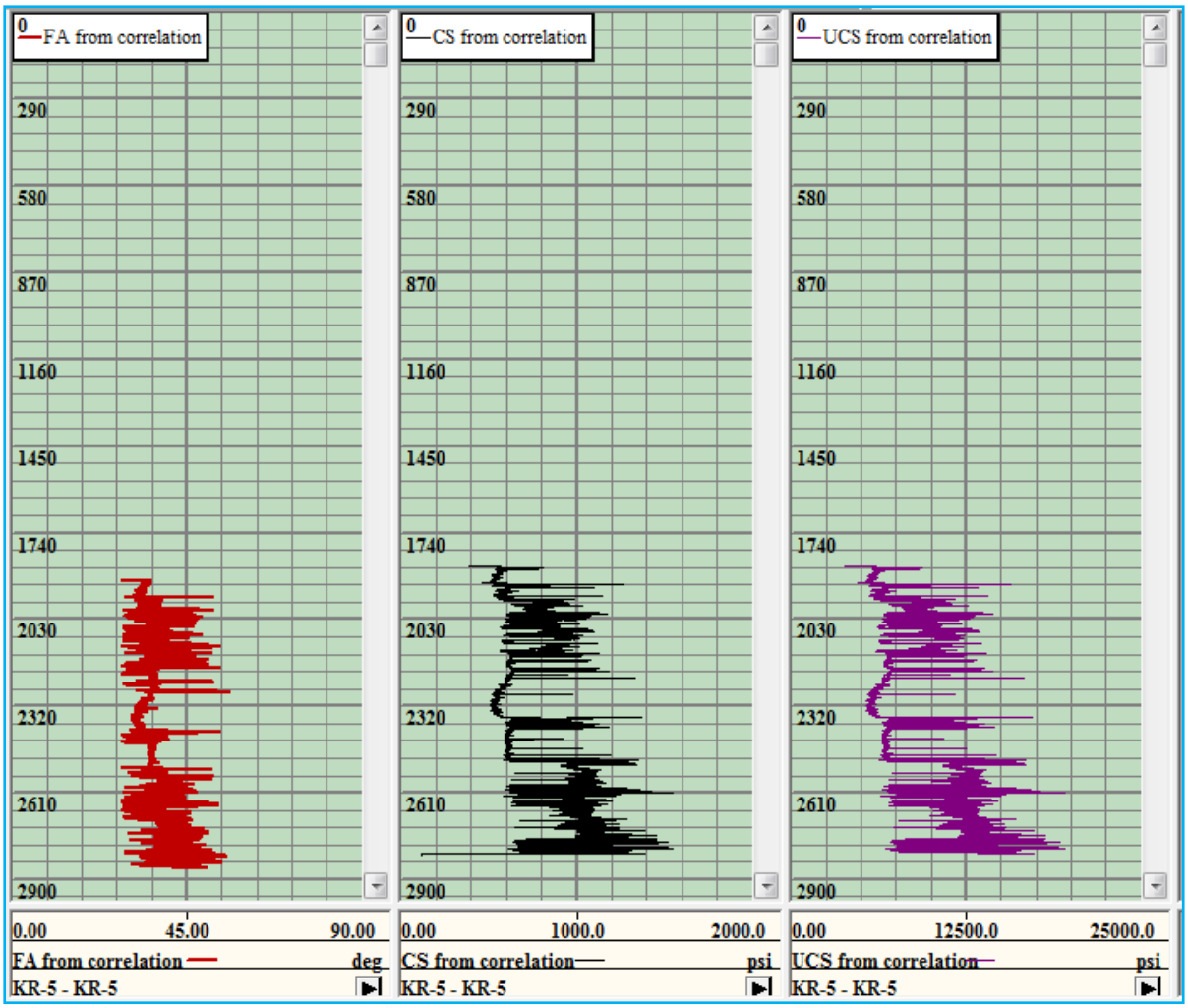

Figure 5.26: Rock mechanical properties for well KR-5.

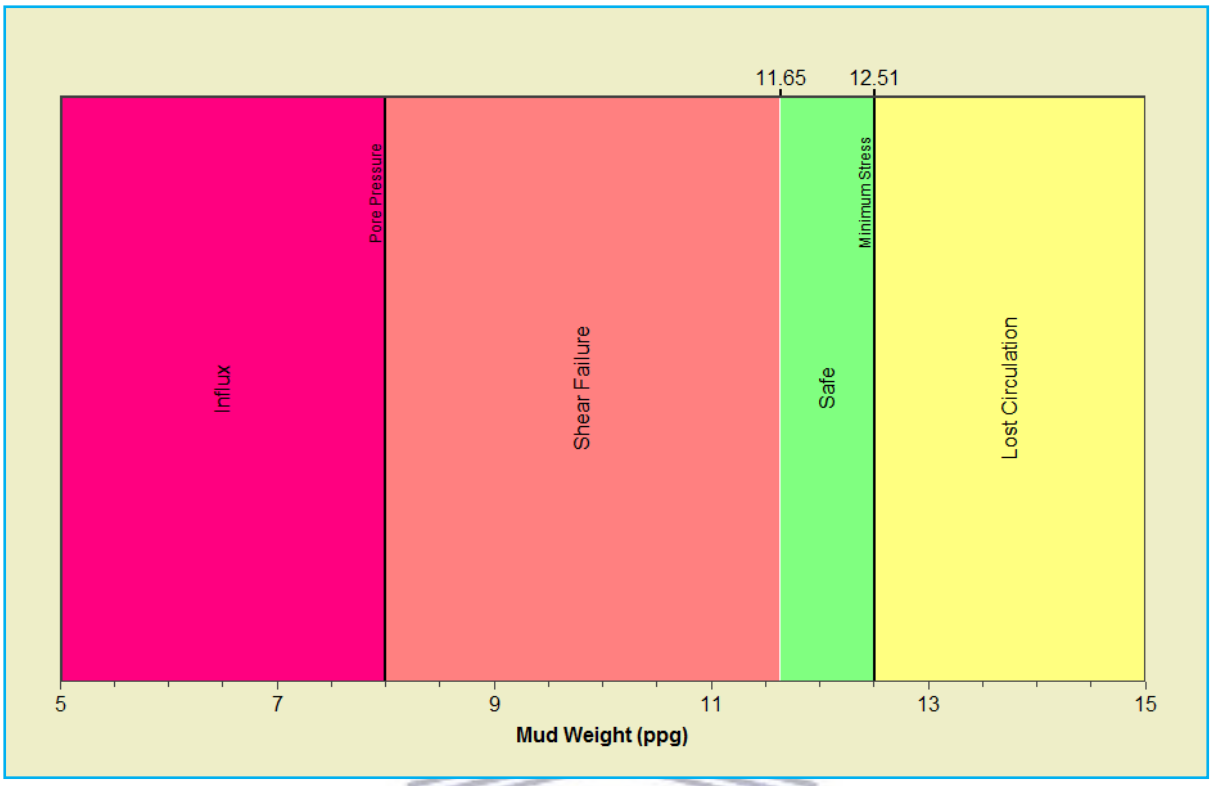

Figure 5.27: Safe mud window for well KR-5 at TUSM.

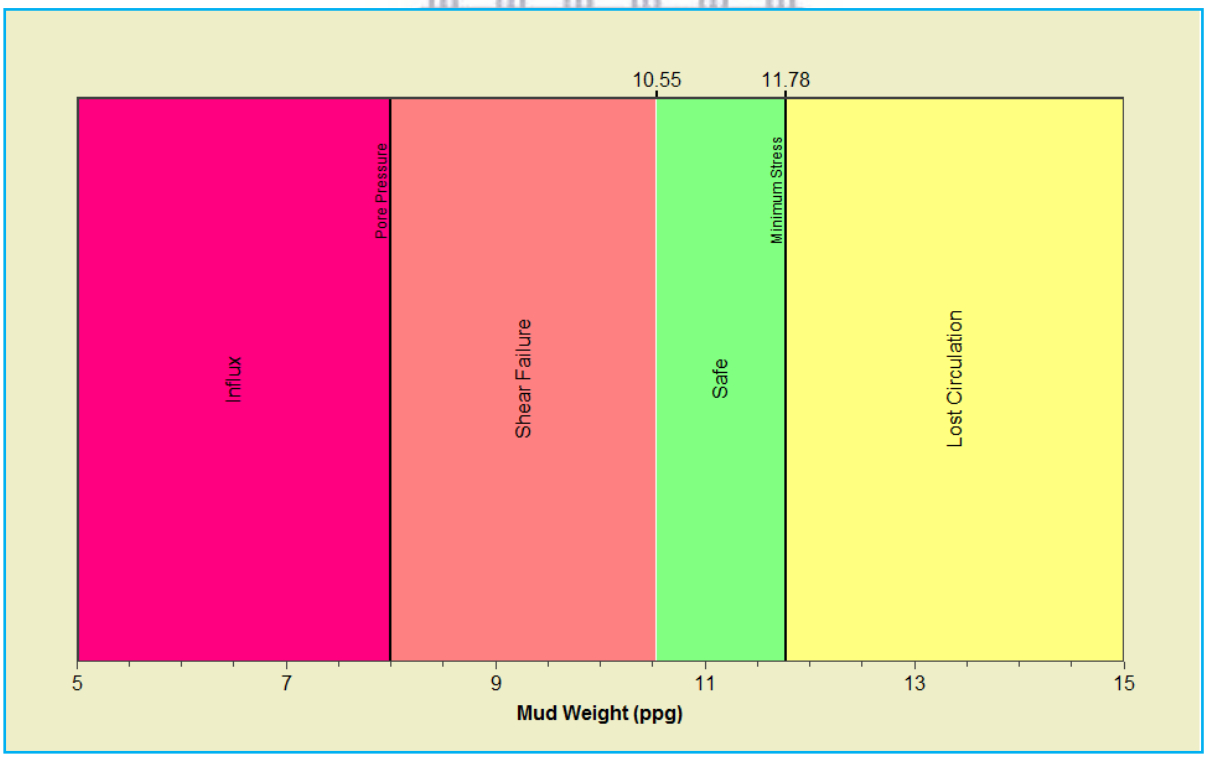

Figure 5.28: Safe mud window for Well KR-5 at BUSM.

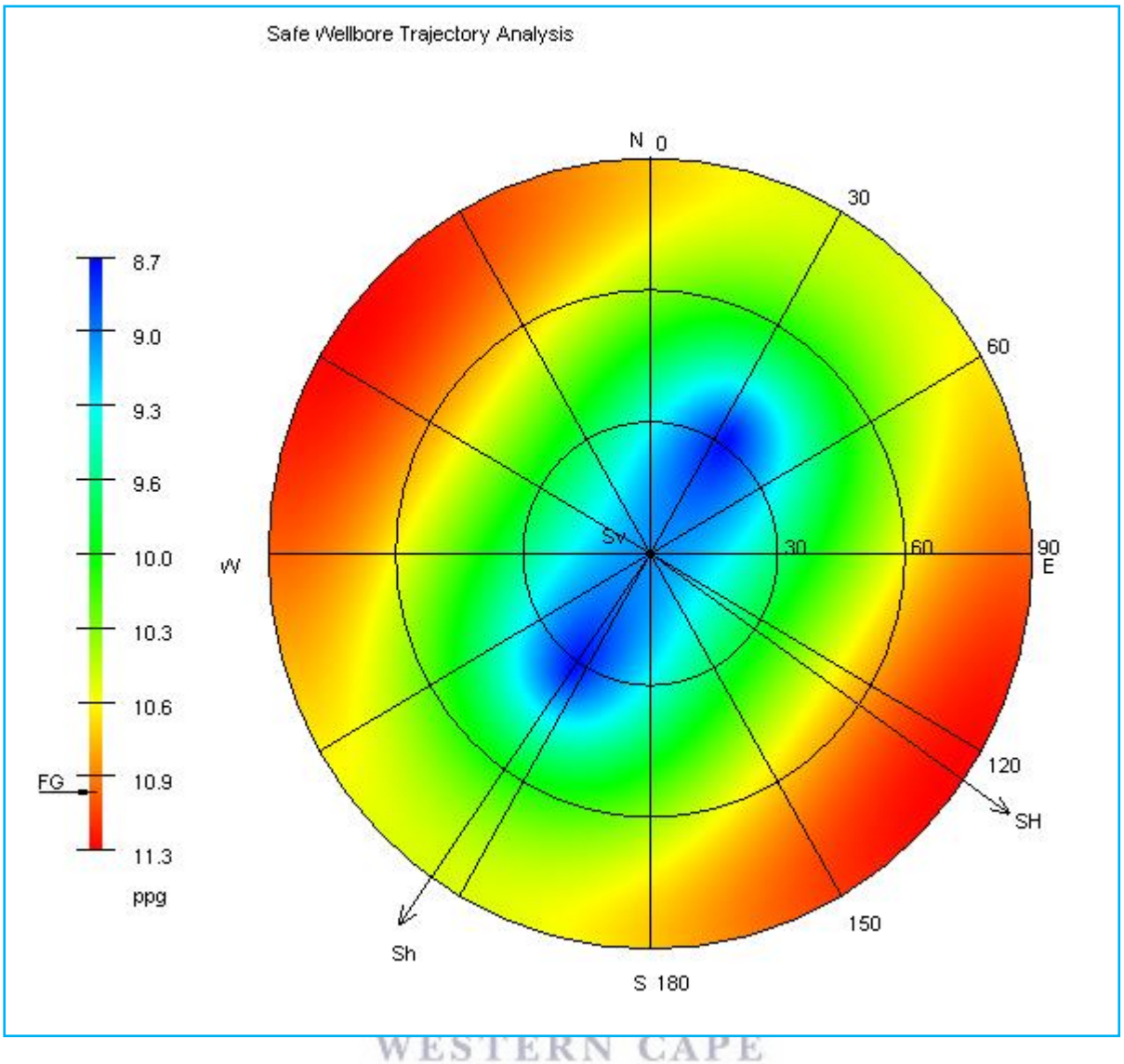

Figure 5.29: Lower Hemisphere plot for well KR-5 at TUSM.

Table 15: Parameters used for safe wellbore trajectory analysis of well KR-5 at TUSM.

Depth (m)	2505.50
Failure criterion	Mohr-Coulomb
Overburden Gradient (ppg)	18.07692
Pore Pressure Gradient (ppg)	8.863
Minimum Horizontal Stress Gradient (ppg)	11.01
Maximum Horizontal Stress Gradient (ppg)	14.55
Maximum Horizontal Stress Azimuth	125
Poisson's Ratio	0.179929264
Friction Angle (deg)	37.159
Cohesive strength (psi)	1291.65

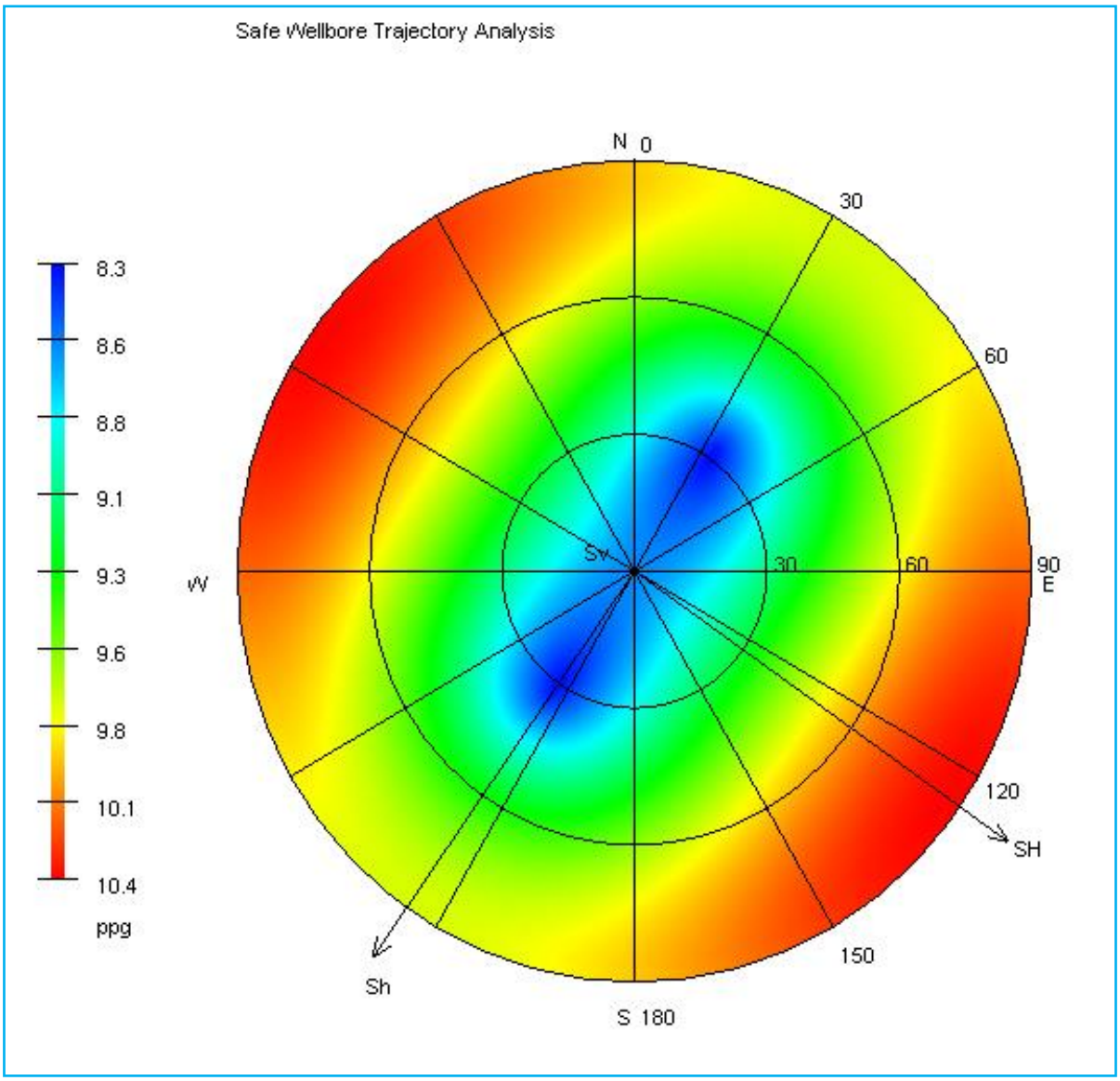

Figure 5.30: Lower Hemisphere plot for well KR-5 at BUSM.

Table 16: Parameters used for safe wellbore trajectory analysis of well KR-5 at BUSM.

Depth (m)	2759
Failure criterion	Mohr-Coulomb
Overburden Gradient (ppg)	18.26923
Pore Pressure Gradient (ppg)	8.983
Minimum Horizontal Stress Gradient (ppg)	11.78
Maximum Horizontal Stress Gradient (ppg)	15.03
Maximum Horizontal Stress Azimuth	125
Poisson's Ratio	0.170696363
Friction Angle (deg)	39.845
Cohesive strength (psi)	1224.26

5.7 Well KR-6

The geopressure gradient curve after calibration is shown in Figure 5.31. Like previous wells, few calibration sources are available. A high pore pressure compartment can be observed at approximate depths of 2412 - 2572m, resulting in an elevated fracture gradient at that depth.

The rock mechanical properties are shown in Figure 5.32. Two erratic sections of high cohesive and unconfined compressive strengths can be observed at depths of approximately 1982 - 2124m and 2541m to the TD of the well.

The safe mud window plots for the top and bottom of the reservoir are shown in Figure 5.33 and Figure 5.34 respectively. The bottom of the reservoir for well KR-6 shows a much larger safe drilling mud window.

The lower hemisphere plots at TUSM and BUSM are shown in Figure 5.35 and 5.36.

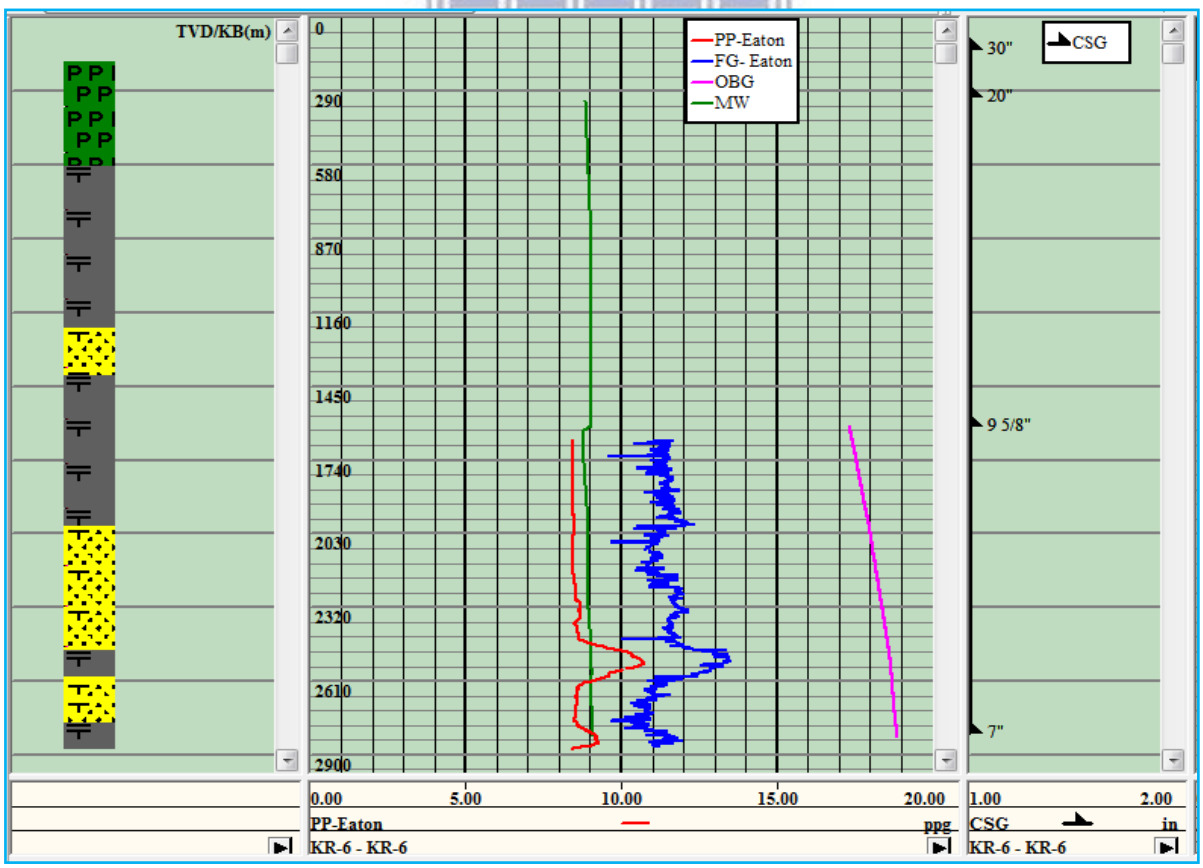

Figure 5.31: Modelled geopressure gradients for well KR-6 post calibration.

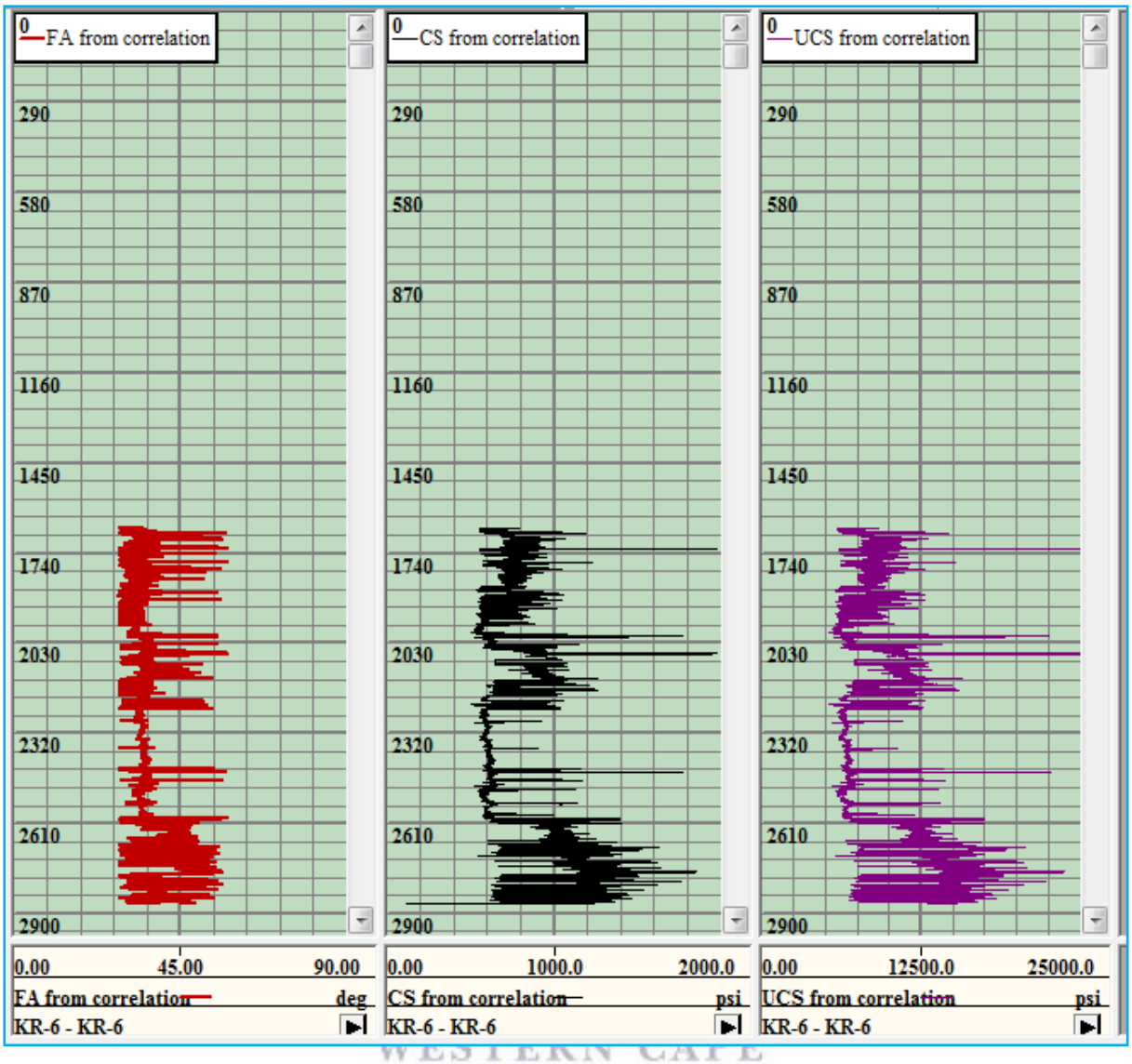

Figure 5.32: Rock mechanical properties for well KR-6.

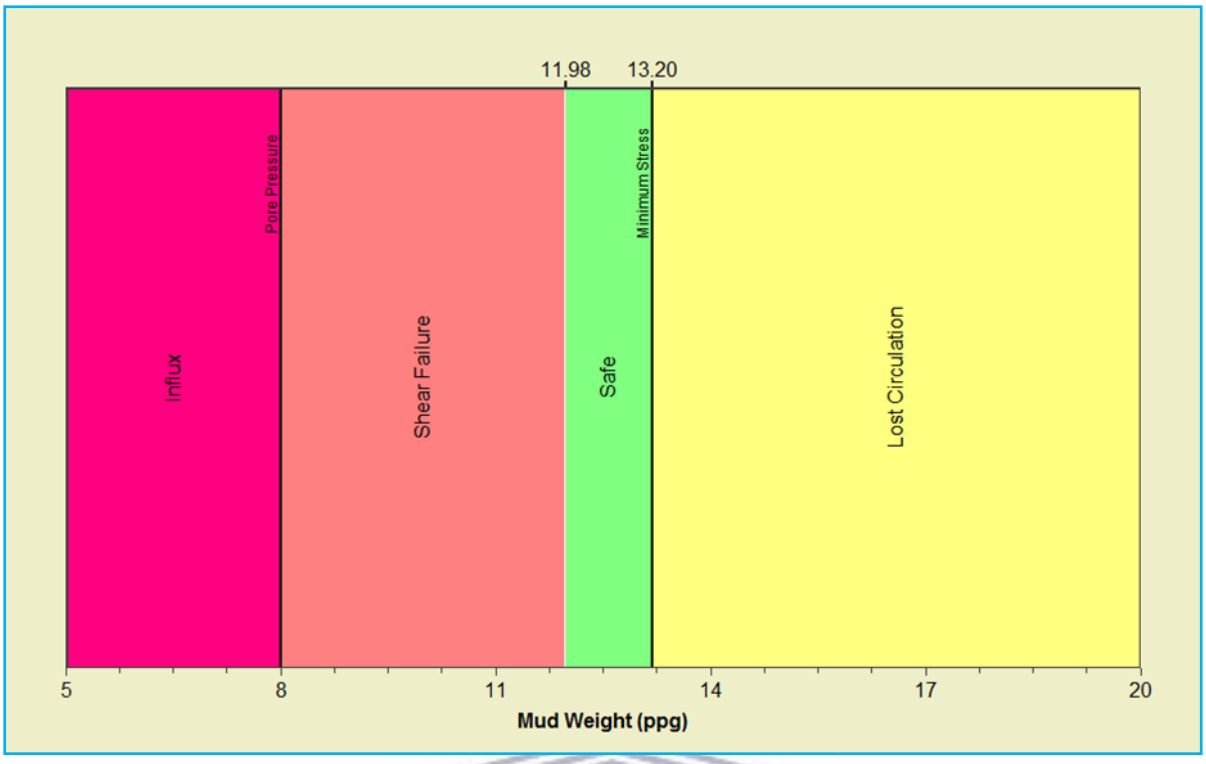

Figure 5.33: Safe drilling mud window for well KR-6 at TUSM.

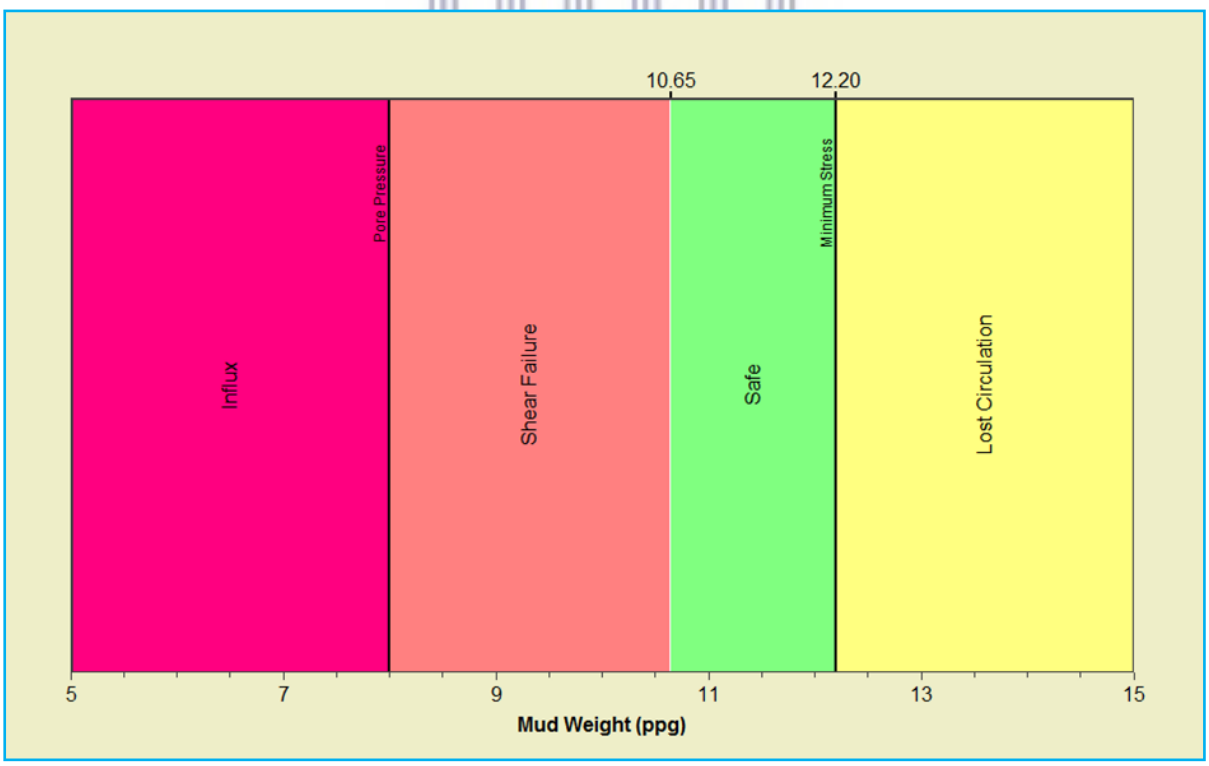

Figure 5.34: Safe drilling mud window for well KR-6 at BUSM.

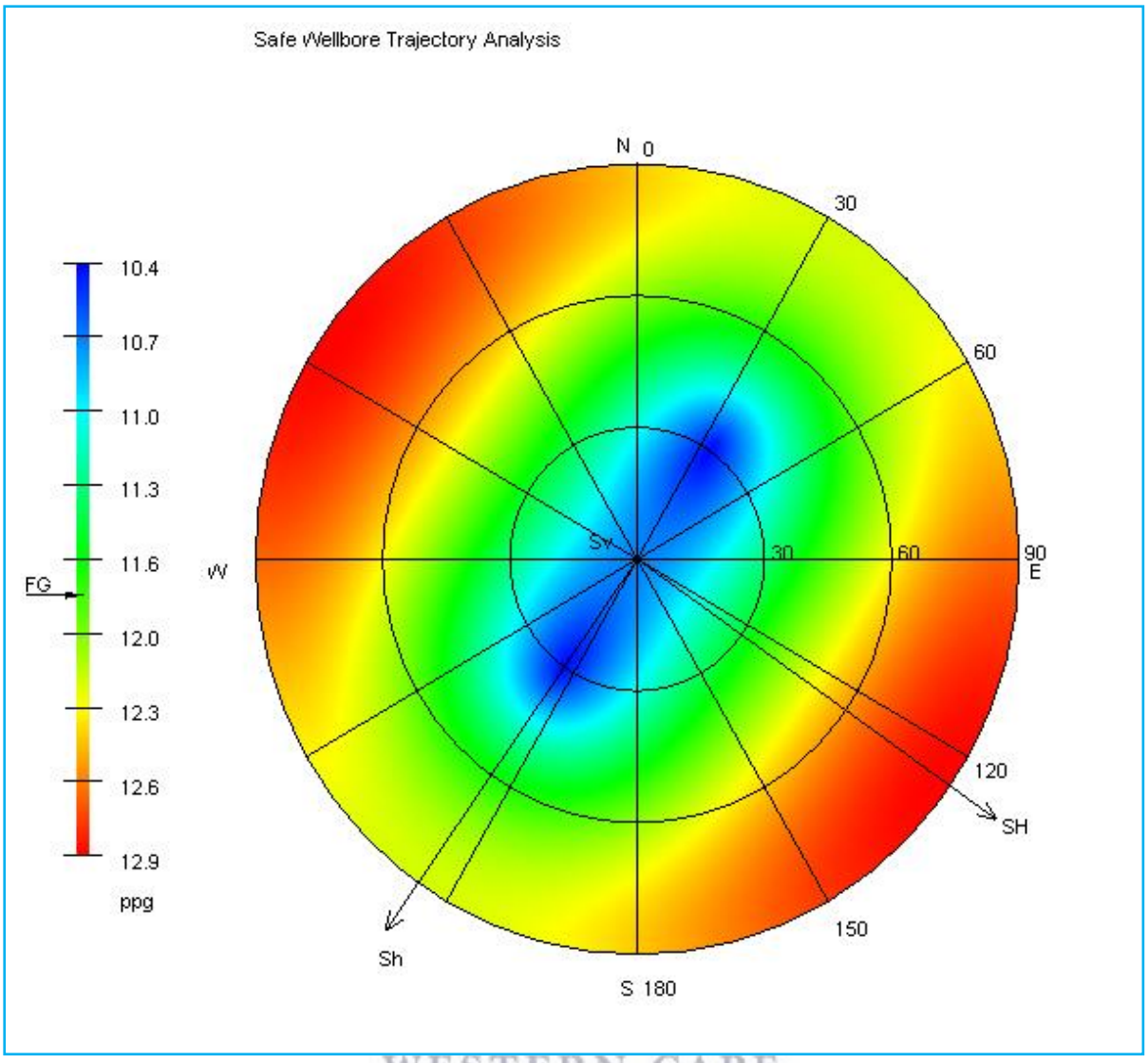

Figure 5.35: Lower hemisphere plot for well KR-6 at TUSM.

Table 17: Parameters used for safe wellbore trajectory analysis of well KR-6.

Depth (m)	2557
Failure criterion	Mohr-Coulomb
Overburden Gradient (ppg)	18.65385
Pore Pressure Gradient (ppg)	9.058
Minimum Horizontal Stress Gradient (ppg)	11.8
Maximum Horizontal Stress Gradient (ppg)	15.24
Maximum Horizontal Stress Azimuth	125
Poisson's Ratio	0.174859984
Friction Angle (deg)	37.753
Cohesive strength (psi)	1183.42

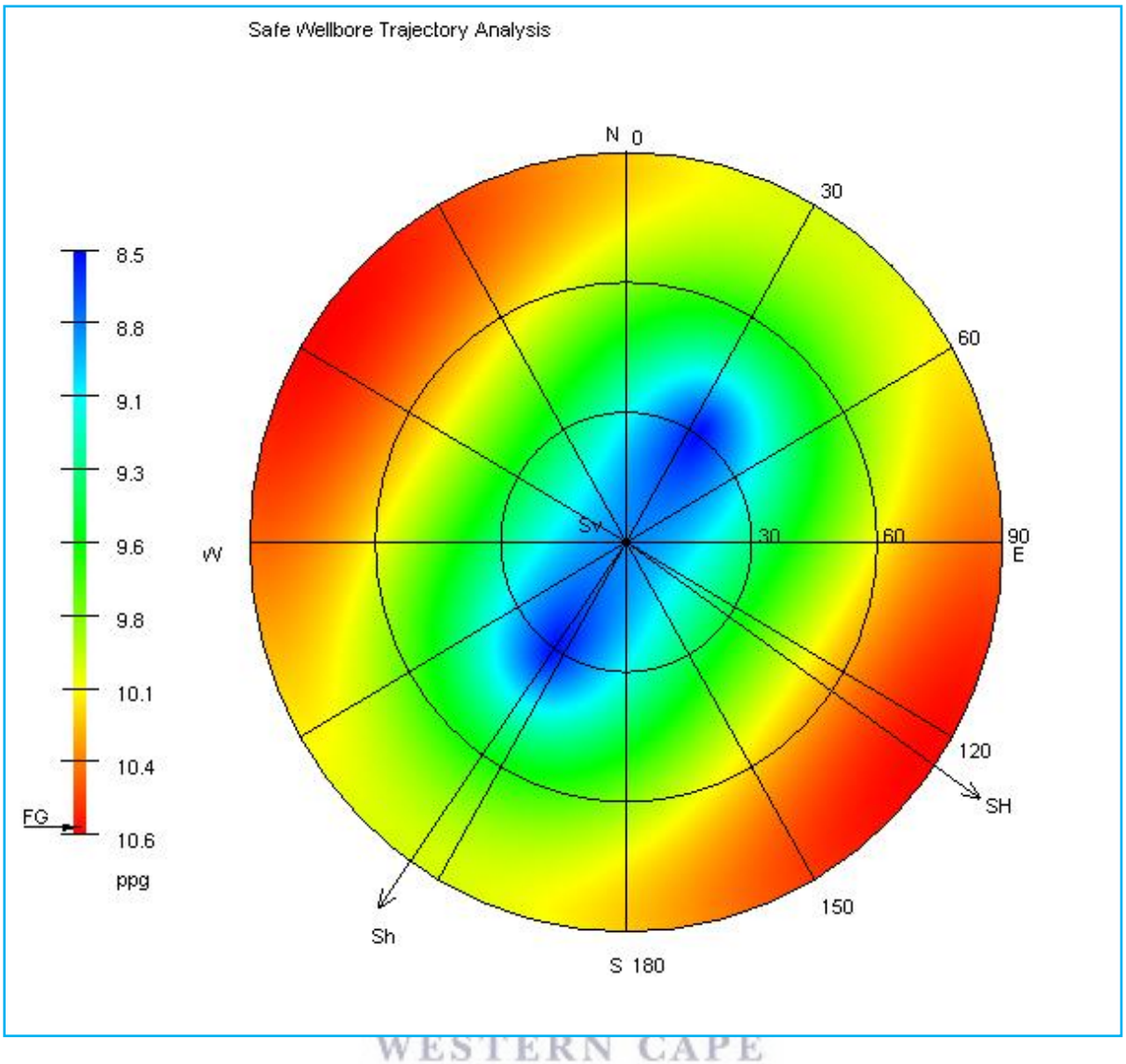

Figure 5.36: Lower hemisphere plot for well KR-6 at BUSM.

Table 18: Parameters used for safe wellbore trajectory analysis of well KR-6.

Depth (m)	2723
Failure criterion	Mohr-Coulomb
Overburden Gradient (ppg)	18.84615
Pore Pressure Gradient (ppg)	8.602
Minimum Horizontal Stress Gradient (ppg)	12.1
Maximum Horizontal Stress Gradient (ppg)	15.48
Maximum Horizontal Stress Azimuth	125
Poisson's Ratio	0.153294957
Friction Angle (deg)	39.594
Cohesive strength (psi)	1403.68

5.8 Well KR-7

This is the most distinct well within the K-R Field. The geopressure gradient curves post calibration presented in Figure 5.37 shows a complete profile of drilling mudweights along the well trajectory and a greater degree of separation between the pore pressure and fracture gradient curves.

The rock mechanical properties shown in Figure 5.38 show a similar trend of increased cohesive and unconfined compressive strength towards the TD of KR-7, as noted in previous wells. This increase starts at approximately 2520m.

The safe mud window plots for the top and bottom of the reservoir are shown in Figure 5.39 and Figure 5.40 respectively. This well has the largest mud window for the K-R Field at both TUSM and BUSM.

The lower hemisphere plots shown in Figure 5.41 and 5.42 differ from all previous well. This well shows the highest minimum and maximum horizontal stress for the K-R Field.

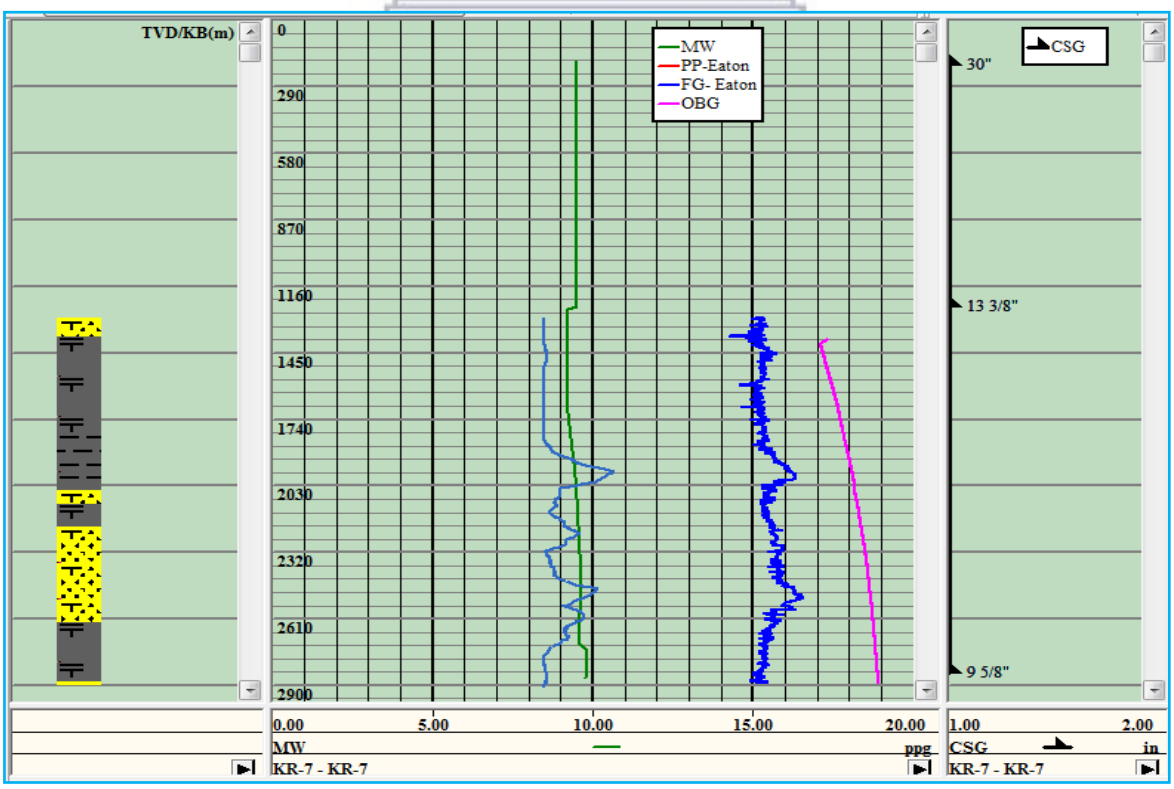

Figure 5.37: Modelled geopressure gradients for well KR-7 post calibration.

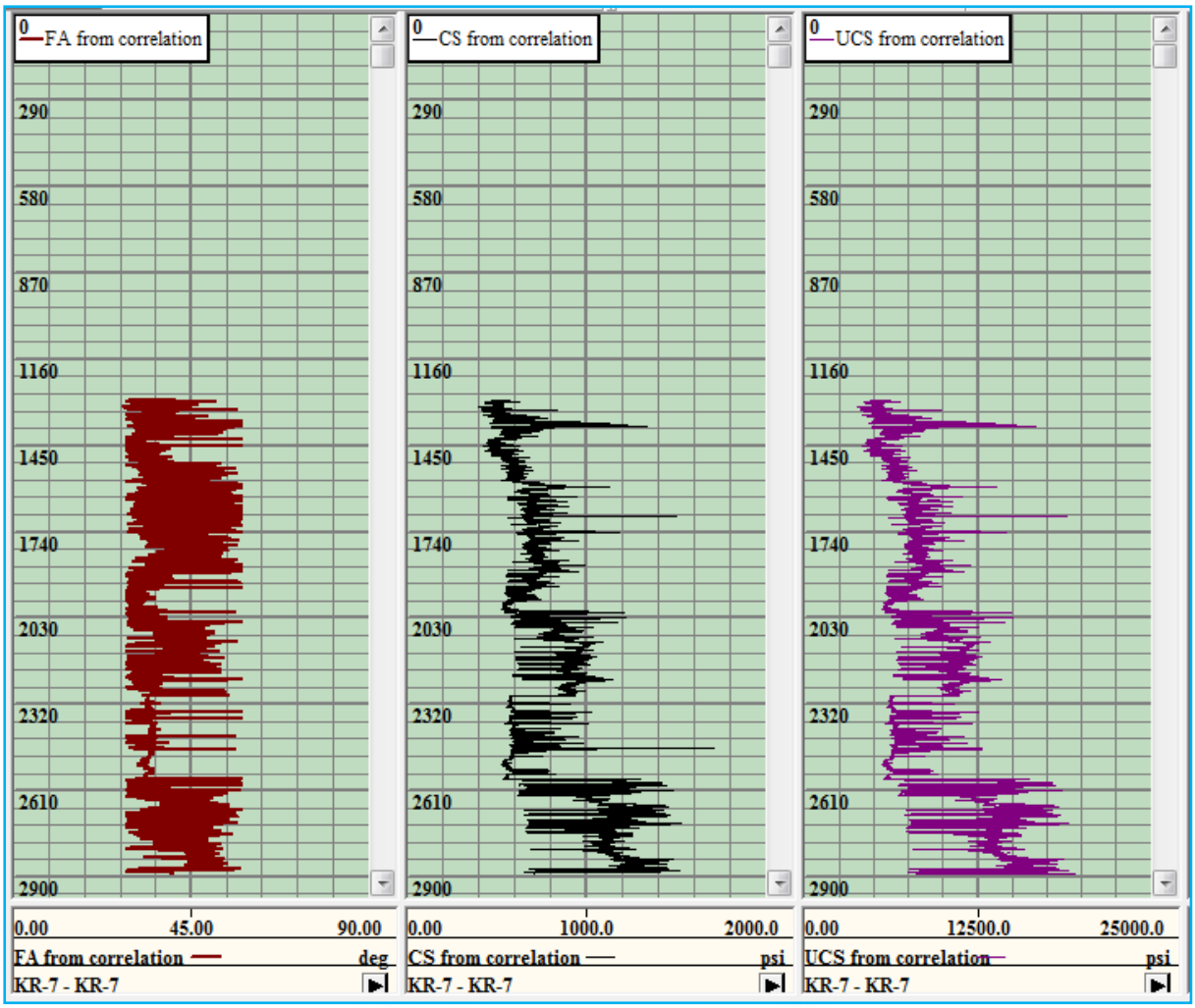

Figure 5.38: Rock mechanical properties for well KR-7.

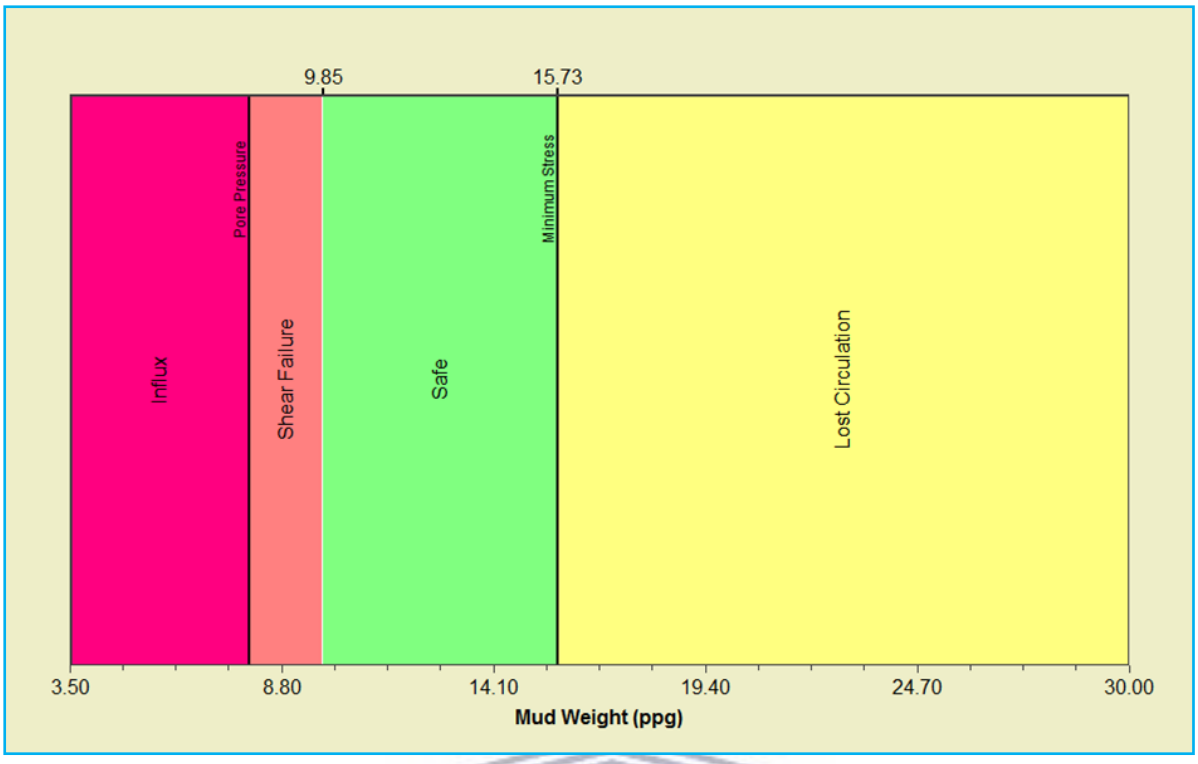

Figure 5.39: Safe drilling mud window for well KR-7 at TUSM.

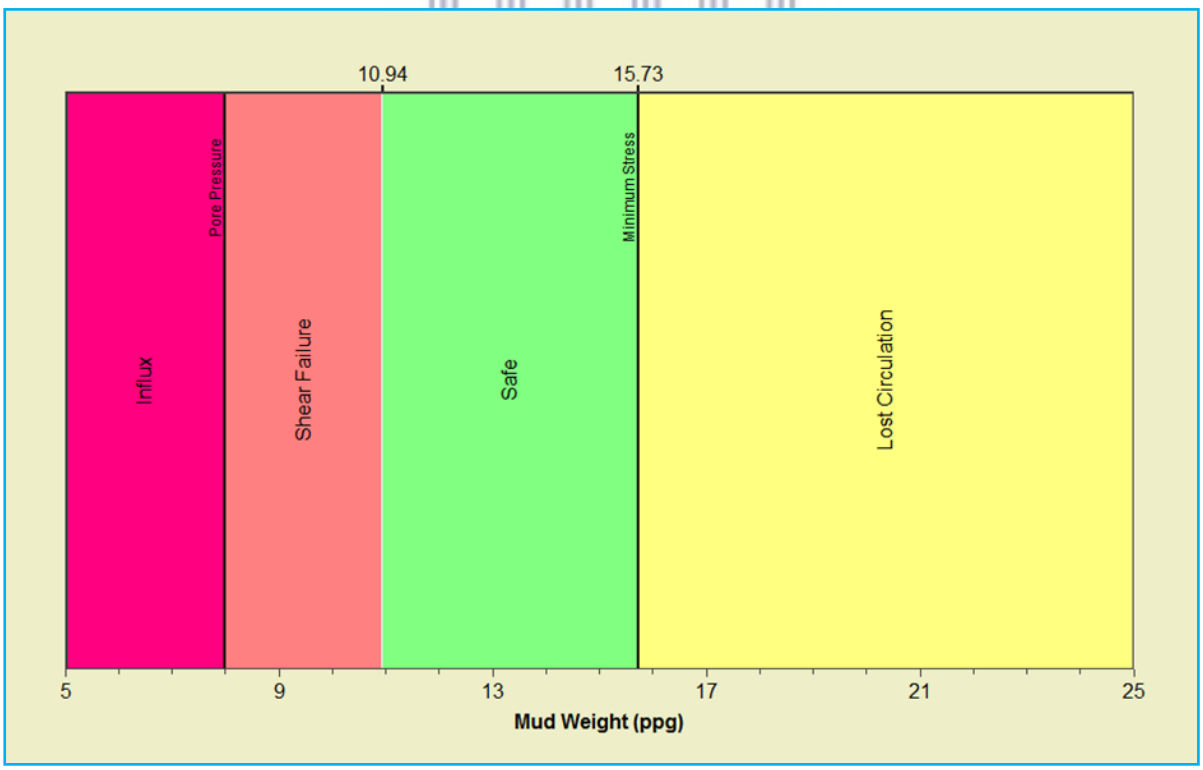

Figure 5.40: Safe drilling mud window for well KR-7 at BUSM.

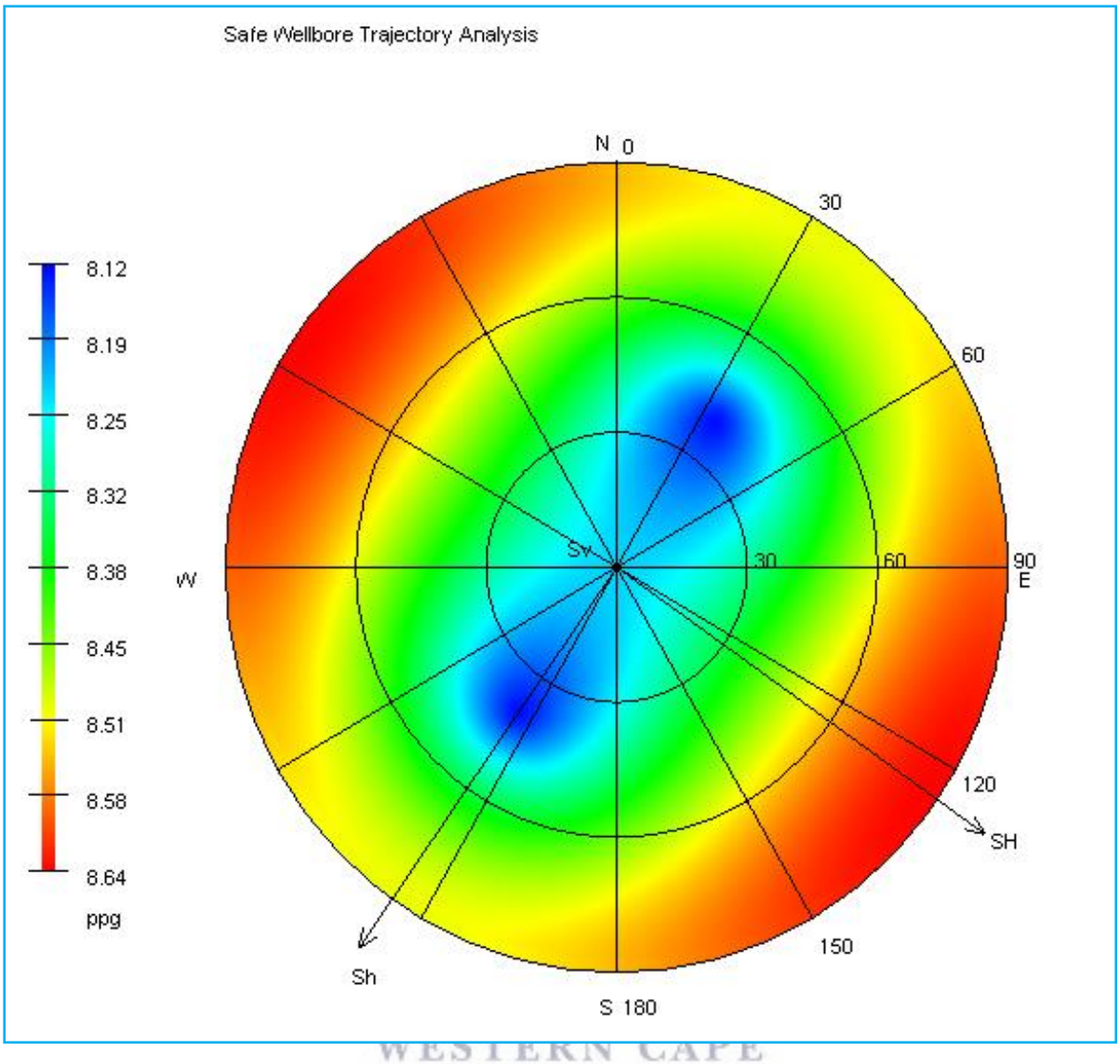

Figure 5.41: Lower Hemisphere plot for well KR-7 at TUSM.

Table 19: Parameters used for safe wellbore trajectory analysis for well KR-7.

Depth (m)	2574
Failure criterion	Mohr-Coulomb
Overburden Gradient (ppg)	18.65385
Pore Pressure Gradient (ppg)	9.254
Minimum Horizontal Stress Gradient (ppg)	15.73
Maximum Horizontal Stress Gradient (ppg)	17.2
Maximum Horizontal Stress Azimuth	125
Poisson's Ratio	0.405761544
Friction Angle (deg)	36.432
Cohesive strength (psi)	617.176

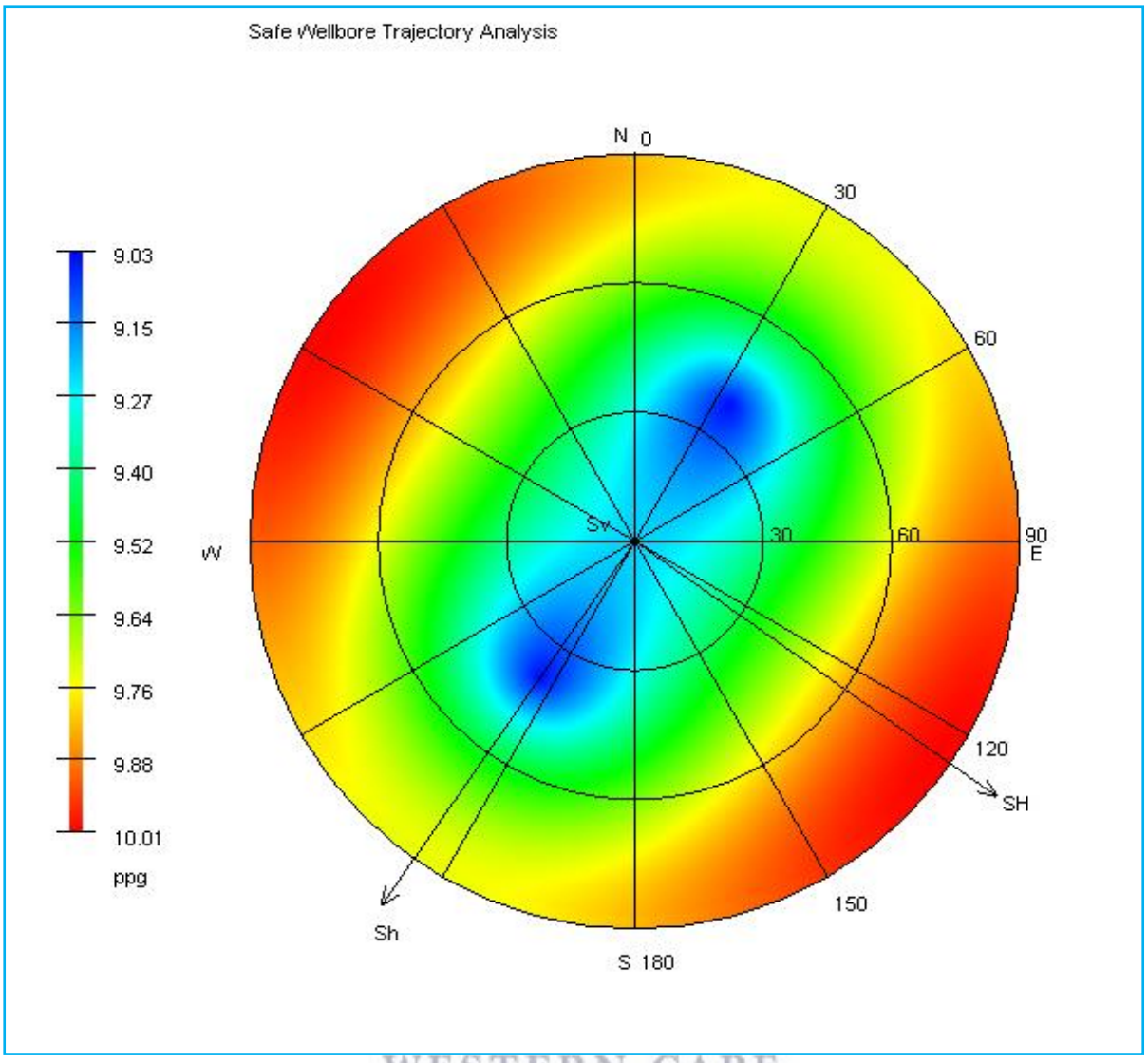

Figure 5.42: Lower Hemisphere plot for well KR-7 at BUSM.

Table 20: Parameters used for safe wellbore trajectory analysis for well KR-7.

Depth (m)	2836
Failure criterion	Mohr-Coulomb
Overburden Gradient (ppg)	18.84615
Pore Pressure Gradient (ppg)	8.55
Minimum Horizontal Stress Gradient (ppg)	15.33
Maximum Horizontal Stress Gradient (ppg)	17.1
Maximum Horizontal Stress Azimuth	125
Poisson's Ratio	0.386497724
Friction Angle (deg)	40.101
Cohesive strength (psi)	719.981

Chapter 6: Discussion of results

6.1 Introduction

The Bredasdorp Basin has been studied extensively by many scholars and authors throughout the years, however; minimal geomechanical research has been carried out since its hydrocarbon discovery. Detailed geological understanding of the K-R structure and the evolution of its petroleum system has been the main focus for most authors.

This dissertation shows a full scale 2D geomechanical model for one of the gas fields; offshore South Africa. The research was based predominantly on well log data and well reports for all seven wells. In areas where there is no well data, correlations have to be made to predict how the stress gradients will behave in the K-R Field. For these correlations, petrophysics was used extensively to derive geomechanical parameters which were modelled on the drillworks software package. The drilling data available from each report is used as calibration sources for geopressure.

6.2 Discussion

Knowledge of formation pressures is imperative to drilling; however, in areas where no drilling has occurred, well planners are essentially drilling "blind". Seismic data that's available may not be ideal as it inherently implies that geopressure gradients are based on correlations. Nonetheless, in areas of scarce data sources, correlations that best fit the data set have to be used. The Geomechanical model built is a prediction of how geopressure will behave in the K-R Field, and is to be used when planning future wells in the area.

When calibrating the modelled pore pressure gradient and fracture gradient, the normal compaction trend line was shifted for all wells, in order for the calibration points and geopressure gradients to coincide. This indicated that the values used to create the normal compaction trendlines were too low at the end point. Thus, the formation is less compacted than initially assumed.

The shifting of the normal compaction trendlines to higher values resulted in a decreased margin between the trendlines and the measured sonic logs. Inevitably, the values derived from Eaton's sonic method for predicting pore pressure will yield lower values, as deduced from Equations 4.4 in Section 4.4.2. The reduction in pore pressure values will have a resulting decrease in fracture gradients values which are linked by the Eaton fracture gradient method - equation 4.6.

Well KR-3 shows a larger drop in pressure gradient than the other wells from the top to the bottom of the reservoir; the pore pressure has been reduced from 9.6ppg to 8.5ppg. The operational drilling windows post calibration shows a similar trend. For depths to 2600m the drilling window is fairly wide and at depths deeper than 2600m the drilling window becomes more constricted. This is the case for all wells except well KR-7 where the drilling window remains wide up until the true depth of the well. It's important to note that all KR-wells have close to zero inclination; in an inclined well, the drilling mud window will be narrower.

The rock mechanical properties for the seven wells show roughly the same trend. A close to constant value over the main part of the well depth, with increasing values towards the short interval, close to the well's true depth. The friction angle shows an average range between 35° - 40° for all wells. Although high, these values are still indicative of sandstone (Horsrud, P., 2001). The cohesive strength and unconfined compressive strength values vary, depending on the sandstone. The values produced within the reservoir are between a ranges of 9000 – 14000 psi for unconfined compressive strength and 800 -1200 psi for cohesive strength.

The safe wellbore trajectory analysis displays the same trend for all KR-wells. The hemisphere plots show a greater variation on the mudweight in the direction of maximum horizontal stress, thus showing the need for lower mudweight when drilling in the minimum horizontal stress direction, NE-SW. This is due to an assumed value of 1.02 for the horizontal stress ratio. The higher the ratio, the greater the difference will be regarding mudweight variation to horizontal stress direction.

The hemisphere plots in Chapter 5 show the maximum horizontal stress azimuth to be 125°. To depict a realistic value, the strike direction of drilling induced fracture can be used to provide an estimation of maximum horizontal stress direction. For this model, the maximum

horizontal stress direction was assumed from the regional strike direction of faults on the structural depth map, shown in figure 2.8.

When modelling on the drillworks software, the model must be compressed to reflect the current formation depth intervals, which allows the well planner to sufficiently determine the mud window. The software allows for flow rate simulation and hydraulics to be run, which results in the equivalent circulating densities and downhole pressures. For this model, the actual mud weight values recorded whilst drilling each well are displayed alongside the simulated geopressure gradients.

The shear failure gradient has not been calculated for this model. This parameter is generally used to ascertain when a rock experiences shear failure. Different models to calculate rock mechanical properties generally have a pronounced effect on the shear failure gradient and thus, creates a lot of uncertainty in the model. The empirical shear gradient values can be validated by observing wellbore cutting where instability issues occurred. The shape and size of the cuttings provides us with tangible information as to whether or not the mud weight used exceeded the shear failure gradient. Any geomechanical model must be history matched and calibrated to minimize the uncertainty. Also, a high number of off-set wells used to build a model will yield a more accurate prediction. However, there are inherent uncertainties during the process of drilling a well; operational observations and drilling incidents that need to be acted on, resulting in changes to pre-drilled safe mud window estimates.

In the geomechanical model, pre-calibration is based only on log data and information from well and driller's reports. This makes the model quite conservative and may not accurately describe reality. The geopressure gradients are dependent on each other and thus, discrepancies in the log data may result in inaccurate values. Quality checking the log data is imperative, to ensure that all values are in alignment with historically validated measurements. A typical example of this is the density of the formations. If these values have been estimated incorrectly, the overburden gradient will be erroneous, which will have a knock-on erroneous effect for pore pressure gradient and fracture gradient estimations. This scenario occurs with the sonic log as well, due to the fact that this particular log is used as the porosity log. When normal compaction trend lines are generated on erroneous sonic datasets, the result is inevitably an incorrect pore pressure estimation. It is quite clear that geopressure gradients in this case, are incredibly sensitive to well log data inaccuracies.

It is mainly through calibration that uncertainties are reduced and the model is validated. This validation is derived directly from calibration sources, which may be a given value at a specific depth or an indication that the modelled gradients are inaccurate as described in Section 4.7. Geomechanical modelling itself is not a 100% scientific solution to all well issues; therefore it is pivotal that calibration sources from all wells are consistent, i.e. leak-off tests are performed as accurately and stringently as possible and the correct values are recorded. This will in turn, lead to a more precise geomechanical model.

Having a fundamental knowledge of the whole cycle of data acquisition is pivotal in understanding the geomechanical model in its entirety. This means understanding geological data, seismic data, well log data as well as well completion and drilling reports. Confusion may arise when these sources of data are collected by different service companies, in which they may be either represented differently, or the technical terminology may be different. It is also essential to have an understanding of the actual drilling process and what caused certain drilling incidents or stability issues to arise. Through merging the physical phenomena and operational observations with the theoretical model, a more correct canvas is painted allowing us to drill as safely and efficiently as possible.

Chapter 7: Conclusions and Recommendations

The Bredasdorp Basin consists of several oil and gas fields, amongst which is the K-R Field. By using offset well data along with various calibration sources, a 2D geomechanical model was built, allowing for estimation of overburden gradient, pore pressure gradient and fracture gradient for future wells drilled in the field. A significant part of this model involves calibration which incorporates operational observations to fit the geopressure curves to actual drilling incidents. The current model built is quite a reliable estimate, and as previously mentioned, the inclusion of more offset wells will yield a more accurate prediction of the safe drilling mud window for the K-R Field.

The 2D geomechanical model for the K-R Field shows how the overburden gradient, pore pressure gradient and fracture gradient will vary with depth. The pore pressure and fracture gradient values are of most relevance as they set the minimum and maximum limits for drilling a well safely. These geopressure gradients were calculated using the Eaton Method; for the upper shallow marine reservoir, these values range between 8.46-9.60 ppg and 10.12-15.33 ppg respectively. The modelled geopressure gradients shows a wider drilling mud window up to about 2600m, becoming slightly narrower as the depth approaches the TD of the wells. This is true for all wells except well KR-7, which subsequently is the most recent and best drilled well, regarding washouts and wellbore failures. The rock mechanical properties show roughly the same trend, with increasing values towards the wells TD.

The importance of applying a density correction prior to any stress calculations has been demonstrated in this research. Accurate density data has a direct effect on the vertical stress gradient which is ultimately linked to the pore pressure and fracture gradient. This model has been created in the hope that reliable drilling mud windows can be estimated for future wells in the K-R Field area, thereby reducing drilling related and wellbore stability issues, ultimately allowing for wells to be drilled safely and cost effectively.

Recommendations

The 2D geomechanical model utilizes data from seven vertical wells. To further enhance this research, more wells and new wells should be added to either validate or invalidate the model. A 2D model is a good representation of geopressure gradients with depth of wells. However, stability issues are often in the form of 3D principal stress problems. If more data becomes available, a full scale 3D geomechanical model may cover certain issues not addressed in this research.

Hydraulic and geochemical related issues have not been explored in this thesis. These factors do play a role in wellbore stability; however to solves these problems, a substantial amount of intricate information is needed. The petroleum industry solves the issue of chemically induced pressure effects by using oil based mud which reduces the mud systems interaction with shales. A study dedicated to effects that shale properties may have on the drilling mud window for the K-R Field could be highly beneficial. Information about shale anisotropy, capillary effects and shale-fluid interactions could be used in estimating failure probability.

A key feature of the drillworks software is its capability to allow us to observe the effects of azimuth and inclination. This would be of utmost relevance in the event of planning a highly deviated well using the 2D geomechanical that has been compiled.

References

Anderson, E.M., (1951). The dynamics of faulting and dyke formation, with applications to Britain, 2 ed. Oliver and Boyd, Edinburgh, pp. 206.

Baker Hughes Inc., (2011). Leibniz Institute for Applied Geophysics. [Online] Available at: http://www.liaghannover.de/fileadmin/user_upload/dokumente/FKPE/11.workshop/Wessling.pdf.

Bourgoyne Jr., A.T., Millheim, K.K., Chenevert, M.E., and Young Jr., F.S., (1986). Applied Drilling Engineering. SPE Textbook Series.

Bowers, G., (1999). State of the Art in Pore Pressure Estimation. Report No. 1. Knowledge Systems, INC. DEA Project 119.

Bratton, T., (2005). Geomechanical Stress Modeling Presentation. Schlumberger.

Bratton, T., Bornemann, T., Li, Q., Dick, P., and Rasmus, J., (1999). *Logging-while-drilling images for geomechanical, geological and petrophysical. interpretations*. SPWLA 40th Annual Logging Symposium, Oslo, Norway, Society of Professional Well Log Analysts.

Brink, G.J., and Winters, S.J., (1989). Overpressure study of the Bredasdorp Basin. SOEKOR unpubl. Rept., pp. 8.

Broad, D., (2004). South Africa Activities and Opportunities. An Unpublished Power Point Presentation to Petro China.

Broad, D.S., Jungslager, E.H.A., McLachlan, I.R., and Roux, J., (1996). Geology of offshore Mesozoic basins: Contribution to a text book on the geology of Africa published by the Geological Society of South Africa, pp. 6-19.

Brown, D.M., (1991). E-AQ1 post-mortem study and implications for overpressure compartments in the Bredasdorp Basin. SOEKOR unpubl. Rept., pp. 15.

Brown, L.F., Benson Jr. J.M., Brink, G.J., Doherty, S., Jollands, A., Jungslager, E.H.A., Keenan, J.H.G., Muntingh, A., and van Wyk, N.J.S., (1995). Sequence stratigraphy in offshore South African divergent basins: An atlas on exploration for Cretaceous lowstand traps, Soekor (PTY) LTD, pp. 83-131.

Cartwright, J.A., (1989). The structural and stratigraphic development of the Gamtoos and Algoa Basins. SOEKOR unpubl. Rept., pp. 26.

Castagna, J.P., Batzle, M.L., Eastwood, R.L. (1985). Relationships between compressional-wave and shear-wave velocities in clastic silicate rocks: Geophysics, 50, pp. 571-581.

Chardac, O., Murray, D., Carnegie, A., and Marsden, J.R., 2005. A Proposed Data Acquisition Program for Successful Geomechanics Projects. 14th SPE Middle East Oil and Gas Show and Conference, Bahrain. SPE # 93182.

Cook, N.G.W., and Jaeger, J.C., (1976). Fundamentals of Rock Mechanics. New York, Halsted Press., pp. 42-64.

Daines, S.R., (1980). The Prediction of Fracture Pressures for Wildcat Wells. *Society of Petroleum Engineers*. SPE 9081, pp. 63-72

Davies, C.P.N., (1988b). Bredasdorp Basin – south flank hydrocarbon expulsion. SOEKOR unpubl. Rept., pp. 17.

Davies, C.P.N., (1995c). Gas: oil ratios. SOEKOR unpubl. Tech. Note No. 23, pp. 7.

Davies, C.P.N., (1996c). Bredasdorp Basin syn-rift study: a review of hydrocarbons and migration. SOEKOR unpubl. Rept., SOE-GCH-RPT-251, pp. 16.

Davies, C.P.N., (1997). Unusual Biomarker maturation ratio changes through the oil window, a consequence of varied thermal history. Organic Geochemistry, Vol. 27, No. 7/8: 537-560.

Dutta, N., (1999). Seismic Prediction of Geopressure: *Some Basic Principles and the Best Practice Methodology*. Report No. 2. Knowledge Systems, INC. DEA Project 119.

Eaton, B.A., (1975). The Equation for Geopressure Prediction from Well Logs. Society of Petroleum Engineers. SPE 5544, pp 4-10.

Eaton, B.A., 1969. Fracture Gradient Prediction and its Application in Oilfield Operations. SPE-AIME, pp. 53-60.

Fjaer, E., Holt R.M., Horstrud, P., Raaen, A.M., and Risnes, R., (1992). Petroleum Related Rock Mechanics. Amsterdam, Elsevier. Developments in Petroleum Science 33, pp. 185-236.

Fjaer, E., Holt, R.M., Horsrud, P., Raaen, A.M., Risnes, R., (2008). Petroleum Related Rock Mechanics, 2 ed. Elsevier, pp. 515.

Fouché, J., Bate, K.J., and Van der Merwe, R., (1992). Plate tectonic setting of the Mesozoic basins, southern offshore, South Africa: a review. In "Inversion tectonics of the Cape Fold Belt, Karoo and Cretaceous Basins of Southern Africa''. (eds.) De Wit, M.J., and Ransome, I.G.D., A.A. Balkema, Rotterdam, pp. 33-59.

Halliburton, (2009). Drillworks® Software Pro Training Manual, Predict and geostress. Training manual. Version 5000.0.3.

Halliburton, (2012). Geomechanics: Orange Basin Drilling Study. [Power Point Presentation]

Hodges, K., (1996). The geology of the deep marine sandstones of the 9At-to-13At interval in the central in the Bredasdorp Basin. SOEKOR unpubl. Rept., SOE-EXP-RPT-342, pp. 16.

Honiball, A., (1995). Palaeogeographic maps of offshore South Africa. SOEKOR unpubl. Rept. Tech Note No. 56, pp. 11.

Horsrud, P., (2001). Estimating mechanical properties of shale from empirical correlations. SPE Drill. Complete. 16, pp. 68-73.

Hugh Je-Marco. S., (2005). Assessment controls on reservoir performance and the effects of granulation seam mechanics in the Bredasdorp Basin South Africa, Master's Thesis. University of the Western Cape, South Africa, pp. 161.

Jaeger, J.C., Cook, N.G.W., Zimmerman, R.W., (2007). Fundamentals of Rock Mechanics, 4 ed. Blackwell Publishing, pp. 475.

Judd, W.R., (1964). Rock stress, rock mechanics and research, in: Judd, W.R. (Ed.), State of stress in the earth's crust. Elsevier, pp. 5-51.

Keaney, G., (2005). Drillworks 2005. Geostress and Wellbore Stability Short Course. Knowledge Systems, pp. 1-6.

Larsen, M., (1995). Overpressure study. SOEKOR unpubl. Tech. Note No. 29, pp. 12.

Li, S., George, J., and Purdy, C., (2012). Pore-Pressure and Wellbore-Stability Prediction to Increase Drilling Efficiency. Journal of Petroleum Technology, pp. 98-101.

McAloon, W., Webster, M., and Elliot, S., (1990). The occurrence of overpressure in the South African continental shelf. Abstracts Geocongress 90, Geol. Soc. S. Afr., pp. 349-352.

McLean, M., and Addis, M.A., (1990). Well bore stability: the effect of strength criteria on mudweight recommendations. *65th Annual Technical Conference and Exhibition of the Society of Petroleum Engineers*, New Orleans, Society of Petroleum Engineers, pp. 7-9.

McMillan, I.K., (1986). Cainozoic planktonic and larger foraminifer's distribution around Southern Africa and their implication for past changes of oceanic water temperature. S. Afr. Jour. Sci., 82, pp. 66-69.

McMillan, I.K., Brink, G.J., Broad, D.S., and Maier, J.J., (1997). Late Mesozoic sedimentary basins off the Coast of South Africa: Sedimentary basins of the world, African basins, 3rd ed. edited by R.C. Selley, p. 319-376.

McNally, G.H.N., (1987). Estimation of coal measures rock strength using sonic and neutron logs. *Geoexploration*, 24, pp. 381–395.

Mimonitu, O., (2010). Petrophysical Evaluation of the Albian Age Gas Bearing Sandstone reservoir of the O-M field, Orange Basin, South Africa, PHD thesis. University of Western Cape, South Africa, pp. 34.

Petroleum Agency SA, (2005). South African Exploration Opportunities, South African Agency for Promotion of Petroleum Exploration and Exploitation, Cape Town, pp. 27.

PetroSA, (2013). Graduate In Training: Lecture Notes. [Powerpoint presentations].

Plumb, R., Edwards, S., Pidcock, G., Lee, D., and Stacey, B., (2000). The Mechanical Earth Model Concept and Its Application to High-Risk Well Construction Projects. IADC/SPE Drilling Conference, New Orleans, Louisiana. IADC/SPE # 59128.

Rahim, Z., Al-Qahtani M.Y., Bartko, K.M., Goodman, H., Hilarides, W.K., and Norman, W.D., (2003). The Role of Geomechanical Earth Modelling in the Unconsolidated PreKhuff Filed Completion Design for Saudi Arabian Gas Wells. SPE Annual Technical Conference and Exhibition, Denver, Colorado. October 2003. SPE # 84259.

Rider, M., (1996). The Geological Interpretation of Well Logs: Scotland, Whittles publishing, 2nd Edition, pp. 280.

Rider, M., (2002). The Geological Interpretation of Well Logs: Scotland, Whittles publishing, 3rd Edition pp. 280.

Rocha, L.A.S., Falcão, J.L., Goncalves, C.J.C., Toledo, C., Lobato, K., Leal, S., Lobato, H. (2004). Fracture Pressure Gradient in Deepwater, IADC/SPE Asia Pacific Drilling Technology Conference and Exhibition, Kuala Lumpur, Malaysia, 13-15., SPE Paper 88011 pp. 17-34.

Rowsell, D.M., and De Swardt, A.M.J., (1976). Diagenesis in Cape and Karoo sediments, South Africa, and its bearing of their hydrocarbon potential. Trans. Geol. Soc. S. Afr., 79/1, pp. 81-145.

Santana, L., (2010). Manual for using the density correction software. Internal Manual, PetroSA, Cape Town, pp. 2-12.

Schlumberger, (1989). Cased Hole Log Interpretation Principles. In: Guide to Petrophysical Interpretation, Ed: Krygowski, D., Austin Texas, U.S.A, 2003, pp. 137.

Schlumberger, (2012). Schlumberger Oilfield Glossary. Available at: http://www.glossary.oilfield.slb.com

Tang, H., Luo, J., Qiu, K., Tan, P.C. (2011). Worldwide Pore Pressure Prediction: Case Studies and Methods.SPE-140954-MS. SPE Asia Pacific Oil and Gas Conference and Exhibition, 20-22 September, Jakarta, Indonesia.

Tiab, D., and Donaldson, E, C., (1996) Petrophysics - Theory and practice of measuring reservoir rock and fluid transport properties. In: Well Logging for physical properties Ed: Joseph, R.H., Philip, H.N., and Fredrick, L.P. John Wiley & Sons Ltd, England, pp. 3-461.

Timetrax, (1999). A biostratigraphic study through the syn-rift section of six wells in the F-O and F-S areas and the F-A field, Bredasdorp Basin, offshore South Africa: Private report for PGS Reservoir (UK) LTD: Project No. B0991, pp. 8-14.

Turner, J.R., Grobbler, N., and Sontudu, S., (2000). Geological modelling of the Aptian and Albian sequences within Block 9, the Bredasdorp Basin, offshore South Africa: *Journal of African Sciences*, 31(1), pp. 80.

Van der Merwe, R., and Fouché, J., (1992). Inversion tectonics in the Bredasdorp Basin, offshore South Africa. In: "Inversion tectonics of the Cape Fold Belt, Karoo and Creataceous Basins of Southern Africa". (Eds.) De Wit, M.J., and Ransome, I.G.D., A.A. Balkema, Rotterdam, pp. 49-59.

Van Der Spuy, D., (2000). Early-Aptian potential source rocks in the South African Cretaceous basins, Journal of African Earth Sciences, Geocongress 2000: A new millennium on ancient crust, 27th Earth science Congress of the Geological Society of South Africa, edited by Kisters, A.F.M., and Thomas, R.J., pp. 83.

Van Wagoner, J.C., Mitchum, R.M., Campion, K.M., Rahmanian, V.D., (1990). Siliciclastic sequence stratigraphy in well logs, cores, and outcrops: Concepts for High-Resolution correlation of time and facies. Am. Association. Petrol. Geol. Methods in exploration series, No. 7, pp. 55.

Verfaille, E.J.J., (1993). A synopsis of RFT data acquired in wells in the Bredasdorp Basin, including regional plots. SOEKOR unpubl. Rept., SOE-PET-RPT-107, pp. 6.
Ward, C.D., Coghill, K., and Broussard, M.D., (1995). Pore- and Fracture-Pressure Determinations: Effective-Stress Approach. JPT, pp. 123-24.

Ward, C.D., and Clark, R., (1999). How to Identify Lost Circulation Problems with Real-time Pressure Measurement: Downhole Pressure Sensing heads off Deepwater Challenege. Elf EP-Editions, pp 86.

Winter, H. de la R., (1981). Progress report on geopressure interpretation: volumes 1 and 2. SOEKOR unpubl. Rept., pp. 57.

Wood, M., (1995). Development potential seen in Bredasdorp basin off South Africa. Petroleum Agency of South Africa. Cape Town, South Africa.

Zoback, M.D., (2007). Reservoir Geomechanics. Cambridge University Press.

Zhang, X., Koutsabeloulis, N., Heffer, K., (2007). Hydromechanical modelling of critically stressed and faulted reservoirs. AAPG Bulletin 91, pp. 31-50.

Knowledge Systems., (2006a). Drillworks Predict. Available [Online]:
http://ks.wholewheatcreative.com/uploads/DrillworksPredict2.pdf

Appendix A: Density vs velocity plots simulated from the density correction software.

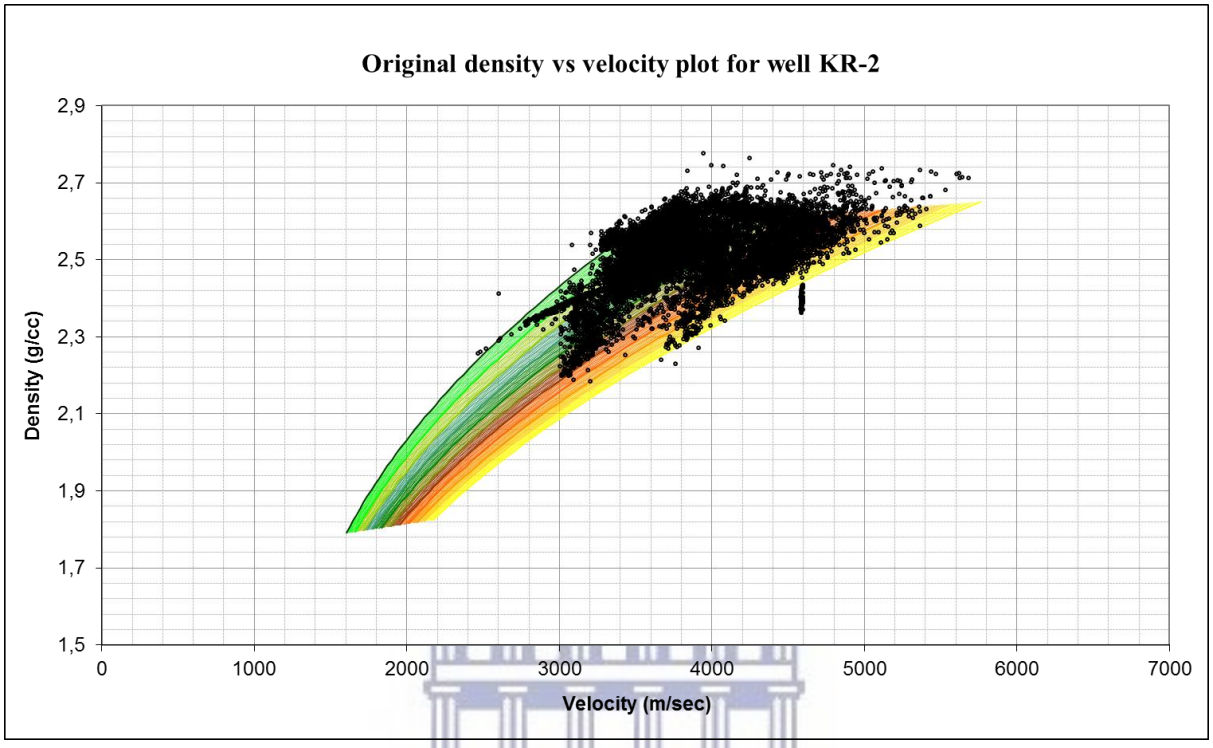

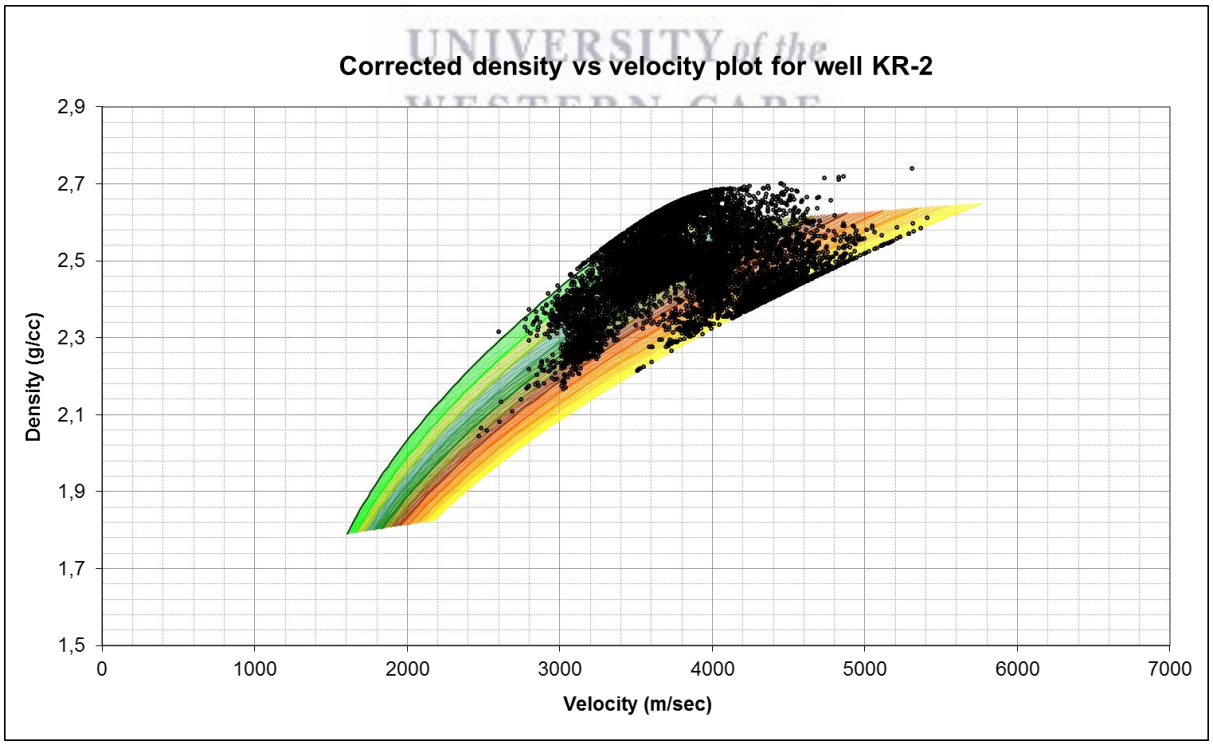

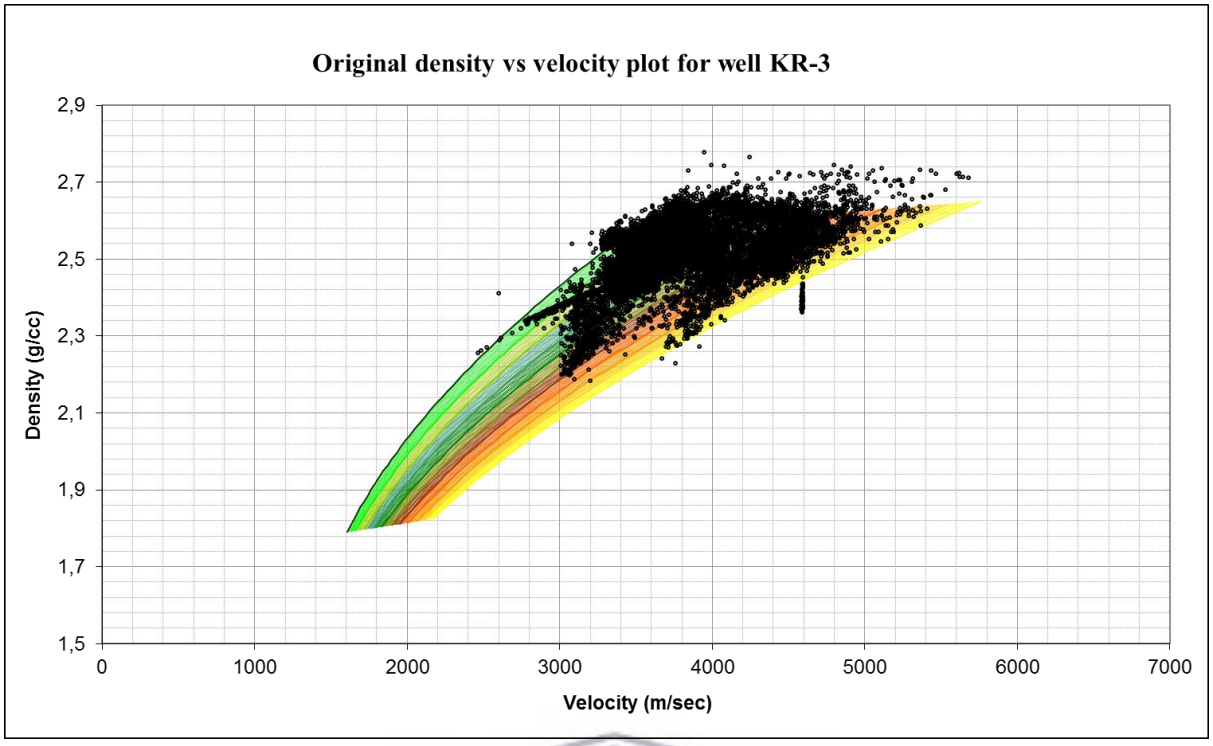

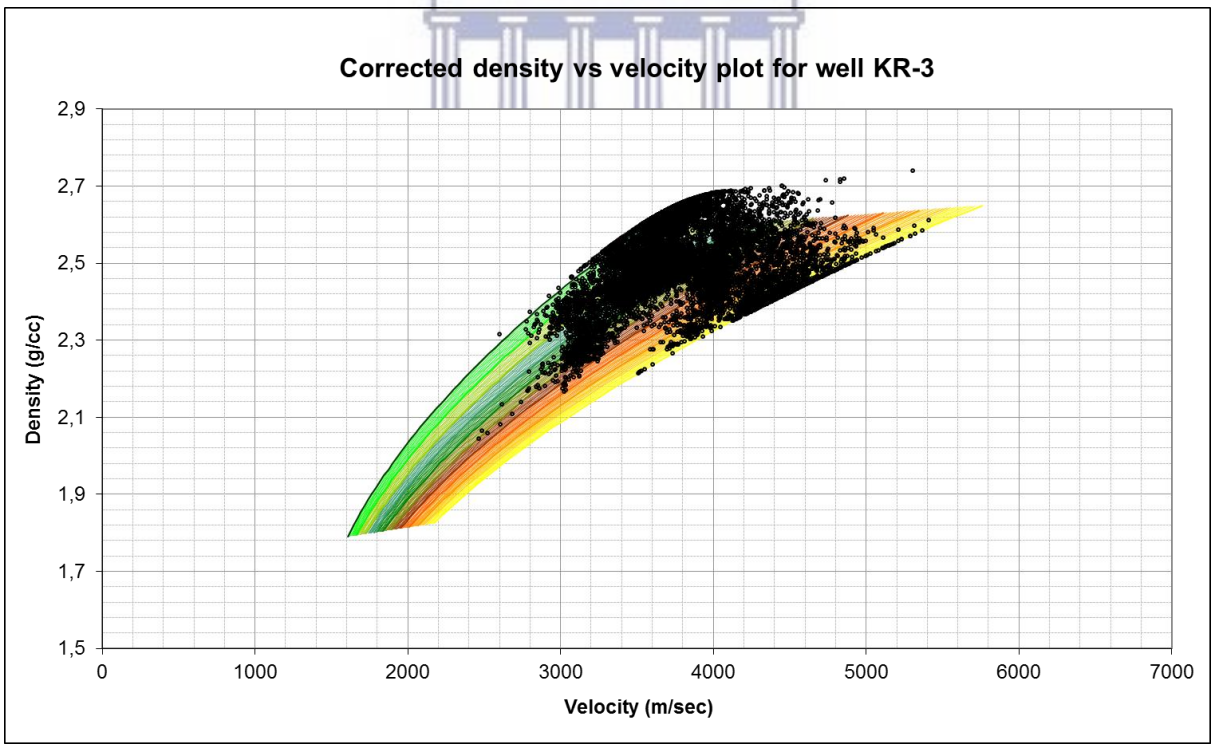

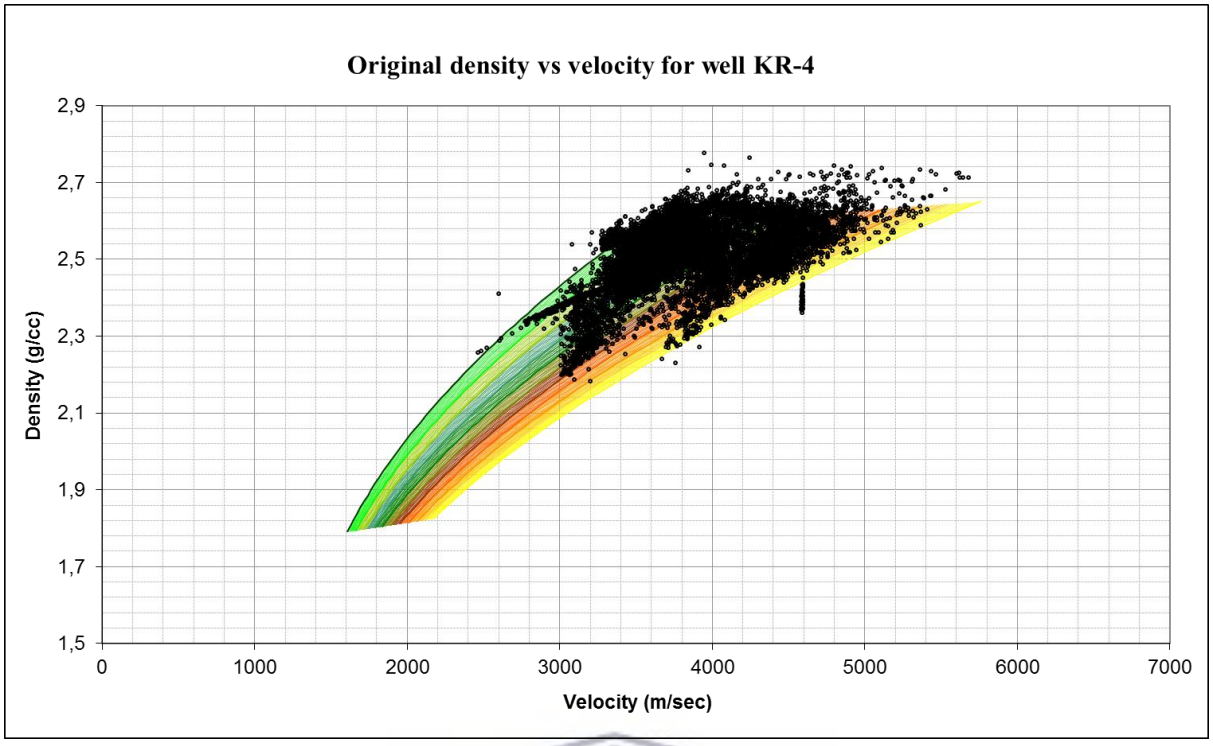

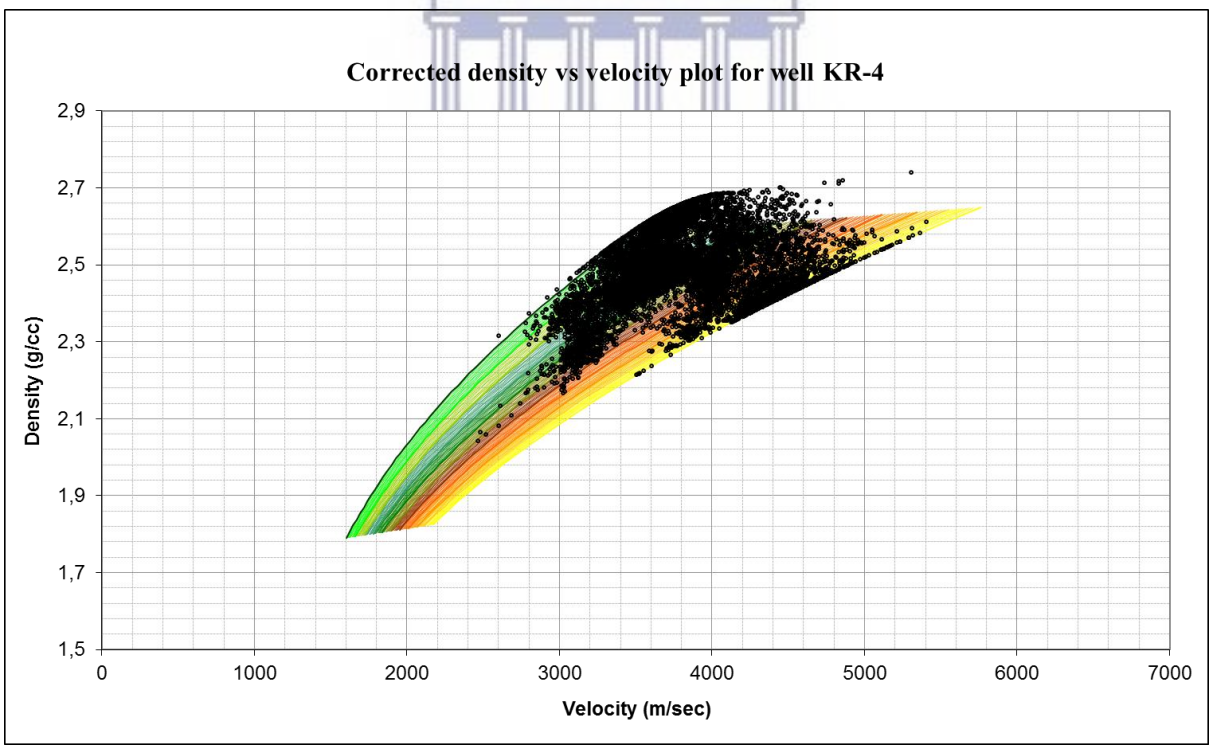

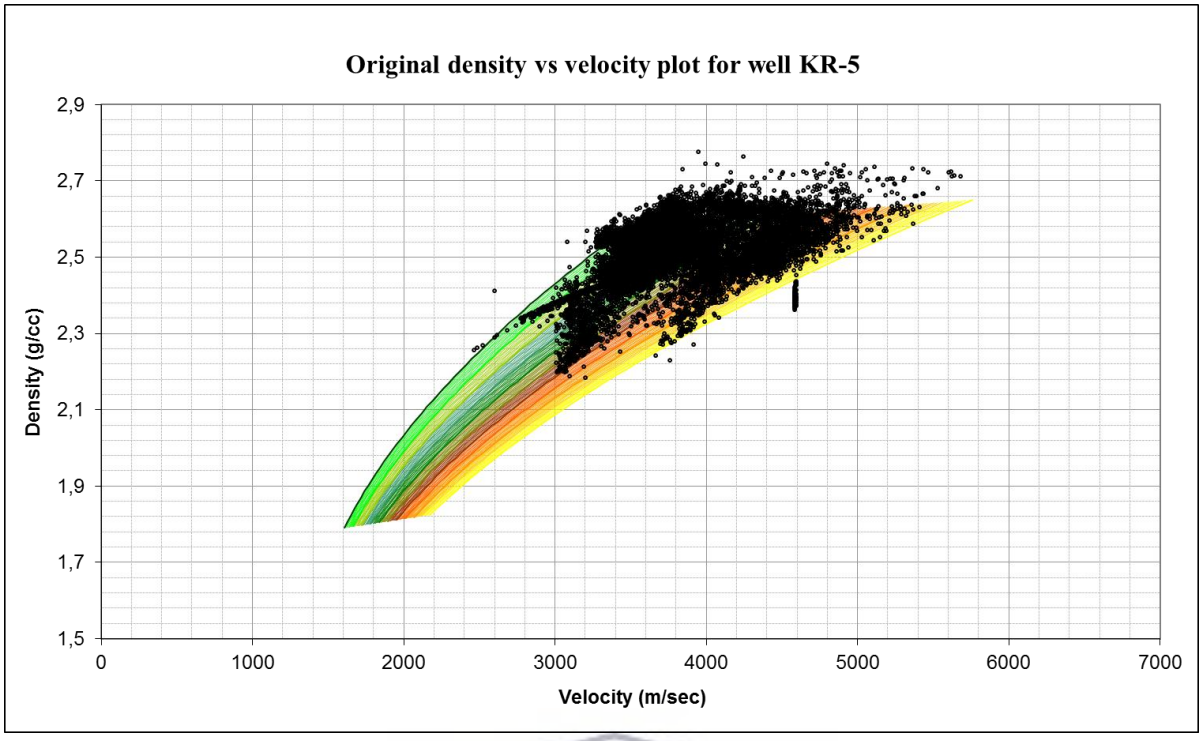

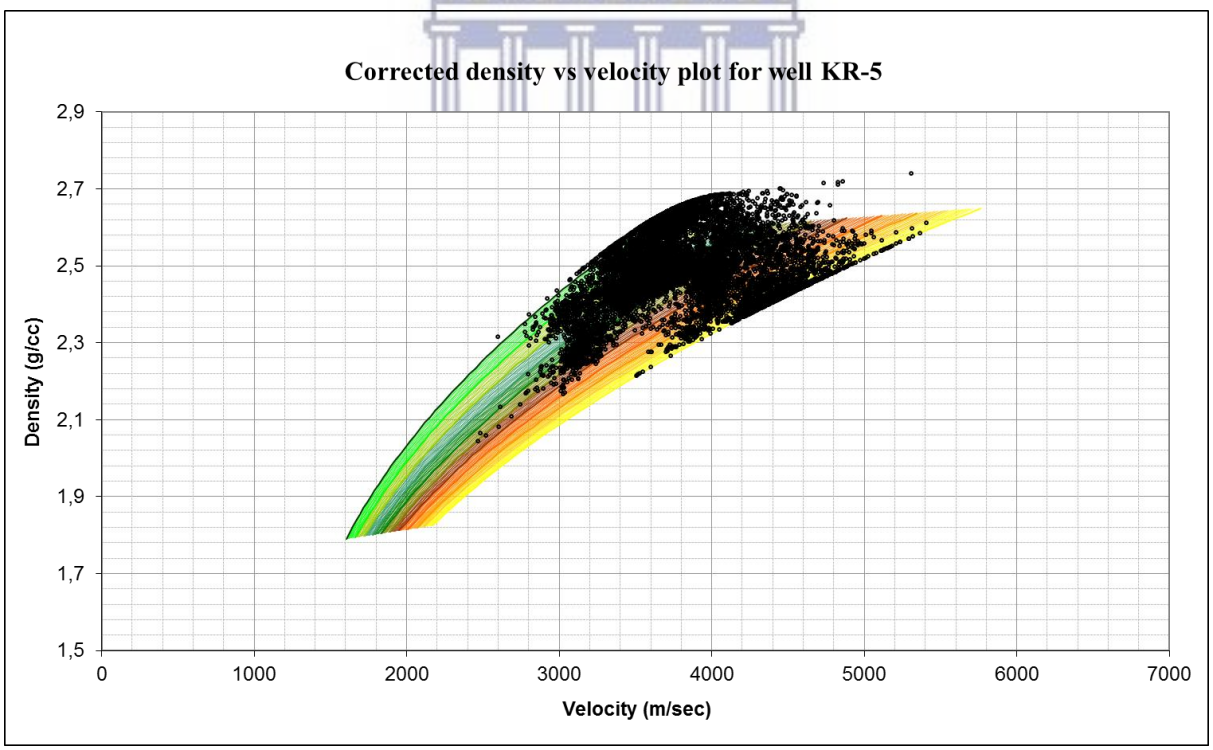

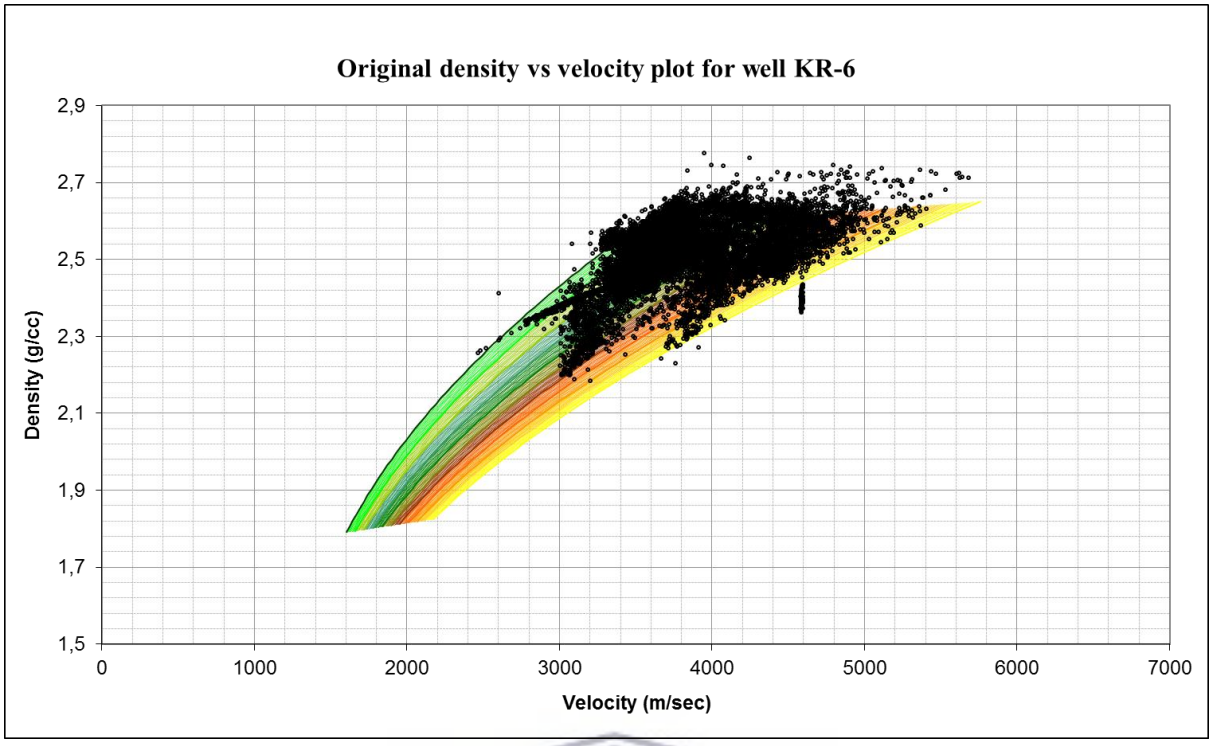

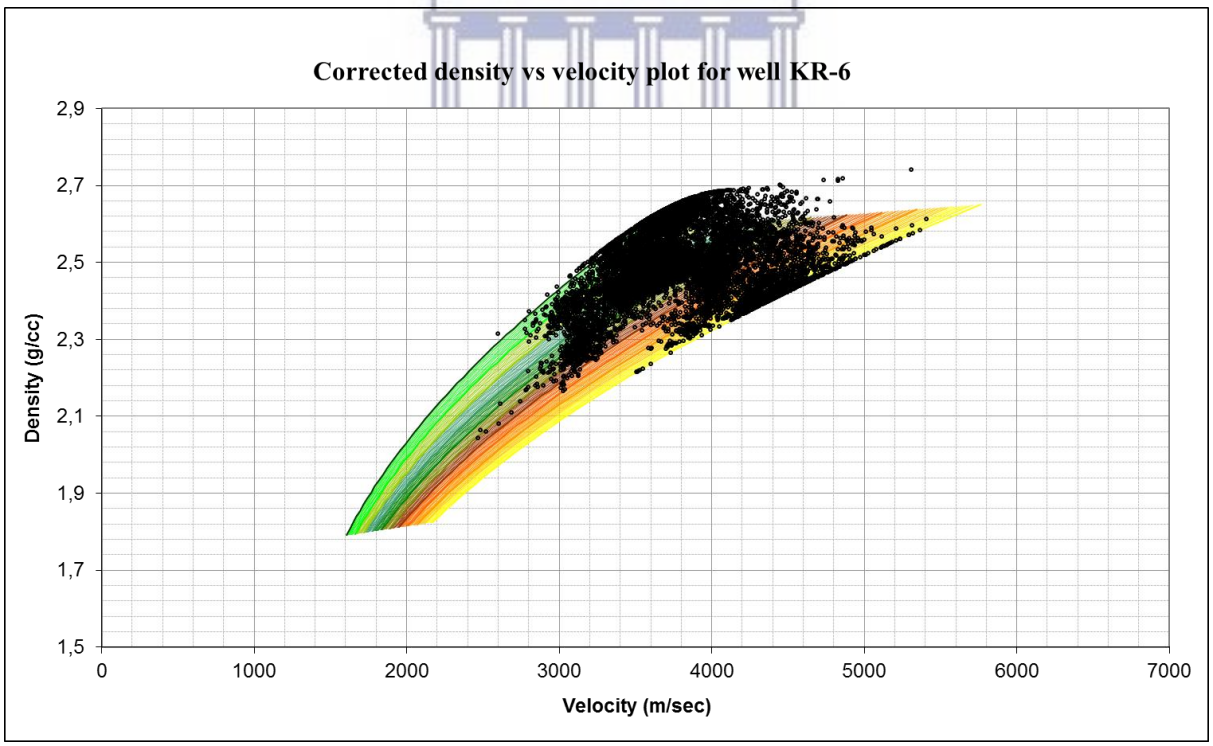

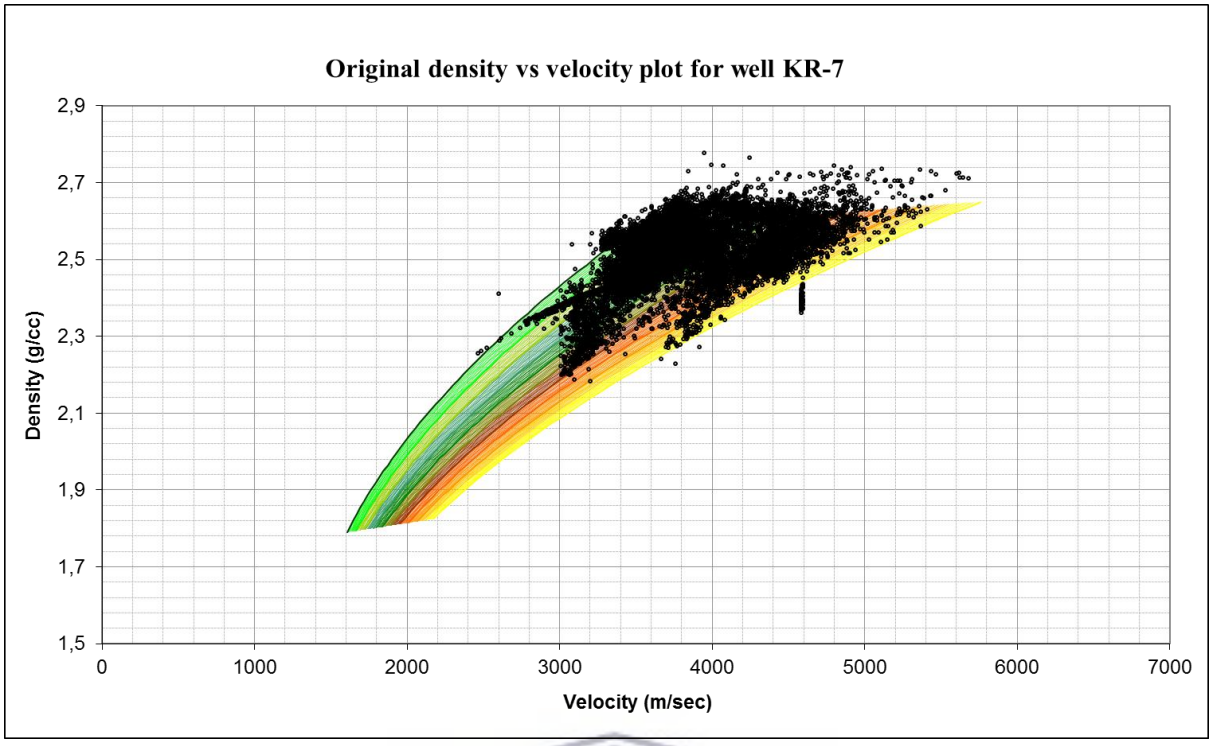

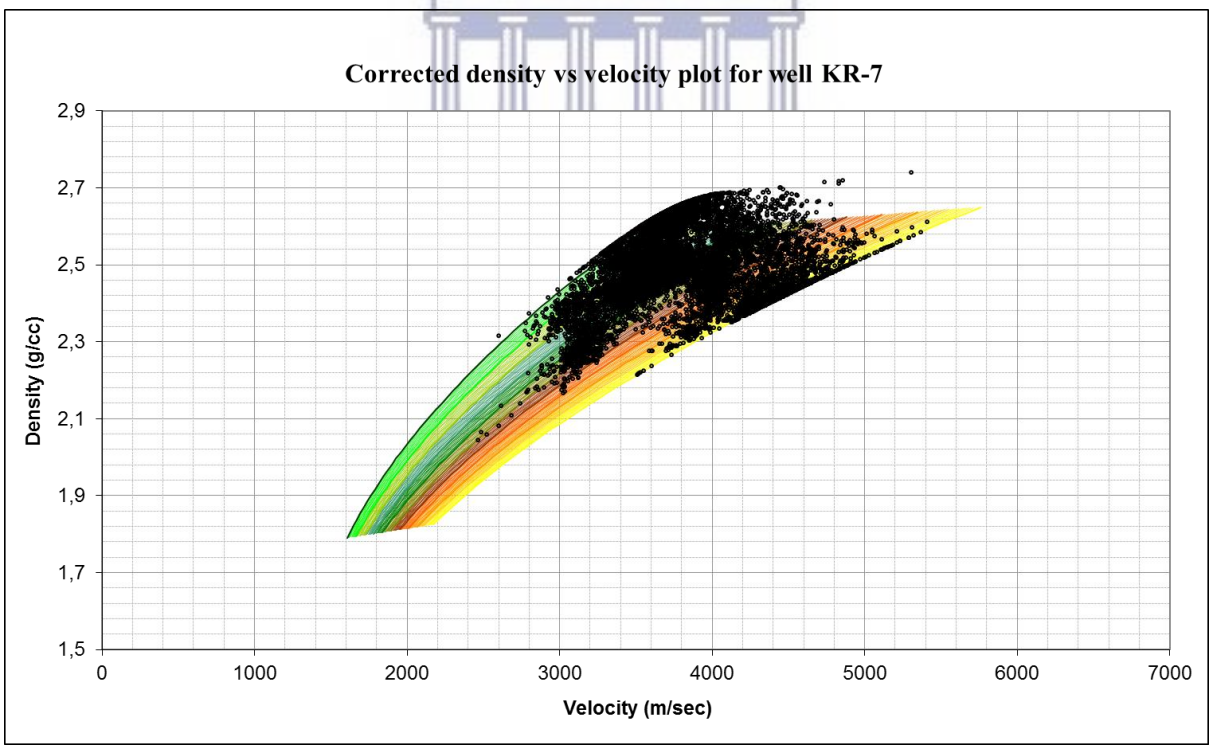

Appendix B: Density plots of corrected and uncorrected density.

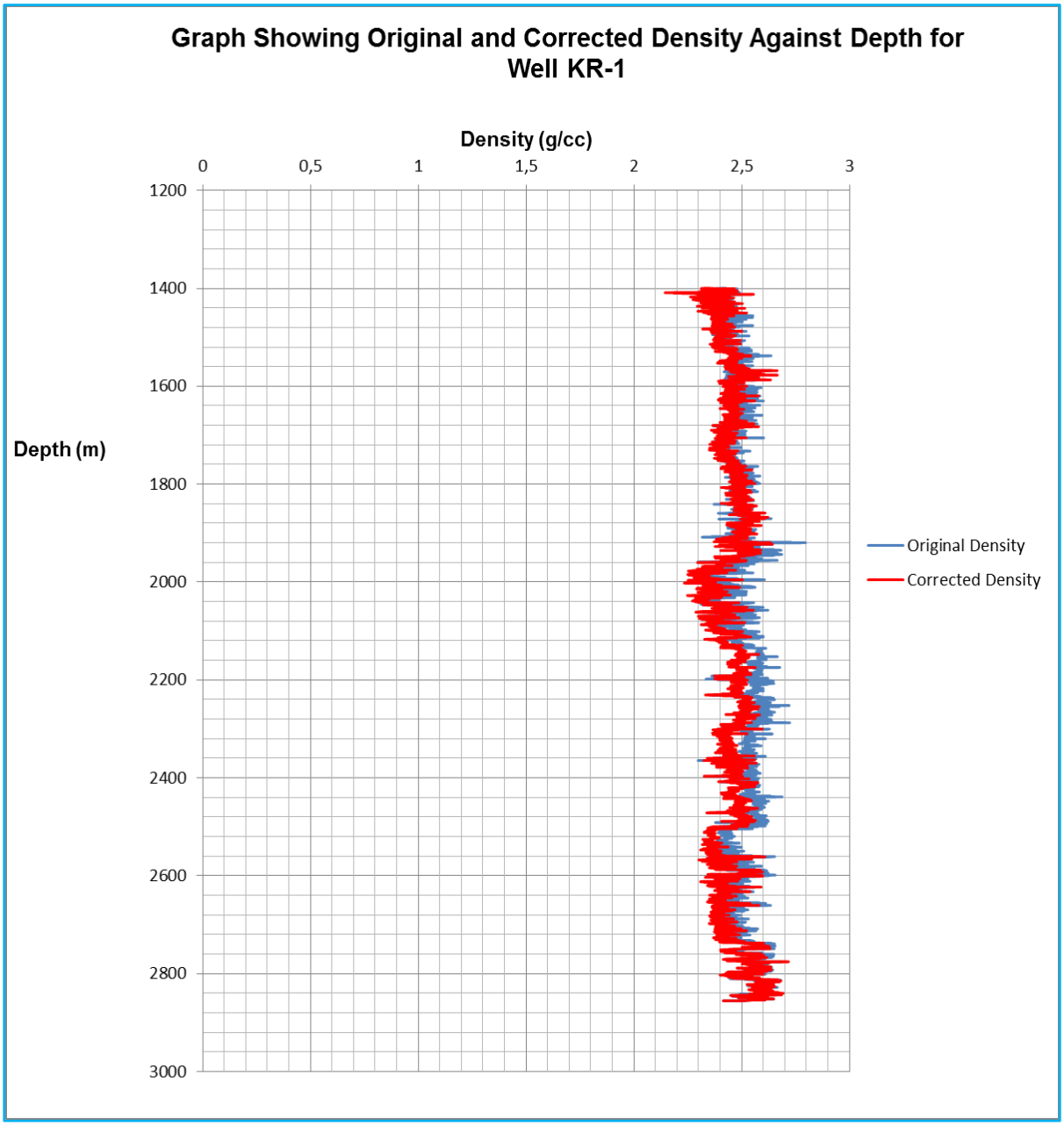

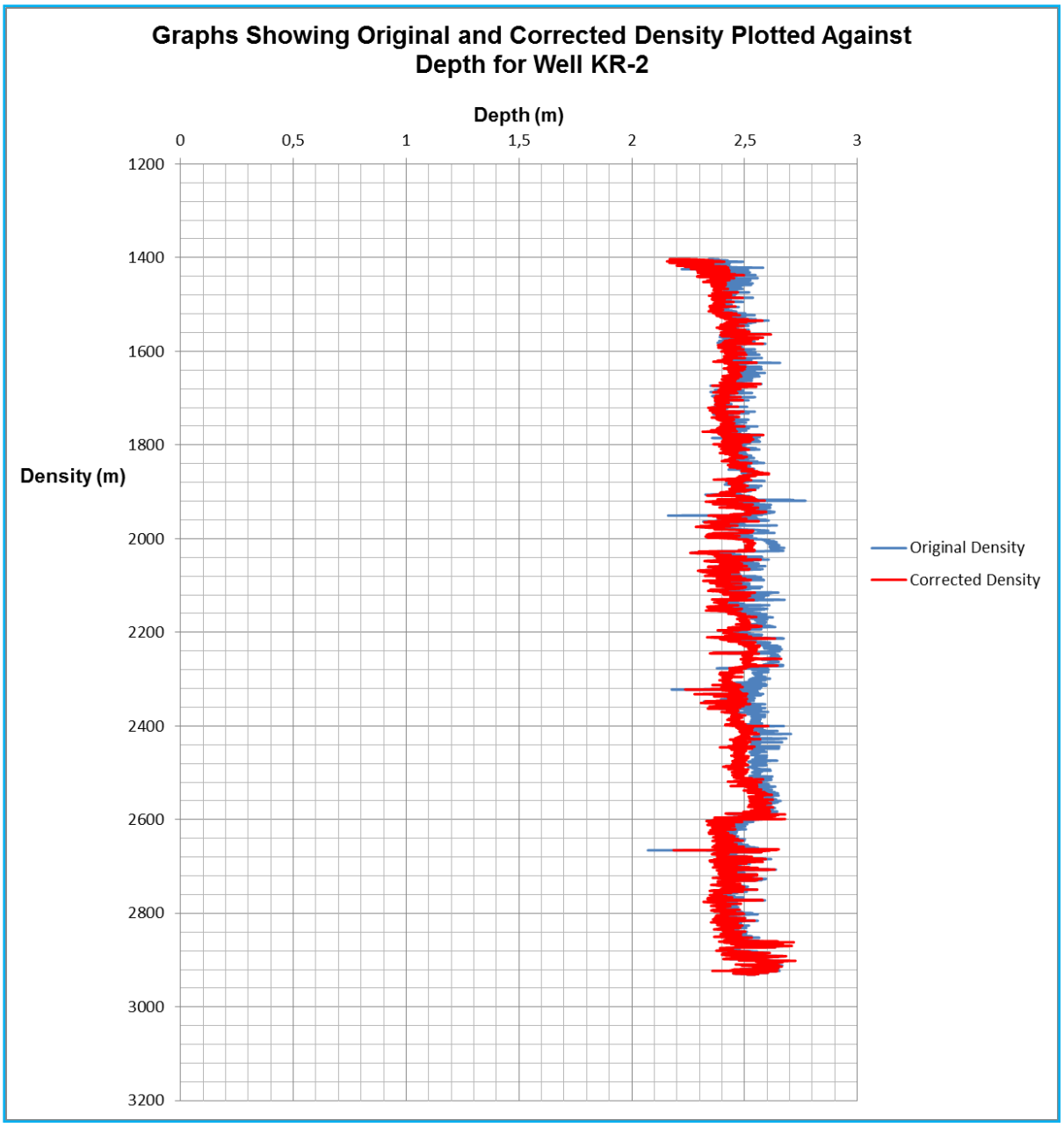

Graph Showing Original and Corrected Density Against Depth for Well KR-3

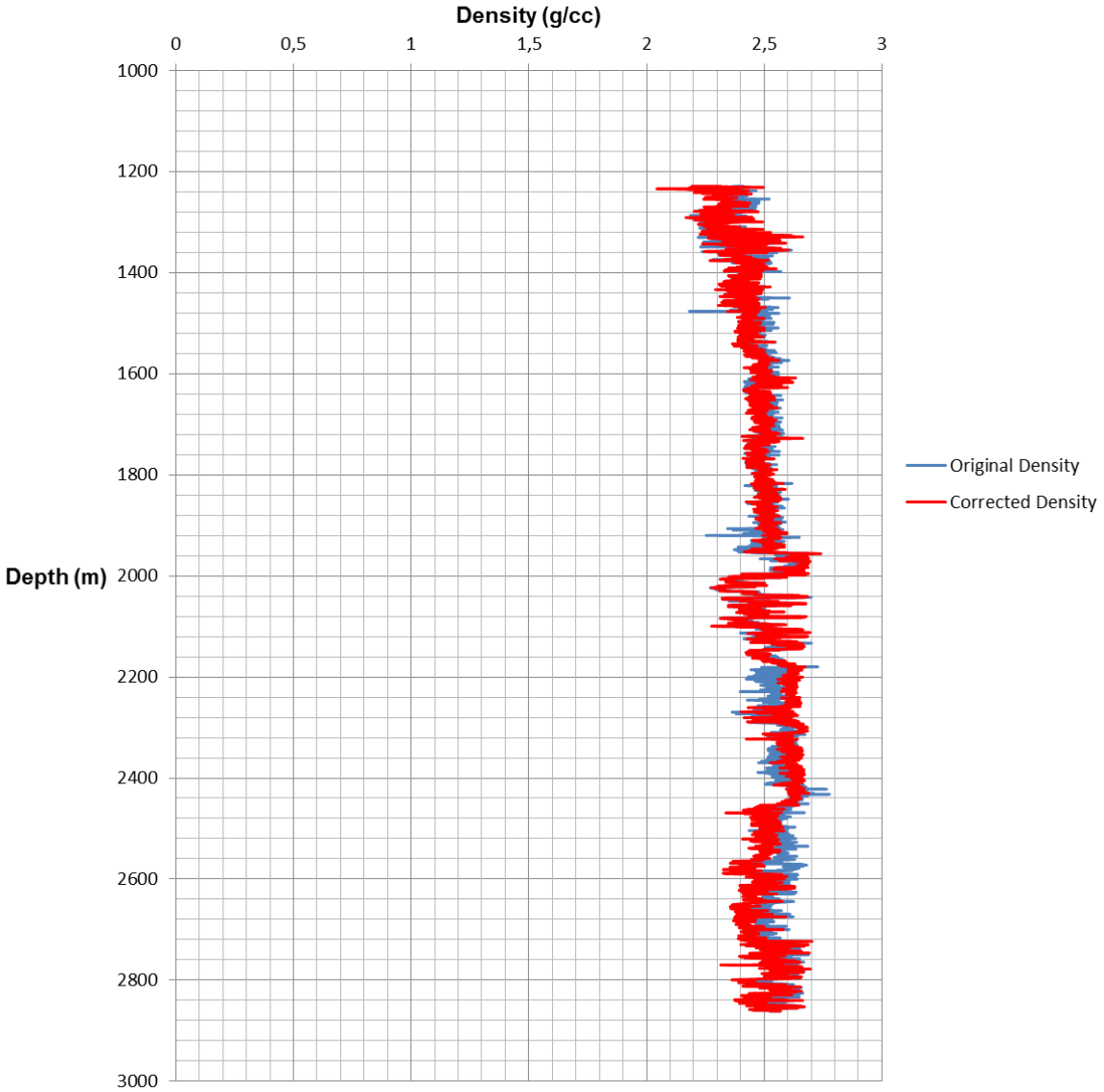

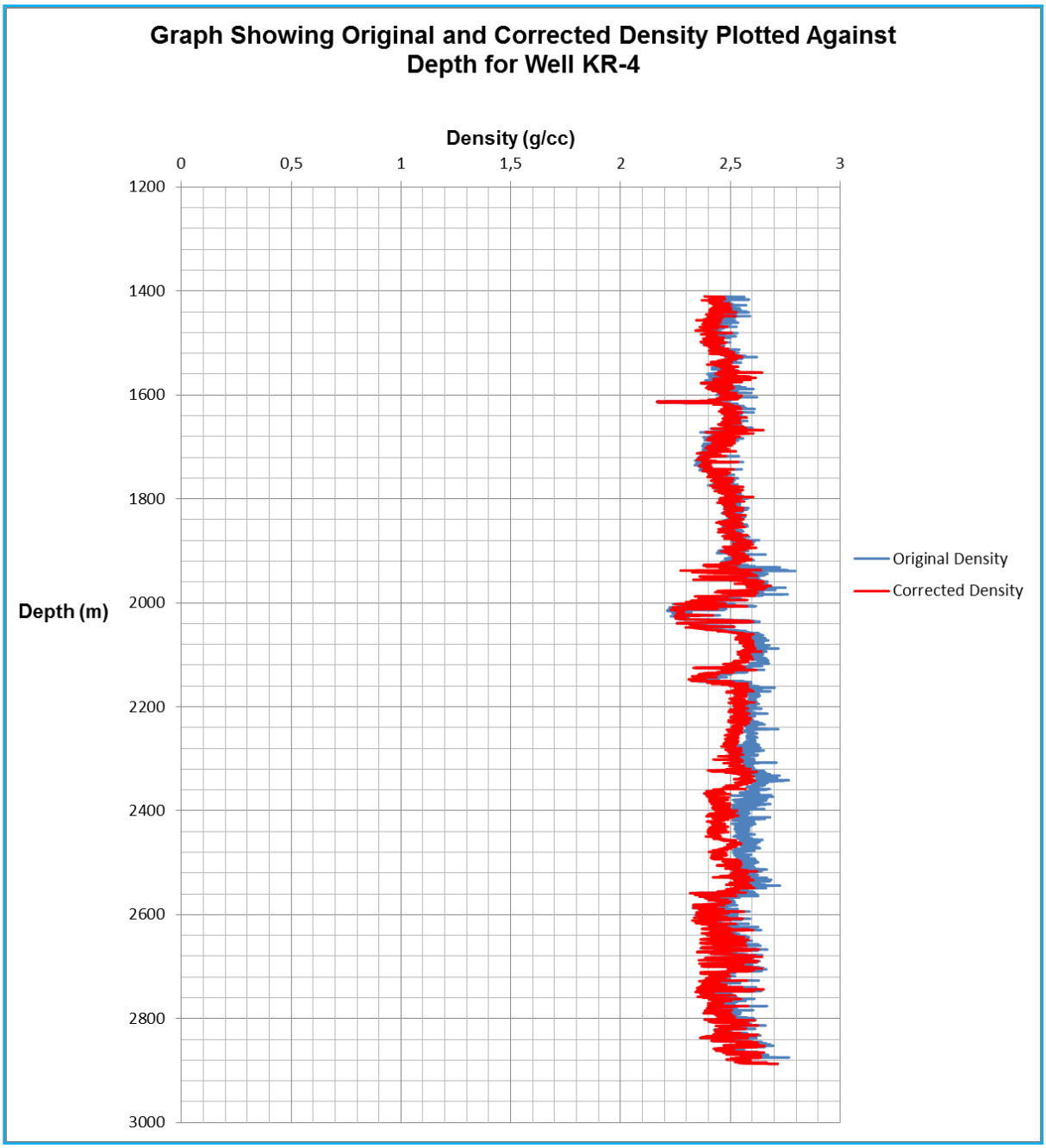

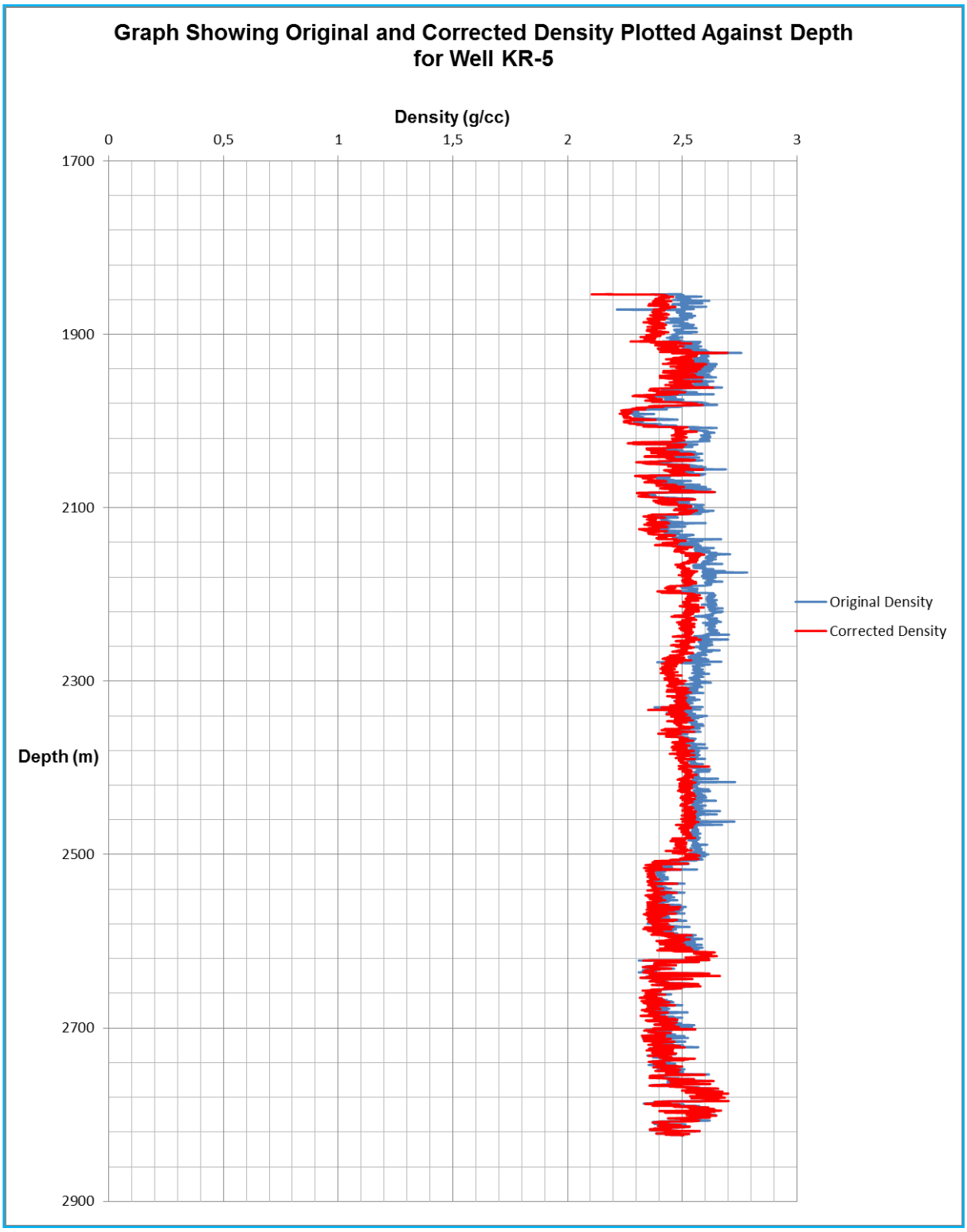

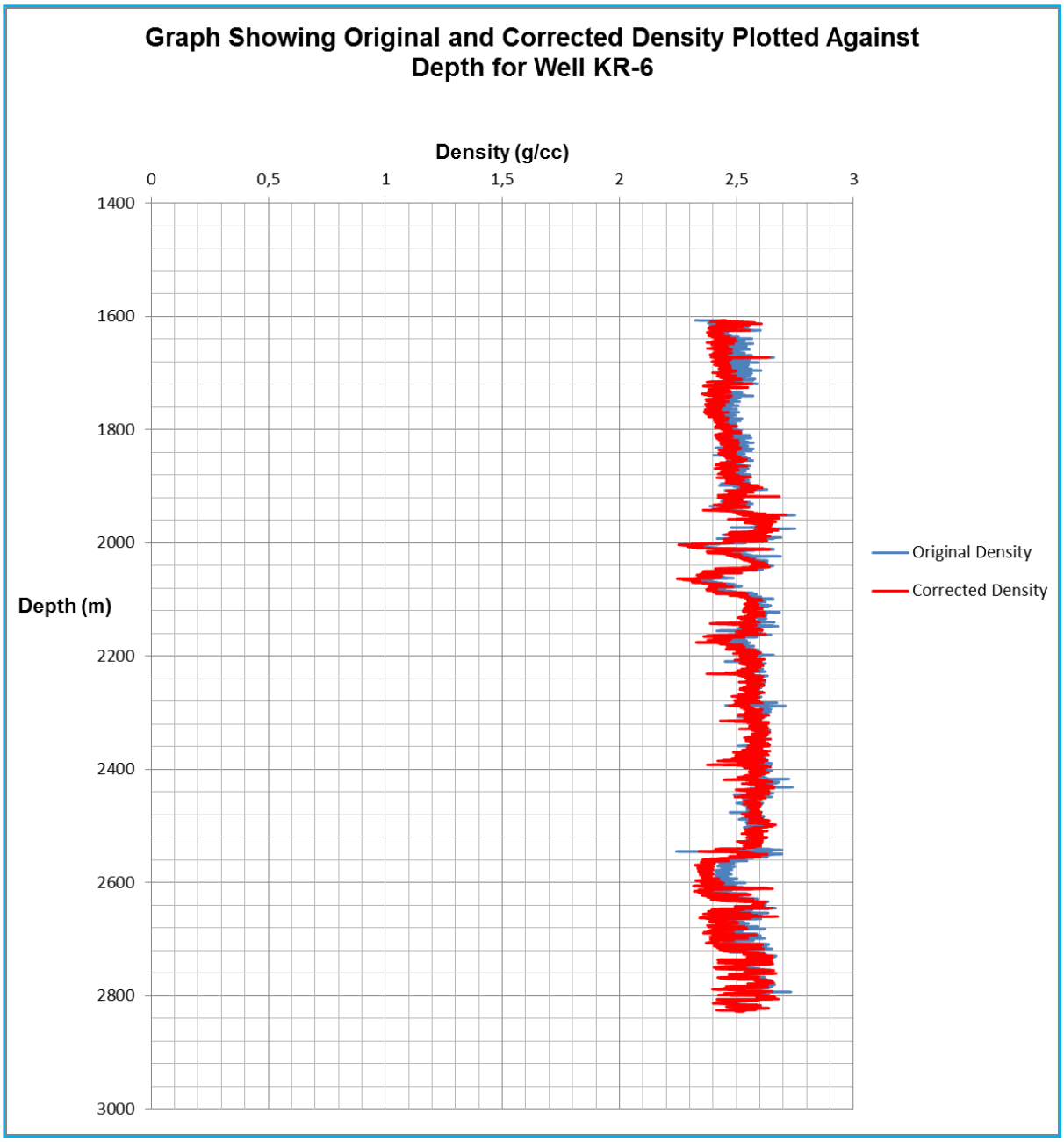

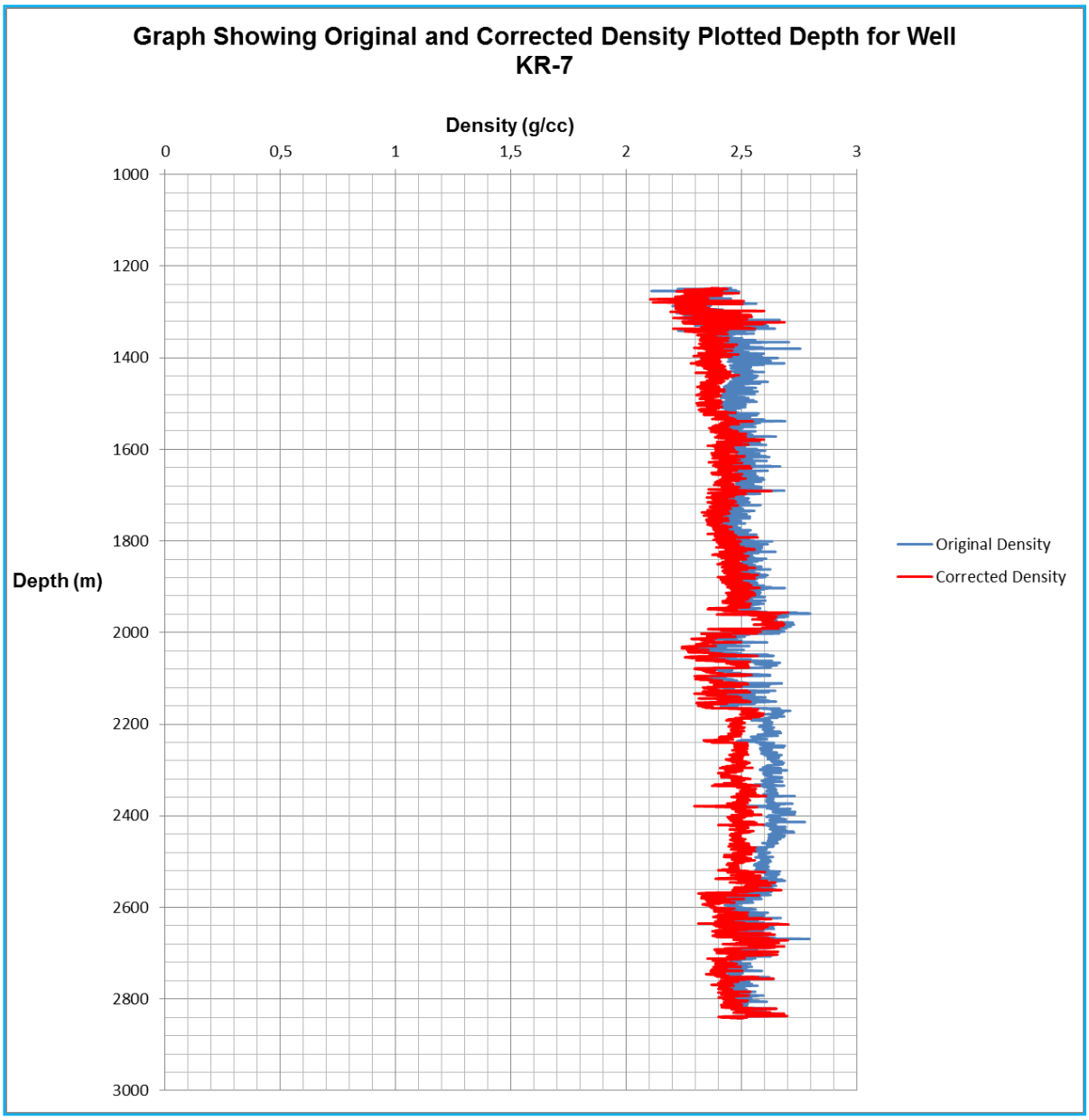

Appendix C: Caliper and bit size graphs along wellbore trajectory

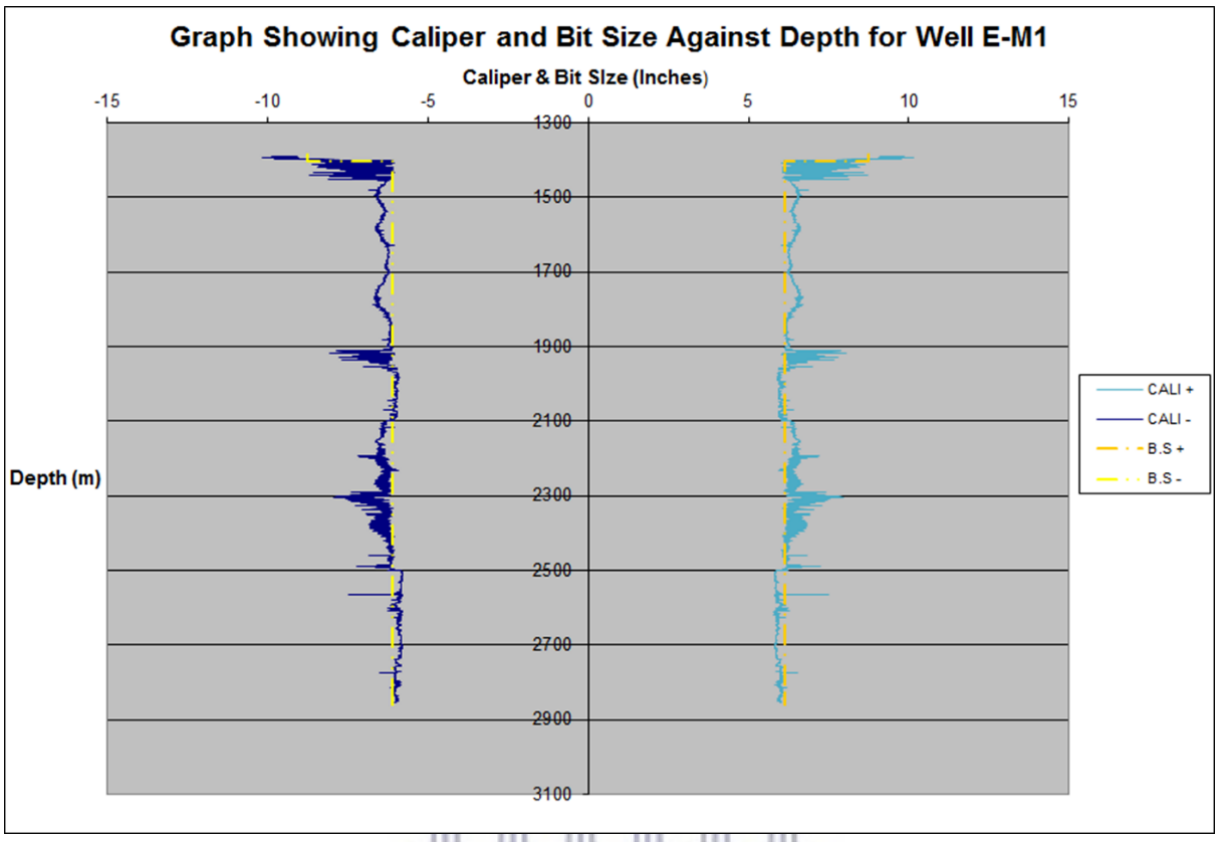

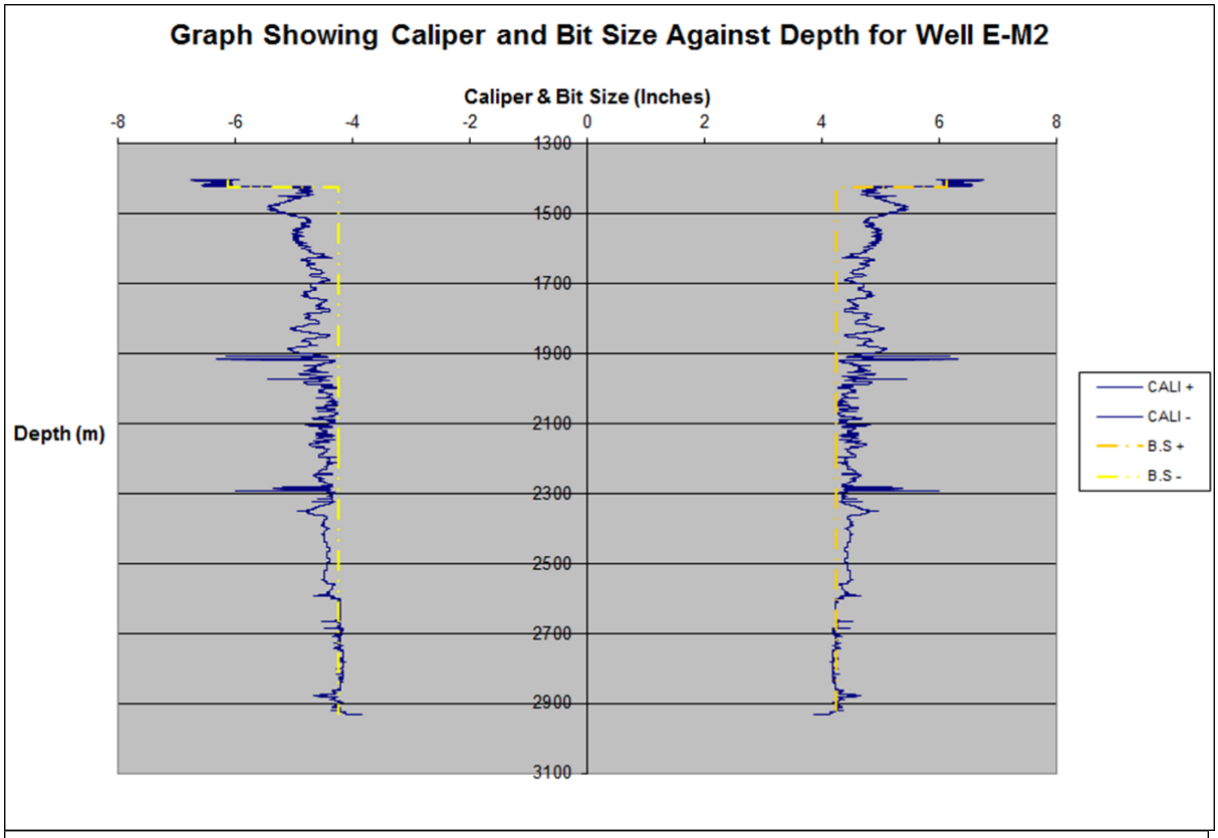

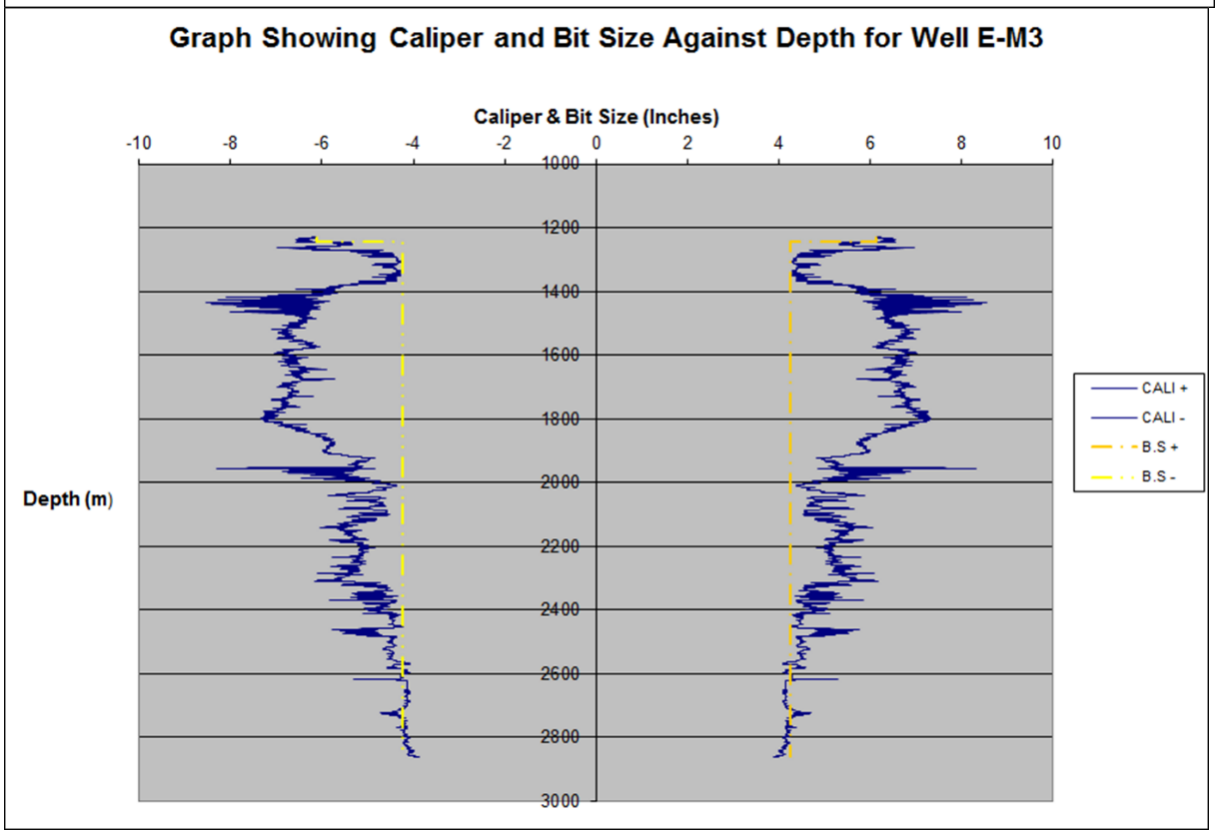

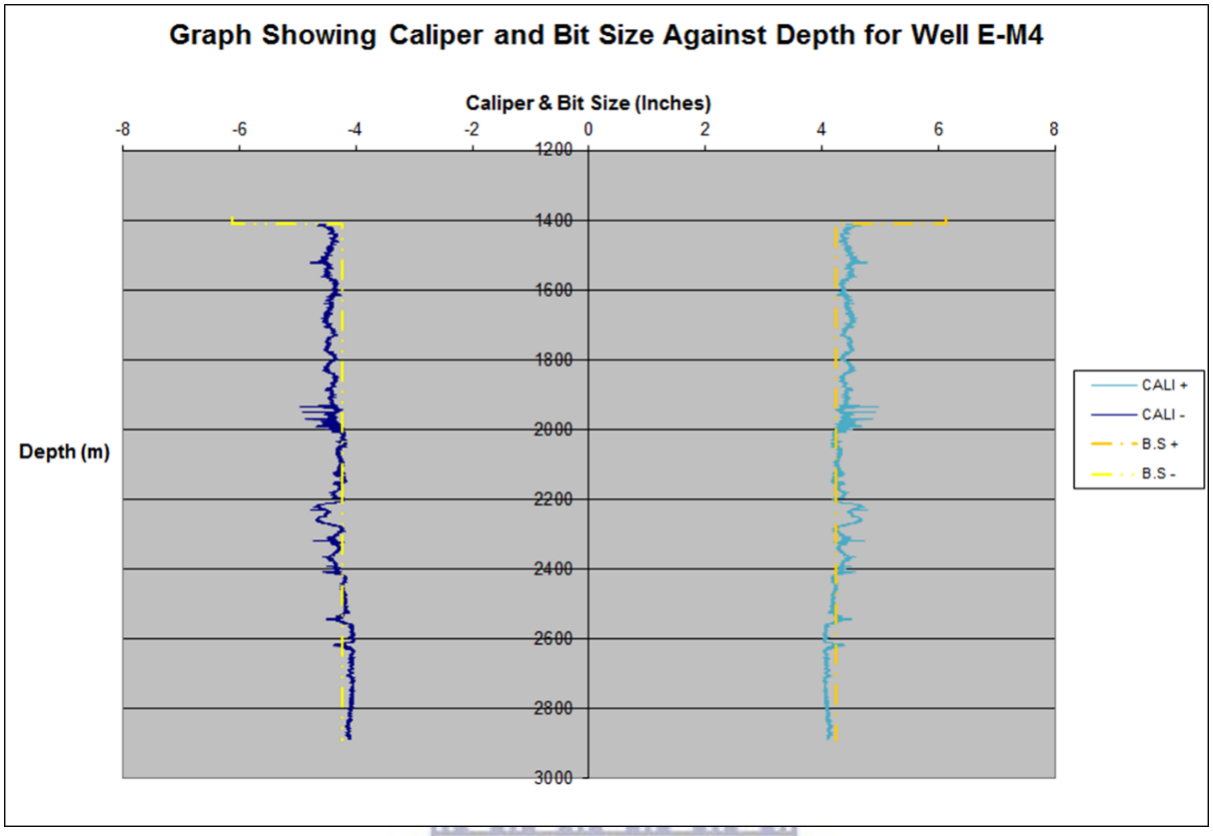

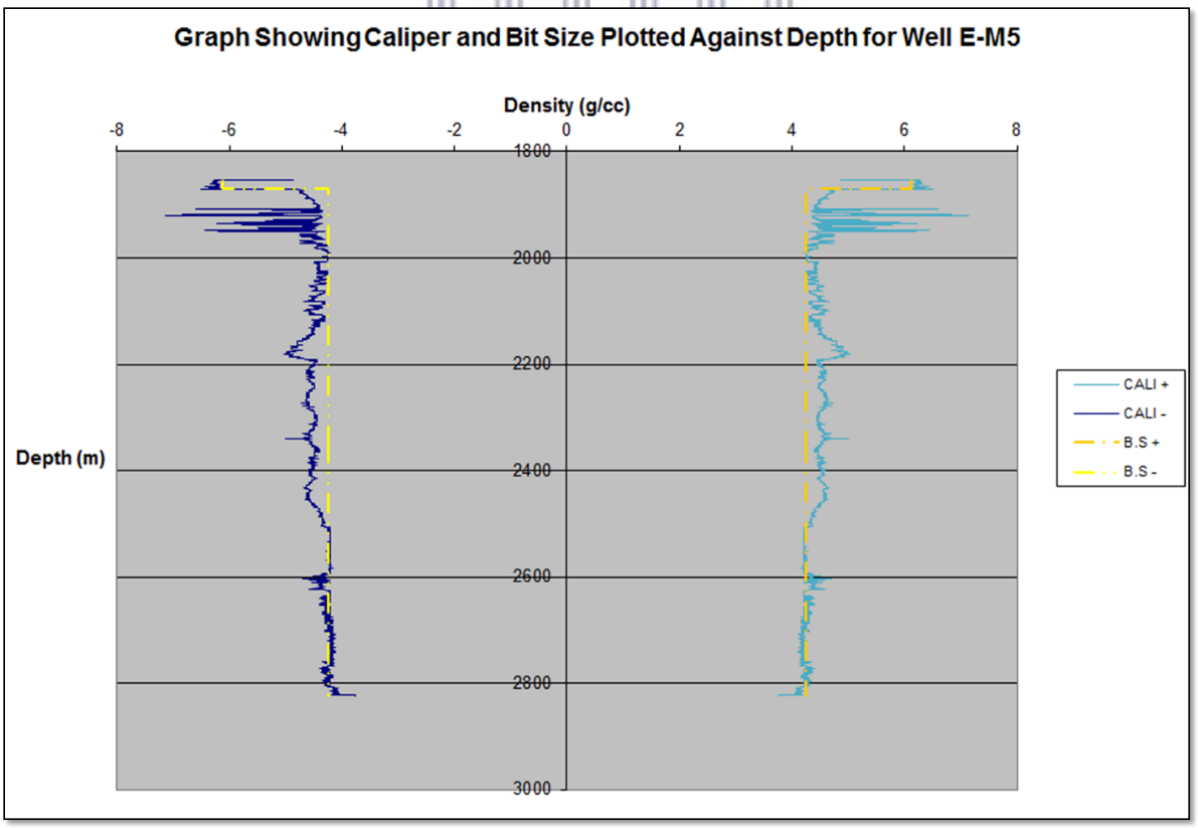

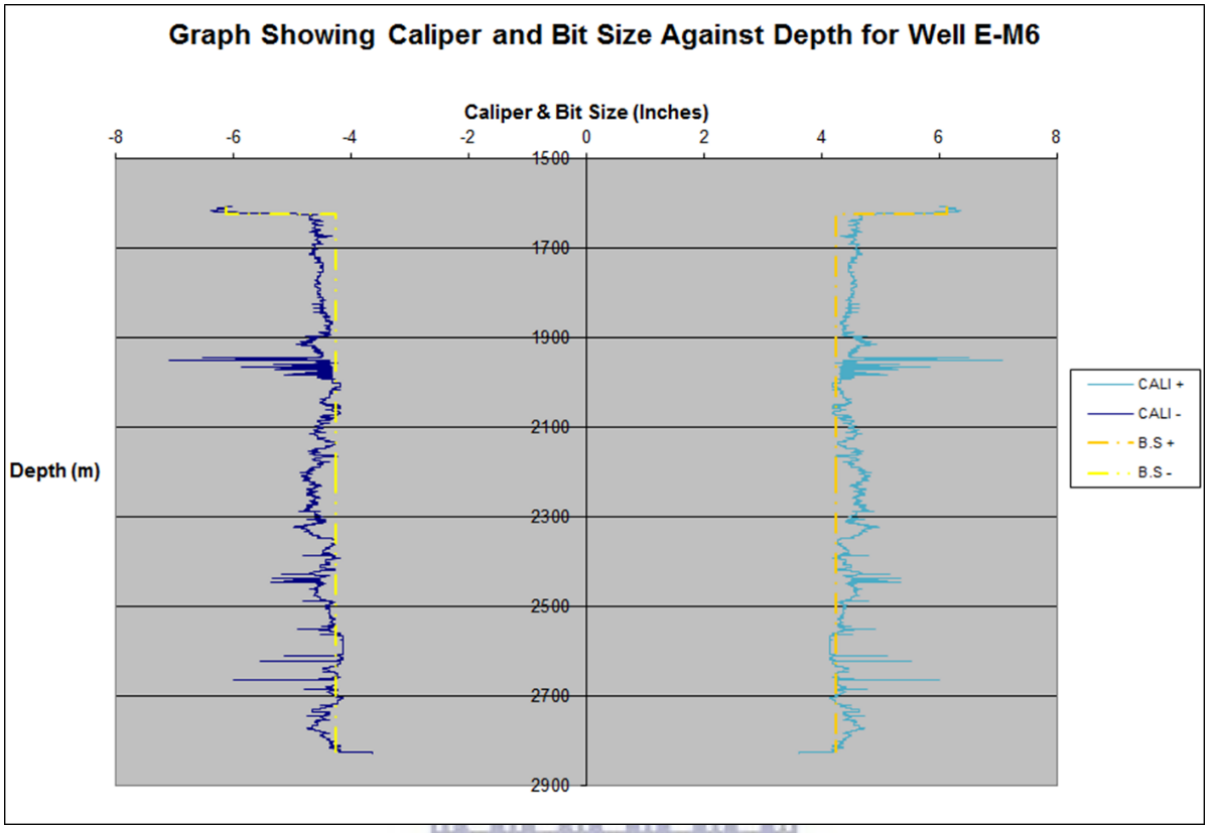

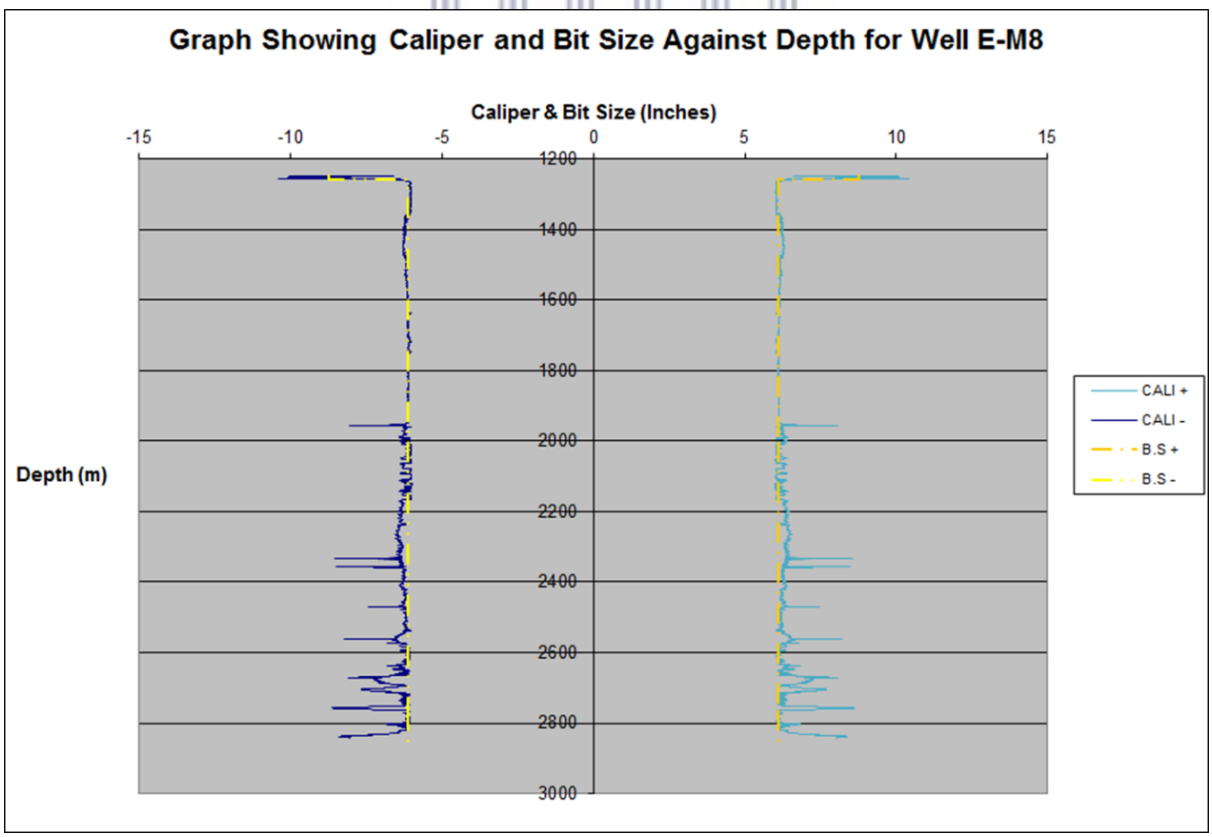

Appendix D: Normal Compaction Trendlines (NCT) for all wells.